DISSERTATION

EVALUATION OF BONE MARROW LESIONS AS A MANIFESTATION OF SUBCHONDRAL BONE DISEASE

Submitted by

Holly Lynn Stewart

Department of Clinical Sciences

In partial fulfillment of the requirements

For the Degree of Doctor of Philosophy

Colorado State University

Fort Collins, Colorado

Fall 2021

Doctoral Committee:

Advisor: Christopher E. Kawcak

Jeremiah T. Easley
Christian M. Puttlitz
Kurt T. Selberg

ABSTRACT

EVALUATION OF BONE MARROW LESIONS AS A MANIFESTATION OF SUBCHONDRAL BONE DISEASE

Osteoarthritis is a debilitating, progressive, and incurable disease affecting animals and humans alike. Degeneration of the articular cartilage and changes in the subchondral bone are considered the hallmarks of osteoarthritis. More recent research efforts have been directed toward detection of early changes within the subchondral bone, as these changes may precede changes in the articular cartilage. Compelling reports have cited bone marrow lesions (BMLs), also termed "bone bruises" or "bone edema," as an early indicator of maladaptive changes and structural deterioration within the subchondral bone. Despite the clinical importance of these lesions, BMLs are a challenge to diagnose as they require magnetic resonance imaging (MRI) to detect fluid signal within bone, and their progression is unpredictable—with some BMLs regressing completely, while others rapidly progress resulting in deterioration of the joint. A comprehensive understanding of the biological behavior of BMLs is made more difficult given that an experimental model of these lesions does not exist. Contemporary techniques in computed tomography (CT) and MRI provide promising new avenues for *in vivo* assessment of BMLs, ultimately translating into a greater ability to interpret their impact on the joint.

The compilation of studies presented in this dissertation were intended to develop an experimental model for BMLs using small and large preclinical animal models, to describe the imaging and histologic characteristics of BMLs, and to explore and optimize volumetric imaging modalities for assessment of fluid within bone. The impact of this work not only increases what

is known about BMLs, but provides a foundation for further work focused on describing the etiopathogenesis of these lesions.

The first part of this work describes three preliminary studies using advanced imaging modalities and techniques in the assessment of subchondral bone. Development of an *ex vivo* model for fluid within bone enabled a comparison for fluid detection across sequences using high-field MRI. Use of more contemporary sequences, such as the Dixon sequence, or modification of conventional imaging parameters of the short tau or short T1 inversion recovery (STIR) sequence improves fluid detection. From this work it was determined high-field MRI cannot distinguish between types of biological fluids based on signal intensity alone. The second described preliminary study evaluated sparse-view imaging with CT. Biological data acquired using μCT demonstrated a superior image quality with pixel sparsity regularization. Diagnostic images could be produced using only 60 projections. Techniques were then applied to cadaveric work with a cone-beam CT unit, where application of a novel algorithm (L1A) demonstrated an improved image quality with reduced artifacts at 60 views. In short, sparse-view CT imaging appears to be a promising technique for rapid evaluation of subchondral bone while preserving the high spatial resolution inherent to CT. The final preliminary study examined tomosynthesis in characterization of the equine metacarpophalangeal joint. Tomosynthesis was comparable or superior to radiography for detection of pathologic lesions, in part due to the ability of this modality to reduce superimposition of structures. Taken together, these studies describe the current and demonstrate some forthcoming techniques for non-invasive imaging assessment of subchondral bone.

Information from the aforementioned *ex vivo* studies were then applied in the context of development of an experimental model of BMLs using the ovine medial femoral condyle.

Findings from this study demonstrated that direct, focal trauma to all layers of the osteochondral unit is sufficient to induce the formation of a BML that persists for 90 days. Transcutaneous extracorporeal shockwave was insufficient for BML induction. When present, BMLs are dynamic and change rapidly as evaluated through serial imaging. Although fluid detection was similar across fluid-sensitive sequences on MRI, chemical-shift imaging sequences (e.g., Dixon sequence) provided a greater amount of information regarding the transition toward increasingly sclerotic bone within the BML. Ante-mortem CT and post-mortem μCT imaging corroborated these findings. Although BMLs were identifiable using a dual-energy technique with CT, the overall volume was less than what was observed with MRI. Although macroscopic evaluation of joints demonstrated minimal signs of degenerative articular cartilage, histologic evaluation of BMLs were consistent with an inflammatory response within the bone, followed by active bone remodeling and fibrous repair tissue within the defect with minimal changes to the articular cartilage.

In all cases, BMLs remained visible within the medial femoral condyle for the duration of the 90-day study. Given this, further work was needed to describe changes in experimental BMLs and the joint over time. In a long-term study using the same model, experimentally-induced BMLs were visible within the medial femoral condyle for 12 months, with subchondral cysts visible within the BML by 6 months after surgery. CT and MRI data demonstrated macroscopic remodeling within the subchondral and trabecular bone. Taken together, these studies suggest a potential etiopathogenesis for how a BML may result in degenerative osteoarthropathy.

This acute, focal experimental model was extrapolated for use in the rat femorotibial joint. Experimentally-induced BMLs in the rat medial femoral condyle mirrored many of the

same observations as compared to the ovine model, including confirmation of BMLs by 14 days after surgery. Notably, quantitative gait analysis identified a decrease in hindlimb loading and compensatory increase in forelimb loading after BML induction. BMLs in the rat had similar histologic characteristics including initial inflammatory cellular infiltrate replaced by fibrous and fibrocartilaginous repair tissue.

In summary, this collection of studies establishes that BMLs can be experimentally induced in both small and large preclinical animal models, and alterations within the subchondral bone can precede gross changes in the articular cartilage, causing what are likely irreversible structural changes that may impact long term joint function and health. Volumetric imaging modalities have an appropriate sensitivity to characterize some aspects of these changes ante-mortem, and newer techniques in both CT and MRI can be optimized for detection of BMLs. Further work histologically validating this experimental model for BMLs against naturally-occurring disease, and additional investigation of the cellular, molecular, and immunologic mechanisms of BMLs are required. Nonetheless, the results of this work provide an opportunity and framework to more deeply evaluate BMLs and the importance between these lesions, subchondral bone health, and joint function with applicability across species and conditions.

ACKNOWLEDGEMENTS

At the risk of stating the obvious, the success of this doctoral work reflects not only my dedicated efforts, but the contributions and support of so many others. I am humbled by and immensely grateful for those people who have defined the impact of this process. I am appreciative not only for the support I have received scientifically, but perhaps more importantly, for the encouragement in my development as a professional, and in learning how to be a veterinary clinical scientist.

First and foremost, I would like to thank my Graduate Committee, with special thanks to Dr. Chris Kawcak. Your exceptional talent, knowledge, and clinical abilities are an unparalleled combination that have benefited and empowered me in this process. You have encouraged me, challenged me, and fostered an environment and a graduate program that has allowed me to thrive. I cannot thank you enough for all the ways you have supported me and championed for my success—your impact on my career now and into the future is and will be immeasurable. I feel infinitely lucky to have you as both a mentor and a friend. To Dr. Jeremiah Easley, thank you for giving me the opportunity to be a part of the extraordinary group that is the Preclinical Surgical Research Laboratory—I will forever be grateful to be a part of this team with you as the leader. Thank you for believing in me, my research, and being unequivocally committed to supporting all my aspirations as a clinical veterinarian and researcher, and throughout it all, for being my friend. Thank you to Dr. Kurt Selberg, you have reminded me to have fun and enjoy this process. Thank you for your patience in teaching imaging to a surgeon, and for the laughs along the way. And to Dr. Christian Puttlitz, you have impacted this process more than you may

realize. Thank you for pushing me to raise my own standards and for the defining moments of guidance and encouragement, this process would not have been the same without you.

The contributions to this work extend far beyond my Graduate Committee. Thank you to everyone who has invested in my success, from Pioneer Equine Hospital, to New Bolton Center at the University of Pennsylvania School of Veterinary Medicine, to Colorado State University. Here at Colorado State University, I would especially like to thank everyone involved in the Preclinical Surgical Research Laboratory, especially Kim Lebsock, Katie Bisazza, Andres Bonilla, Katie Sikes, Cat Hersh, Niki Adams, Izzy Olaes, Lisa Mangin, Meaghan Monahan, and Wendy Villavicencio; the Equine Orthopaedic Research Center, especially Jennifer Daniels; the Orthopaedic Bioengineering Research Laboratory, especially Ben Gadomski, Cecily Broomfield, Lucas Nakamura and Jimmy Johnson; and at the Veterinary Teaching Hospital—thank you for every moment of learning, word of encouragement, and for all the fun along the way.

These studies would not have come to fruition without the generous financial backing of many groups and organizations. I would like to first acknowledge and thank the NIH Ruth Kirschstein Institutional National Research Service Award Training Grant (T32 NRSA), Biomedical Research Training for Veterinarians, as this funding is responsible for so much of my success and has inspired my future goals. Financial support for these projects has also been provided by the Zoetis Dual Training Grant through the American College of Veterinary Surgeons Foundations, the Storm Cat Career Development Award through the Grayson-Jockey Club Research Foundation, the Grayson-Jockey Club Research Foundation, the Graduate Research Grant Award through the American Association of Equine Practitioners Foundation for the Horse, the Wayne and Nancy Orthopaedic Fellowship, and the College Research Council at

Colorado State University. I have been exceedingly fortunate and I extend my sincerest appreciation to these sources for funding this work.

Thank you to my friends, both in this profession and outside of it. Thank you to Dr. Erin Contino, for your belief in my abilities as a young veterinary student a decade ago. Thank you for setting this whole course of events into motion and for the unwavering friendship throughout. Thank you to Drs. Jodie Daglish, Katie Ellis, Sherry Johnson, Kelly and Kristin Zersen, and Katie Bisazza for being equally as invested in my happiness as my success. Thank you to Dr. Kyla Ortved, for intrinsically supporting me through every part of this process—your optimism and perspective encouraged me every step of the way. And finally, thank you to Dr. Brad Nelson. I am not sure that I have the words to accurately express the depth of my gratitude and appreciation for you. You have always made the time to talk, teach, mentor, and help me through these past years. Thank you most of all for your friendship—you are an exemplary example of a professional and a friend.

Finally, thank you to my parents and family, to Carol, Bruce, Woolley, and Lauren. Thank you for loving me unconditionally and demanding that I pursue my passions; my accomplishments would not have been possible without you and the foundation of love you provided for me. Mom, thank you for being there for me every step of the way—you are extraordinary beyond measure, the greatest role model, and an unparalleled cheerleader; you have never stopped believing in my abilities, helping me to find my way through the greatest challenges. Thank you most of all to my husband, Ethan. Thank you for embracing this entire process, encouraging me to dream bigger, igniting my curiosity, and for never extinguishing my flames. You are the ultimate teammate and partner, and your steadfast loyalty is the backbone of

my success. I love you, Avery, and Cameron more than I could ever express—thank you for helping me make all of this possible.

TABLE OF CONTENTS

ABSTRACT....ii
ACKNOWLEDGEMENTS....vi

Chapter 1 – The Importance of Subchondral Bone in the Pathophysiology of Joint Disease....1
1.1 Introduction....1
1.2 Anatomy and Physiology of Subchondral Bone....2
1.3 Biomechanics and Pathophysiology of Subchondral Bone....4
1.4 Subchondral Bone Disease and Chronic Fatigue Injury....7
1.5 Bone Marrow Lesions....11
1.6 Principles of Diagnosis and Diagnostic Imaging....16
1.7 Computed Tomography....18
1.8 Purpose of Study....39
1.9 Research Overview....39
1.10 Specific Aims and Hypotheses....40
1.11 Figures....44
1.12 References....51

Chapter 2 – Imaging Characterization of Subchondral Bone Injury....61
2.1 Introduction....61
2.2 Ex Vivo Fluid Cannulation Model....62
2.2.1 Introduction....62
2.2.2 Materials and Methods....63
2.2.3 Results....67
2.2.4 Discussion....68
2.3 Limited-View Computed Tomography....71
2.3.1 Introduction....71
2.3.2 Materials and Methods....72
2.3.3 Results....75
2.3.4 Discussion....76
2.4 Comparative Evaluation of Tomosynthesis....78
2.4.1 Introduction....79
2.4.2 Materials and Methods....79
2.4.3 Results....85
2.4.4 Discussion....87
2.5 Figures....96
2.6 Tables....100
2.7 References....103

Chapter 3 – Development of an Experimental Model of Bone Marrow Lesions using the Ovine Femoral Condyle....108
3.1 Introduction....108
3.2 Materials and Methods....111

3.3 Results....126
3.4 Discussion....137
3.5 Figures....153
3.6 Tables....166
3.7 References....174

Chapter 4 – Long-Term Advanced Imaging Investigation of an Experimental Model of Bone Marrow Lesions using the Ovine Femoral Condyle....184
4.1 Introduction....184
4.2 Materials and Methods....187
4.3 Results....194
4.4 Discussion....197
4.5 Figures....206
4.6 Tables....212
4.7 References....214

Chapter 5 – Development of an Experimental Model of Bone Marrow Lesions using the Rodent Femoral Condyle....221
5.1 Introduction....221
5.2 Materials and Methods....223
5.3 Results....229
5.4 Discussion....234
5.5 Figures....241
5.6 Tables....245
5.7 References....246

Chapter 6 – Summary, Conclusions, and Future Directions....250
6.1 Significance of Work....250
6.2 Future Directions....255

CHAPTER 1:

THE IMPORTANCE OF SUBCHONDRAL BONE IN THE PATHOPHYSIOLOGY OF JOINT DISEASE

1.1 Introduction

Osteoarthritis (OA) is a debilitating, progressive, and incurable disease affecting animals and humans alike. In humans, OA is estimated to currently affect 32.5 million adults, costing over $486 billion annually in the US alone.[1–3] The substantial economic impact of OA is due to direct-health related costs associated with disability, co-morbidities, and the expense of treatment and pain management. The prevalence of OA continues to increase, as symptomatic knee OA is estimated to affect over 10% of the US population by the age of 60.[4] Similarly, in veterinary species, approximately 60% of equine lameness is attributable to OA, and it is estimated that owners spend $15,000 per year per horse on OA-related treatment, totaling nearly $80 billion annually across the 7.3 million horses in the US.[5] In dogs, management of joint disease associated with cranial cruciate injury alone was most recently estimated at $1.32 billion annually in the US.[6] The similarities in joint disease across species provides an opportunity to investigate the etiopathogenesis of different facets of OA, while exploring new diagnostic methods, and foci for intervention. Given both the economic and social impact of OA, understanding the causes of joint disease is of imperative importance, and focused efforts have been made toward identification of early changes within the joint that may precede the development of OA to ultimately improve patient outcomes and welfare.

Historically, OA has been characterized as a disease of degeneration of the articular cartilage, however it is now well-understood that the pathogenesis is increasingly complex. OA

is now recognized as a disease not just of articular cartilage, but of the osteochondral unit. The osteochondral unit is composed of the articular and calcified cartilage, subchondral and trabecular bone. Subchondral bone has received particular attention in recent years, as derangements in this essential tissue have been recognized for their contribution to the development and progression of OA. There is an intimate mechanical and biological interaction between the subchondral bone and articular cartilage, and alterations in the structure or composition of either tissue modulate the function of the unit as a whole.[7–9] Changes in the subchondral bone and associated joint disease are a common clinical problem in the horse.[10] Published equine research has explored the relationship between pathologic structural changes to the subchondral bone (and other osteochondral tissues) in the equine metacarpophalangeal (fetlock) joint and the development of clinical OA.[11–13] Using both these studies and clinical studies and reports from the human literature as a foundation for knowledge across species has enabled a more comprehensive understanding of the spectrum of pathologic lesions within the subchondral bone, aiding in greater attention to the role this tissue has in joint disease.

1.2 Anatomy and physiology of subchondral bone[1]

The subchondral bone is located deep to the articular cartilage, but remains connected to it through a layer of calcified cartilage. The subchondral bone varies in architecture and physiology by region, from the more compact layer of bone adjacent to the calcified cartilage (subchondral bone plate), to the trabecular bone closer to the medullary cavity. The normal subchondral bone plate in the horse is a thin layer of bone ranging from 10 μm to 3 mm in

[1] This chapter section is published in part in: Stewart HL and Kawcak CE. The importance of subchondral bone in the pathophysiology of osteoarthritis. *Front Vet Sci* 2018; 5:178.

thickness, depending on the location. The character of subchondral bone also differs depending on the thickness: the thinner areas are predominantly appositional layers continuous with trabeculae and with a low number of haversian canals; while the thicker areas are composed predominantly of a network of osteons.[14] The function of the subchondral bone is to attenuate forces generated through locomotion, with the compact subchondral bone plate providing firm support and the subchondral trabecular component providing elasticity for shock absorption during joint loading.[15] Maintenance of this intrinsic joint elasticity is essential for the biomechanical principles of locomotion.

Subchondral bone is a biphasic material, which includes an inorganic component composed of hydroxyapatite crystals for rigidity, and an organic component composed of predominantly type I collagen, proteoglycan, glycosaminoglycans and water affording elasticity and pliancy.[15] The composition of subchondral bone is uniquely designed to disperse axial loads across the joint, sparing the overlying articular cartilage.[16–19] Subchondral bone has the innate ability to display a range of responses, reflecting both acute stresses as well as more prolonged, chronic, adaptive responses within the joint. At one end of the spectrum, subchondral bone is responsible for dissipating forces generated by locomotion, considering it has been shown to be 10 times more deformable than the cortical shaft of long bones.[20] Further along the spectrum, subchondral bone is able to physically adapt its morphology in response to stresses placed on the joint, and models and remodels in accordance with Wolff's Law—stating that bone will adapt in response to the loading under which it is subjected.[21] The adaptive response is facilitated through the formative and resorptive activities of osteoblasts and osteoclasts, respectively. The rich vascularization and innervation of subchondral bone facilitates a comprehensive and extensive systemic response to both physiologic and pathologic alterations within the bone.

1.3 Biomechanics and pathophysiology of subchondral bone

Subchondral bone is highly responsive to loading, with the ability to respond quickly to training and injury. The forces incurred by the articular cartilage are transmitted to the subchondral bone across the calcified cartilage layer, which is uniquely adapted to distribute forces and minimize shear stresses on the articular cartilage layer through an undulating association with subchondral bone.[22] Deeper within the joint, compliance of the trabecular bone is essential for the joint to deform during loading and help to dissipate this energy across the layers of the joint. The different layers of the joint work in concert with one another to facilitate support and force distribution: the articular cartilage is supported by the calcified cartilage, which is supported by the subchondral bone plate, which is in turn is supported by the subchondral trabecular bone and ultimately the cortical bone.

The complex balance of function between the different layers must compensate for the rate and coordinated loading of the joint, as these are the two most important factors in the bone's ability to respond to imposed stresses. Joint shape and ligamentous attachments confine joint motion and in doing so affect the pattern of response observed within the subchondral bone. The muscles or tendons which span the joint are the primary contributors of surface loads, which are generated to counteract the rotational forces secondary to the ground reaction force acting on the moment arm of the limb.[23,24] The generated forces are not equal however, as the moment arm of the tendon is typically shorter than that of the limb. Because of this, the force generated from the tendon is much larger than the ground reaction force, resulting in an amplification of contact forces within the joint and at the subchondral bone.

The joint is able to respond to repetitive loading through the adaptive processes of bone modelling and remodeling. Bone modelling is defined as bone formation and resorption at anatomically distinct sites to produce functionally and mechanically purposeful architecture.[25] The processes of bone formation and resorption are asynchronously coupled, where small packets of abnormal or damaged bone are resorbed by osteoclasts, which is followed by recruitment of osteoblastic precursors that differentiate and replace the removed bone.[26] Modelling occurs at both the macroscopic and microscopic levels, with variation in the size and shape of the joints and microarchitecture observed over time. Modelling in subchondral bone typically manifests as changes in the microarchitecture, with trabecular infilling and changes in mechanical properties resulting in stiffer bone with decreased elasticity and less capacity for shock absorption. In remodeling, packets of diseased bone are removed and replaced through coordinated, balanced physiological processes.[27]

When the adaptive capabilities of the bone are exceeded—especially in cases of corresponding degradation of the articular cartilage layer—sclerosis, osteophytes, and fibrocartilaginous repair tissues are visible within the osteochondral unit. Subchondral bone follows the innate properties of all tissues, as there is a strain threshold beyond which normal adaptive processes are unable to compensate and pathological events progress resulting in subchondral bone damage. One of the most common signs of subchondral bone damage is sclerosis, which results in a decreased elasticity within the subchondral bone plate and trabecular bone. This thickening within the subchondral bone in turn affect the ability of the articular cartilage to withstand mechanical loading, by increasing transverse stresses at the base of the articular cartilage layer, resulting in horizontal clefts within the deep zone of cartilage. With continued loading, these clefts can progress to the articular surface of the cartilage, perpetuating

the cycle of OA changes within the joint (Figure 1.1).[28–30] The point at which this adaptive process becomes pathological is influenced by a multitude of factors, and includes (but is not limited to) location (i.e., within and between joints), horse size, speed, discipline and amount of training.[23] Clinically these changes result in the perception of pain, as the rich nerve supply of subchondral bone is one of the main mechanisms of pain perception in the joint disease.[15]

The complex balance of adaptive and maladaptive bone modelling is further complicated by the fact that microdamage is observed even in well-adapted bones. Osteoclasts remove damaged bone, which is then replaced with new bone by osteoblasts. Fatigue injuries, such as "repetitive stress injury" and "chronic fatigue injury" as observed in Thoroughbred and Standardbred racehorses, occurs when microdamage accumulates faster than remodeling can repair. Additionally, it is also accepted that remodeling activities are inhibited in a high load environment due to reduced recruitment of osteoclasts.[31] Pathologically fatigued bone clinically manifests in one of two ways: either as overt, mechanical failure in the form of a fracture, or as biological or functional failure where subtle changes occur resulting in the inability of the bone to sustain the expected demands of activity. Biological or functional failure is typically the result of more insidious changes within the joint, resulting in abnormal or inefficient transmission of loads, incongruent articular surfaces, and may include compromised perfusion or inadequate physical support from the adjacent articular cartilage.[23] Fractures of fatigued bone can be further characterized as to whether they are the result of supra-physiological loads or the result of cumulative microdamage resulting in excessive fatigue within the bone. Taken together, the more contemporary research has demonstrated strong evidence that subchondral bone changes are not simply a secondary sign of OA, but rather can be an initiating factor of degeneration of the health of the joint.[32,33]

1.4 Subchondral bone disease and chronic fatigue injury

Historically, traumatic arthritis has been held as a condition of synovial-mediated degradation of articular cartilage and direct mechanical damage to the joint surface. More recently, the joint has been re-conceptualized as an organ system, within which multiple tissues can be damaged and contribute to overall injury and dysfunction. A general approach to understanding the fundamental mechanisms for OA have been noted as either abnormal loading on normal cartilage or normal loading on abnormal cartilage.[34] Damage of the articular cartilage can occur from a variety of different circumstances, including damage to the subchondral bone, synovial membrane, fibrous joint capsule, peri-ligamentous support structures, or direct trauma to the articular cartilage itself.[35] Damage to the subchondral bone has received increasing interest for its role in joint injury, as changes in the composition or mechanical properties of the subchondral bone appear to mediate some of the changes observed in OA. For example, sclerosis reduces the shock-absorbing capability of the subchondral bone, and increases the risk of shear-induced tensile failure of the articular cartilage cross-links;[22] and subchondral bone has also been demonstrated as a potential source of inflammatory mediators that have been associated with degradation of deeper layers of articular cartilage.[36,37] Changes are also observed on the microarchitectural level, with the coalescing of microcracks or microfractures within the bone. Rapid, excessive bone formation may result in the development of bone sclerosis, which may be of reduced mineral quality and integrity.[38] Furthermore, expansion of the trabecular bone observed in subchondral bone undergoing excessive new bone formation, reduces the size of the bone marrow spaces, potentially resulting in an ischemic state, or at the very least a change in tissue nutrition.[39] Integration between the old bone and the newly added bone also takes time,

and if there is a disparity between mineral properties, this may further predispose this area of bone to failure.[38]

Although many terms are used by clinicians and researchers alike, the term "subchondral bone disease" most accurately represents the different phases and spectrum of pathologic changes observed within the subchondral bone. At the 2015 Dorothy Russell Havemeyer Foundation workshop in Newmarket, UK focused on subchondral bone, a consensus definition for subchondral bone disease included, 'a repetitive stress injury of subchondral bone.'[23] The delay between bone resorption and remodeling, where bone is resorbed at a faster rate than it is replaced, leaves the equine athlete susceptible to injury, especially when it is subjected to excessive training and stress. Compensation for these stresses is only possible up to a point, after which time the bone enters a spectrum of pathologic changes, which may be further complicated by the concurrent presence of clinical disease. The degree of the adaptive response tolerated by a given horse before showing clinical signs indicative of greater pathology appears somewhat individualized, which makes understanding the line between 'normal' and 'pathologic' responses difficult to distinguish.

The athletic horse is a well-studied model for repetitive stress injury, with multiple locations and manifestations of the disease. The metacarpal and metatarsal condyles are the most recognized locations of repetitive stress response and injury, with macroscopic abnormalities including increased radiopharmaceutical uptake on nuclear scintigraphy, radiolucency within the condyles on radiography, increased sclerosis within the bone on computed tomography (CT) and longitudinal fractures within the bone. Slab fractures of the carpal and tarsal bones, parasagittal fractures of the proximal phalanx, mid-body fractures of the proximal sesamoid bone, dorsoproximal fractures of the third metacarpal and metatarsal bones, wing fractures of the distal

phalanx, palmar/plantar osteochondral disease and intra-articular fragmentation are some of the other well-recognized examples of this condition. In some cases, it may be difficult to distinguish whether these injuries are primary diseases of subchondral bone, or whether they reflect more complex traumatic injuries to the bone, cartilage and supporting soft tissues of the joint. An acute injury to a ligamentous structure around or within a joint may alter weight-bearing during exercise and stimulate alterations within the subchondral bone that may result in the development of disease. Subchondral bone disease is most frequently recognized in racehorses, but can affect horses in a variety of disciplines, including steeplechasers, jumpers and three-day event horses.

Investigation of injury in subchondral bone has been reported in both clinical cases and experimental models. Microdamage within the subchondral bone has been experimentally investigated using an equine model with controlled treadmill exercise, showing that it can develop early under exercising conditions.[28] The metacarpal condyles of these horses displayed changes indicative of a milder version of what has been observed in clinical cases. Investigation of subchondral bone changes in clinical cases of racehorses euthanized for other catastrophic injuries has revealed changes on both a macroscopic and microscopic level. On gross examination, the metacarpo/tarsophalangeal joints from racehorses without catastrophic fractures displayed a spectrum of disease, ranging from fibrillation of the articular cartilage to focal cartilage erosions and cavitation within the subchondral bone.[12] Lesions in the subchondral bone varied from thickening of the subchondral and trabecular bone to advancing sclerosis with increasing amounts of osteocyte necrosis, the presence of vascular channels with filled with matrix debris and osteoclastic remodeling. Changes in the subchondral bone were not limited to architectural microdamage alone, as osteocyte death was also identified. Changes in the

subchondral bone—such as necrosis and sclerosis—could also be present in the face of intact articular cartilage (as has been observed in the palmar/plantar aspect of the distal third metacarpal/tarsal bones).[12] In many of these cases, on gross examination the articular cartilage appeared largely viable, with limited erosion and degeneration within the superficial layers (Figure 1.2). Focal disruption of the calcified cartilage layer appeared to result in cartilage in-folding. The disparity between these experimental and clinical findings is not necessarily unexpected, as it is unrealistic to believe clinical conditions can be perfectly modeled in a laboratory setting. Taken together however, these findings would suggest that microdamage within the subchondral bone not only results in the loss of mechanical support to the articular cartilage, but local factors (i.e., cytokines) released from the bone can influence—potentially permanently—the state and health of the articular cartilage.[12,27,28] Furthermore, progressive injury within the subchondral bone can result in complete failure, with pathologic changes within the third metacarpal/tarsal bones culminating in condylar fracture.[27,40–42] More recently "impact fracture" has been used to describe these types of pathologic fractures that correspond to radiographically lucent areas within the bone.[43]

"Chronic fatigue injury" has also been used to describe injury to the subchondral bone. Chronic fatigue injury is a more encompassing term, as the subchondral bone is typically not the only tissue affected. Chronic fatigue injuries result from cyclic loading of the tissue below the biomechanical threshold of tissue failure, and occurs commonly in the subchondral bone of the equine athlete.[15,27] Chronic fatigue injury in the subchondral bone was initially described in clinical cases of injured racehorses;[44] and validated through numerous clinical studies and experimental models.[12,28,29,45–47] There are three mechanisms by which damage can occur: (1) microdamage formation within the tissues; (2) an area of weakness within tissues secondary to

biomechanical and tissue responses to cyclic loading, predisposing this tissue to damage; or (3) adaptive tissue responses that chronically fatigue the tissue, resulting in a change in material properties and ultimately to injury.[15] One of the best clinical examples of chronic fatigue injury is in the palmar aspect of the third metacarpal condyles. In young Thoroughbred racehorses in training, sclerosis in the palmar aspect of the condyles is common, but the difficulty lies in discerning when these changes are indicative of a pathologic response. It is rare to observe clinical abnormalities in this region until these processes have resulted in subchondral bone pain or gross damage within the joint.[48]

Advances in diagnostic imaging have improved identification of these pathologic changes and is an attractive avenue for further research into understanding subchondral bone disease. Although the significance of osteochondral injury in joint disease has been well-discussed,[49] our understanding of the complex relationship between the subchondral bone and articular cartilage in repetitive stress injury and chronic fatigue injury continues to evolve, as great progress in understanding have and will likely continue to be made over the next decade through advancements in imaging and experimental disease models.

1.5 Bone marrow lesions

Although the late-stage manifestations of subchondral bone disease are relatively well-characterized, early changes within the subchondral bone that may precede more severe pathologic lesions are less well-understood. Bone marrow edema, bone bruises, or bone contusions are all terms that have been used interchangeably for what are now referred to as bone marrow lesions (BMLs).[50] BMLs are a non-specific finding that have been described in associated with a number of conditions in humans including transient osteoporosis of the hip,

bone marrow edema syndrome, osteonecrosis, osteomyelitis, trauma and infiltrative neoplastic disease.[51] In humans, BMLs may be observed incidentally, but are commonly associated with clinical pain and morbidity, and may perpetuate inflammation within the joint. Compelling reports have been published citing BMLs as early indicators of structural deterioration of the subchondral bone, suggesting that BMLs may serve as a marker for maladaptive changes within the subchondral bone and articular cartilage.[52–55] Conversely, in horses, BMLs may or may not be related to pain and lameness, and have been observed in the first, second and third phalanges[56], metacarpus/tarsus[57,58], and tarsal joints[59,60]. Despite the frequency that BMLs are observed across species, there is a paucity of information about the biological behavior of this condition and the long-term implications for joint health.

Normal bone marrow follows a predictable pattern of change from infancy to adulthood. At birth, all marrow is hematopoietically active, and termed red marrow, and then is gradually replaced by yellow marrow, or hematopoietically inactive marrow.[61] The conversion of red marrow (40% water, 40% fat) to yellow marrow (15% water, 80% fat[62]) begins at the central diaphysis and expands outward within each long bone, while simultaneously conversion is occurring in the epiphysis with ossification.[63] This predictable conversion give a characteristic and straightforward appearance of bone marrow on magnetic resonance imaging (MRI). The term “bone marrow edema” originated from the fact that the signal intensity characteristics are consistent with increased water or edema within the normal fatty marrow of the bone.[51] Regardless of the underlying etiology, alteration of the normal signal on MRI of bone marrow with a BML is consistent. BMLs have a characteristic intermediate-to-decreased signal intensity on T1-weighted imaging, and an increased signal on T2-weighted imaging (Figure 1.3).[64] BMLs appear hyperintense on fat suppressed images relative to the normal bone marrow, and other

identifying features include homogeneity within the BML itself, a lack of sharp peripheral margins and no regard for normal anatomical boundaries such as physeal scars.[63] The characteristic MRI signal that defines BML may represent physical microdamage or a response to damage of the subchondral bone, but this has yet to be fully elucidated.[65]

In an effort to further differentiate BMLs, chemical-shift imaging with MRI has the ability to distinguish fat from water, and has shown great application for characterization of BMLs.[66] In the case of differentiating malignant and benign lesions, a signal intensity loss from in-phase to opposed-phase images is a threshold that has been proposed to confirm benignity of a BML.[67] Of the available chemical-shift imaging techniques that also include fat suppression, the Dixon method has been documented to provide higher signal-to-noise ratios than more conventional imaging with the short time inversion recovery (STIR) sequence[68,69], and higher contrast-to-noise ratios than conventional bone fluid protocols.[70] The greatest challenge in the diagnosis of BMLs is the fact that they cannot be identified using conventional radiography, and only recently are being described using CT.[71–73]

Multiple theories and etiologies have been proposed for the formation of BMLs, as a variety of traumatic and non-traumatic pathologies may exhibit similar imaging characteristics. Broadly, BMLs can be classified based on the proposed underlying mechanisms: ischemic, mechanical, and reactive.[74–76] Of primary interest here are BMLs that are observed associated with OA and degenerative cartilage lesions, which typically stem from mechanical causes. Additionally, BMLs that occur as a primary or secondary result of inflammatory conditions within the joint may also be relevant, all of which have been more comprehensively described in humans over veterinary species. BMLs are commonly observed in both early and advanced OA, and may be associated with thinning or defects of the articular cartilage.[77] BMLs are frequently

observed in cases of overloading, extremity malalignment, and overuse, suggesting that repeated microtrauma likely plays a role in the genesis of these lesions.[75,78,79] BMLs have also been observed secondary to an inflammatory process or stimulus, such as in the cases of infection, osteomyelitis, or neoplasia.[80–82] Alternatively, intraosseous hypertension, secondary to venous stasis may result in hypoperfusion and hypoxia resulting in a BML.[83] The "Overloading Theory" has been proposed to explain the etiology of BMLs. In this theory, there is an increase in the force on a focal area of articular cartilage, which may be secondary to increased activity on the joint overall or the result of injury to the soft tissues, or possibly secondary to weakened subchondral bone due to repetitive stress or a decreased vascular supply. In response to this site of heightened stress, bone remodeling occurs, increasing the density or sclerosis. A force gradient is then created between this remodeled area and the adjacent bone, creating an environment of persistent shear forces, creating local inflammation, hemorrhage, and fibroplasia within the subchondral bone. If structural changes in bone occurs at a rate that is insufficient compared to demands, a chronic inflammatory state is created, and subsequently a BML.[76] Importantly and regardless of the underlying mechanism, increased signal within the bone on MRI and structural alterations within the subchondral bone may precede cartilage defects, affirming the clinical relevance of early detection of these lesions.

Bone marrow lesions do not follow a prescribed evolution, with different studies reporting a variety of clinical outcomes. Current theories agree that the presence of a BML is indicative of a lack of normal equilibrium within the joint. This loss of joint equilibrium may be due to either damage or increased stress on the subchondral bone in a situation of normal healing, or impaired healing that causes subchondral bone to behave in a pathologic manner.[84] Although once considered to be predominantly transient, it appears that BMLs can progress,

fluctuate in size, as well as completely regress. It does seem to be agreed that enlargement of the BML—and arguably persistence of this lesion—is a negative prognostic indicator, predictive for a need for arthroplasty, compared to subjects without BMLs.[84–86] The association between BMLs and pain, OA, bone density, cartilage and meniscal pathologic lesions, and subchondral cysts have all been suggested, but further work is needed to further elucidate the relationship between conditions.[76]

Histologic examination of these lesions have identified a wide spectrum of abnormalities.[87] Bone remodeling characterized by an increased thickness and mineral density of the subarticular trabeculae, microcracks, edema, hemorrhage within the subchondral region and subchondral bone cysts have all been described in BMLs associated with OA.[88] Previous work by Zanetti et al found that edema likely comprises only a very small amount of a BML, with fibrosis, necrotic and remodeled trabeculae, and bone marrow necrosis being observed more commonly.[87] The greatest challenge with understand these findings is the fact that BMLs are frequently observed with other conditions and surgical treatment to obtain histologic data is frequently not undertaken until greater pathologic lesions have occurred.

BMLs have been observed in 13-57% of the general human population >40 years of age. Furthermore, 52-72% of patients >50 years old with a history of OA in any joint and >75% of patients with OA in the knee joint have BMLs.[89–91] The regularity with which BMLs are observed across conditions suggests both a commonality and non-specificity to these observed changes within the subchondral bone. Arguably, large gaps still exist in what is known about the pathophysiology of these lesions and their overall relationship to subchondral bone health. Based on what is recognized in both humans and horses about subchondral bone, further investigation of BMLs may be a promising avenue for early detection of disease.

1.6 Principles of diagnosis and diagnostic imaging

The tenants of diagnosis for subchondral bone disease remain the same as for many other musculoskeletal conditions in the horse—a thorough clinical examination (including static and dynamic, and subjective and objective evaluations) to localize the source of lameness, diagnostic analgesia, and diagnostic imaging examination. Subchondral bone injury may be identified on standard radiographic projections, but also may be missed depending on the location and time-course of the disease. Diseased bone may radiographically have the appearance of areas of decreased opacity surrounded by areas of increased opacity, or may be visible as a distinct fracture. A lack of radiographically observable abnormalities does not rule out the presence of subchondral bone disease and repeat imaging (in 10-14 days) or use of a different, more advanced imaging modality should be considered. Depending on the severity and chronicity of the injury, nuclear scintigraphy, MRI, and CT can be considered for further evaluation of changes within the subchondral bone. In severe cases where overlying articular cartilage damage is also present, diagnostic arthroscopy may be considered for further evaluation of the subchondral bone. Volumetric imaging techniques, such as MRI and CT that provide information in three-dimensions have arguably revolutionized our clinical ability to assess subchondral bone and the health of the joint as a whole.

Magnetic resonance imaging has facilitated the identification of diseased subchondral bone. In addition to identification of BMLs, increased bone mineral density or sclerosis is frequently identified on MRI in areas of signal changes. These changes are identified as areas of low signal intensity, but this depends on the sequences used for evaluation. Furthermore, diseased subchondral bone is not always sclerotic and although increased bone density may be

present, signal changes on MRI are non-specific and may represent an increased volume of lower density bone. Sclerosis is truly a mechanical term and thus diagnosis based on intensity of MRI signal should be used with caution.[23]

Magnetic resonance imaging is considered the gold-standard modality capable of identifying fluid within bone; however, CT is considered as the superior modality for structural imaging of bone given its high spatial resolution. Fine bone detail can be very challenging to identify using MRI, as the appearance of bone and soft tissue can overlap. In cases of confluent tissue—such as in a joint with osseous proliferation with adjacent soft tissue thickening—the signal intensity of MRI will be the same and it can be challenging or impossible to distinguish between the structures. The volumetric information from reconstructed CT images can illustrate subtle to extensive internal and external osseous remodeling (Figure 1.4). In specific sites, remodeling changes in the subchondral bone observed on CT have been validated to indicate pathologic change and impending fractures.[92] The tissue density observed on CT can be translated into numerical values known as Hounsfield Units (HU). Information about the specific densities of the bone may provide valuable insight into unique patterns of bone change, and furthermore provides an objective metric for comparison if serial examinations are performed. The information afforded through volumetric imaging modalities such as CT and MRI, have increased our knowledge in the behavior of subchondral bone and its response to training and injury.

1.7 Computed tomography[2]

Recent innovations[93–95] in imaging technologies have revolutionized the clinical applicability of CT, including the development of cone-beam CT (CBCT) for equine use. CBCT has been used for years for characterizing maxillofacial diseases in people,[93] and has recently been introduced in the human medical field for extremity imaging.[94] Equine medicine has paralleled human medicine with increasing interest in high-resolution three-dimensional imaging, coupled with more specialized demands for portability, faster scan times, reduced cost and reduced risks from exposure to ionizing radiation to the patient and personnel. Arguably, these demands have been integral catalysts for the development of CBCT, one of the newest facets of CT technology. These principles have been extrapolated toward veterinary applications allowing for a relatively low-cost, rapid, high resolution volumetric scanning system that can be used to imaging for not only subchondral bone disease, but a wide variety of conditions and diseases. Currently, there are two dedicated CBCT scanners for equine use (Pegaso, Epica Medical Innovations, San Clemente, CA, USA; 4DDI Equimagine, Equine Imaging LLC, Milwaukee, WI, USA). Given the advent and availability of this modality for clinical equine practice, a critical evaluation of this technology for the imaging of subchondral bone and joint disease is warranted.

1.7.1 Development and image acquisition using CBCT

CT scanners can be categorized based on the geometry of the x-ray beam applied to the subject (Figure 1.5). Traditional, or fan-beam CT (FBCT) scanners have an x-ray source and

[2] This chapter section is published in part in: Stewart HL, Siewerdsen JH, Nelson BB, Kawcak CE. Use of cone-beam computed tomography for advanced imaging of the equine patient. *Equine Vet J* 2021; 53:872-885.

solid-state detector mounted on a rotating gantry. Images of the patient are typically acquired in the axial plane, and each thin, fan-shaped slice of a two-dimensional image is compiled into a stack to form a three-dimensional image that can be reconstructed into any anatomical plane and the grayscale can be manipulated to highlight the structures of interest (Figure 1.6A, B). This fan-beamed image acquisition is used in the traditional helical multi-detector CT (MDCT) scanners, and depending on the detector array configuration, between 16 and 320 slices are obtained simultaneously. Conceptually, the x-ray source for traditional CT can be considered as a highly-collimated three-dimensional cone-beam of ionizing radiation. As the fan-beam is opened and the number of detectors are increased to acquire more slices simultaneously, the scanning time and radiation dose are reduced (compared to single-detector FBCT units).[96,97]

Cone-beam scanners differ from fan-beam in that they use a divergent pyramidal- or cone-shaped source of ionizing radiation and a large-area detector (commonly, a flat-panel detector) on the opposite side of the gantry. The patient remains stationary and is not linked to the scanner. The current commercially-available CBCT units have been developed with a separate generator and detector that move independently around the patient (4DDI Equimagine) or a portable unit with a closed gantry that rotates around the patient (Pegaso). The x-ray source and detector synchronously rotate up to 360-degrees around a fulcrum, acquiring multiple sequential planar projections within the field of view. The cone-beam shaped radiation generated by a single x-ray source is received by a 215 x 265 mm detector on the opposite side of the gantry (x and y planes). A single rotation around the patient acquires a 150 mm volume in a rostral-to-caudal (z plane) direction, referred to as a stack. Single exposures are made at specific degree intervals, providing projection images known as basis projections. These images are slightly offset from one other and the complete series of images is formally referred to as the

projection data.[97] If the region of interest is greater than 150 mm (e.g., equine cervical spine), additional rotations of the gantry can be used to acquire further stacks of projection images. These stacks can be merged together for a complete study. The greater the amount of projection data, the more information that is available to reconstruct the image, resulting in greater spatial and contrast resolution, and creating "smoother" images with an increased signal-to-noise ratio. Acquiring a larger amount of projection data comes at a cost of increased scan time, a higher radiation dose to the patient, and a longer primary reconstruction time of images. Due to the large area of coverage of the beam with CBCT across the x, y and z planes, there are many instances where only one rotation—or even a partial rotation—of the gantry may be necessary to acquire an entire volumetric data set for complete reconstruction (Figure 1.6C). This is in contrast to MDCT systems where the x-ray beam is collimated, reducing the coverage per rotation in the z plane. Obvious advantages of CBCT technology include flexibility in system geometry that is adaptable to many configurations (including imaging in the standing, weight-bearing patient) and the ability to acquire a diagnostic, volumetric image with some motion of the patient (Figure 1.7).

Clinical CBCT use has been made possible largely by the development of compact, high-quality, two-dimensional (flat panel) detector arrays. Detectors were initially produced using a configuration of scintillation screens, image intensifiers, and charge-coupled device detectors. Image intensifiers consist of an input phosphor which convert x-rays to optical photons that are then converted to electrons within the photocathode. A series of electrodes are responsible for both accelerating and focusing the electrons. Cesium iodide has typically been used as the input phosphor, given its efficiency for absorbing x-rays. Although image intensifier systems are economical, and have a wide surface with good sensitivity, they are also large, require

calibration, may suffer from peripheral truncation effects, and image quality (distortion) may be influenced by the magnetic field of the earth.[97]

More recently, high-resolution, flat-panel detectors have become available. These are composed of an x-ray detection layer and an active matrix array of hydrogenated amorphous silicon thin-film transistors. X-rays are detected indirectly by means of a scintillator which converts x-rays into visible light, and the output is then registered in the photodiode array. The intensity of emitted light corresponds to the intensity of the incident x-ray beam. Although these detectors have reduced peripheral distortion, they also are associated with a slightly higher radiation dose since greater amounts of x-rays are required to generate a given signal level (compared to high-gain x-ray image intensifiers) and flat-panel detectors typically have increased levels of electronic noise (compared to high-quality MDCT detectors).

The spatial resolution of CBCT images is determined primarily by the properties of the x-ray focal spot, flat-panel detector, and system geometry, while traditional CT resolution is determined based on the configuration of the detector array elements and acquired slice thickness. The acquired volumetric data set is composed of individual volume elements, or voxels, which are directly related to the detail or resolution of the final CT images. In CBCT imaging, voxel dimensions primarily depend on the size of the detector area, while traditional CT depends on the matrix size, field of view and slice thickness. Reconstruction of acquired data with a CBCT system requires unique algorithms, compared to those used with traditional CT units. Traditional CT uses the "fan-beam filtered back projection" technique to sequentially reconstruct the acquired axial slices of the patient. "Cone-beam reconstruction" refers to the CBCT technique whereby a three-dimensional image volume is created and then two-dimensional "slices" are generated from this data. Common algorithms for 3D "cone-beam

filtered back projection" account for the divergence of the beam by modified weights applied to the projection data. As with traditional CT, optimum visualization of certain anatomic structures with CBCT depends on application of both specific algorithms to favor the tissue type of interest (i.e., bone vs. soft tissue) as well as adjustment of window level and window width settings and/or use of specific filters. As the potential and realized clinical applications for CBCT in both human and veterinary medicine continue to increase and evolve, substantial efforts have been undertaken to improve three-dimensional image reconstruction and manage inherent artifacts. These advancements will ultimately allow for CBCT-acquired data to be further optimized for both bone and soft tissue assessment of the equine patient.

1.7.2 Scanner and beam-related CT artifacts

While potential equine applications for CBCT continue to grow, images acquired using CBCT technology may suffer from many of the same artifacts as traditional CT. The presence of artifacts and their impact on image quality persist as a critique surrounding CT technology. Generally speaking, the presence of artifacts on a CT image reduces contrast resolution, increases image noise, and reduces soft-tissue assessment. Artifacts can be classified according to their cause, and include x-ray beam artifacts (i.e., beam hardening), scanner-related artifacts (i.e., circular or ring-shaped artifacts, partial volume averaging), or patient-related artifacts (i.e., motion resulting in an unsharp image). Additionally, CBCT has a few unique artifacts related to its pyramidal beam geometry, including the cone-beam effect associated with incomplete sampling from a single circular scan of the volume of interest.

Beam hardening is one of the most prominent sources of x-ray artifacts for all CT systems. The applied x-ray beam is composed of multiple x-rays at different energies

(polychromatic beam). Lower energy x-rays in the beam are selectively absorbed as they pass through a highly attenuating object, and the beam then "hardens" since the higher-energy photons are not absorbed.[98] Hypodense bands are then generated on the final reconstructed image in the direction of the high-attenuating structure since the detector has assumed greater penetration of the x-ray beam has occurred, thus assigning a lower Hounsfield Unit and may vary based on different projection angles due to the heterogeneity across anatomic structures. The use of DE CT can reduce beam hardening effects by scanning at two different x-ray energies. Streak artifacts can also occur at high-contrast interfaces with sharp or abrupt borders secondary to scatter, or diffraction of photons from their original path after interaction with matter (Figure 1.6C). Data received by the detectors from different x-ray projections are inconsistent, resulting in fine white streaking across the image. Highly attenuating structures may result in both white and black streaks on the final reconstructed image. The larger the detector, the higher the probability that scattered photons affect the reconstructed image. Because of this, the image-degrading effects of scatter radiation may affect CBCT more than traditional, highly-collimated FBCT systems.

Although CBCT systems are more susceptible to scatter artifacts, they are superior at reducing volume averaging (also called "partial volume effect"). Volume averaging results because all densities that lie within a particular voxel are averaged to a single value. In CBCT imaging, voxel dimensions primarily depend on the size of the detector elements, while in traditional CT, voxel dimensions are dependent on slice thickness. CBCT commonly has isotropic voxels (equal in all three dimensions/directions), whereas traditional CT may use either anisotropic or isotropic voxels.[99] The isotropic voxel configuration is one of the reasons why CBCT can produce higher resolution images and more accurate reconstructions compared to

traditional CT systems using anisotropic voxels.[97] Despite higher resolution images, CBCT suffers from higher image "noise", characterized as fluctuations arising from random events. This should be distinguished from an "artifact", which bias or modify the image from non-random events. Noise is therefore stochastic because it does not appear exactly the same in successive scans, whereas artifacts are deterministic and appear exactly the same in successive scans, and are hypothetically even predictable events. Regardless, noise should still be considered as an image deteriorating factor and results in inconsistent attenuation values when a constant attenuation should be present.[100] For CBCT units, the physical geometry of the x-ray beam results in a large volume being irradiated with each basis projection. Most of the produced scattered radiation is omnidirectional, and recorded by the cone-beam detector, but does not reflect the actual attenuation of the object. This additional, non-linear attenuation biases the detected signal in a way that underestimates the true attenuation and results in shading or streaks in the three-dimensional image. The scatter-to-primary beam ratios for CBCT have been reported as high as 0.4-2.0, whereas for traditional fan-beam CT ranges from 0.05-0.15, resulting in degradation of the final image and poor contrast resolution.[97,98] In addition to image noise, CBCT systems are subject to a unique cone-beam effect associated with the divergent x-ray beam. The amount of data collected by each detector pixel corresponds to the total amount of recorded attenuation along a specific beam projection angle. For a circular orbit of the x-ray source and detector, the projected rays leave certain structural content under-sampled (specifically, flat edges perpendicular to the axis of rotation), resulting in so-called "cone-beam" artifacts (Figure 1.8). Overall, due to noise artifacts, the soft-tissue contrast for CBCT tends to be less than that of traditional FBCT, although the high-contrast three-dimensional spatial resolution tends to be better for CBCT.

1.7.3 Patient-related CT artifacts and motion correction software

Motion is the primary patient-related CT artifact, which results in distortion and decreased spatial resolution in the reconstructed image, and can be a substantial issue with both CBCT and traditional CT. Voluntary (i.e., respiration) and involuntary (i.e., cardiac motion, gastrointestinal peristalsis) motion can result in the presence of radiating lines, ghosting (faint double margin of an organ or soft tissue) or blurring on the final image. In human medicine, positioning aids and occasional sedation (usually in pediatric or claustrophobic patients) may be used to prevent voluntary motion. Additionally, use of short scan times in regions prone to movement helps reduce these types of artifacts. Patient motion artifacts must be balanced against the risk of undersampling secondary to rapid scans, where too few projections are provided for reconstruction, and the resulting image has view sampling artifacts and increased image noise.[101] View sampling artifacts can occur with either CBCT or FBCT, as the larger the angle of the x-ray beam to the area of interest, the more sensitive the reconstructed image is to this artifact.[102]

It is not as easy to overcome these challenges in veterinary medicine, as many of these artifacts are encountered in both the standing and anesthetized equine patient. Traditional CT systems minimize motion artifacts by primarily using three strategies: (1) overscan, halfscan or underscan modes; (2) cardiac gating; and (3) motion correction software.[103] In regards to different scan modes, the maximum discrepancy in detector readings occur between views obtained toward the beginning and end of a 360-degree scan. Some scanners use an overscan mode for axial body scans, which involves adding approximately 10% additional rotation beyond the standard 360-degrees. The repeated projections are averaged, which then helps reduce the severity of motion artifacts. Partial scan modes can also be used to reduce motion artifacts by

reducing scan times, but this may be at the expense of image quality.[104] Cardiac gating is used to correct for the rapid motion of the heart and can be used to produce images by using data from a fraction of the cardiac cycle. Prospective ECG triggering is one approach to cardiac gating and uses data from the ECG to control scanning so that x-rays are generated and projection data are acquired only during cardiac diastole, the phase of the cardiac cycle with the least amount of motion. Retrospective ECG gating involves acquisition of projections while simultaneously recording the ECG signal. Partial or segmented adapted scanning algorithms can then be used to sort the data from different phases of the cardiac cycle for image reconstruction.[105,106]

Motion correction software remains a frequent area of investigation for CT technology. The use of motion correction software and various post-processing algorithms are many times automatically applied, with reduced weighting of the starting and ending views, thus suppressing their contribution to the final image. Numerous reconstruction algorithms are reported in the literature; however filtered back projection, pixel-specific back projection and iterative reconstruction are three commonly reported techniques to reduce noise due to motion for traditional CT.[107,108] Filtered back projection refers to a well-known, standard image reconstruction technique for traditional CT where a filter is applied to each of the one-dimensional views to create a set of filtered images. These filtered views are then "back-projected" against the initial images to create a reconstructed two- or three-dimensional image.[109] Although this technique provides good reconstruction images with traditional CT, and for areas of interest that are in isocenter with CBCT, this technique involves basic limitations to noise and spatial resolution in the resulting image. To address such effects, several other approaches have been proposed for CBCT projection data. Pixel-specific back projection builds on the image reconstruction technique of filtered back projection to reduce motion artifacts by locally

correcting for motion on a pixel-by-pixel basis, as opposed to attempting to describe patient motion by a single set of parameters. Because of this focus on local correction, the in-plane motion of every pixel must be known before this technique can be used to reduce artifacts. This technique uses node points, which are uniquely identifiable areas on the patient (such as ribs or blood vessels in the chest), to measure position and displacement secondary to patient motion. From these node points, the displacement of each point can be measured at the time of each projection and can then be accounted for in the final reconstructed image.[108] Iterative reconstruction uses a slightly different approach compared to pixel-specific back reconstruction, whereby a correction loop is used. Ray tracing, a technique where the path of the x-ray projection is traced through pixels in an image, is employed once an image has been reconstructed from the projection data. This step of image correction is formally called "reprojection," referring to the fact that via the process of ray tracing in the image, a new projection is created to represent the reconstructed image. The deviation between measured and calculated projections is then used to derive correction projections, reconstruct a correction image, and create an updated and motion-corrected version of the original image. This process is repeated and each time the original image is updated, non-linear image processing algorithms are used to enhance spatial resolution at areas of higher contrast and reduce noise at areas of lower contrast.[107] The ultimate goal of these techniques would be to completely eliminate motion-related artifacts, and despite the fact this has not been achieved, improvements in this technology have resulted in the substantial reduction in these types of artifacts and production of a diagnostic image.

The potential challenge of pronounced artifacts secondary to patient movement is an inherent concern with the CBCT systems, especially in standing, sedated patients. Both of the

currently available CBCT scanners rely on rapid data acquisition, with scanning times that are comparable or decreased when compared to traditional CT scanners.[110] For the Pegaso system, a single rotation of the gantry takes less than one minute, which may provide complete evaluation of the region of interest. Complete scans of the equine skull and cervical spine can be acquired standing under moderate sedation, while the entirety of the fore and hind limbs (including the stifle) can be accommodated by the gantry under general anesthesia and scanned within minutes (unpublished observations, see section on Equine Imaging with CBCT). In addition to these rapid scan times, respiratory and cardiac-related motion is minimal in the standing patient relative to mechanical ventilation.

Correction for patient movement is not solely dependent on post-processing software with the Pegaso, closed-gantry CBCT unit. A proprietary grid marker is applied to the standing patient and then frontal and lateral stationary video cameras are used throughout the process of data acquisition for continuous detection of patient movement. These data are then used during reconstruction to create a final, motion-corrected image. Preliminary work has demonstrated the use of cameras in conjunction with motion correction software can produce diagnostic images with over 100 mm of patient movement (Figure 1.7 and unpublished observations). The combination of the video cameras for real-time assessment of patient movement in conjunction with traditional motion-correction software and CBCT-specific algorithms for motion correction[111] results in a superior ability account and correct for movement in the standing patient.

Correction of patient motion, and compensation for image noise secondary to scatter and x-ray beam or scanner artifacts remains an ongoing area of improvement across CT systems. To some degree, all these factors contribute to reduced image quality and may interfere with

generation of a diagnostic image from the CT data. Limited contrast resolution of soft tissues is one example of an area where artifacts and noise may cause poor diagnostic quality images, and has been cited as one of the largest limitations of CBCT technology.[97,98] Although this limitation cannot be completely resolved at this time with software algorithms, remarkable progress has been made in the past few years on iterative techniques for reducing artifacts and increasing soft tissue contrast and resolution.[112] When artifacts appear in a CBCT study, they can make images more difficult to interpret, but it is unknown whether these limitations will truly prevent a clinician from making a diagnosis or generating an appropriate treatment plan. In the veterinary section, the ability to scan an equine patient under sedation instead of under general anesthesia reduces costs and oftentimes provides clients under budgetary constraints with an option for diagnostic evaluation. In these cases, even a limited interpretation may be all that is necessary to pursue a treatment. In addition, for areas such as the equine caudal cervical spine, MDCT imaging is more challenging as the muscle restricts advancement of the gantry. There are limited reports of use of MDCT for imaging this region[113,114], while imaging of this region can be performed using CBCT in the standing or anesthetized live horse. Therefore, imperfect interpretation of lesions may be better than inconclusive planar imaging interpretation. Controlled clinical case comparisons of CBCT to clinical signs, radiography, ultrasonography and traditional CT imaging in horses are warranted to better determine the clinically relevant limitations of CBCT technology. Furthermore, continued efforts toward developing and refining CBCT technology will yield additional improvements in diagnostic imaging.

1.7.4 CBCT Imaging of Subchondral Bone

Within the fields of human and veterinary medicine, CBCT is beginning to be used as a quantitative method to assess bone density and for assessment of the musculoskeletal system. Recent reports in human medicine have quantitatively assessed healthy and osteoarthritic knees, and menisci on three-dimensional images acquired using an extremity CBCT system.[115,116] The isotropic three-dimensional spatial resolution yielded unique, non-degenerate, symmetric and dense characterization of the joint space which was superior to other imaging modalities, such as traditional radiography.[117] Techniques to evaluate soft tissues,[94] bone mineral density,[118] and bone marrow edema (using a dual-energy technique)[119] are in progress with CBCT, but further optimization of the technique is required to improve the accuracy and sensitivity of analysis.

1.7.5 Equine Imaging with CBCT

In the last decade, CT and MRI have been increasingly utilized for evaluation of the equine musculoskeletal system. Evaluation and identification of pathologic changes of the equine distal limb have been arguably revolutionized by the availability and use of both low- and high-field MRI units. Most comparative imaging studies in equine medicine focus on differences between MRI, MDCT and digital radiography. CT is traditionally cited as being superior for spatial resolution, while better contrast resolution is observed with MRI.[120] Assessment of the equine distal limb with high-field MRI provides high contrast resolution facilitating a comprehensive evaluation of the bones, articular cartilage, tendons, ligaments and connective tissues that comprise the distal limb. Digital radiography is used as a comparative standard for CT and MR; however, radiography retains the advantage of being technically easier, more accessible, and cheaper to acquire than either of the aforementioned advanced imaging

techniques. Given that even standing MRI units are associated with prolonged scan times and typically reduced imaged quality, the feasibility of CT technology is being more thoroughly explored for imaging of the equine distal limb[121], as scan times are reported to be comparable or decreased versus radiography.

CBCT may have a beneficial—or even vital—role in the evaluation of subchondral bone and the distal limb. The ability to detect subtle changes in the subchondral bone using a rapid, economical, volumetric imaging technique, stands to revolutionize the understanding of the etiopathogenesis of joint disease. CT is already well-validated for pre- and intra-operative surgical planning for assisted internal fixation, including for fractures of the distal phalanx and distal sesamoid bone[122] as well as anecdotally reported for fractures of the carpal and tarsal bones. Assessment of the health of the subchondral bone and joint as a whole is an integral aspect of these procedures. CBCT units also have the ability to scan the proximal aspect of the limb—including the elbow and stifle joints—and may prove to provide additional insights about the bone changes in these regions.

Regardless of the region imaged, scan times for the equine patient are substantially shorter when compared to MRI and single-stack scans using traditional CT (with comparable scan times in multi-stack protocols). For the Pegaso unit, a typical scan time for a 150 mm section of a patient is approximately 50 seconds (unpublished observations), regardless of whether the patient is standing or anesthetized. Reconstruction of images of this 150 mm section takes approximately 2 minutes. A single 150 mm stack is sufficient to scan an entire joint, including the foot, fetlock, carpus or tarsus, facilitating rapid and repeated scans for comprehensive pre-operative planning. A multi-stack scan of the equine distal limb—from carpus through foot or tarsus through foot—takes less than 20 minutes, including image

acquisition and reconstruction. Depending on the specific MDCT system, scan and reconstruction times may be comparable or slightly faster. However, positioning of the animal in isocenter within the gantry is more laborious, resulting in a longer duration of the horse under anesthesia for a comparable scan region. Although the anatomy of interest should ideally be positioned within isocenter, the Pegaso CBCT unit is able to provide diagnostic images even when this is not the case.

1.7.6 Dual-Energy Computed Tomography

An emerging area of exploration is the use of dual-energy (DE) CT for assessment of fluid within subchondral bone, while preserving the high level of spatial resolution inherent to CT. Because of this, DE with CBCT and may overcome some of the critiques of soft tissue assessment.[123] DE CT involves the acquisition of two CT datasets at different energies, which can better characterize the chemical composition of a material by its differential absorption of the x-ray beam at the two different energy levels.[124] This technology has been used in human medicine most prominently in angiography, abdominal imaging, characterization of urinary stones and for gout arthropathy, and has also been reported to identify BMLs, visualize tendons and ligaments, and minimize beam-hardening artifacts from bone prostheses.[124–130] Although the underlying principles are the same, it is important to note that DE CT can be accomplished by using single- or dual-source CT scanners. Single-source CT scanners used for DE CT rapidly (i.e., 0.5 second intervals) switch between high- and low-energy during a single rotation of the gantry. Conversely, dual-source CT scanners are equipped with two x-ray tubes to allow for simultaneous acquisition at the different energy levels in traditional CT scanners.[131] MRI remains the gold-standard for assessment of BMLs and soft tissue imaging; however, CBCT can

also characterize fluid by using this DE technique and combine images using post-processing software.[119,132] The combination of this DE capability, rapid scan times and a large field view, may validate CBCT as a viable alternative to MRI—especially in cases which may benefit from continued monitoring to evaluate a response to interventional therapies.

1.7.7 Preliminary Investigation of CBCT for Equine Orthopedic Use

Two preliminary studies have been performed at Colorado State University, in collaboration with the I-STAR Laboratory at Johns Hopkins University, directly comparing CBCT to traditional CT for characterization of the equine foot, metacarpophalangeal joint and carpus in cadaver limbs. For the first study, two thoracic equine cadaver limbs from middle-age horses (ages 15 and 17 years) were evaluated. Limbs were disarticulated at the elbow joint and the distal limb was left intact. Limbs were maintained at room temperature at the time of imaging. Images were acquired using conventional, FBCT (Gemini TF Big Bore, Philips Healthcare, Andover, MA, USA) and an early prototype version of a weight-bearing CBCT system for musculoskeletal extremity imaging[94]. For FBCT, each limb was scanned hoof first, to mimic clinical imaging. Acquisition parameters for FBCT included a beam energy of 140 kVp, 630 mAs, and a pitch of 0.4, with a 0.8 mm (bone algorithm) and a 1.5-mm (soft tissue algorithm) slice thickness throughout the joint surface. The field of view was 180 mm, and a 512 X 512 voxel matrix (giving 0.35 x 0.35 mm voxels with 0.8 mm or 1.5 mm slice thickness). Data from the CT scanner were saved in DICOM format. Acquisition parameters for CBCT included a beam energy of 80 kVp (+0.2 mm Cu added filtration) and tube output of 108 mAs. The reconstructed image field of view was 18 x 18 x 18 cm^3. Image reconstruction was performed using 3D filtered back projection at isotropic voxel size of 0.26 x 0.26 x 0.26 mm^3 and ramp

filter for visualization of bone and 0.78 x 0.78 x 0.78 mm^3 and Hann filter for visualization of soft tissue. The data were stored in DICOM format on an external hard drive.

Images were subjectively evaluated by two board-certified radiologists with a bone preset and custom window/level for soft tissue evaluation, using a commercial DICOM viewer (ClearCanvas)[a]. Subjective evaluation focused on a relative visual grading analysis[133] evaluating the following criteria: (1) sharpness of periosteal and articular surfaces; (2) corticomedullary definition and trabecular pattern; (3) ability to identify soft tissue structures; (4) detectability of a potential lesion; and (5) presence of artifacts. MDCT images were used as the reference images and CBCT were used as the comparative images. For objective evaluation, thresholding was used to extract the condyle from the imaging data. Reconstructed, three-dimensional surface models were used for measurements of condylar width. Measurements were performed at nine distinct areas (centered at the transverse ridge, and four equally spaced locations on both the dorsal and palmar sides) of the articular surface of each condyle. The width from the parasagittal groove to the corresponding lateral or medial abaxial edge was also measured. The differences between measurements for each limb were compared with the differences between measurements for each scanner. The measurement protocol was repeated for a randomly chosen condylar surface from the scanner to assess the error inherent in the measuring method. The exploratory nature of this preliminary study did not support a prospectively powered statistical analysis; however, a subjective description of the observed differences between the imaging systems is provided.

Subjective evaluation found that CBCT was superior for visualization of the cortico-medullary distinction and trabecular detail, small subchondral bone lesions, and periosteal and articular surfaces. CBCT was slightly inferior compared to MDCT in overall image quality, due

to the presence of artifacts on the reconstructed images, including beam hardening and streaking (unpublished observations). Since this original work was performed, correction algorithms have been developed and have substantially reduced these previously observed artifacts.

Small lesions were detectable with both systems; however, CBCT showed slightly better conspicuity of the lesions and adjacent trabecular bone. Soft tissue structures of the pastern region, such as the superficial and deep digital flexor and common digital extensor tendons, and distal sesamoidean ligaments were equally identified with both systems. The contrast of soft tissue structures was slightly reduced with CBCT compared to MDCT; however, adequate contrast resolution was achieved to differentiate the margins of soft tissues and the surrounding hypoattenuating tissue.

Objective evaluation compared condylar width measurements in paired thoracic cadaver limbs between MDCT and CBCT images. The average percent error in total width measurement between the scanners for limbs was 1.0%, while between limbs for both scanners was 2.4%. Measurements of lateral condylar width showed no difference in percent error at 4.7% for differences between scanners and between limbs. Medial condylar width measurements indicated a lower percent error between scanners at 3.4% than that between limbs at 5.2%. Upon repeating the condylar width measurement on a randomly chosen surface, the error in the total condylar width was calculated at 1.2% while the error in the lateral and medial condylar width was found at 5.2% and 3.3% respectively. These findings indicate there was a minimal and acceptable degree of variation between measurements performed using a CBCT unit compared with a MDCT unit. Geometrical differences between the two scan methods were lowest for lengths where anatomical markers were easiest to identify (total width) and largest when measuring the shortest distances (lateral condylar width). However, this pattern holds true for disparities

between repeated measurements on the same scan, demonstrating that geometrical variation between scanning methods were no different than variations inherent in the measuring method itself. The high resolution of volumetric slices using CBCT provided increased detail in the density pattern of the palmar aspect of the condylar surface relative to MDCT (Figure 1.9). Characterization of these types of density patterns may increase our understanding the adaptive remodeling process in equine bone, and may help identify subtle lesions that could respond to early interventional therapies.[134,135]

For the second study, three thoracic equine cadaver limbs were evaluated, and the study design was modeled after a previously published study in the human literature[112], comparing CBCT and FBCT image quality for clinical imaging. Images were acquired using the same FBCT and CBCT systems as previously described. Images were reconstructed with smooth or sharp filters suitable to visualization of bone or soft-tissue, respectively. The structures and tissue types of the equine MCP joint were evaluated according to both satisfaction and preference rating tests by two board-certified veterinary radiologists. The order of images was randomized using a free, online random selector and the veterinary radiologists were blinded to the order. Each radiologist assessed the images independently using an open-sourced software for viewing DICOM images (Horos Project, version 3.3.6). For satisfaction tests, individual FBCT or CBCT images were evaluated based on a five-point satisfaction rating scale with a score of 1 corresponding to "Very poor / Non-diagnostic quality," and 5 corresponding to "Excellent diagnostic quality with minimal influence of artifacts." For preference rating tests, FBCT and CBCT images of the same limb in the same plane were displayed side-by-side and observers rated which image they preferred on a five-point scale analogous to the Likert scale[112], with a ±2 indicating a definite preference, a ±1 indicating a slight preference, and 0 indicating no

preference. The preference for FBCT and CBCT image was then compared. The Shapiro-Wilk test was used to confirm data was not normally distributed. The statistical significance of observed differences between FBCT and CBCT images was evaluated using the Kruskal-Wallis test for satisfaction tests and Wilcoxon signed-rank test for preference tests with R software (version 3.6.1 "Action of the Toes", R Foundation for Statistical Computing 2017) in RStudio (version 1.2.1335). A value of $P < 0.05$ was used to determine significance.

Results of satisfaction scores comparing MDCT and CBCT images were that the two modalities were equivalent for bone evaluation, with a median score of 5 for both modalities, corresponding to "excellent" diagnostic quality (Figure 1.10A). CBCT images were rated as less superior than MDCT images for evaluation of the ligaments, tendons, and peri-articular soft tissue structures of the metacarpophalangeal joint. MDCT rated as "good" (median score 4) for all ligamentous structures, and "adequate" (median score 3) for CBCT images, but the difference was significant ($P < 0.001$, Figure 1.10B). A notable exception for both modalities was the collateral ligament where the image quality was rated as "poor" with a median score of 1.5 for both MDCT and CBCT images. Tendon images on MDCT were rated as "good" with a median score of 4, while CBCT images rated as "adequate" with a median score of 3 ($P < 0.001$). Visibility of peri-articular soft tissues of the metacarpophalangeal joint were superior on MDCT images (median score 3) compared to CBCT images (median score 1.5, $P = 0.005$). These results demonstrate the CBCT is equivalent to MDCT for imaging of bone, while conventional CT images are preferred for imaging of soft tissue structures at the current time.

Side-by-side preference tests between MDCT and CBCT images for bone and soft tissue are summarized in Figure 1.10C, D. Although ligaments, tendons and peri-articular soft tissues rated as "adequate" on satisfaction tests, there was a strong preference for MDCT images for

evaluation of soft tissues ($P < 0.001$). For bone, each reviewer differed in their preferences, with one reviewer strongly trending towards CBCT images as superior for bone evaluation ($P = 0.004$), while the second reviewer tended to grade CBCT images equal with conventional CT images for bone evaluation. A difference was not detected ($P = 0.167$) between MDCT and CBCT in image preference when evaluating bone. Variability was observed between reviewers in how they rated the quality of the images, with a maximum of 75% agreement in scores for bone evaluation. This lower-than-expected level of agreement does not mean that images were not diagnostic, as if scores from satisfaction tests were group into a binary outcome of "diagnostic" (scores 3-5) or "non-diagnostic" (scores 1-2), inter-reviewer agreement increased to 100% for bone, 75% for ligament, 87% for tendon, and 60% for peri-articular soft tissues. These findings suggest that there are still improvements that need to be made in quality for CBCT images—especially in regards to soft tissue imaging—but in comparison to the previous pilot work demonstrate the substantial improvements that have been made in CBCT technology and image processing in a relatively short period of time.

Taken together, CBCT should be viewed as both as a developing alternative and adjunctive tool for advanced imaging of subchondral bone. The potential strengths of this modality include its portability, efficient scan times, ability to acquire diagnostic images of the complete length of the appendicular skeleton, head and cervical spine, and economical cost. More objective and clinical studies are needed moving forward, especially in examining the sensitivity of CBCT for detection of early changes within the subchondral bone, however preliminary work demonstrates the potential for numerous clinical benefits for CBCT use moving forward.

1.8 Purpose of study

Osteoarthritis is well-recognized as a multifactorial disease where multiple joint tissues ultimately contribute to articular cartilage degeneration. More recently, alterations in the subchondral bone have been recognized for their contribution to both joint health and joint deterioration. Although changes in subchondral bone are typically associated with late-stage disease, compelling evidence suggests BMLs may be one of the earliest signs of changes within the joint, preceding damage to the articular cartilage. Advancements in volumetric imaging have enabled new techniques for identification of these lesions, including use of both MRI and CT. Currently, understanding of BMLs is restricted to clinical data and small animal models, limiting the interpretation and conclusions that can be drawn. The purpose of this collection of studies was to develop a reproducible experimental model of BMLs that mimics clinical disease, to optimize volumetric imaging for fluid detection within bone, to characterize the histologic attributes of BMLs without the influence of other pathologic lesions within the joint, and concurrently, to establish and validate novel translational research models to better understand this condition across species and clinical scenarios.

1.9 Research Overview

The first objective of this group of studies was to explore and optimize different techniques for characterization of fluid signal in bone using MR and CT. Preliminary work for this objective was focused on smaller, cadaveric studies evaluating different techniques for evaluation of the subchondral bone. These smaller studies aimed to identify differences in the appearance of fluid signal within bone across high-field MR sequences, and to investigate innovative imaging techniques for the evaluation of changes within subchondral bone. Findings

from these preliminary studies were then applied to an *in vivo* model as a part of the second objective. The second objective was to develop a reproducible experimental model of BMLs using the medial femoral condyle of the ovine femorotibial joint. As a part of this objective, this study aimed to identify the layers of the osteochondral unit that needed to be stimulated in order to generate a BML, and determined whether physical trauma to the articular surface is a prerequisite for BML generation. The third objective was to describe histopathologic changes associated with BMLs alone, in the absence of other pathologic changes within the joint. The fourth objective was to evaluate the long-term impact of BMLs on joint health using non-invasive volumetric imaging. Finally, the fifth objective was to develop a model for BMLs using the rodent femoral condyle, in order to both validate this experimental model and distinguish unique clinical attributes of BMLs not previously addressed in the ovine model. To address these research objectives, the following specific aims and hypotheses were developed.

1.10 Specific Aims and Hypotheses

1.10.1 Specific Aim 1 (Chapter 2: Imaging Characterization of Subchondral Bone Injury)

Computed tomography and MRI are advanced volumetric imaging modalities with a plethora of capabilities. The two modalities are frequently discussed in a complimentary fashion with MRI as the superior imaging modality for characterization of soft tissue or cartilage injuries, and CT as the superior imaging modality for characterization of bone. BMLs, or fluid within bone presents a challenge to diagnose using either modality. With the advent of new sequences available with high-field MR, and new techniques available for CT imaging, improved detection of fluid and bone detail should be possible within both modalities. Additional musculoskeletal imaging techniques, such as tomosynthesis, are also becoming more frequently

utilized for musculoskeletal imaging and warrant further investigation. Therefore, smaller-scale studies exploring the capabilities and limitations of these imaging modalities are warranted and was the overarching specific aim of this chapter. It was hypothesized that alterations in the subchondral bone will be best detected and characterized using volumetric imaging modalities, with comparable findings between CT and MRI.

1.10.2 Specific Aim 2 (Chapter 3: Development of an Experimental Model of Bone Marrow Lesions using the Ovine Femoral Condyle)

Persuasive reports have cited BMLs as early indicators of maladaptive remodeling within the subchondral bone, which may precede changes in the articular cartilage. The current understanding of BMLs primarily comes from what has been observed in clinical practice in both human and veterinary medicine. The current lack of a validated experimental model has prohibited more thorough investigation of the significance of these lesions and their relationship to joint health and disease. The specific aims of this chapter were multi-fold: first, to develop a consistent, reproducible experimental model for BMLs using a validated preclinical animal model for the human knee joint. Multiple methods, including focal, acute damage to varying layers of the osteochondral tissues, as well as transcutaneous extracorporeal shockwave were used. The second aim was to optimize advanced volumetric imaging for non-invasive characterization of these lesions over time. It was hypothesized that it would be possible to create a reproducible experimental model for BMLs that mimicked clinically-relevant disease as observed in both humans and veterinary species.

1.10.3 Specific Aim 3 (Chapter 3: Development of an Experimental Model of Bone Marrow Lesions using the Ovine Femoral Condyle)

BMLs are frequently observed in conjunction with other co-morbidities, including OA, traumatic soft tissue and ligamentous injuries, rheumatoid arthritis, and osteoporosis. The impact of this is that the current understanding of BMLs is predominantly limited to the clinical literature, little is understood about the effects of BMLs on the osteochondral tissues in isolation from other disease. In conjunction with Specific Aim 2, post-mortem histologic characterization of BMLs in isolation from other pathologic changes is critical. Knowledge regarding the histological characteristics of these lesions informs the current understanding about the etiopathogenesis of these lesions, as well as the biological and biomechanical effects. It was hypothesized that the presence of a BML alone is sufficient to create an inflammatory response followed by remodeling with the subchondral bone, without altering the articular cartilage.

1.10.4 Specific Aim 4 (Chapter 4: Long-Term Advanced Imaging Investigation of an Experimental Model of Bone Marrow Lesions using the Ovine Femoral Condyle)

The evolution of BMLs in the clinical setting is unpredictable. In some cases, BMLs resolve completely over the course of weeks or months, while in other cases they persist for years. Additionally, because BMLs require MRI for diagnosis, logistical and financial limitations often negate the ability for serial monitoring of these lesions alone. The long-term effects of BMLs alone have not been described, and may elucidate the postulated relationship between BMLs and degenerative joint disease. Therefore, the specific aim of this study was to follow and characterize experimentally induced BMLs in the ovine femorotibial joint for 12 months using

CT and MRI. It was hypothesized that persistence of a BML within the subchondral and trabecular bone would create irreversible changes to the bone and joint.

1.10.5 Specific Aim 5 (Chapter 5: Development of an Experimental Model of Bone Marrow Lesions using the Rodent Femoral Condyle)

The use of a large animal preclinical model has numerous advantages and limitations. Extrapolation of the previously developed ovine model into a small animal preclinical model would enable additional opportunities for cellular, molecular, and immunologic characterization. The femorotibial joint of the rat has been described as a translational model for the human knee, validating its use for development of an experimental model of BMLs. Additionally, extrapolation of this experimental model would demonstrate that observed results were not somehow inherent to physiological processes within the sheep. It was therefore the specific aim of this study to develop an experimental model of BMLs using the rat medial femoral condyle and compare the similarities and differences to that of the ovine model. It was hypothesized that it would be possible to adapt the previously developed experimental model, and BMLs would have similar imaging and histologic characteristics across preclinical animal models.

1.11 Figures

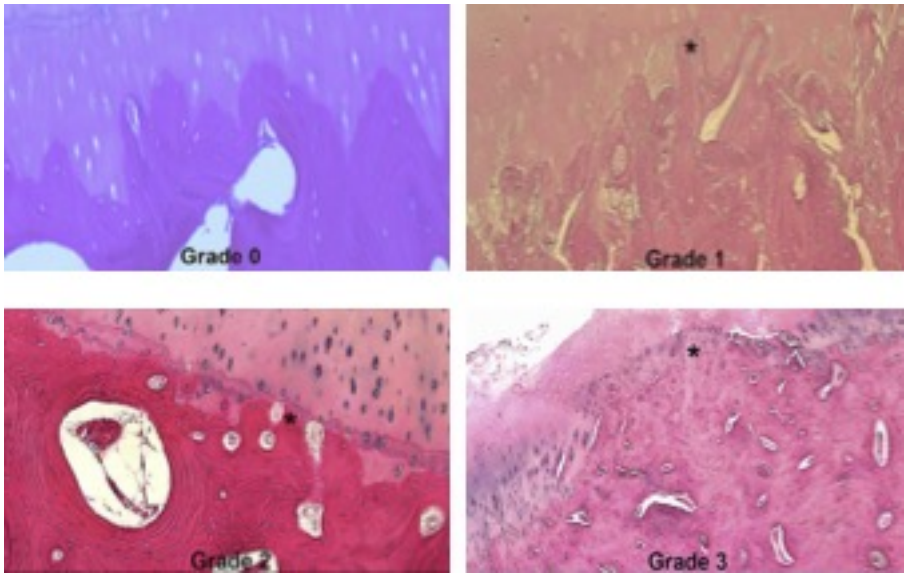

Figure 1.1 – Histopathologic grading examples of osteochondral lesions in spontaneous osteoarthritis cases in equine metacarpophalangeal joints. Microscopic images showing advancement of subchondral bone remodeling through calcified cartilage layer (star). *With permission from McIlwraith CW, et al. The OARSI histopathology initiative. Osteoarthritis Cartilage 2010;18:S93-105.*

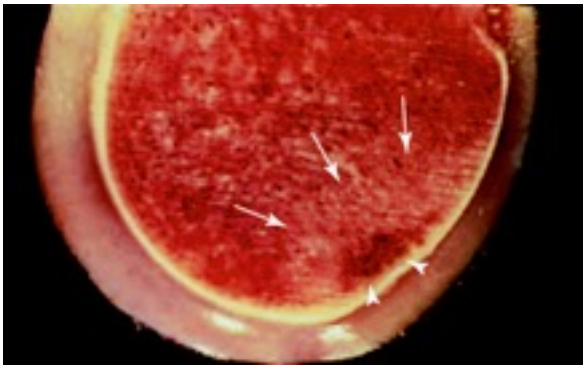

Figure 1.2 – Postmortem sample of a distal metacarpus from the leg opposite to that suffering a catastrophic injury in a racehorse. Although there is intact articular cartilage, subchondral bone necrosis (arrowheads) and sclerosis (arrows) can be seen. *With permission from McIlwraith CW, et al. Joint Disease in the Horse (Second Edition), 2016:33-48.*

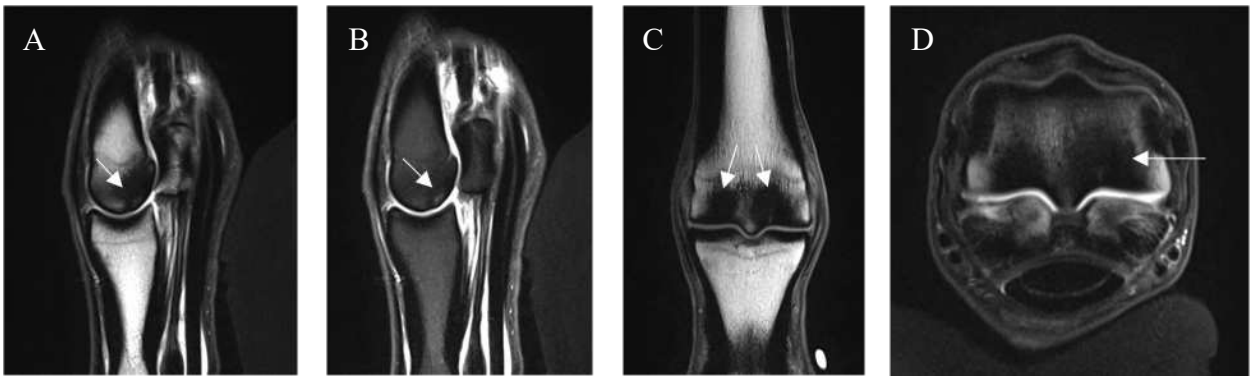

Figure 1.3 – Images of subchondral bone injury as detected using magnetic resonance imaging (MRI). An intermediate-weighted T1 TSE sequence with (A) and without (B) fat suppression in the sagittal (A, B), dorsal (C), and transverse (D) planes. There is marked subchondral and trabecular bone sclerosis in the palmar aspect of the third metacarpal condyle (white arrows), with the lateral condyle slightly more affected than the medial condyle. There is a fissure visible within the bone on the palmar-axial aspect of the lateral condyle that also exhibits increased signal (D, arrow). *With permission from Stewart HL and Kawcak CE. The importance of subchondral bone in the pathophysiology of osteoarthritis. Front Vet Sci 2018;5:178.*

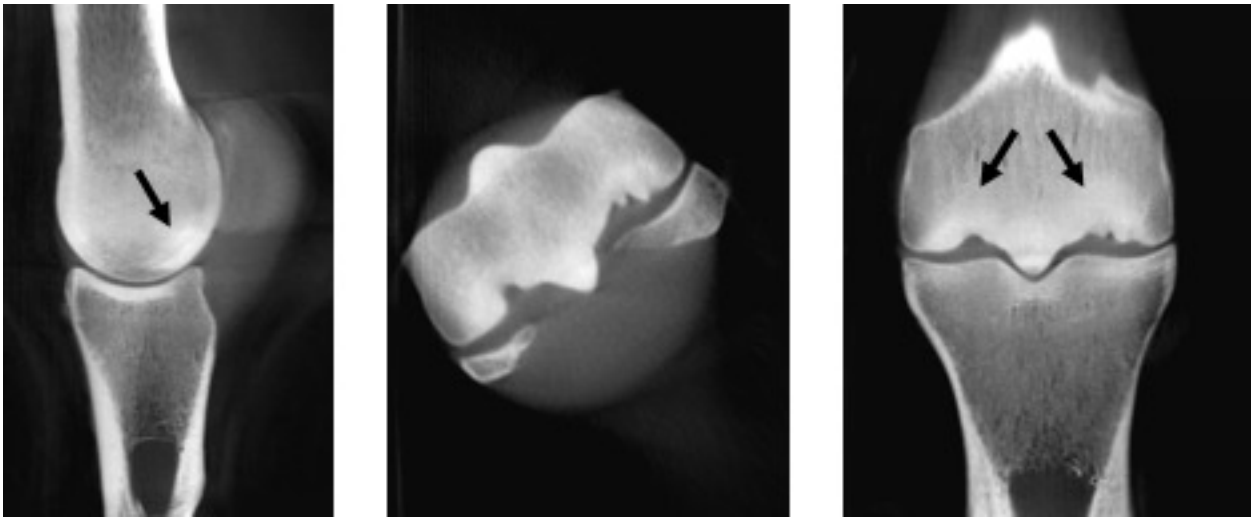

Figure 1.4 – Postmortem image of the distal metacarpus of a 10-year-old Thoroughbred racehorse with marked palmar osteochondral disease obtained using computed tomography (CT) in the sagittal, transverse and dorsal planes. Subchondral bone sclerosis and lysis (black arrows) and extensive articular cartilage loss is visible on these images and was present on gross evaluation. *With permission from Stewart HL and Kawcak CE. The importance of subchondral bone in the pathophysiology of osteoarthritis. Front Vet Sci 2018;5:178.*

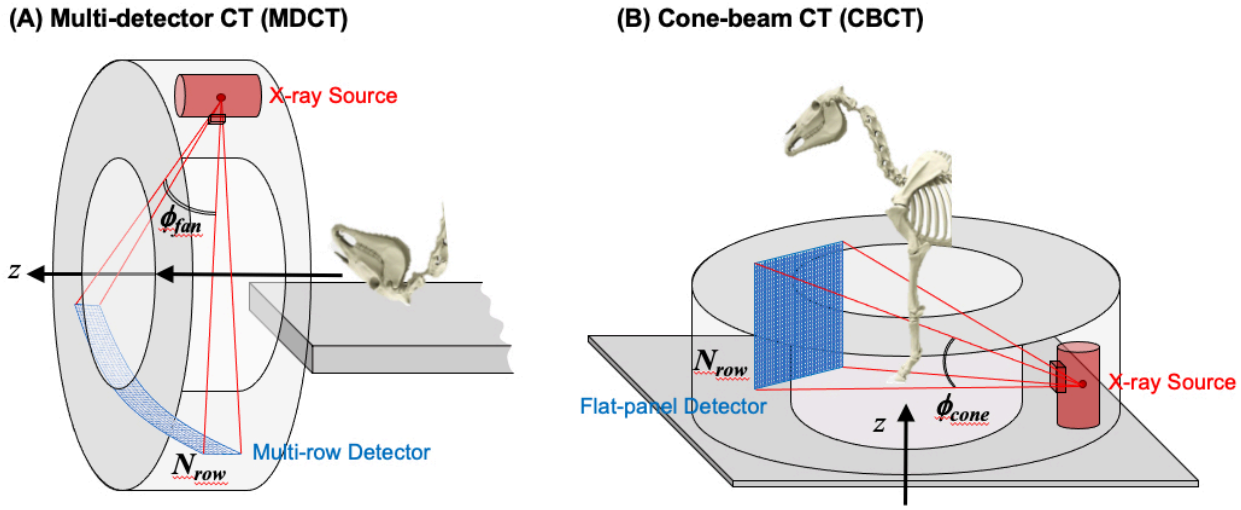

Figure 1.5 – Illustrative figures of example (A) multi-detector computed tomography (MDCT) and (B) cone-beam computed tomography (CBCT) setup and geometry. Key differences in mechanical components between MDCT and CBCT include: x-ray tube power (lower for CBCT); detector type (a large area of flat-panel detector for CBCT); patient setup (typically dorsal recumbency for MDCT, standing for CBCT); and image acquisition mode (helical motion with patient translation along the z axis for MDCT, and circular motion without movement of the patient for CBCT). Key differences in 3D image characteristics include: field of view (smaller for CBCT); soft tissue contrast resolution (lower for CBCT); and spatial resolution (higher for CBCT). *With permission from Stewart HL, et al. Use of cone-beam computed tomography for advanced imaging of the equine patient. Equine Vet J 2021;53:872-885.*

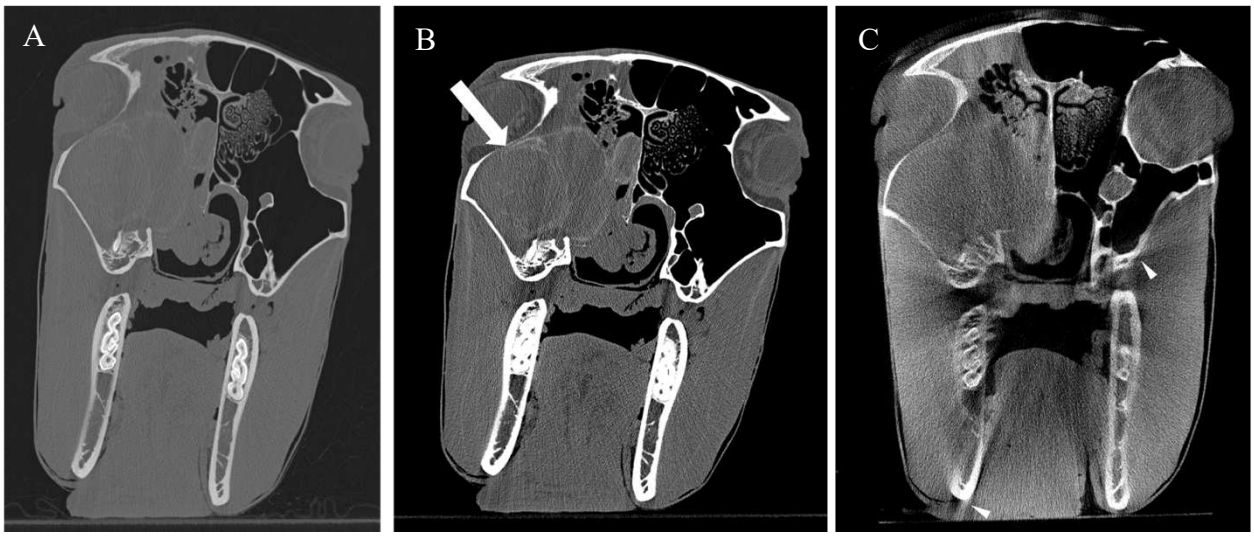

Figure 1.6 – Comparative images of the equine skull acquired using different computed tomographic techniques. An ethmoid hematoma (white arrow, image (B)) was identified in the right paranasal sinus. Images acquired using fan-beam computed tomography (CT), windowed for (A) bone and (B) soft tissue, using 140 kVp for the fan-beam scanner and 110 kVp for the cone-beam scanner. Notice how the (A) and (B) images have been manipulated and enhanced to best demonstrate the lesion. (C) Image acquired using cone-beam CT at a similar location after a single rotation of the gantry. The cone-beam CT image has a greater amount of overall noise as well as the presence of streaking artifacts (white arrowheads, image (C)). These factors contribute to an image (C) with lower contrast and soft tissue resolution compared to the soft tissue-windowed image (B) acquired using fan-beam CT. *With permission from Stewart HL, et al. Use of cone-beam computed tomography for advanced imaging of the equine patient. Equine Vet J 2021;53:872-885.*

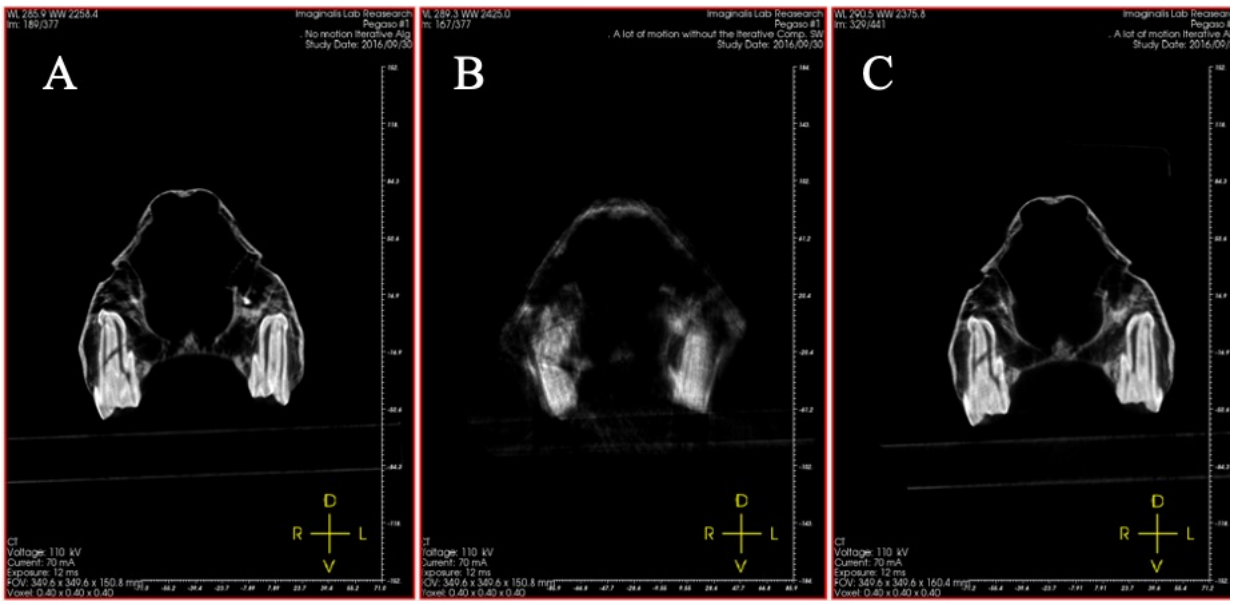

Figure 1.7 – Comparative images of axial views of an equine skull using the Pegaso cone-beam CT unit (Epica Medical Innovations, San Clemente, CA, USA). All images were acquired using the same technique; however, image (A) was acquired with no motion, image (B) was acquired with over 50 mm of motion in all directions without the motion correction software applied, and image (C) was acquired with over 50 mm of motion in all directions and has the iterative algorithm for motion correction applied. Notice there is excellent resolution of bone detail in image (A), which is lost secondary to motion in image (B). After application of the iteration algorithm for motion correction, a high-resolution image is able to be reconstructed, as observed in image (C). *With permission from Stewart HL, et al. Use of cone-beam computed tomography for advanced imaging of the equine patient. Equine Vet J 2021;53:872-885.*

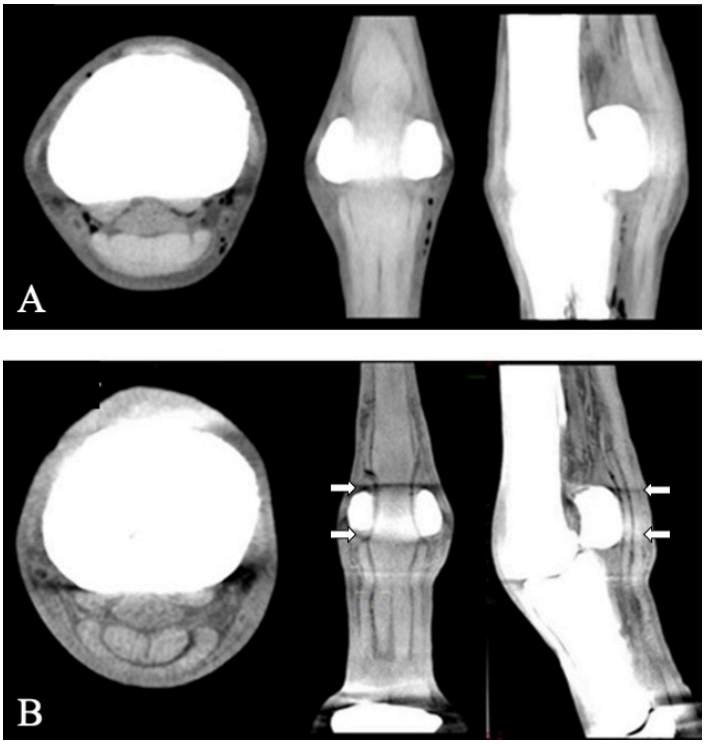

Figure 1.8 – Transverse, dorsal and sagittal image reconstructions windowed to visualize soft-tissue structures of the metacarpophalangeal joint acquired with (A) traditional fan-beam and (B) cone-beam computed tomography from preliminary work. Note the similar conspicuity of the superficial and deep digital flexor tendons, and straight distal sesamoidean ligaments and ability to distinguish the margins of these soft tissue structures from one another. The artifacts visible in (B) are cone-beam artifacts (white arrows). Cone-beam artifacts are the result of incomplete sampling from a circular orbit of the source and detector. *With permission from Stewart HL, et al. Use of cone-beam computed tomography for advanced imaging of the equine patient. Equine Vet J 2021;53:872-885.*

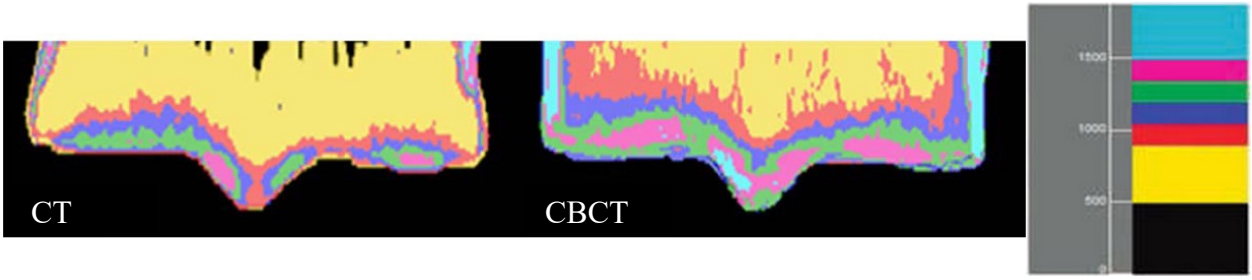

Figure 1.9 – Slices acquired from three-dimensional renderings from the metacarpophalangeal joint of a horse using both (A) traditional fan-beam (CT) and (B) cone-beam computed tomography (CBCT). The slices are in the dorsal plane, 30-degrees caudal to the transverse ridge. A reference color scale for computed tomography data is included; all numbers are in Hounsfield units. Increasing numbers correspond to increasing density. Notice the enhanced spatial resolution of the density distribution in the image acquired with CBCT as compared to the image constructed from traditional fan-beam computed tomography data. *With permission from Stewart HL, et al. Use of cone-beam computed tomography for advanced imaging of the equine patient. Equine Vet J 2021;53:872-885.*

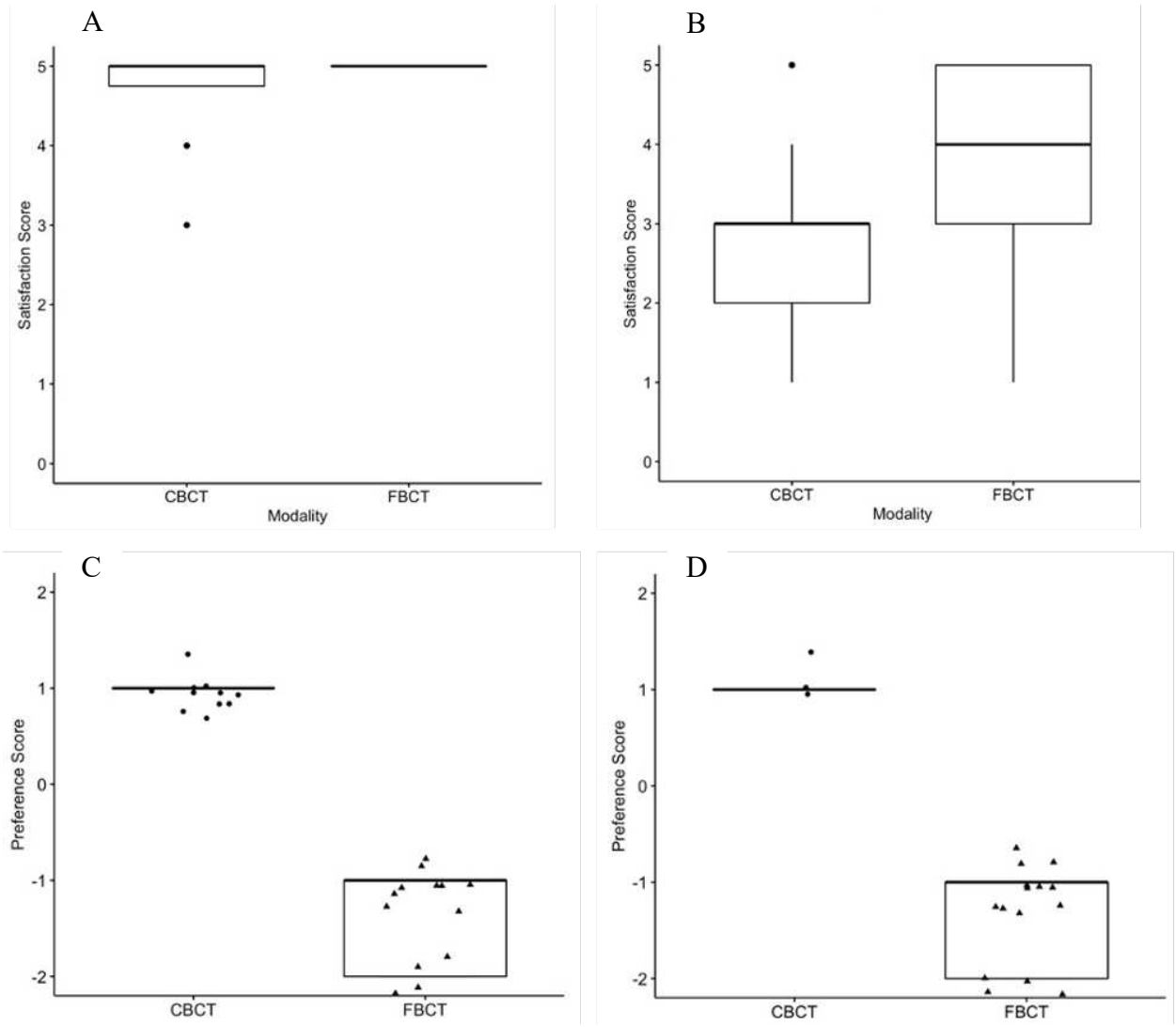

Figure 1.10 – (A, B) Satisfaction and (C, D) preference tests for fan-beam computed tomography (FBCT) and cone-beam computed tomography images (CBCT). The distribution of scores is shown for bone evaluation (left plots; A, C) and soft tissue evaluation (right plots; B, D) in the equine metacarpophalangeal joint. (A, B) For satisfaction tests, the median is represented by a solid line, the box marks the first and third quartiles, and outliers are represented by the dots. For satisfaction tests, CBCT images were equivalent to FBCT images for evaluation of bone (A), but were less superior for evaluation of soft tissues compared to FBCT images (B). (C, D) For preference tests, the median is represented by a solid line, the box marks the first and third quartiles, and scores are represented by the dots (CBCT) or triangles (FBCT). A difference in preference was not observed between CBCT and FBCT for images evaluating bone (C), but FBCT was preferred for images windowed to evaluate soft tissues (D).

1.12 References

1. Cisternas MG, Murphy L, Sacks JJ, et al. Alternative Methods for Defining Osteoarthritis and the Impact on Estimating Prevalence in a US Population-Based Survey. Arthritis Care Res 2016;68:574–580.

2. Hootman JM, Helmick CG. Projections of US prevalence of arthritis and associated activity limitations. Arthritis Rheum 2006;54:226–229.

3. Hootman J, Helmick C, Barbour K, et al. Updated Projected Prevalence of Self-Reported Doctor-Diagnosed Arthritis and Arthritis-Attributable Activity Limitation Among US Adults, 2015-2040. Arthritis Rheumatol 2016;68:1582–1587.

4. Zhang Y, Jordan JM. Epidemiology of Osteoarthritis. Clin Geriatr Med 2010;26:355.

5. Oke SL, Mcilwraith CW, Acvs D. Review of the Economic Impact of Osteoarthritis and Oral Joint-Health Supplements in Horses.; 2010.

6. Griffon DJ. A Review of the Pathogenesis of Canine Cranial Cruciate Ligament Disease as a Basis for Future Preventive Strategies. Vet Surg 2010;39:399–409.

7. Goldring SR. Alterations in periarticular bone and cross talk between subchondral bone and articular cartilage in osteoarthritis. Ther Adv Musculoskelet Dis 2012;4:249–258.

8. Goldring SR. Cross-talk between subchondral bone and articular cartilage in osteoarthritis. Arthritis Res Ther 2012 142 2012;14:1–8.

9. Pan J, Wang B, Li W, et al. Elevated cross-talk between subchondral bone and cartilage in osteoarthritic joints. Bone 2012;51:212–217.

10. McIlwraith CW, Frisbie DD, Kawcak CE. The horse as a model of naturally occurring osteoarthritis. Bone Joint Res 2012;1:297–309.

11. Neundorf R, Lowerison M, Cruz A, et al. Determination of the prevalence and severity of metacarpophalangeal joint osteoarthritis in Thoroughbred racehorses via quantitative macroscopic evaluation. Am J Vet Res 2010;71:1284–1293.

12. Norrdin RW, Kawcak CE, Capwell BA, et al. Subchondral bone failure in an equine model of overload arthrosis. Bone 1998;22:133–139.

13. Drum MGM, Kawcak CEC, Norrdin RRW, et al. Comparison of gross and histopathologic findings with quantitative computed tomographic bone density in the distal third metacarpal bone of racehorses. Vet Radiol Ultrasound 2007;48:518–527.

14. Clark JM, Huber JD. The structure of the human subchondral plate. J Bone Joint Surg Br 1990;72:866–73.

15. McIlwraith CW, Frisbie DD, Kawcak CE, et al. Joint disease in the horse. 2nd ed. (McIlwraith CW, Frisbie DD, Kawcak CE, et al., eds.). St. Louis, Missouri: Elsevier Inc; 2016.

16. Radin EL, Paul IL. Response of Joints to Impact Loading — I: In Vitro Wear. Arthritis Rheum 1971;14:356–362.

17. Simon SR, Radin EL, Paul IL, et al. The response of joints to impact loading — II: In vivo behavior of subchondral bone. J Biomech 1972;5:267–272.

18. Radin EL, Parker HG, Pugh JW, et al. Response of joints to impact loading — III: Relationship between trabecular microfractures and cartilage degeneration. J Biomech 1973;6:51–57.

19. Brama PAJ, Holopainen J, Weeren PR, et al. Influence of exercise and joint topography on depth-related spatial distribution of proteoglycan and collagen content in immature equine articular cartilage. Equine Vet J 2009;41:557–563.

20. Mankin H, Radin E. Structure and function of joints. In: McCarthy D, ed. Arthritis and allied conditions: a textbook of rheumatology. 12th Ed. Philadelphia, PA: Lea & Febiger; 1993:189.

21. Auer JA, Stick JA eds. Equine Surgery. 4th Editio. St. Louis, Missouri; 2012.

22. Radin EL, Rose RM. Role of subchondral bone in the initiation and progression of cartilage damage. Clin Orthop Relat Res 1986:34–40.

23. Smith MRW, Kawcak CE, McIlwraith CW. Science in brief: Report on the Havemeyer Foundation workshop on subchondral bone problems in the equine athlete. Equine Vet J 2016;48:6–8.

24. Merritt JS, Davies HMS, Burvill C, et al. Calculation of joint reaction forces in the equine distal forelimb during walking and trotting. Proc Front Converg Biosci Inf Technol FBIT 2007 2007;2008:587–590.

25. Frost HM. Skeletal structural adaptations to mechanical usage (SATMU): 2. Redefining Wolff's Law: The remodeling problem. Anat Rec 1990;226:414–422.

26. Sims NA, Martin TJ. Coupling the activities of bone formation and resorption: a multitude of signals within the basic multicellular unit. Bonekey Rep 2014;3.

27. Kawcak CE, McIlwraith CW, Norrdin RW, et al. The role of subchondral bone in joint disease: a review. Equine Vet J 2001;33:120–126.

28. Kawcak CE, McIlwraith CW, Norrdin RW, et al. Clinical effects of exercise on subchondral bone of carpal and metacarpophalangeal joints in horses. Am J Vet Res 2000;61:1252–1258.

29. Norrdin RW, Kawcak CE, Capwell BA, et al. Calcified cartilage morphometry and its relation to subchondral bone remodeling in equine arthrosis. Bone 1999;24:109–114.

30. Norrdin RW, Kawcak CE, Wayne McIlwraith C. Subchondral bone failure in an equine model of OA.pdf. Bone 1998;22:133–139.

31. Holmes J, Mirams M, Mackie E, et al. Thoroughbred horses in race training have lower levels of subchondral bone remodelling in highly loaded regions of the distal metacarpus compared to horses resting from training. Vet J 2014;202:443–447.

32. Lajeunesse D, Massicotte F, Pelletier J-P, et al. Subchondral bone sclerosis in osteoarthritis: not just an innocent bystander. Mod Rheumatol 2003;13:0007–0014.

33. Radin E. Subchondral bone changes and cartilage damage. Equine Vet J 1999;31:94–5.

34. Goldring MB, Goldring SR. Osteoarthritis. J Cell Physiol 2007;213:626–634.

35. McIlwraith CW. From Arthroscopy to Gene Therapy—30 Years of Looking in Joints. In: AAEP Proceedings.; 2005:65–113.

36. Berenbaum F. Osteoarthritis as an inflammatory disease (osteoarthritis is not osteoarthrosis!). Osteoarthr Cartil 2013;21:16–21.

37. Kapoor M, Martel-Pelletier J, Lajeunesse D, et al. Role of proinflammatory cytokines in the pathophysiology of osteoarthritis. Nat Rev Rheumatol 2011;7:33–42.

38. Boyde A. The real response of bone to exercise. J Anat 2003;203:173–189.

39. Pool R. Pathological manifestations of joint disease in the athletic horse. In: Mcilwraith CW, Trotter GW, eds. Joint disease in the horse. 1st Editio. Philadelphia, PA: Saunders Elsevier; 1996:98–99.

40. Riggs C. Aetiopathogenesis of parasagittal fractures of the distal condyles of the third metacarpal and third metatarsal bones - review of the literature. Equine Vet J 1999;31:116–120.

41. Riggs C, Whitehouse GH, Boyde A. Pathology of the distal condyles of the third metacarpal and third metatarsal bones of the horse. Equine Vet J 1999;31:140–148.

42. Martinelli M. Subchondral bone and injury. Equine Vet Educ 2009;21:253–256.

43. Cullimore A, Finnie J, Marmion W, et al. Severe lameness associated with an impact fracture of the proximal phalanx in a filly. Equine Vet Educ 2009;21:247–251.

44. Pool RR, Meagher DM. Pathologic Findings and Pathogenesis of Racetrack Injuries. Vet Clin North Am Equine Pract 1990;6:1–30.

45. Martig S, Chen W, Lee PVS, et al. Bone fatigue and its implications for injuries in racehorses. Equine Vet J 2014;46:408–415.

46. Drum MG, Les CM, Park RD, et al. Comparison of mean bone densities of three preparations of the distal portion of the equine third metacarpal bone measured by use of quantitative computed tomography. Am J Vet Res 2008;69:891–893.

47. Turley SM, Thambyah A, Riggs CM, et al. Microstructural changes in cartilage and bone related to repetitive overloading in an equine athlete model. J Anat 2014;224:647–658.

48. Tull TM, Bramlage LR. Racing prognosis after cumulative stress-induced injury of the distal portion of the third metacarpal and third metatarsal bones in Thoroughbred racehorses: 55 cases (2000–2009). J Am Vet Med Assoc 2011;238:1316–1322.

49. Riggs CM. Osteochondral injury and joint disease in the athletic horse. Equine Vet Educ 2010;18:100–112.

50. Eriksen EF. Treatment of bone marrow lesions (bone marrow edema). Bonekey Rep 2015;4:755.

51. Hayes CW, Conway WF, Daniel WW. MR imaging of bone marrow edema pattern: transient osteoporosis, transient bone marrow edema syndrome, or osteonecrosis. Radiographics 1993;13:1001–11.

52. Felson DT, McLaughlin S, Goggins J, et al. Bone Marrow Edema and Its Relation to Progression of Knee Osteoarthritis. Ann Intern Med 2003;139:330.

53. Xu L, Hayashi D, Roemer FW, et al. Magnetic resonance imaging of subchondral bone marrow lesions in association with osteoarthritis. Semin Arthritis Rheum 2012;42:105–118.

54. Hunter DJ, Zhang Y, Niu J, et al. Increase in bone marrow lesions associated with cartilage loss: A longitudinal magnetic resonance imaging study of knee osteoarthritis. Arthritis Rheum 2006;54:1529–1535.

55. Haavardsholm EA, Bøyesen P, Østergaard M, et al. Magnetic resonance imaging findings in 84 patients with early rheumatoid arthritis: bone marrow oedema predicts erosive progression. Ann Rheum Dis 2008;67:794–800.

56. Olive J, Mair TS, Charles B. Use of standing low-field magnetic resonance imaging to diagnose middle phalanx bone marrow lesions in horses. Equine Vet Educ 2009;21:116–123.

57. Zani DD, De Zani D, Biggi M, et al. Use of magnetic resonance imaging in the diagnosis of bone marrow edema in the equine distal limb: Six cases. Vet Res Commun 2009;33:225–228.

58. De Guio C, Ségard-Weisse E, Thomas-Cancian A, et al. Bone marrow lesions of the distal condyles of the third metacarpal bone are common and not always related to lameness in sports and pleasure horses. Vet Radiol Ultrasound 2019;60:167–175.

59. Biggi M, Zani DD, De Zani D, et al. Magnetic resonance imaging findings of bone marrow lesions in the equine distal tarsus. Equine Vet Educ 2012;24:236–241.

60. Barrett MF, Selberg KT, Johnson SA, et al. High field magnetic resonance imaging contributes to diagnosis of equine distal tarsus and proximal metatarsus lesions: 103 horses. Vet Radiol Ultrasound 2018;59:587–596.

61. Andrews CL. Evaluation of the Marrow Space in the Adult Hip. RadioGraphics 2000;20.

62. Sasiponganan C, Yan K, Pezeshk P, et al. Advanced MR imaging of bone marrow: quantification of signal alterations on T1-weighted Dixon and T2-weighted Dixon sequences in red marrow, yellow marrow, and pathologic marrow lesions. Skeletal Radiol 2020;49:541–548.

63. Starr AM, Wessely MA, Albastaki U, et al. Bone Marrow Edema: Pathophysiology, Differential Diagnosis, and Imaging. Acta radiol 2008;49:771–786.

64. Bonadio MB, Filho AGO, Helito CP, et al. Bone Marrow Lesion: Image, Clinical Presentation, and Treatment. Magn Reson Insights 2017;10:1178623X17703382.

65. Alliston T, Hernandez C, Findlay D, et al. Bone marrow lesions in osteoarthritis: What lies beneath. J Orthop Res 2018;36:1818–1825.

66. Douis H, Davies A, Jeys L, et al. Chemical shift MRI can aid in the diagnosis of indeterminate skeletal lesions of the spine. Eur Radiol 2016;26:932–940.

67. Zajick D, Morrison W, Schweitzer M, et al. Benign and malignant processes: normal values and differentiation with chemical shift MR imaging in vertebral marrow. Radiology 2005;237:590–596.

68. Del Grande F, Santini F, Herzka DA, et al. Fat-Suppression Techniques for 3-T MR Imaging of the Musculoskeletal System. Radiographics 2014;34:217–233.

69. Kirchgesner T, Perlepe V, Michoux N, et al. Fat suppression at 2D MR imaging of the hands: Dixon method versus CHESS technique and STIR sequence. Eur J Radiol 2017;89:40–46.

70. Maeder Y, Dunet V, Richard R, et al. Bone Marrow Metastases: T2-weighted Dixon Spin-Echo Fat Images Can Replace T1-weighted Spin-Echo Images. Radiology 2018;286:948–959.

71. Pache G, Krauss B, Strohm P, et al. Dual-energy CT virtual noncalcium technique: detecting posttraumatic bone marrow lesions--feasibility study. Radiology 2010;256:617–624.

72. Björkman A-S, Koskinen SK, Lindblom M, et al. Diagnostic accuracy of dual-energy CT for detection of bone marrow lesions in the subacutely injured knee with MRI as reference method. Acta radiol 2019;61:749–759.

73. Gosangi B, Jacob Mandell MC, Weaver MJ, et al. Bone Marrow Edema at Dual-Energy CT: A Game Changer in the Emergency Department. RadioGraphics 2020;40:859–874.

74. Hofmann S, Kramer J, Vakil-Adli A, et al. Painful bone marrow edema of the knee: differential diagnosis and therapeutic concepts. Orthop Clin North Am 2004;35:321–333.

75. Hofmann S, Kramer J, Breitenseher M, et al. Bone marrow edema in the knee: differential diagnosis and therapeutic possibilities. Orthopade 2006;35:463–477.

76. Collins JA, Beutel BG, Strauss E, et al. Bone marrow edema: chronic bone marrow lesions of the knee and the association with osteoarthritis. Bull NYU Hosp Jt Dis 2016;74:24–36.

77. Kon E, Ronga M, Filardo G, et al. Bone marrow lesions and subchondral bone pathology of the knee. Knee Surg Sport Traumatol Arthrosc 2016;24:1797–1814.

78. Schweitzer M, White L. Does altered biomechanics cause marrow edema? Radiology 1996;198:851–853.

79. Breitenseher MJ, Kramer J, Mayerhoefer ME, et al. Differential diagnosis of bone marrow edema of the knee joint. Radiologe 2006;46:46–54.

80. McQueen FM. Bone marrow edema and osteitis in rheumatoid arthritis: the imaging perspective. Arthritis Res Ther 2012;14:224.

81. Karchevsky M, Schweitzer ME, Morrison WB, et al. MRI Findings of Septic Arthritis and Associated Osteomyelitis in Adults. Am J Roentgenol 2004;182:119–122.

82. Gondim Teixeira PA, Hossu G, Lecocq S, et al. Bone marrow edema pattern identification in patients with lytic bone lesions using digital subtraction angiography-like bone subtraction on large-area detector computed tomography. Invest Radiol 2014;49:156–164.

83. Manara M, Varenna M. A clinical overview of bone marrow edema. Reumatismo 2014;66:184–196.

84. Scher C, Craig J, Nelson F. Bone marrow edema in the knee in osteoarthrosis and association with total knee arthroplasty within a three-year follow-up. Skeletal Radiol 2008;37:609–617.

85. Roemer FW, Guermazi A, Javaid MK, et al. Change in MRI-detected subchondral bone marrow lesions is associated with cartilage loss: the MOST Study. A longitudinal multicentre study of knee osteoarthritis. Ann Rheum Dis 2009;68:1461–1465.

86. Tanamas S, Wluka A, Pelletier J, et al. Bone marrow lesions in people with knee osteoarthritis predict progression of disease and joint replacement: a longitudinal study. Rheumatology 2010;49:2413–2419.

87. Zanetti M, Bruder E, Romero J, et al. Bone marrow edema pattern in osteoarthritic knees: correlation between MR imaging and histologic findings. Radiology 2000;215:835–840.

88. Madry H, van Dijk C, Mueller-Gerbl M. The basic science of the subchondral bone. Knee Surg Sport Traumatol Arthrosc 2010;18:419–433.

89. Felson DT, Chaisson CE, Hill CL, et al. The Association of Bone Marrow Lesions with Pain in Knee Osteoarthritis. Ann Intern Med 2001;134:541–549.

90. Baranyay F, Wang Y, Wluka A, et al. Association of bone marrow lesions with knee structures and risk factors for bone marrow lesions in the knees of clinically healthy, community-based adults. Semin Arthritis Rheum 2007;37:112–118.

91. Guymer E, Baranyay F, Wluka A, et al. A study of the prevalence and associations of subchondral bone marrow lesions in the knees of healthy, middle-aged women. Osteoarthr Cartil 2007;15:1437–1442.

92. Tucker RL, Sande RD. Computed tomography and magnetic resonance imaging in equine musculoskeletal conditions. Vet Clin North Am Equine Pract 2001;17:145–157.

93. Pauwels R, Araki K, Siewerdsen JH, et al. Technical aspects of dental CBCT: state of the art. Dentomaxillofacial Radiol 2015;44:20140224.

94. Carrino JA, Al Muhit A, Zbijewski W, et al. Dedicated Cone-Beam CT System for Extremity Imaging. Radiology 2014;270:816–824.

95. Jaffray DA, Siewerdsen JH. Cone-beam computed tomography with a flat-panel imager: Initial performance characterization. Med Phys 2000;27:1311–1323.

96. Hu H, He HD, Foley WD, et al. Four Multidetector-Row Helical CT: Image Quality and Volume Coverage Speed. Radiology 2000;215:55–62.

97. Scarfe WC, Farman AG. What is cone-beam CT and how does it work? Dent Clin North Am 2008;52:707–730.

98. Nagarajappa AK, Dwivedi N, Tiwari R. Artifacts: The downturn of CBCT image. J Int Soc Prev Community Dent 2015;5:440–445.

99. Dalrymple NC, Prasad SR, El-Merhi FM, et al. Price of isotropy in multidetector CT. Radiographics 2007;27:49–62.

100. Schulze R, Heil U, Groβ D, et al. Artefacts in CBCT: a review. Dentomaxillofacial Radiol 2011;40:265–273.

101. Zhao Z, Gang GJ, Siewerdsen JH. Noise, sampling, and the number of projections in cone-beam CT with a flat-panel detector. Med Phys 2014;41:061909.

102. Joseph PM, Schulz RA. View sampling requirements in fan beam computed tomography. Med Phys 1980;7:692–702.

103. Boas FE, Fleischmann D. CT artifacts: causes and reduction techniques. Imaging Med 2012;4:229–240.

104. Barrett JF, Keat N. Artifacts in CT: Recognition and Avoidance. RadioGraphics 2004;24:1679–1691.

105. Barrett J, Keat N, Platten D, et al. Cardiac CT Scanning. London, England; 2003.

106. Desjardins B, Kazerooni EA. ECG-Gated Cardiac CT. Am J Roentgenol 2004;182:993–1010.

107. Pontana F, Pagniez J, Flohr T, et al. Chest computed tomography using iterative reconstruction vs filtered back projection (Part 1): evaluation of image noise reduction in 32 patients. Eur Radiol 2011;21:627–635.

108. Ritchie CJ, Crawford CR, Godwin JD, et al. Correction of computed tomography motion artifacts using pixel-specific back-projection. IEEE Trans Med Imaging 1996;15:333–342.

109. Flohr TG, Schaller S, Stierstorfer K, et al. Multi-detector row CT systems and image-reconstruction techniques. Radiology 2005;235:756–773.

110. Scarfe WC, Farman AG, Sukovic P. Clinical applications of cone-beam computed tomography in dental practice. J Can Dent Assoc 2006;72:75–80.

111. Sisniega A, Stayman J, Yorkston J, et al. Motion compensation in extremity cone-beam CT using a penalized image sharpness criterion. Phys Med Biol 2017;62:3712–3734.

112. Demehri S, Muhit A, Zbijewski W, et al. Assessment of image quality in soft tissue and bone visualization tasks for a dedicated extremity cone-beam CT system. Eur Radiol 2015;25:1742–1751.

113. Gough SL, Anderson JDC, Dixon JJ. Computed tomographic cervical myelography in horses: Technique and findings in 51 clinical cases. J Vet Intern Med 2020;34:2142–2151.

114. Lindgren CM, Wright L, Kristoffersen M, et al. Computed tomography and myelography of the equine cervical spine: 180 cases (2013–2018). Equine Vet Educ 2020:eve.13350.

115. Honkanen JTJ, Danso EK, Suomalainen J-S, et al. Contrast enhanced imaging of human meniscus using cone beam CT. Osteoarthr Cartil 2015;23:1367–1376.

116. Thawait GK, Demehri S, AlMuhit A, et al. Extremity cone-beam CT for evaluation of medial tibiofemoral osteoarthritis: Initial experience in imaging of the weight-bearing and non-weight-bearing knee. Eur J Radiol 2015;84:2564–2570.

117. Cao Q, Thawait G, Gang GJ, et al. Characterization of 3D joint space morphology using an electrostatic model (with application to osteoarthritis). Phys Med Biol 2015;60:947–960.

118. Muhit AA, Arora S, Ogawa M, et al. Peripheral quantitative CT (pQCT) using a dedicated extremity cone-beam CT scanner. In: Weaver JB, Molthen RC, eds. Proc. SPIE 8672, Medical Imaging 2013: Biomedical Applications in Molecular, Structural, and Functional Imaging. International Society for Optics and Photonics; 2013:867203.

119. Zbijewski W, Sisniega A, Stayman JW, et al. Dual-Energy Imaging of Bone Marrow Edema on a Dedicated Multi-Source Cone-Beam CT System for the Extremities. Hoeschen C, Kontos D, Flohr TG, eds. Proc SPIE--The Int Soc Opt Eng 2015;9412:94120V.

120. Olive J, D'Anjou MA, Alexander K, et al. Correlation of signal attenuation-based quantitative magnetic resonance imaging with quantitative computed tomographic measurements of subchondral bone mineral density in metacarpophalangeal joints of horses. Am J Vet Res

2010;71:412–420.

121. Mageed M. Standing computed tomography of the equine limb using a multi-slice helical scanner: Technique and feasibility study. Equine Vet Educ 2020:eve.13388.

122. Gasiorowski JC, Richardson DW. Clinical use of computed tomography and surface markers to assist internal fixation within the equine hoof. Vet Surg 2015;44:214–222.

123. Han C, Choi S, Lee C, et al. Dual energy approach for cone beam artifacts correction. In: Flohr TG, Lo JY, Gilat Schmidt T, eds. Medical Imaging 2017: Physics of Medical Imaging. International Society for Optics and Photonics; 2017:1013228.

124. Nicolaou S, Liang T, Murphy DT, et al. Dual-Energy CT: a promising new technique for assessment of the musculoskeletal system. Am J Roentgenol 2012;199:S78–S86.

125. Karçaaltincaba M, Aktas A. Dual-energy CT revisited with multidetector CT: review of principles and clinical applications. Diagn Interv Radiol 2011;17:181–194.

126. Johnson TRC, Krauß B, Sedlmair M, et al. Material differentiation by dual energy CT: initial experience. Eur Radiol 2007;17:1510–1517.

127. Watanabe Y, Uotani K, Nakazawa T, et al. Dual-energy direct bone removal CT angiography for evaluation of intracranial aneurysm or stenosis: comparison with conventional digital subtraction angiography. Eur Radiol 2009;19:1019–1024.

128. Graser A, Johnson TRC, Chandarana H, et al. Dual energy CT: preliminary observations and potential clinical applications in the abdomen. Eur Radiol 2009;19:13–23.

129. Graser A, Johnson TRC, Bader M, et al. Dual energy CT characterization of urinary calculi: initial in vitro and clinical experience. Invest Radiol 2008;43:112–119.

130. Scheffel H, Stolzmann P, Frauenfelder T, et al. Dual-energy contrast-enhanced computed tomography for the detection of urinary stone disease. Invest Radiol 2007;42:823–829.

131. Kaza RK, Platt JF, Cohan RH, et al. Dual-energy ct with single- and dual-source scanners: Current applications in evaluating the genitourinary tract. Radiographics 2012;32:353–369.

132. Zbijewski W, Gang GJ, Xu J, et al. Dual-energy cone-beam CT with a flat-panel detector: Effect of reconstruction algorithm on material classification. Med Phys 2014;41:021908.

133. Ludewig E, Richter A, Frame M. Diagnostic imaging - Evaluating image quality using visual grading characteristic (VGC) analysis. Vet Res Commun 2010;34:473–479.

134. Easton KL, Kawcak CE. Evaluation of increased subchondral bone density in areas of contact in the metacarpophalangeal joint during loading in horses. Am J Vet Res 2007;68:816–821.

135. Young BD, Samii VF, Mattoon JS, et al. Subchondral bone density and cartilage degeneration patterns in osteoarthritic metacarpal condyles of horses. Am J Vet Res 2007;68:841–849.

CHAPTER 2:

IMAGING CHARACTERIZATION OF SUBCHONDRAL BONE INJURY

2.1 Introduction

Joint disease is a substantial problem across species with notable economic and social impact. Early detection of changes within the osteochondral tissues is of paramount importance in order to better understand disease progression, as well as opportunities for therapeutic interventions. Although historically the discussion surrounding joint disease has primarily focused on articular cartilage, it is now clear that other joint tissues are crucially important in the process. Changes to bone tissues, such as subchondral bone sclerosis and osteophyte formation, are well established as signs of late-stage joint disease, but more recently bone marrow lesions (BMLs) have been described in early states of joint disease. BMLs, all referred to as "bone edema," or "bone bruises," are defined as hyperintense signal on fluid-sensitive, fat-suppressed sequences using magnetic resonance imaging (MRI). These lesions cannot be observed using radiography, making them challenging to diagnose and monitor. Interestingly, BMLs may appear before changes in the articular cartilage, suggesting they may be an early indicator of alterations in joint health.[1] Furthermore, there is already strong evidence for the relationship between BMLs and joint disease—the presence of a BML increases the risk of cartilage loss[2], likelihood of progression of disease,[3] and causes clinical pain[4,5].

Non-invasive, in-life assessment of remodeling processes within subchondral bone is possible with the use of advanced imaging modalities such as MRI, and potentially even computed tomography (CT). High-field (>1.0 Tesla) MR units can highlight fluid signal with reduced field inhomogeneity from incomplete fat suppression.[6] CT is able to produce images

with high spatial resolution, and remains the gold standard imaging modality for visualizing bone damage, including bone erosions and sclerosis. The advent of new technologies, such as limited-view and dual-energy, have enabled innovative applications of CT for imaging beyond bone. Novel imaging techniques, such as tomosynthesis, are also being evaluated for musculoskeletal imaging and may prove to be adjunctive tools for evaluating the subchondral bone and serial monitoring of pathologic lesions. The following three projects were intended as preliminary studies exploring advanced imaging techniques and development of *ex vivo* models for evaluation of subchondral bone disease, primarily BMLs. The outcomes of these projects provided additional insight in developing an experimental model for BMLs and optimizing advanced imaging for BML detection.

2.2 Ex Vivo Fluid Cannulation Model

2.2.1 Introduction

BML is a descriptive term for signal observed within the subchondral and trabecular bone on fluid-sensitive sequences on MRI. BMLs appear as hyperintense signal on T2-weighted images, and hypointense on T1-weighted images. BMLs are observed with a number of different pathologic states, but are a clinically-relevant entity as they can cause pain and morbidity, and their presence may signify physiologic remodeling of the subchondral bone which may incite or accelerate damage of the articular cartilage. There is an outstanding need to better understand the tissue characteristics of BMLs across species and conditions. Knowledge of these lesions is important to better understand arthropathies, such as OA, as both cartilage- and bone-based conditions.

Diagnosis of BMLs is a challenge, as they cannot be observed using radiography, but require MRI. There are numerous techniques described for fluid detection with high-field (> 1.0 T) MR, including fat saturation, inversion-recovery, and opposed-phase imaging.[7] Commonly used sequences include short inversion time recovery or short tau or short T1 inversion recovery (STIR), proton density fat saturation (PD FS), Dixon techniques, chemical shift selective (CHESS) fat saturation, and hybrid pulse sequences with spectral and inversion recovery (e.g., SPAIR); with the latter mentioned sequences used with 3 T MR systems.[8] Distinguishing fat from water signal is a valuable feature of many of these sequences, enabling a greater level of information about the specific tissue composition of a lesion.

Limited histological information is available regarding BMLs and demonstrate they may be composed of a variety of different biological fluids and tissue types.[9] It remains to be determined whether these more specific fluid-sensitive MR sequences may be helpful in elucidating the underlying composition of these lesions. The objectives of this study were to (1) compare the signal intensity of different biological fluids on MRI; and (2) develop an *ex vivo* experimental model to evaluate fluid signal within bone using the equine metacarpus. We hypothesized that the relative signal intensities would vary between biological fluids and utilization of newer techniques available with high-field MRI would be sufficiently sensitive to distinguish between these fluids, increasing the current understanding of the fluid composition of BMLs.

2.2.2 Materials and Methods

Biological fluid collection for experimental phantom

Whole blood was collected from healthy, adult horses and aliquoted into blood collection tubes (BD Vacutainer blood collection tubes, Becton, Dickinson and Company, Franklin Lakes, NJ, USA). For samples, heparinized tubes were used for blood; standard glass tubes without an anticoagulant were used for serum, and tubes containing EDTA were used for plasma. Synovial fluid samples were aseptically collected from the femorotibial, tarsal, and carpal joints immediately following euthanasia in horses euthanized for reasons unrelated to this study and stored in standard glass tubes without anticoagulant. A total of 60 ml of each biological fluid was collected for the study.

A 15-sample fluid phantom was created for evaluation. Biological fluids (heparinized blood, serum, plasma, synovial fluid) were placed in sterile 10 ml polypropylene centrifuge tubes (Fisher Scientific, Thermo Fisher Scientific, Waltham, MA, USA). Each tube was filled with 10 ml of the specific biological fluid, and each biological fluid was used twice, with one sample containing 1 ml of new methylene blue (NMB, 16 μg/ml) dye, and the second sample without NMB dye. Saline (0.9% NaCl) fluid was used in combination with NMB dye to create additional dilutions in centrifuge tubes for evaluation, including 1:1, 2:1, 3:1, 9:1, saline:NMB dye, respectively. A single tube with air only and without any biological fluids was also included in the phantom.

Animal specimens

Twenty-eight, adult, equine cadaveric distal forelimbs were used for this study. Horses were euthanized for reasons unrelated to this study and were free of known pathologic lesions in the metacarpophalangeal joint. Limbs were collected within 24 hours of euthanasia and

maintained at 4ºC until the time of the study. Limbs were transected distal to the carpus, in the proximal metacarpus, and all bone and soft tissues were left intact.

Cannulated drilling and fluid injection

Limbs were placed with the medial aspect of the limb in contact with the table. A 2 cm stab incision was made using a No. 15 surgical blade centered within or slightly proximal to the epicondylar fossa of the lateral condyle. A 20 mm length 3.2 mm glide hole was drilled parallel to the joint surface. A 4.5 mm diameter standard tap was used to cut threads in the length of the glide hole. A 35 mm length 4.5 mm cannulated screw with a custom-made head adapted for integration with a Luer lock syringe was then inserted and engaged the threads in at least half the length of the glide hole. A total of 10 ml of fluid (9 ml fluid of interest + 1 ml NMB dye) was injected through the cannulated screw into the hole and bone. Limbs were randomly assigned to injection with saline, heparinized whole blood, or serum. NMB dye was added to each biological fluid for identification of the distribution of fluid on subsequent gross evaluation of the limbs. Following injection, the cannulated screw was removed and a single suture was placed in the skin using a 2-0 non-absorbable monofilament suture.

Magnetic resonance imaging

The biological fluid phantom was imaged using a 1.5 T magnetic resonance scanner (GE Signa HDxt, General Electric Company, Fairfield, CT, USA) with a bore diameter of 60 cm. The custom-made biological fluid phantom was placed in isocenter and imaged using STIR sequence (TR 3250, TE 45.92, inversion time 135 or 120, flip angle 90).

Twenty-four cadaveric specimens were imaged using the 1.5 T MR scanner, and four cadaveric specimens were imaged using a 3 T magnetic resonance scanner (Siemens Magnetom Skyra, Siemens Medical Solutions USA, Inc., Malvern, PA, USA) with a bore diameter of 70 cm. Cadaveric specimens were imaged at baseline and following cannulated drilling and fluid injection. Limbs were randomly assigned to injection with saline, heparinized whole blood, or serum (N = 8 limbs/group with 1.5 T unit, N = 4 limbs with saline for 3 T unit). For imaging, limbs were placed with the medial aspect in contact with the scan table and the foot entering the magnet first, to replicate clinical positioning. The metacarpophalangeal joint was placed in isocenter, a limb coil for image acquisition with the 1.5 T unit, and a knee coil was used with the 3 T unit.

For imaging with the 1.5 T unit, sequences included STIR in the sagittal (TR 3000, TE 42.016, TI 135 or 120, flip angle 90) and transverse (TR 3150, TE 41.888, TI 135, flip angle 90) planes. Two different STIR sequences were performed in the sagittal plane with slight differences in inversion time in an effort to identify differences in visibility of fluid. A T1 fast spin echo (FSE) sequence was also performed in the sagittal plane (TR 509, TE 10.36, flip angle 90). All images had a 288 x 256 matrix with voxel dimensions of 0.3 x 0.4 x 2 mm.

For imaging with the 3 T unit, sequences included STIR (TR 4130, TE 39, TI 200, flip angle 120), intermediate-weighted fat suppression (TR 3900, TE 39, flip angle 120), and Dixon (TR 3580, TE 37, flip angle 120) in the sagittal planes. Images had a 320 x 320 matrix with voxel dimensions of 0.3 x 0.3 x 3 mm.

Image evaluation

All digital imaging obtained via MR and CT were stored within the picture archiving and communication system (PACS) at Colorado State University or the University of Georgia. Open-sourced software (Horos Project, version 3.3.6) was used for viewing and evaluating DICOM images. For the fluid phantom, a 10 mm^2 circular region of interest (ROI) was used to identify the signal of each tube, and background air. For cadaveric specimens, a 10 mm^2 circular ROI was used to identify the signal within the bone and background air. The ROI was positioned immediately adjacent to the visible drill tract highlighted by hyperintense fluid signal. From these parameters, the signal-to-noise (SNR) ratio was calculated.[10]

Gross evaluation of metacarpophalangeal joints

Following imaging, limbs were grossly evaluated to assess for the extent of perfusion of the injected fluid. The third metacarpal bone was isolated and then sectioned in either the dorsal or sagittal plane. NMB dye was used to confirm the successful perfusion of the bone with injected fluid.

2.2.3 Results

Signal intensities for all biological fluids (blood, serum, plasma, synovial fluid) were similar to one another and greater than saline (Table 2.1). NMB dye did not affect the signal intensity of the biological fluids, and did not create an artifact when imaging on MR.

Injection of fluid was successful in all cadaveric limbs. Fluid signal was visible within the screw tract on all limbs. Fluid within the trabecular bone was minimally visible using a STIR sequence. When visible, the signal intensity was hypointense relative to the trabecular bone.

Modification of TI from the standard 135 to 120 facilitated increased visualization of fluid signal in most samples with the 1.5 T MR unit. For comparative imaging with the 3 T MR unit, fluid signal appeared hyperintense relative to the trabecular bone on both IW FS and Dixon water only sequences (Figure 2.1). Subjectively, fluid signal was greater with Dixon water only images compared to IW FS images. SNRs were greater across all fluid-sensitive sequences on the 3 T magnet strength compared to the 1.5 T magnet strength. SNRs were highest on the STIR sequence with the 120 TI on the 1.5 T unit, and with the Dixon water only images on the 3 T unit (Table 2.2). No difference in SNR was observed between fluid groups.

Fluid within the trabecular bone was visible on gross evaluation of sectioned limbs and with all tested fluids. Subjectively, the distribution of fluid was large on gross evaluation compared to the region of signal visible on MRI (Figure 2.2).

2.2.4 Discussion

This study validates a viable *ex vivo* experimental model for create fluid signal within the bone as evaluated using MRI. Variation in magnet strength, sequences, and sequence parameters alters the ability to detect fluid signal within the trabecular bone. Additionally, different biological fluids have similar SNRs making it challenging to distinguish the underlying type of biological fluid based on the signal intensity alone.

BMLs are a common finding on MRI and have a consistent appearance regardless of etiology. Histologically, BMLs consist of a combination of necrosis, hemorrhage, edema, and fibrosis,[9] making it challenge to define a clear pathophysiology. It would be ideal if there were a way to distinguish the predominant fluid type(s) to better understand a potential etiology of this condition. Unfortunately, biological fluids have a similar signal intensity to one another, and MR

sequences are not sensitive enough at the current time to distinguish specific characteristics of fluids. More than likely, BMLs represent a mixture of fluids but further work is needed to define the source and progression of this fluid accumulation within the trabecular bone.

Newer techniques, such as dual-energy CT (DE CT) may be a viable technique to differentiate the material properties corresponding to the fluid signal within a BML. Dual-energy CT depends on the fact that different tissues (e.g., fat, water, bone) attenuate differently a varying photon energies. X-ray attenuation in part depends on the photoelectric effect, which is greatly affected by the atomic number of the tissue—generally, the higher the atomic number the greater the photoelectric effect.[11,12] The differences in the spectral behavior of different tissues can be detected and measured using CT. Practically, a region of interest is scanned with CT simultaneously or sequentially with two different tube voltage settings (i.e., 80 kVp and 120 kVp). Data is then post-processed to extract dual-energy information. The most straightforward method involves subtraction between equivalent projections and application of a filtered back projection algorithm to reconstruct the difference as spectral information. A second method involves taking standard CT images composed of voxels and extract spectral information based on differences in voxels determined by Hounsfield Units.[11] Applying the DE CT technique for the detection of BMLs, it may be possible to distinguish larger fluid types (i.e., fat vs. fluid), but it is unlikely—at least at the present—to be able to distinguish between biological fluids (i.e., blood vs. synovial fluid).

Fat suppression techniques to highlight water signal is an important aspect of musculoskeletal imaging. Generation of a water- or fluid-focused image with MRI requires sequences that exploit the different MR properties between fat and water, namely the precessional (Larmor) frequencies and T1 relaxation times.[8] Due to the greater electronic

shielding, the protons in fat molecules precess at a slightly lower frequency than protons in water, also known as chemical shift. Importantly, there is a linear proportional relationship between the chemical shift and the external magnetic field. It follows then that with a 3 T system, there is a wider chemical shift between fat and water, allowing for more selection fat saturation. T1 relaxation time refers to the time for protons to restore their magnetization after excitation from a radiofrequency pulse, and is the basis for inversion-based fat suppression sequences. Each tissue has a characteristic T1 relaxation time, and fat has a shorter relaxation time than water.[13] Additionally, stronger magnetic fields lengthen the T1 relaxation time, which accounts for some differences between the 1.5 T and 3 T systems evaluated here.[14–16]

STIR sequences are widely used in musculoskeletal imaging but are limited by their relatively long imaging times compared to other fluid-sensitive sequences now available, and low SNR, as seen in this study. Modification of the TI improved visualization of fluid and increased the SNR in this experimental setting, but it is unclear whether this would be sufficient for complete detection of fluid signal in a clinical scenario. Based on observations in this study, it seems plausible that BMLs may be under-recognized using conventional STIR sequence imaging parameters. Additionally, the extent of fluid signal observed on both 1.5 T or 3 T systems across sequences was subjectively less than what was observed on gross evaluation of limbs, suggesting that a clinical BML may be larger than what is observed with MRI.

The *ex vivo* model described here is a sufficient method for experimentally inducing fluid signal within bone that can be detected using MRI. This model does not encompass the coordinated physiological response to a BML (or the underlying cause) seen in a living horse. The results of this study, differences in fluid detection across sequences and MR magnet

strengths provoke additional questions about how to optimize volumetric imaging for detection of BMLs.

2.3 Limited-View Computed Tomography

2.3.1 Introduction

Musculoskeletal injuries in the athletic horse continues to be a major concern within the equine industry. Repetitive stress response within the subchondral bone can accumulate and create subtle—but potentially catastrophic—pathologic lesions.[17,18] Computed tomography has become increasingly available in equine medicine, and the high spatial resolution of this volumetric imaging modality make it ideal for assessment of injuries within the subchondral bone. Given its applicability, there are mounting demands for increasing resolution, decreasing scan time, and minimizing artifacts.

One method to decrease scan time and radiation dose is to use sparse-view techniques, which decrease the projection data for image reconstruction.[19,20] Gradient sparsity regularization has been used to reduce streaks due to sparse-view sampling and reduce artifacts secondary to noise.[21,22] Sparsity regularization is a relatively new iterative algorithm that uses sparse knowledge of the Fourier transform to obtain an image.[23] The algorithm is similar to previous iterative algorithms, but aims toward an exact interpolation of the under-sampled data, as opposed to the general assumption of zero values for the data between sample points, as seen with filtered-back projection algorithms. Another method to decrease scan time is to modify the geometry of the x-ray beam, which is the technique used for cone-beam CT (CBCT).[24] The downside of modification of the x-ray beam is the development of artifacts that increase image noise and decrease contrast resolution within the reconstructed image with conventional

algorithms. The combination of iterative image reconstruction techniques with CBCT has not yet been explored for imaging in veterinary medicine, but holds monumental potential, especially in the realm of equine imaging.[25]

For this preliminary investigation, sparsity regularization was adapted to pixel sparsity and compared to conventional gradient sparsity regularization using data obtained with μCT. Outcomes were then applied to image a cadaveric equine limb using sparse-view sampling with CBCT to evaluate for the ability to identify a known pathologic lesion within the subchondral bone. The objectives of these studies were to evaluate the potential for sparsity regularization for imaging of bone, and to further evaluate it in combination with sparse-view imaging. We hypothesized that a pixel sparsity model would yield increased trabecular detail compared to gradient sparsity with μCT; and a novel total variation algorithm (TVA) would exceed image quality compared to existing algorithms, reducing noise and streak artifacts with CBCT.

2.3.2 Materials and Methods

Data and Sparsity Regularization Model

Raw, non-DICOM CT data was used for all image reconstructions. The formula for image reconstruction is based off a standard linear model, $g = X f$, where f is the image vector consisting of the pixel values (i.e., the discrete representation of an image), X is the mathematical matrix encoding the x-ray projection, and g is the projection data. In sparse-view imaging, the gray-level variations in f are on a smaller scale than the sampling resolution of the system, so the size of f is greater than the size of g, which means generation of a unique image is not possible. More simply, for sparse-view sampling, the number of image pixels is greater than the number of projection data samples. Practically speaking, there is a mismatch in spatial resolution

since the image pixels are smaller than the detector pixels, which may result in artifacts that ultimately degrade the image.

Preliminary algorithm development was then used to create images based on (a) sparsity regularization (pixel and gradient-based) and (b) incorporate a blurred object model.[26] A bone phantom was created using high-resolution images obtained using μCT data in order to conduct a realistic simulation of the algorithm prior to application with CBCT.

Micro-Computed Tomography (μCT)

Due to the high spatial resolution, μCT imaging was used for algorithm evaluation in mitigation of streak artifacts with sparse-view imaging. The third metacarpus of the horse was selected as a test phantom due to its clinical relevance for pathologic lesions in the subchondral bone. The third metacarpal bone was collected from an adult horse euthanized for reasons unrelated to this study. All soft tissues were removed for imaging. The distal metacarpus, including the medial and lateral metacarpal condyles were imaged with μCT (Scanco μCT 80, Scanco Medical AG, Brüttisellen, Switzerland) using an isotropic voxel resolution of 37 μm, 70 kVp tube voltage, 11 μAmp current, and 300 ms integration time. The metacarpus was oriented with the most distal aspect of the bone at the bottom of the tube.

A single image was used for algorithm comparison in the transverse plane. The width of the pixels was increased from 37 μm to 74 μm, which is much higher resolution (due to the smaller pixel width) than available for clinical scanning. Two images were generated: a binary bone image focused on the detection of bone versus non-bone, and an actual bone image incorporating variation in tissue attenuation. For the binary bone image, the projection matrix models the CBCT projection by using the line-intersection method with four ray averaging for

each detector pixel, and then the blur operation (as defined in preliminary work) is applied. For the actual bone image, no blurring of pixels is necessary and ray averaging of the acquired transmission data is sufficient for high-resolution imaging (Figure 2.3).

Sparse-view sampling on both data sets (binary and actual) was applied, ranging from 45-360 projections over the 360º scan trajectory. The effective pixel width is then 222 μm at iso-center, which is appropriate for CBCT modeling, and three times larger than the test image pixel size.

Cadaveric Imaging with Cone-Beam Computed Tomography

The distal limb of one Thoroughbred racehorse was used for clinical validation of algorithms and sparse-view imaging. Racehorse were euthanized for reasons unrelated to this study. The limb was imaged with a commercially-available CBCT system specific for equine use (Pegaso, Epica Medical Innovations, San Clemente, CA, USA). DICOM-format reconstructed images were used to identify a clinically-relevant pathologic lesion in the distal metatarsus. Raw, non-DICOM CT data was then used for algorithm application and sparse-view image reconstruction. Images were generated using standard filtered back projection (FBP)[27–29], the TVA, and a novel L_1-norm-based algorithm (L1A). TVA utilizes gradient sparsity and reconstructs an image from incomplete data by minimizing the total variation under the constraints of data fidelity and positivity.[23,30,31] The total variation of an image is defined as a measure to evaluate the sum of the intensity gradient at each pixel, also termed the L_1-norm of gradients of the image.[32] The L_1-norm is defined as the sum of the absolute values of pixel values in an image, and the L1A described here is a novel algorithm prioritizing pixel sparsity for image reconstruction.

Image evaluation

Outcomes of this study were purely descriptive in nature. Images generated from μCT across algorithms were compared for diagnostic quality. Conspicuity of lesions across algorithms with sparse-view imaging were compared for CBCT.

2.3.3 Results

Binary bone images were used to compare pixel and gradient sparsity regularization with μCT on a 120-view scan. Both blurred and unblurred images were generated. For blurred images, blur widths extended 0-, 1-, or 2-pixel widths. For pixel sparsity regularization, minimal spurious artifacts were observed at the scale of the pixel size (74 microns). For gradient sparsity regularization, streak artifacts are present in the non-bone regions. Taken together, pixel sparsity controls streak artifacts better than gradient sparsity (Figure 2.4).

Using the pixel sparsity regularization model, projections were varied from 45-360 over a 360º scan comparing the blurred and unblurred images. The binary bone phantom was unable to be recovered at 360 views due to the fact the detector pixels are larger than the bone phantom pixels. Substantial image degradation was visible below 60 views for blurred and unblurred images (Figure 2.5). Data from μCT imaging and binary bone phantom provided a reference for image generation using CBCT.

Complete CBCT evaluation identified an ovoid, hypoattenuating region in the subchondral bone relative to the surrounding subchondral and trabecular bone in the plantar aspect of lateral condyle of the third metatarsal bone, immediately proximal to the metatarsophalangeal joint and plantar aspect of the proximal phalanx. Applying findings from

μCT, the threshold of 60 views was selected for algorithm application from cadaveric scans with CBCT. Substantial streaking artifacts and increased image noise were present on transverse plane images using the FBP algorithm. Reduced streaking artifact and image noise were present with the TVA image. The abnormal region in the subchondral bone was visible on both images, but more clearly defined with TVA (Figure 2.6).

2.3.4 Discussion

These preliminary results demonstrate that sparse-view imaging with CBCT is a viable technique to generate diagnostic images of subchondral and trabecular bone. Pixel sparsity regularization with unblurred images reduces image-degrading artifacts as determined using μCT; and diagnostic quality images are possible when projection views are decreased to 60. For CBCT image, conspicuity of pathologic lesions within the subchondral bone can be increased with the application of novel algorithms, compared to conventional techniques.

CT imaging has become an integral aspect of clinical imaging, but growing concerns have been expressed regarding radiation exposure for patients. Aside from reducing the x-ray exposure time and the current of the x-ray tube, the second strategy has focused on reducing the amount of projection data required for image reconstruction, otherwise known as sparse- or limited-view CT imaging. Sparse-view imaging has the potential to reduce the number of projections to one-tenth of what is currently used by only obtaining a partial or subset of the Fourier transform of an image, and then from these measurements be able to reconstruct the entire original image. The challenge of sparse-view imaging is that conventional image reconstruction techniques, such as FBP are not sufficient to create diagnostic quality images. The "solution" to this sparse-view limitation came from the compressed sensing (CS) theory,

introduced by Candés et al in 2006.[20] The CS theory consists of a cost function consisting of a data fidelity term, and a penalty term called regularization. In order to create an optimal image, the cost function is minimized through convex optimization techniques, and the regularization is used to compensate for the missing information, with different regularizations leading to different image production "solutions".[33,34]

The TVA and L1A are both penalty functions used for optimization-based image reconstruction. The total variation is one type of regularization used in CS, and its success in sparse-view image reconstruction is well-described.[23,30,32] The TVA requires computation of an image gradient, wherein the absolute value is obtained after taking the difference between pixels. The TVA exploits gradient sparsity and assumes the gradient of the image consists of only a few nonzero pixel values.[35] In recent years the limitations of this algorithm, including incorrect object boundaries, loss in image textures or intensity changes, have been more frequently reported.[34,36–38] The limitations with the TVA were also observed in the results of this study, with an increased number of streak artifacts in images generated using gradient sparsity regularization compared to pixel sparsity regularization. Instead of relying on an image gradient, the L1A represents an absolute value sum of the image pixels. An ideal penalty function for bone imaging would then be able to capture the detailed trabecular structure by identification of differences in the data on a pixel-specific basis. The superior image generated using pixel sparsity regularization and a novel L1A from μCT clinical phantom data improves on TVA and provides valuable insight to inform the development of appropriate algorithms for best quality image generation. Although CT evaluation was performed on cadaveric specimens, the evaluation of these image reconstruction methods on biological specimens over computed generated images

provides a pragmatic link for the application of these developing techniques for musculoskeletal imaging.

There is a growing need within equine medicine for an economical volumetric imaging technique that can provide point-of-care evaluation of musculoskeletal injuries. The incomplete acceptance of CBCT within equine practice is largely due to the influence of image-degrading artifacts.[39] The findings from this study demonstrate that image quality can be substantially improved through the modification of currently accepted imaging algorithms which address the inherent difference in CBCT technology. The rapid image acquisition and ability to scan a standing patient are notable advantages of CBCT technology, which are under-recognized. When combined with the sparse-view imaging concepts described here, the possibilities for CBCT are expanded. Sparse-view CBCT imaging has the potential to be used as a screening tool to identify morphological changes within the subchondral bone, which may be used to prevent injuries in performance horses.

Without question, further work is needed to fully characterize the strengths and limitations of sparse-view imaging with CBCT. These preliminary results are promising, but more objective work in this area is needed. Comparison between conventional fan-beam CT, CBCT and limited-view CT is needed to assess the ability to identify pathologic lesions, but also to characterize the resolution of bone and contrast between soft tissue structures. Ultimately application of these findings will help to identify horses at risk of injury, improving animal welfare and increasing understanding the role of subchondral bone in the pathophysiology of joint disease.

2.4 Comparative Evaluation of Tomosynthesis[3]

2.4.1 Introduction

Diagnostic characterization of osteochondral pathology in the equine joint typically relies on a combination of imaging modalities. Conventional radiography for assessment of bone and ultrasonography for assessment of soft tissues are currently the standard of initial diagnostic assessment of equine musculoskeletal injuries.[40] However the sensitivity of these diagnostic imaging modalities is limited compared to volumetric imaging modalities such as CT and MRI, which can be used for more comprehensive identification and characterization of pathologic lesions, especially those within the subchondral bone. Disadvantages of volumetric imaging include cost, general anesthesia in some instances, prolonged scan times and the need for dedicated space for equipment installation. The ideal modality for equine diagnostic imaging would be inexpensive, portable, produce real-time images that are easy to obtain, yield a detailed anatomical assessment of a variety of different tissue types enabling accurate assessment of pathologic lesions, and would provide complimentary information to what can already be observed using radiography and ultrasound.

Tomography-based techniques were initially developed in the 1950s to reduce the effects of anatomical overlap on conventional radiography.[41] Despite the high radiation dose, the technique persisted even after the advent of computed tomography for applications such as intravenous pyelograms. More recently, with the advent of advanced reconstruction techniques, digital tomosynthesis has been commonly used for human mammography,[42,43] and for musculoskeletal imaging of the human knee,[44,45] wrist,[46] and hand.[47,48] Digital tomosynthesis

[3] This chapter section is published in part in: Stewart HL, Kawcak CE, Inscoe CR, et al. Comparative evaluation of tomosynthesis: a preliminary equine cadaveric study of the metacarpophalangeal joint. *Am J Vet Res* 2021;82(11):872-879.

uses radiographic projections obtained at different angles within a single plane to create multiple slices of a structure of interest, at significantly reduced radiation dose compared to CT. This image set helps to resolve the problem of masking caused by superimposition of structures—a frequent limitation of radiography.[49,50] The potential ability to rapidly obtain three-dimensional information using modified radiographic technology makes tomosynthesis attractive as a potentially powerful addition for routine clinical diagnostic imaging. The objective of this preliminary study was to investigate the technique of tomosynthesis for imaging of the equine distal limb, with a special interest in imaging of subchondral bone. Strengths and weaknesses in characterization of the different tissues of the metacarpophalangeal (MCP) joint were evaluated; and the appearance of pathologic lesions between tomosynthesis and radiography were compared, using MRI as the imaging standard for articular cartilage and peri-articular soft tissues, and CT as the imaging standard for subchondral, trabecular, and cortical bone, as well as bony margins. We hypothesized that tomosynthesis would give a more complete characterization of the MCP joint compared to radiography for lesions in a specific plane, but would not provide as comprehensive assessment as CT or MRI; and that tomosynthesis could be validated as a volumetric imaging technique with potential benefits for diagnostic assessment of the equine MCP joint.

2.4.2 Materials and Methods

The study used a cross-sectional, method comparison design. Equine cadavers euthanized for reasons unrelated to this study were obtained and imaged using radiography, CT, MRI, and tomosynthesis of the MCP joint. After imaging, MCP joints were disarticulated and evaluated for the presence of gross lesions in the bones, articular cartilage, and peri-articular soft tissues of the

joint. Gross evaluation was used to confirm what was observed on CT and MR imaging and as a reference category for imaging comparisons. The size and shape of the lesions were also noted for comparison to imaging modalities.

Radiography

Five standard radiographic projections of the MCP joint (lateromedial, flexed lateromedial, dorso15-20°proximal-palmarodistal oblique, dorso15°proximal 45° lateral-palmaromedial oblique, dorso15°proximal 45° medial-palmarolateral oblique) were acquired using a digital radiography system (Mark II, Sound, Carlsbad, CA, USA). A technique of 80 kVp and 1.6 mAs were used for all radiographs.

Computed tomography

The distal aspect of each limb was scanned from the mid-metacarpus through the foot using a fan-beam CT system. Limbs were placed with the lateral aspect against the couch and scanned using a 160-slice helical PET/CT scanner (Philips Gemini TF Big Bore PET/CT scanner, Philips Healthcare, Andover, MA, USA) with a pitch of 0.4, technique of 100 kVp, 120 mAs, slice thickness: 0.8 mm for adequate bone resolution and 2.0 mm to increase signal-to-noise ratio for soft tissue evaluation, 1024 x 1024 matrix. The raw CT data was reconstructed into transverse, sagittal, and dorsal plane images at 0.8 mm thickness x 0.8 mm increment (bone reconstruction kernel) and 2.0 mm thickness x 1.0 mm increment (standard reconstruction kernel).

Magnetic resonance imaging

Distal limbs were positioned with the lateral aspect in contact with the scan table and the foot entering the magnet first, to replicate clinical positioning. Images were acquired using a limb coil, isocentered within a 1.5 T magnetic resonance scanner (GE Signa HDxt, General Electric Company, Fairfield, CT, USA) with a bore diameter of 60 cm. Sequences included proton density (PD; sagittal plane settings: TR 3516, TE 11.296, flip angle 130; transverse plane settings: TR 3014, TE 11.296, flip angle 130) and short inversion time recovery (STIR; sagittal plane settings: TR 3000, TE 42.624, inversion time 135, flip angle 90; transverse plane settings: TR 3000, TE 38.88, inversion time 150, flip angle 90) sequences in the sagittal and transverse planes, 3D fast spin gradient echo in the sagittal plane (TR 10.828, TE 3.688, flip angle 20), and T1 sequence in the dorsal plane (TR 559, TE 11.44, flip angle 90). All images had a 320 x 256 matrix with voxel dimensions of 0.5 mm x 0.6 mm x 2 mm.

Tomosynthesis

Distal limbs were imaged using a compact benchtop tomosynthesis device, constructed for this preliminary feasibility study using existing equipment. The system was comprised of a carbon nanotube (CNT) X-ray source array and an off-the-shelf flat panel detector (Hamamatsu Photonics K.K., Model C7940DK-02, Figure 2.7). The linear source array contains seven individually addressable X-ray focal spots, ~1 mm x 1 mm each, spanning approximately 85 mm. Originally designed for human intraoral tomosynthesis imaging[51], the source array has a maximum anode voltage of 70 kVp and a maximum tube current of 10mA. The system was constructed for this feasibility study using a source-to-detector distance of 40 cm, resulting in an angular span of 12 degrees. Each limb was positioned for tomosynthesis scan by an experienced

board-certified veterinary surgeon in a mounting fixature to ensure clinical relevance. The limb was either oriented with the long axis parallel to or perpendicular to the source array. A tomosynthesis scan consisted of electronic triggering to the source array to produce seven individual basis projection images at seven discrete angulations with respect to the limb. Images were acquired with no mechanical motion. These projection images were processed in a reconstruction algorithm to generate a quasi-three-dimensional image stack parallel to the detector plane. A total of 80-100 reconstruction slice images were generated for each scan in a given plane, each representing 1 mm of object thickness. Images for each MCP joint were acquired in multiple views, including lateromedial, dorsopalmar, dorsolateral-palmaromedial oblique and dorsomedial-palmarolateral oblique views. Images were obtained using the following parameters: 70 kVp anode voltage, 7 mA anode current, 80 ms exposure per source (560 ms total for 7 sources), 3.92 mAs exposure for the tomosynthesis scan, 400 mm source-detector distance, 12° angular span, 1.7 mGy estimated entrance dosage. Total scan time per limb orientation (e.g., dorsopalmar) was 15 seconds.

Gross evaluation protocol

After radiography, tomosynthesis, CT, and MR imaging, all MCP joints were disarticulated and gross lesions were evaluated and photographed. Wear lines, articular cartilage erosions, osteochondral fragments, and palmar metacarpal arthroses were measured and documented when present.

Image evaluation

Studies were randomized, and images were evaluated and graded by consensus by a board-certified veterinary radiologist and two, board-certified veterinary surgeons with expertise in equine musculoskeletal diagnostic imaging and experience with tomosynthesis imaging prior to this study, who were blinded to the horse. The evaluator assessed each set of images independently using an open-sourced software for viewing DICOM images (OsiriX MD 11.0, Pixemo SARL, Bernex, Switzerland) to identify first whether a lesion was present or absent, and if present, to describe the location and size. Suspected lesions identified on imaging were confirmed on gross evaluation. An overall image quality score was given for each image set within a modality. Image quality score was defined as the diagnostic usefulness of the image for assessment of the region of interest. Three sites within the MCP joint were separately evaluated and graded, including the third metacarpal (MC3), proximal phalanx (P1), and proximal sesamoid bones (PSB), within each study for the appearance and conspicuity of four different regions of interest: subchondral bone, articular cartilage, peri-articular margins and the appearance of adjacent bone. A semi-quantitative 0-4 scale was used for scoring, where 0 = unable to discriminate detail; 1 = poor detail discrimination; 2 = fair detail discrimination; 3 = good detail discrimination; 4 = maximum detail discrimination.

Statistical analysis

Descriptive statistics were reported as to whether the imaging modality was able to correctly identify the presence or absence of a lesion. CT was used as a comparative imaging technique for osseous lesions, and MRI was used as a comparative imaging technique for cartilage and soft tissue lesions. Gross evaluation of the joints by a board-certified surgeon was

used to as a reference for comparison to all imaging modalities and to confirm the presence of suspected lesions visible on the articular surface based on imaging, and evaluate their size and shape.

Median scores and interquartile ranges were reported for each imaging modality for the overall image quality score, as well as individual assessments of each of the regions of interest of subchondral bone, articular cartilage, peri-articular margins, and adjacent bone. Adjacent bone was defined as the trabecular bone within each of the bones of the MCP joint. A Shapiro-Wilk test was used to confirm the non-normality of the data. Scores for the different sites of MC3, P1 and PSB for each of the aforementioned regions of interest were then individually compared between modalities using the Mann-Whitney U test. All data was analyzed using R software (version 3.5.1, "Feather Spray," R Foundation for Statistical Computing, 2017) in RStudio (Version 1.0.143). The Mann-Whitney U test was implemented in the dplyr package for R. Statistical significance was set at $P < 0.05$.

2.4.3 Results

Descriptive analysis and ability of modalities to identify lesions

A total of 4 distal equine cadaver limbs were used in this study. Equine Limb 1 was normal with no grossly visible lesions with an intact surface of the articular cartilage on the distal aspect of MC3; Limb 2 was also grossly normal; Limb 3 had marked palmar osteochondral disease characterized by subchondral bone erosion and extensive articular cartilage loss; and Limb 4 had an incomplete, non-displaced chronic fracture of the medial PSB. Both CT and MR evaluation of Limb 2 revealed a focal subchondral fissure associated with a fissure lesion in the medial condyle of MC3. All lesions were correctly identified on all imaging modalities, except

for Limb 2, where radiography was not sufficient to identify the focal subchondral lesion (Table 2.3, Figure 2.8).

The appearance and size of observed lesions for Limbs 1, 3 and 4 were similar between radiography and tomosynthesis. With the exception of Limb 2, the extent and physical characteristics of the lesions observed on imaging modalities were similar to what was observed on gross evaluation of the joints. For Limb 2, the focal subchondral lesion was most thoroughly represented on CT and MRI and was minimally visible on evaluation of the articular surface of the joint.

Image evaluation

MRI had the highest overall image quality score; whereas the other modalities were equivocal. The volumetric imaging modalities of CT and MR were superior to radiography and tomosynthesis for evaluation of subchondral bone, adjacent bone, and peri-articular margins. MR was superior to all other imaging modalities for assessment of articular cartilage. Tomosynthesis image grades across all regions of interest were relatively similar to radiography scores (Table 2.4).

Comparison between imaging modalities revealed that volumetric imaging modalities of CT and MRI were superior to tomosynthesis and radiography in evaluation of subchondral bone, peri-articular margins, and adjacent bone ($P < 0.05$, Table 2.5). Radiography was superior to tomosynthesis for evaluation of peri-articular margins ($P < 0.05$), but the two imaging modalities were equivocal for evaluation of the other regions. There was no significant difference in assessment of articular cartilage between imaging modalities, although MRI evaluation

approached significance for superior assessment of articular cartilage compared to both tomosynthesis and radiography ($P = 0.072$).

2.4.4 Discussion

This study provides a comparative analysis between radiography and a proof-of-concept benchtop tomosynthesis system for evaluation of the equine MCP joint in a limited number of cases. Results indicate that tomosynthesis can provide valuable information of bone with an increased ability to detect subtle lesions of the subchondral bone compared to radiography. This was demonstrated by the ability to detect a single, radiographically-occult lesion in this study. Although tomosynthesis is not able to provide an equivalent level of detail of bone and articular cartilage compared to CT and MRI, respectively, this study demonstrates there may be valuable applications for tomosynthesis as an adjunctive, rapid imaging modality of the equine distal limb.

Radiography and tomosynthesis both utilize x-ray projections for analysis of a given region of interest. Intuitively, multiple projections acquired within a single plane using tomosynthesis have the potential to provide more information than a single image acquired using radiography. Tomosynthesis improves spatial resolution in the x-y plane, reducing the superimposition of structures as observed using radiography, which may enable identification of more subtle lesions, as observed in this study. The subchondral lesion with surrounding sclerosis observed in Limb 2 was readily viewed using tomosynthesis, but due to its location on the distal articular margin of MC3 and superimposition of sclerotic bone tissue, it was not visible using conventional radiography. A small fissure in the articular cartilage was visible on gross evaluation of the limb, but under-represented the degree of change within the subchondral bone

compared to CT imaging. The radiographic images were reviewed after grading was complete, and this pathological change was not visible even with prior knowledge of the location and characteristics. The authors generated 80-100 reconstruction slice images, each representing 1 mm of object thickness, in a given plane for each tomosynthesis scan. In reality the tomosynthesis reconstruction algorithm can generate a variable number of slice images to represent an object volume.[52] Table 1 highlights this difference between radiography and tomosynthesis in identification of this pathologic change. Given the small number of limbs evaluated in this study, the percentage difference (i.e., 100% vs. 75% for lesion identification) between these two imaging modalities should not be overstated. Despite this lesion identification using tomosynthesis, there was lack of significance between radiography and tomosynthesis for evaluation of subchondral bone and adjacent bone. Tomosynthesis is an extrapolation of radiography, so we would expect the appearances in grading of these lesions to be similar, however given the improved ability to reduce superimposition, we would have expected to find a significant difference between these modalities—especially in detection of lesions and the appearance of subchondral bone. A notable limitation in the study design was in selecting cases with lesions that were distinct enough to be seen on radiographs. Further studies should be focused on evaluation of tomosynthesis for the detection of subtle lesions, especially those associated with subchondral bone. Previous work by Hayashi et al compared tomosynthesis and conventional radiography for evaluation of radiographic features of osteoarthritis in the human knee. Osteophytes and subchondral cysts were more accurately identified with tomosynthesis compared to conventional radiography and furthermore subjects with lesions identified on tomosynthesis were more likely to report pain than those without.[44] Osteophytes and subchondral bone cysts were not specifically present in the equine limbs evaluated in this study, but further

studies are needed to see if these trends persist across species. Similar to humans, the health of the subchondral bone has a direct impact on the health of the equine joint,[53–55] and development of non-invasive imaging methods of evaluation of this specialized bone will allow clinicians to have a more complete understanding of many commonly observed injuries. Injury to subchondral bone in athletic horses may result in clinical pain and lameness, predisposing to fracture, or inciting or perpetuating osteoarthritis.[56–59] Detection of such lesions using tomosynthesis may enable early intervention and reduce the likelihood of catastrophic injury.

This study demonstrated that it is possible to obtain high-quality diagnostic images using tomosynthesis for the equine MCP joint. The tomosynthesis system used in this study is for research purposes only but is substantially smaller than the commercial tomosynthesis systems used for mammography. The tomosynthesis system used in this study used seven projection images and a 12-degree angular span, both lower than reported values used in orthopedic tomosynthesis studies in human medicine.[60] Increasing the number of projections and/or angular span may provide additional information on a specific region of interest, but an objective comparison between different configurations for equine imaging evaluation was outside of the scope of the current study. The source array used in this study was also originally fabricated for a dental application, with a maximum of 70 kVp. A future purpose-built system would need to incorporate up to 80-90 kVp to be appropriate for distal limb imaging. Through optimization studies would be required to balance image quality and physical size. A purpose-built system would likely contain a source array with additional focal spots, smaller focal spot size for increased system resolution, and provide increased angular coverage, as well as a larger flat panel detector. The tomosynthesis system used in this study is configured in such a way where the source array required no mechanical motion or complex gantry setup to acquire the

projections, enabling the hardware to be compact and relatively simple compared to other commercially available tomosynthesis systems. This configuration lends itself to be packaged into a portable footprint, with the potential to be configured for standing equine imaging in a clinical or field setting. Though not assessed in this study, there is one portable tomosynthesis system is commercially available for equine imaging[d], and initial clinical impressions of the system are promising for imaging of the equine distal limb and head (KTS, personal communication). The focus of the current study was to evaluate the capabilities of the technology of tomosynthesis and could be strengthened by evaluation of the usability of the commercially available portable tomosynthesis unit for equine use. The current commercially available portable tomosynthesis unit also has the capability to perform digital radiography and has a similar system setup, with the horse appropriately positioned under standing sedation. Images are then acquired with the horse standing squarely and the plate and generator are placed around the area of interest on the distal limb. The combination of a radiography and tomosynthesis in a single, portable system that can be used in the field emphasizes the relevance of considering these techniques together. Although planar imaging techniques, such as radiography, remain inferior to volumetric imaging techniques such as computed tomography and magnetic resonance imaging, they remain as the mainstay preliminary assessment technique for many equine veterinarians.

Another clear advantage of tomosynthesis is the rapid time for image acquisition. Similar to radiography, where images can be acquired in less than 1 second, tomosynthesis can acquire many images rapidly. In this study, all images within a single plane were acquired over approximately 15 seconds, while CT and MRI examinations of the distal limb took approximately 5 minutes and 30 minutes, respectively. The tomosynthesis system described here

with a 12-degree angular span was an early prototype and has now been modified to perform a scan with a 40-degree angular span in approximately the same time, and a scan with a 12-degree angular span takes approximately 1 second to perform.[61] Future studies using this adapted system are expected to have improved lesion conspicuity. Furthermore, despite advances in artifact reduction software, metal implants in the distal limb create numerous artifacts on both CT and MRI, making image interpretation more challenging. Tomosynthesis appears to be less susceptible to metal artifacts when compared to CT, and post-processing techniques have been reported[62] to mitigate these artifacts and improve image quality, expanding the potential clinical applications of this modality. The utilization of synthetic radiographs, which are generated from tomosynthesis reconstruction data, is also rapidly emerging to prevent the excess patient dose of using both modalities.[63]

When considering a clinical equine case, tomosynthesis can be used as a complimentary and synergistic imaging modality with radiography. Once the region of lameness has been localized with diagnostic analgesia a standard series of radiographic projections can be obtained. If a lesion is identified on radiographic images—even within a single plane—then repeat images can be obtained using tomosynthesis to further characterize an observed abnormality. Additional diagnostic imaging recommendations can be made based on what is observed. Alternatively, if a clinical lameness has been localized but no lesions are observed with radiography, tomosynthesis may be used in multiple planes in an attempt to identify and characterize a suspected lesion. Future tomosynthesis studies can be directed toward assessment of the navicular apparatus. Middle and distal phalanges were also imaged in two equine cadavers in this study, but images were not specifically graded. Previous work by Johnson et al has demonstrated conspicuity of lesions along the palmar or plantar cortex of the navicular bone is directly impacted by the

projection angle of radiographs.[64] It is the impression of the authors that tomosynthesis will aid in identification and characterization of these types of lesions. Further clinical work is needed to confirm these assumptions.

This study presents our initial assessment of tomosynthesis technology for equine imaging. Given the inherent challenge of limited angle sampling, it is not surprising that there are still significant differences between tomosynthesis and CT in evaluation of bone that cannot be overcome by multiple images across a given plane. This study also confirmed that articular cartilage cannot be appropriately assessed using a tomosynthesis system with this angular span, and of the imaging modalities using in this study, MRI was the strongest imaging method for cartilage evaluation. MRI was not the only imaging modality for evaluation of the articular cartilage, as appropriate contrast resolution does also allow some evaluation of the articular cartilage using CT. Although not specifically addressed in this study, there is a "learning curve" for evaluation of images obtained using tomosynthesis. Instead of a single image obtained using radiography, the evaluator is required to scroll through multiple images within a given plane. As discussed, this reduces confusion caused by superimposition of structures, but takes time to learn, similar to any imaging modality. If a suspected lesion is present, it is imperative that this region of interest is centered in the tomosynthesis beam to reduce the effect of data truncation and improve the ability to characterize the lesion. Tomosynthesis generates reconstruction volumes in the shape of a truncated pyramid. As the angular span increases, it becomes more critical for the suspected lesion to be centered in the field-of-view, as the effective angular coverage is decreased for thick objects approaching the detector edge. The impact of data truncation is well-discussed in digital breast tomosynthesis,[65,66] and when considering using this technology for equine imaging, it is important that the operator have a working knowledge of

where lesions may be more likely to occur (i.e. the palmar aspect of the joint surface of the MCP joint). Another consideration is that a tomosynthesis reconstruction enhances anatomical features of a region that may be present on one or more projection images. If the goal is to visualize a joint space or articular surface, one or more of the basis projection images should be oriented to allow the beam to traverse parallel to this region of interest. This is similar to the approach described for radiography, in which the image contrast is improved when the x-ray beam is properly angulated and the limb is positioned to open the joint space or expose the lesion. The importance of proper positioning of the region of interest and beam angle have been well-described in equine literature.[67–70]

Tomosynthesis generally offers some flexibility in positioning due to the acquisition of data from multiple angles. In this study, the angular span and number of basis projection images was lower than typical literature values for human tomosynthesis systems[71] and the detector area (12 cm x 12 cm) was relatively small, posing additional challenges to positioning. Arguably, the largest limitation of tomosynthesis is that it is most helpful to perform tomosynthesis to look at a given plane of interest. Although it would be possible to obtain tomosynthesis images in multiple planes, it is likely best used to further delineate a suspected pathologic lesion observed on radiographs. Thus, the need for radiographs is not negated by the presence of tomosynthesis, but the information obtained between the two modalities should be viewed as complimentary. The focus of the current study was to evaluate the capabilities of the technology of tomosynthesis and could be strengthened by evaluation of the usability of the commercially available portable tomosynthesis unit in a sample of live horses. Further work is required to evaluate the ease of using this system with clinical cases, and larger equine clinical case studies are warranted. In comparing the median scores for subchondral bone between radiography and tomosynthesis, an a

posteriori power calculation was performed and determined a total of 40 randomly selected limbs—to avoid the potential bias of using lesions identified with radiography—would be required in a blinded, multi-reader study to detect if a true difference exists between radiography and tomography for evaluation of the MCP joint—including reporting on the percentage of any false positives and false negatives—and validate the observations from this study. The authors chose to use the CT and MR as the standards for comparison between imaging modalities, however gross evaluation was used as ultimate reference for the presence of lesions visible on the articular surface. The findings for Limb 2 demonstrate that subchondral bone lesions in some cases may be more thoroughly represented through volumetric imaging than what is visible on the articular surface. Arguably, histopathology of specimens would have been required for a gold-standard assessment of these lesions. Further information about radiation dose to the patient should also be investigated, but was outside the scope of this initial study.

Taken together, this pilot study validates tomosynthesis as a diagnostic modality for imaging of the equine MCP joint, and suggests it may be offer additional benefits for imaging of the equine distal limb. In this limited study of the MCP joint, tomosynthesis is comparable to radiography for evaluation of the subchondral bone and in the ability to identify the borders of adjacent bones, and slightly inferior to radiography for characterizing peri-articular margins. Importantly, in one case, tomosynthesis was more accurate than radiography for identification of a pathologic lesion within the subchondral bone, which may be obscured due to superimposition of bone and soft tissue structures on radiographs. Further work is needed to explore whether the ability to identify non-radiographically detectable lesions is a repeatable strength of this modality. The ability of tomosynthesis to obtain sequential images of a structure across a single plane, suggests this may be a complimentary and adjunctive imaging modality. Based on this

initial report, but tomosynthesis appears to have promising applications for clinical equine use. Further studies will be necessary to determine if equine orthopedic tomosynthesis will achieve the image quality and diagnostic accuracy previously reported in human studies.

2.5 Figures

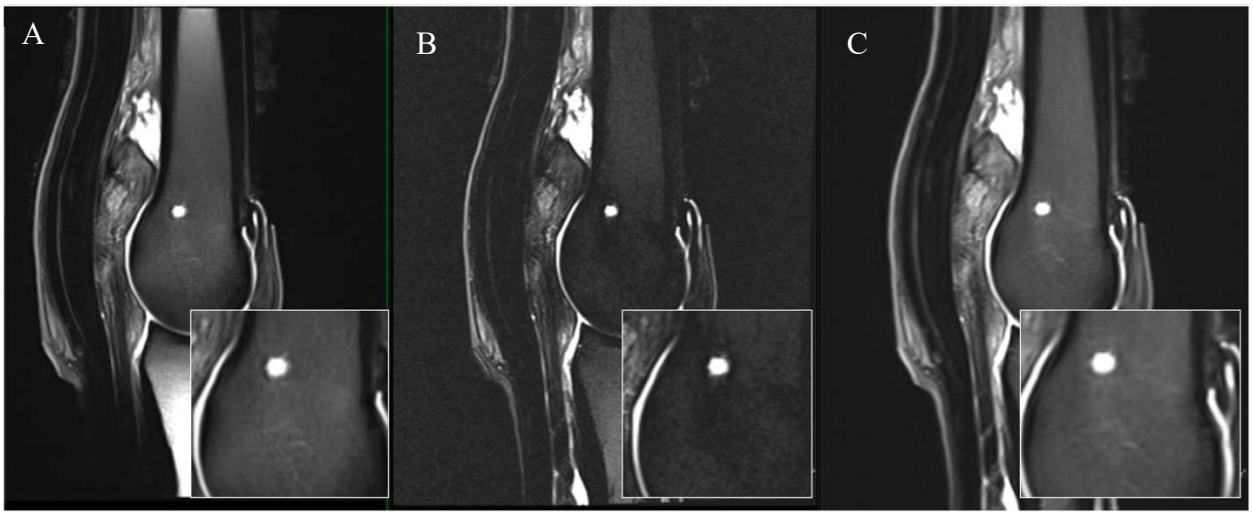

Figure 2.1 – Sagittal plane images of the equine distal metacarpus after experimental fluid injection into trabecular bone, obtained using fluid-sensitive sequences with 3 T magnetic resonance imaging. Fluid-sensitive sequences included (A) intermediate-weighted fat suppression (IW FS); (B) short-tau inversion recovery (STIR); and (C) Dixon, water only. The focal, circular hyperintense drill tract is surrounded by regions of hyper- (IW FS and Dixon water only) or hypointense signal relative to trabecular bone. Inserts provide a magnified view of the region corresponding to fluid signal for each image.

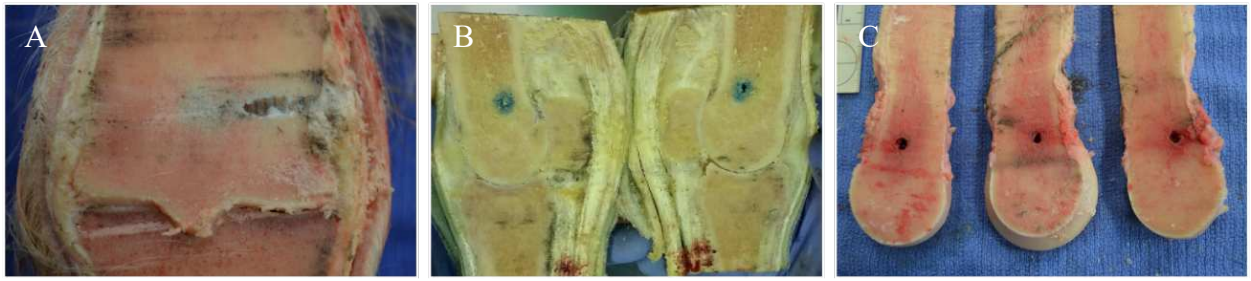

Figure 2.2 – Gross images of the equine distal metacarpus after experimental fluid injection into the trabecular bone. (A, B) Dorsal and sagittal plane sections after injection of 10 ml total volume with 0.9% NaCl and new methylene blue dye. (C) Sagittal plane sections after injection of 10 ml total volume of heparinized whole blood and new methylene blue dye. The extent of fluid distribution on gross evaluation is subjectively similar or slightly more than what is visible on high-field magnetic resonance imaging with fluid-sensitive sequences.

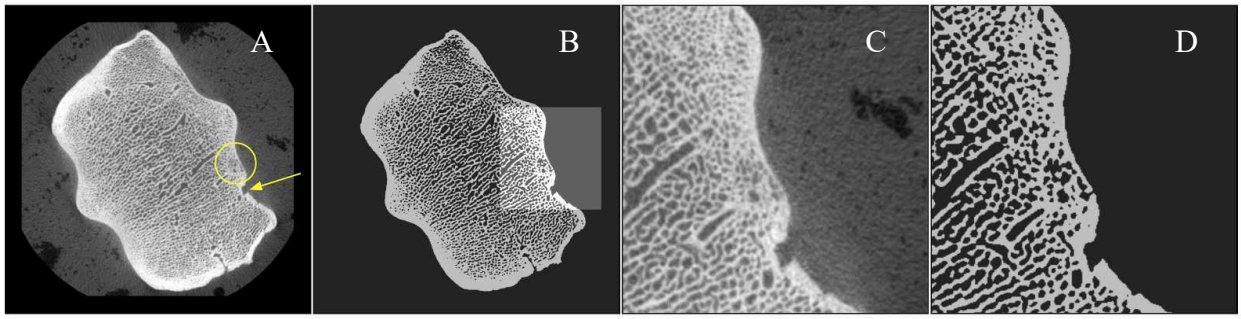

Figure 2.3 – Transverse plane micro-computed tomography images of the distal equine third metacarpal bone. (A) Comparative test image set with a 904 x 904 matrix, with a pixel width of 74 microns. (B) Binary bone test image generated by thresholding the image in (A) after processing. The highlighted square depicts a region of interest (ROI) shown for all µCT images. (C) ROI of the µCT image with two distinguishing features: (1) a hypoattenuating region within the subchondral bone (indicated by the yellow circle in (A)), and (2) a focal defect in the palmar surface (indicated by the yellow arrow in (A)). (D) ROI of the binary bone image which is used as a pixel-sparse representation of the actual bone structure. Non-bone pixels are set to zero, bone pixels are set to one. *Images provided courtesy of Dr. Emil Sidky, University of Chicago*.

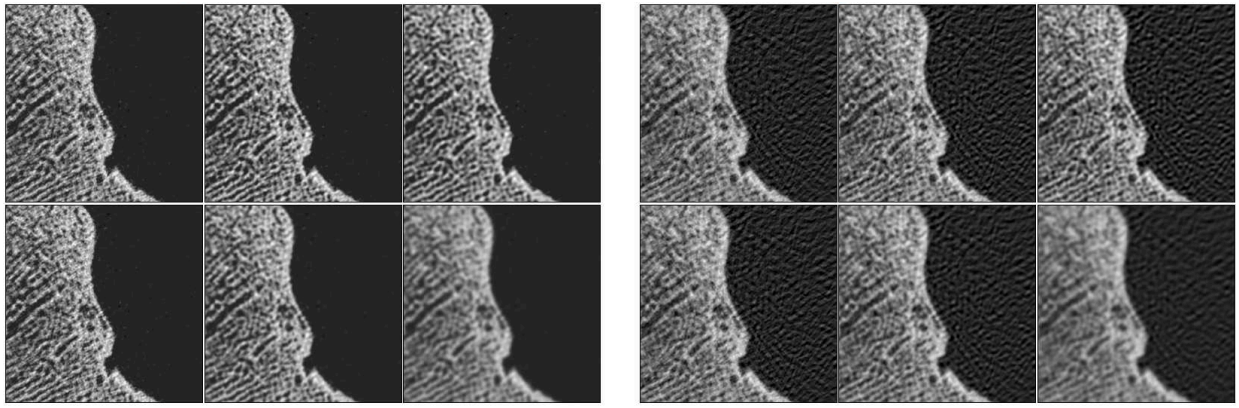

Figure 2.4 – Reconstructed images from 120-view projection data of the binary bone phantom (see Figure 2.3), comparing the use of pixel (left six images) and gradient (right six images) sparsity regularization. Within image sets, each of the three columns represents a different width for image blur. From left to right, widths are 0, 74 and 148 microns. Within image sets, images are either unblurred (top row) or blurred (bottom row). When the width = 0, blurred and unblurred images are the same. Pixel sparsity is more effective at reducing streak artifacts. There is also a loss of resolution in all reconstructed images due to the detector pixel size. *Images provided courtesy of Dr. Emil Sidky, University of Chicago*.

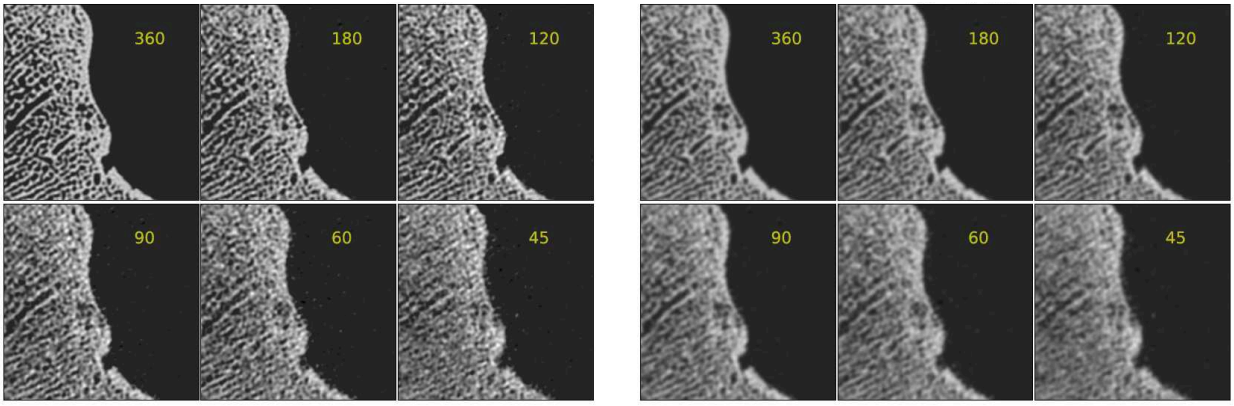

Figure 2.5 – Survey of reconstructed images from the binary bone phantom (see Figure 2.3) for varying number of views. The number of projections for each image is shown in yellow in the upper right of each panel. The six images on the left show unblurred images, the six images on the right show blurred images, with blur width set at 148 microns. *Images provided courtesy of Dr. Emil Sidky, University of Chicago*.

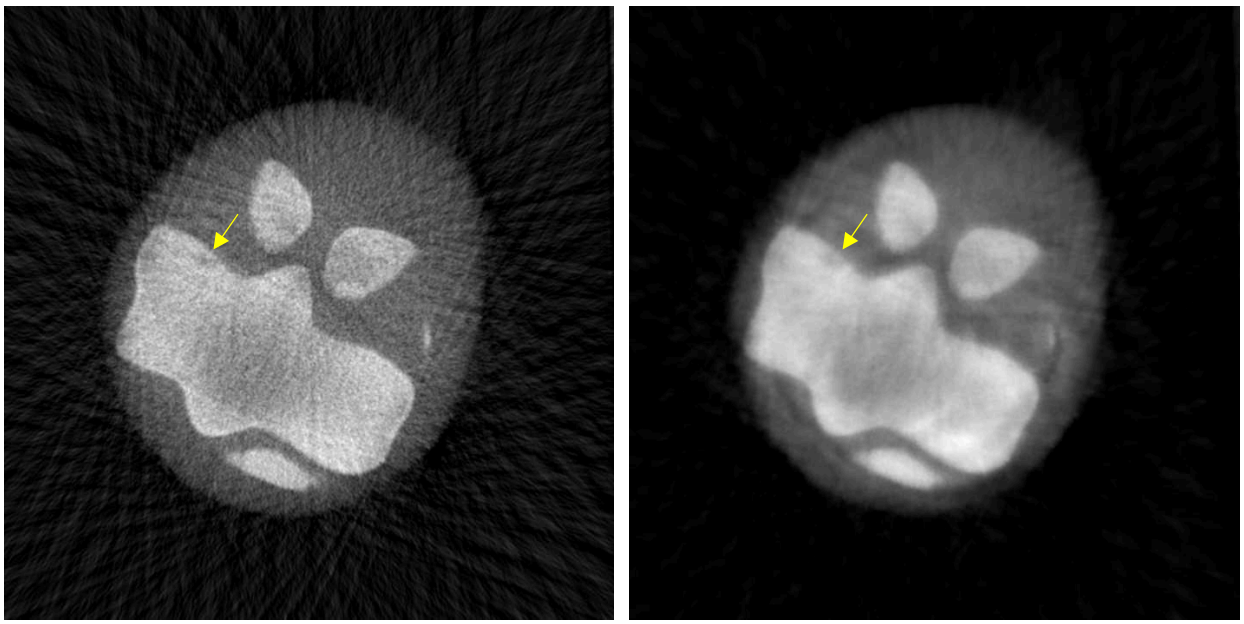

Figure 2.6 – Reconstructed images from 60-view projection data of the distal third metatarsus of an equine cadaver using filtered-back projection (left) or total variation algorithm (right). The previously identified ovoid hypoattenuating region in the subchondral bone of the lateral condyle is identified with a yellow arrow. Increase streaking artifact and image noise is visible with the filtered-back project compared to the total variation algorithm. *Images provided courtesy of Dr. Emil Sidky, University of Chicago*.

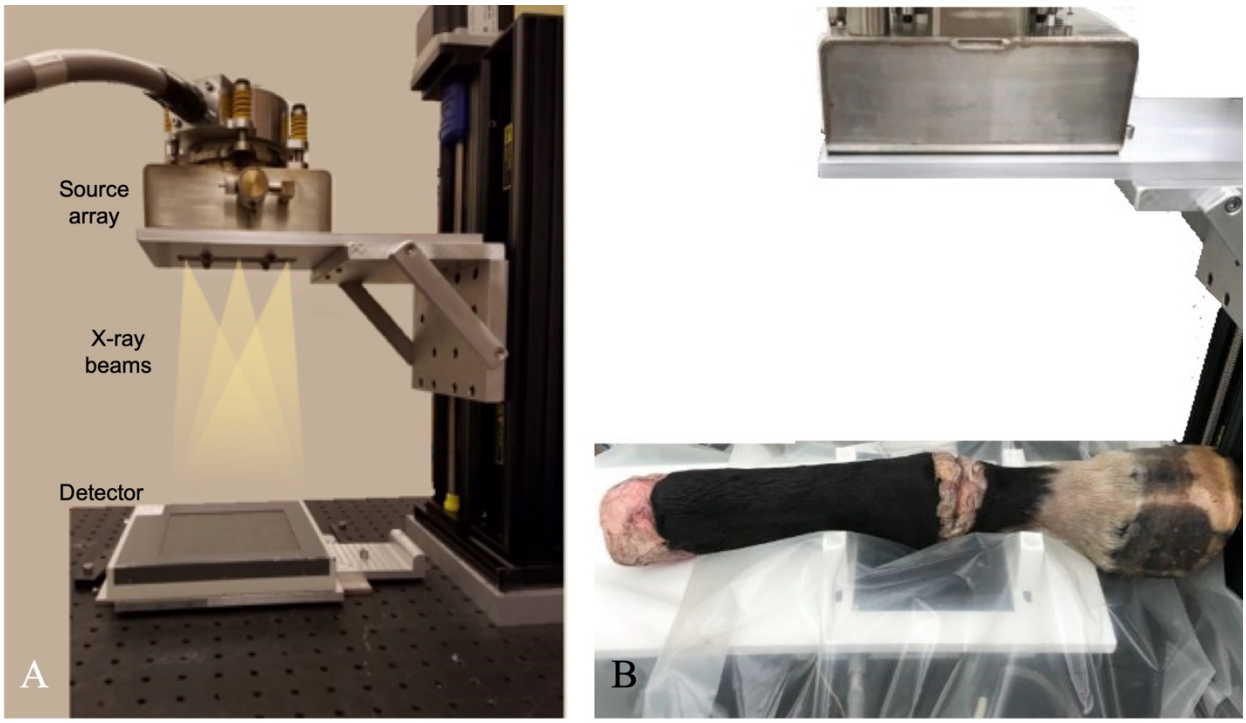

Figure 2.7 – Images of a custom-built compact tomosynthesis device and flat panel detector. (A) The source array and detector set up for cadaver limb scanning with schematic representation of x-ray beams; and (B) cadaver equine distal limb positioned for a dorsal scan of the metacarpophalangeal joint. The cadaver limbs were supported in a custom-made holder which slightly increased the object-detector distance, but allowed for scanning of limbs at a fixed position.

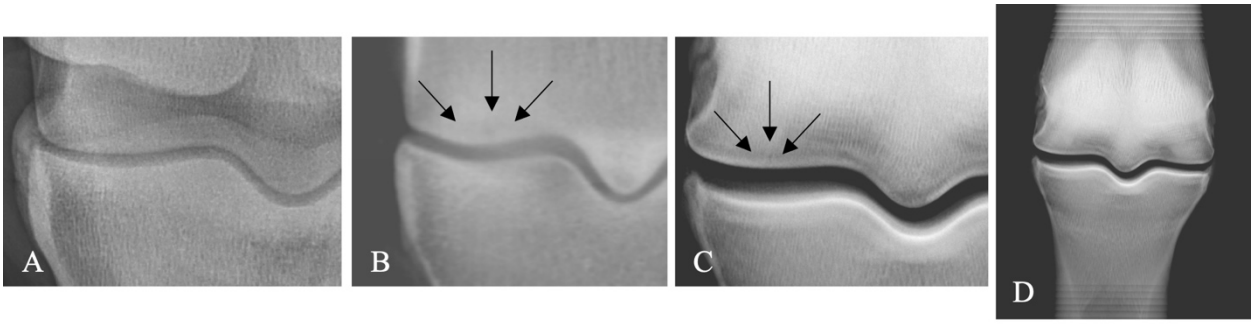

Figure 2.8 – Comparative images of Limb 2 between (A) radiography, (B) computed tomography, and (C, D) tomosynthesis. A subchondral fissure bordered by sclerosis (black arrows) was identified in the medial condyle of the distal third metacarpal bone. This lucent area was observed on tomosynthesis and computed tomography but was not observed using radiography.

2.6 Tables

Table 2.1 – Mean ± standard error signal-to-noise ratios (SNRs) between different biological fluids from a custom-made fluid phantom on magnetic resonance imaging using a short tau or short T1 inversion recovery (STIR) sequence.

Fluid	Saline	Blood	Serum	Plasma	Synovial Fluid	Air
SNR	106.629 ± 1.967	155.917 ± 11.534	159.411 ± 8.871	171.447 ± 2.707	140.796 ± 1.457	1.884 ± 0.194

Table 2.2 – Mean ± standard deviation (for scans with the 1.5 T) signal-to-noise ratios (SNRs) of fluid signal between different fluid-sensitive sequences in the sagittal plane on 1.5 T and 3 T magnetic resonance imaging (MRI) units. Higher SNRs were calculated for all fluid-sensitive sequences with the 3 T magnet strength, compared to the 1.5 T. The Dixon water only images had the highest SNR between fluid-sensitive sequences at the 3 T magnet strength.

Magnet Strength	**Sequence**	**SNR of Fluid**
1.5 T	STIR (135 inversion time)	4.777 ± 1.817
	STIR (120 inversion time)	7.446 ± 1.771
3 T	IW FS	6.671 ± 0.157
	STIR	12.674 ± 11.641
	Dixon, water only	91.467 ± 31.740

Table 2.3 – Percentage of cases where the presence or absence of a lesion in the metacarpophalangeal joint were correctly identified with each unique imaging modality. Computed tomography (CT) was used as a comparative imaging technique for osseous lesions, and magnetic resonance imaging (MRI) was used as a comparative technique for cartilage and soft tissue lesions. The metacarpophalangeal joints were also grossly evaluated for comparison to all imaging modalities and to confirm the presence of suspected lesions visible on the articular surface.

Modality	Radiography	Tomosynthesis	CT	MRI
Percentage (and number) of cases	75% (3/4)	100% (4/4)	100% (4/4)	100% (4/4)

Table 2.4 – Median and interquartile range semi-objective combined scores for all imaging modalities across three sites (i.e., third metacarpal, proximal phalanx and proximal sesamoid bones), including overall image quality score and the four regions of interest for the four equine cadaver limbs evaluated in the study. CT: computed tomography; MRI: magnetic resonance imaging.

Modality	**Image quality score**	**Subchondral bone**	**Articular cartilage**	**Peri-articular margins**	**Adjacent bone**
Radiography	3 [3-3]	3 [2-3]	0 [0-0]	3 [3-3]	2 [2-2]
Tomosynthesis	2.5 [2-3]	2.5 [2-3]	0 [0-0]	2 [2-2]	2 [2-3]
CT	3 [3-3]	4 [4-4]	0 [0-0]	4 [4-4]	4 [4-4]
MRI	4 [4-4]	4 [4-4]	3 [3-3]	4 [3-4]	4 [4-4]

Table 2.5 – Reported *P* values from comparisons made using the paired Wilcoxon tests for non-parametric data. Each column denotes a comparison between two diagnostic methods used to evaluate each structure. ROI: region of interest, MC3: third metacarpal bone, P1: proximal phalanx, PSB: proximal sesamoid bones, CT: computed tomography, Xray: radiography, MRI: magnetic resonance imaging, SCB: subchondral bone, AC: articular cartilage, PAM: peri-articular margins, Adj Bone: appearance of adjacent bone; NSD: no significant difference; --: comparisons could not be made where grading values were not different from one another.

ROI	Site	CT vs Xray	CT vs Tomosynthesis	MRI vs Xray	MRI vs Tomosynthesis	Xray vs Tomosynthesis
SCB	MC3	0.018	0.019	0.018	0.019	NSD (0.608)
	P1	0.013	0.019	0.013	0.019	NSD (0.181)
	PSB	0.018	0.019	0.018	0.019	NSD (0.608)
AC	MC3	--	--	NSD (0.072)	NSD (0.072)	--
	P1	--	--	NSD (0.072)	NSD (0.072)	--
	PSB	--	--	NSD (0.072)	NSD (0.072)	--
PAM	MC3	0.013	0.013	NSD (0.060)	0.018	0.013
	P1	0.013	0.013	NSD (0.181)	0.019	0.013
	PSB	0.013	0.013	NSD (0.089)	0.018	0.018
Adj Bone	MC3	0.013	0.018	0.013	0.018	NSD (0.453)
	P1	0.013	0.018	0.013	0.018	NSD (0.453)
	PSB	0.013	0.018	0.013	0.018	NSD (0.453)

2.7 References

1. Alliston T, Hernandez C, Findlay D, et al. Bone marrow lesions in osteoarthritis: What lies beneath. J Orthop Res 2018;36:1818–1825.

2. Lawrence R, Felson D, Helmick C, et al. Estimates of the prevalence of arthritis and other rheumatic conditions in the United States. Part II. Arthritis Rheum 2008;58:26–35.

3. Taljanovic MS, Graham AR, Benjamin JB, et al. Bone marrow edema pattern in advanced hip osteoarthritis: Quantitative assessment with magnetic resonance imaging and correlation with clinical examination, radiographic findings, and histopathology. Skeletal Radiol 2008;37:423–431.

4. Zhang Y, Nevitt M, Niu J, et al. Fluctuation of knee pain and changes in bone marrow lesions, effusions, and synovitis on magnetic resonance imaging. Arthritis Rheum 2011;63:691–699.

5. Laslett LL, Doré DA, Quinn SJ, et al. Zoledronic acid reduces knee pain and bone marrow lesions over 1 year: a randomised controlled trial. Ann Rheum Dis 2012;71:1322–1328.

6. Ma J. Dixon techniques for water and fat imaging. J Magn Reson Imaging 2008;28:543–558.

7. Delfaut EM, Beltran J, Johnson G, et al. Fat Suppression in MR Imaging: Techniques and Pitfalls. Radiographics 1999;19:373–382.

8. Del Grande F, Santini F, Herzka DA, et al. Fat-Suppression Techniques for 3-T MR Imaging of the Musculoskeletal System. Radiographics 2014;34:217–233.

9. Zanetti M, Bruder E, Romero J, et al. Bone marrow edema pattern in osteoarthritic knees: correlation between MR imaging and histologic findings. Radiology 2000;215:835–840.

10. Edelstein W, Glover G, Hardy C, et al. The intrinsic signal-to-noise ratio in NMR imaging. Magn Reson Med 1986;3:604–618.

11. Johnson TRC. Dual-Energy CT: General Principles. Am J Roentgenol 2012;199:S3–S8.

12. Johnson TRC, Krauß B, Sedlmair M, et al. Material differentiation by dual energy CT: initial experience. Eur Radiol 2007;17:1510–1517.

13. Gold GE, Han E, Stainsby J, et al. Musculoskeletal MRI at 3.0 T: Relaxation Times and Image Contrast. Am J Roentgenol 2004;183:343–351.

14. Duewell S, Ceckler T, Ong K, et al. Musculoskeletal MR imaging at 4 T and at 1.5 T: comparison of relaxation times and image contrast. Radiology 1995;196:551–555.

15. Bydder G, Pennock J, Steiner R, et al. The short TI inversion recovery sequence--an approach to MR imaging of the abdomen. Magn Reson Imaging 1985;3:251–254.

16. Bydder G, Young I. Clinical use of the partial saturation and saturation recovery sequences in MR imaging. J Comput Assist Tomogr 1985;9:1020–1032.

17. Smith MRW, Kawcak CE, McIlwraith CW. Science in brief: Report on the Havemeyer Foundation workshop on subchondral bone problems in the equine athlete. Equine Vet J 2016;48:6–8.

18. Kawcak CE. Pathologic manifestations of joint disease. In: McIlwraith CW, Frisbie DD, Kawcak CE, et al., eds. Joint Disease in the Horse. Second. St. Louis, Missouri: Elsevier; 2016:49–56.

19. Kudo H, Suzuki T, Rashed EA. Image reconstruction for sparse-view CT and interior CT—introduction to compressed sensing and differentiated backprojection. Quant Imaging Med Surg 2013;3:147.

20. Candès EJ, Romberg J, Tao T. Robust uncertainty principles: Exact signal reconstruction from highly incomplete frequency information. IEEE Trans Inf Theory 2006;52:489–509.

21. Sidky EY, Duchin Y, Pan X, et al. A constrained, total-variation minimization algorithm for low-intensity x-ray CT. Med Phys 2011;38:S117.

22. Han X, Pearson E, Pelizzari C, et al. Algorithm-enabled exploration of image-quality potential of cone-beam CT in image-guided radiation therapy. Phys Med Biol 2015;60:4601.

23. Sidky EY, Kao C-M, Pan X. Accurate image reconstruction from few-views and limited-angle data in divergent-beam CT. J Xray Sci Technol 2006;14:119–139.

24. Scarfe WC, Farman AG. What is cone-beam CT and how does it work? Dent Clin North Am 2008;52:707–730.

25. Stewart HL, Siewerdsen JH, Nelson BB, et al. Use of cone-beam computed tomography for advanced imaging of the equine patient. Equine Vet J 2021;53:872–885.

26. Sidky EY, Stewart HL, Kawcak CE, et al. Bone sparsity model for computed tomography image reconstruction. Proc SPIE 11072, 15th Int Meet Fully Three-Dimensional Image Reconstr Radiol Nucl Med 2019:117.

27. Pontana F, Pagniez J, Flohr T, et al. Chest computed tomography using iterative reconstruction vs filtered back projection (Part 1): evaluation of image noise reduction in 32 patients. Eur Radiol 2011;21:627–635.

28. Ritchie CJ, Crawford CR, Godwin JD, et al. Correction of computed tomography motion artifacts using pixel-specific back-projection. IEEE Trans Med Imaging 1996;15:333–342.

29. Flohr TG, Schaller S, Stierstorfer K, et al. Multi-detector row CT systems and image-reconstruction techniques. Radiology 2005;235:756–773.

30. Sidky EY, Pan X. Image reconstruction in circular cone-beam computed tomography by constrained, total-variation minimization. Phys Med Biol 2008;53:4777.

31. Sidky E, Pan X, Reiser I, et al. Enhanced imaging of microcalcifications in digital breast tomosynthesis through improved image-reconstruction algorithms. Med Phys 2009;36:4920–4932.

32. Rudin LI, Osher S, Fatemi E. Nonlinear total variation based noise removal algorithms. Phys D Nonlinear Phenom 1992;60:259–268.

33. Sidky EY, Jørgensen JH, Pan X. Convex optimization problem prototyping for image reconstruction in computed tomography with the Chambolle–Pock algorithm. Phys Med Biol 2012;57:3065.

34. Dong J, Han C, Qin Z, et al. Evolution from total variation to nonlinear sparsifying transform for sparse-view CT image reconstruction. bioRxiv 2019:785261.

35. Maleh R, Gilbert AC, Strauss MJ. Sparse gradient image reconstruction done faster. Proc - Int Conf Image Process ICIP 2007;2.

36. Dong A, Wang Y, Dong H, et al. Inflammatory myofibroblastic tumor: FDG PET/CT findings with pathologic correlation. Clin Nucl Med 2014;39:113–121.

37. Cai J-F, Dong B, Osher S, et al. Image Restoration: Total Variation, Wavelet Frames, and Beyond. J Amer Math Soc 2012;25.

38. Guo W, Qin J, Yin W. A new detail-preserving regularization scheme. SIAM J Imaging Sci 2014;7:1309–1334.

39. Nagarajappa AK, Dwivedi N, Tiwari R. Artifacts: The downturn of CBCT image. J Int Soc Prev Community Dent 2015;5:440–445.

40. Barrett MF, Werpy NM, Selberg K. Principles of Diagnosis. In: Mcilwraith CW, Frisbie DD, Kawcak CE, et al., eds. Joint Disease in the Horse. 2nd Ed. St. Louis, Missouri: Elsevier Inc; 2016:119–178.

41. Vallebona A. Axial transverse laminagraphy. Radiology 1950;55:271–273.

42. Niklason LT, Christian BT, Niklason LE, et al. Digital tomosynthesis in breast imaging. Radiology 1997;205:399–406.

43. Baker JA, Lo JY. Breast tomosynthesis: state-of-the-art and review of the literature. Acad Radiol 2011;18:1298–310.

44. Hayashi D, Xu L, Roemer FW, et al. Detection of osteophytes and subchondral cysts in the knee with use of tomosynthesis. Radiology 2012;263:206–215.

45. Roemer FW, Guermazi A. Osteoarthritis year 2012 in review: imaging. Osteoarthr Cartil 2012;20:1440–1446.

46. Ottenin M-A, Jacquot A, Grospretre O, et al. Evaluation of the diagnostic performance of tomosynthesis in fractures of the wrist. Am J Roentgenol 2012;198:180–186.

47. Aoki T, Fujii M, Yamashita Y, et al. Tomosynthesis of the wrist and hand in patients with rheumatoid arthritis: comparison with radiography and MRI. Am J Roentgenol 2014;202:386–390.

48. Canella C, Philippe P, Pansini V, et al. Use of tomosynthesis for erosion evaluation in rheumatoid arthritic hands and wrists. Radiology 2011;258:199–205.

49. Gavin P. Physical principles and technical considerations for equine computed tomography and magnetic resonance imaging. Vet Clin North Am Equine Pract 2001;17:115–130.

50. Tucker RL, Sande RD. Computed tomography and magnetic resonance imaging in equine musculoskeletal conditions. Vet Clin North Am Equine Pract 2001;17:145–157.

51. Inscoe CR, Platin E, Mauriello SM, et al. Characterization and preliminary imaging evaluation of a clinical prototype stationary intraoral tomosynthesis system. Med Phys 2018;45:5172–5185.

52. Dobbins JT, McAdams HP. Chest tomosynthesis: Technical principles and clinical update. Eur J Radiol 2009;72:244–251.

53. Kawcak CE, McIlwraith CW, Norrdin RW, et al. The role of subchondral bone in joint disease: a review. Equine Vet J 2001;33:120–126.

54. Lacourt M, Gao C, Li A, et al. Relationship between cartilage and subchondral bone lesions in repetitive impact trauma-induced equine osteoarthritis. Osteoarthr Cartil 2012;20:572–583.

55. Dykgraaf S, Firth EC, Rogers CW, et al. Effects of exercise on chondrocyte viability and subchondral bone sclerosis in the distal third metacarpal and metatarsal bones of young horses. Vet J 2008;178:53–61.

56. Riggs C. Aetiopathogenesis of parasagittal fractures of the distal condyles of the third metacarpal and third metatarsal bones - review of the literature. Equine Vet J 1999;31:116–120.

57. Riggs C, Whitehouse GH, Boyde A. Pathology of the distal condyles of the third metacarpal and third metatarsal bones of the horse. Equine Vet J 1999;31:140–148.

58. Doube M, Firth EC, Boyde A, et al. Combined nanoindentation testing and scanning electron microscopy of bone and articular calcified cartilage in an equine fracture predilection site. Eur Cell Mater 2010;19:242–51.

59. Cruz A, Hurtig MB. Multiple pathways to osteoarthritis and articular fractures: is subchondral bone the culprit? Vet Clin North Am Equine Pract 2008;24:101–116.

60. Inscoe CR, Billingsley AJ, Puett C, et al. Tomosynthesis imaging of the wrist using a CNT x-ray source array. Proc SPIE Med Imaging 2019;10948:197.

61. Inscoe CR, Billingsley AJ, Puett C, et al. Preliminary imaging evaluation of a compact tomosynthesis system for potential point-of-care extremity imaging. Proc SPIE Med Imaging 2020;1131204:4.

62. Gomi T, Hirano H, Umeda T. Evaluation of the X-ray digital linear tomosynthesis reconstruction processing method for metal artifact reduction. Comput Med Imaging Graph 2009;33:267–274.

63. Choi JS, Han BK, Ko EY, et al. Comparison of synthetic and digital mammography with digital breast tomosynthesis or alone for the detection and classification of microcalcifications. Eur Radiol 2019;29:319–329.

64. Johnson SA, Barrett MF, Frisbie DD. Additional palmaroproximal-palmarodistal oblique radiographic projections improve accuracy of detection and characterization of equine flexor cortical lysis. Vet Radiol Ultrasound 2018;59:387–395.

65. Lu Y, Chan HP, Wei J, et al. A diffusion-based truncated projection artifact reduction method for iterative digital breast tomosynthesis reconstruction. Phys Med Biol 2013;58:569–587.

66. Zhang Y, Chan HP, Sahiner B, et al. Artifact reduction methods for truncated projections in iterative breast tomosynthesis reconstruction. J Comput Assist Tomogr 2009;33:426–435.

67. Redden RF. Radiographic imaging of the equine foot. Vet Clin North Am Equine 2003;19:379–392.

68. Contino EK, Barrett MF, Werpy NM. Effect of limb positioning on the radiographic appearance of the distal and proximal interphalangeal joint spaces of the forelimbs of horses during evaluation of dorsopalmar radiographs. J Am Vet Med Assoc 2014;244:1186–1190.

69. Hornof WJ, O'Brien TR. Radiographic evaluation of the palmar aspect of the equine metacarpal condyles: a new projection. Vet Radiol 1980;21:161–167.

70. Jeffcott L, Kold SE. Radiographic examination of the equine stifle. Equine Vet J 1982;14:25–30.

71. Machida H, Yuhara T, Tamura M, et al. Whole-body clinical applications of digital tomosynthesis. Radiographics 2016;36:735–750.

CHAPTER 3:

DEVELOPMENT OF AN EXPERIMENTAL MODEL OF BONE MARROW LESIONS USING THE OVINE FEMORAL CONDYLE

3.1 Introduction

Joint disease, as a result of any underlying etiology has a substantial economic and social impact. Osteoarthritis (OA) is the most commonly recognized arthropathy, and remains an incurable and debilitating condition for animals and humans alike, resulting in pain, lameness and decreased athletic performance. Research efforts are directed at detecting early changes in articular cartilage and subchondral bone, as loss of articular cartilage and alterations in subchondral bone are the hallmarks of OA. A generic term, bone marrow lesions (BMLs), also sometimes referred to as "bone marrow edema," "bone bruises," or "bone contusions," have a high signal intensity on fluid-sensitive T2-weighted sequences on magnetic resonance imaging (MRI),[1] and have been documented in humans and multiple veterinary species, including horses[2–4] and dogs.[5] Compelling reports have been published citing BMLs as an early indicator of structural joint deterioration and may serve as a marker for maladaptive changes occurring within the articular cartilage and subchondral bone.[6–9] It remains to be investigated whether BMLs are a specific response to changes within the articular cartilage and joint, or whether changes within the bone catalyze changes within the articular cartilage, ultimately resulting in joint deterioration. Understanding this pathologic process is key to developing diagnostic and management principles in the future.

Despite the observed frequency and clinical relevance of BMLs, there is a relative paucity of information about the etiology, behavior, and histopathologic appearance of these

lesions. Clinically, pain and morbidity are observed in humans with BMLs[10–12], and horses may display marked lameness isolated to the region of increased signal on MRI.[2–4] The evolution of BMLs remain unpredictable, with some progressing rapidly toward degenerative processes in the joint, while others resolve completely following a period of rest.[11,13] Proposed theories for the observed signal change on MRI include capillary leakage or increased intravascular pressure within the marrow space secondary to increased blood flow or decreased venous clearance. Additionally, work by Zanetti et al, found that BMLs diagnosed on MRI corresponded to a variety of different histological findings, including bone marrow necrosis, abnormal trabeculae, bone marrow fibrosis and bone marrow bleeding.[14] The variable findings on histopathology support the multiple etiologies implicated in the formation of BMLs, including osteochondral trauma, degenerative, inflammatory, infectious, and ischemic lesions. It has been suggested that BMLs may be part of a non-specific, maladaptive response of bone to trauma or inflammation. Work by Taljanovic et al, correlated BMLs observed in the hip on MRI with clinical, histopathologic and radiographic findings and found that 100% of patients had evidence of microfractures; reinforcing the postulated relationship between trauma at the articular surface and formation of BMLs.[12]

The association between BMLs and trauma has been well-described in the clinical literature.[11,13,15–17] In many cases, BMLs are reported in conjunction with other conditions, including end-stage joint disease, meniscal or ligamentous injury, focal osteonecrosis, or bone fracture. Additionally, BMLs have been incidentally observed in the experimental setting, secondary to acute trauma to the osteochondral tissues. Despite this, an orderly investigation of the specific requirements of osteochondral trauma necessary to incite BMLs have not been evaluated. Arguably, it would also be valuable to create an experimental model for BMLs

without direct manipulation of the osteochondral tissues, in order to better mimic repetitive concussive injury to the joint as is observed in more chronic injuries with BMLs. Limited studies have found that transcutaneous extracorporeal shockwave (ESW) application is reported to induce periosteal detachment with subperiosteal hemorrhage, microfractures within the trabeculae of the medullary cavity, thickening and even complete fractures to cortical bone.[18,19] Case reports in humans have also described transcutaneous application of ESW is capable of inducing osteonecrosis of the bone.[20] ESW has a dose-dependent effect on bone, where 10,000 pulses applied at an energy of 0.60 mJ/mm^2 is sufficient to induce complete fractures in the mid-diaphysis of cortical bone of the tibia.[18] Given that BMLs are frequently reported in association with fractures and osteonecrosis, it seemed reasonable to postulate that an excessive number of pulses at a very high energy using ESW would be sufficient to create a BML.

The prevalence and translational aspects of BMLs, as well as their relationship with OA, mandate further exploration of this condition. The overarching goal of this study was to develop an experimental model for BMLs, using the ovine femorotibial joint. The first aim of the study was to identify the specific layers of the osteochondral unit that need to be stimulated in order for a BML to be produced. We hypothesized that (1) microtrauma induced by intra-articular methods extending from the articular cartilage to subchondral bone would be sufficient to create BMLs that mimic naturally-occurring lesions; (2) that volumetric imaging modalities, such as computed tomography (CT) and MRI could be optimized to detect BMLs using fluid-sensitive sequences and techniques; and (3) imaging findings would be highly correlated to histopathologic findings of BMLs within the bone. The second aim of this study was to validate the use of transcutaneous ESW as a non-invasive traumatic method for generation of BMLs. We hypothesized that (1) it would be possible to induce BMLs through non-invasive traumatic

method with ESW, and (2) that BMLs induced by ESW would have a similar appearance on volumetric imaging and histopathology to BMLs induced using direct, intra-articular methods. Ultimately, development of an experimental model enhances the understanding of BMLs, and can applied toward future efforts toward molecular and cellular characterization of the etiopathogenesis of these lesions, with the eventual intention to develop targeted interventional therapies to mitigate degenerative arthropathies across species.

3.2 Materials and Methods

3.2.1 Animals

Eighteen, skeletally-mature, Dorper or Dorper-cross female sheep were used for this prospective study. All animals were vaccinated, dewormed and confirmed to be healthy prior to the start of the study. Animals were housed indoors, indoors with outdoor run access, or outdoors, depending on the phase of the study, and fed a diet in accordance with the National Research Council. All procedures were approved by the Institutional Animal Care and Use Committee of Colorado State University (Protocol ID: 17-7373A, approved 09/05/2018).

3.2.2 Experimental protocol

Physical and lameness examinations, computed tomography (CT) and MRI were performed prior to surgery. Sheep were monitored daily throughout the study for attitude, appetite, and level of comfort. On day 0, sheep were placed under general anesthesia and each medial femoral condyle (MFC) was assigned to a treatment group of either transcutaneous ESW application or penetration with a surgical pin. Sheep were monitored daily for the first week, and then weekly for the first month, and then prior to each imaging timepoint for degree of weight-

bearing in each hind limb. Serum was collected prior to surgery and at each imaging timepoint. Bilateral imaging of the femorotibial joints with MRI and CT was performed every 2 weeks under each animal's endpoint. Sheep were euthanized 30 (N = 4 animals), 60 (N = 4 animals), or 90 (N = 10 animals) days after surgery with an overdose of sodium pentobarbital (88 mg/kg IV). All femorotibial joints were evaluated for the presence of gross lesions, followed by microCT (μCT) and histologic evaluation of the medial femoral condyles.

3.2.3 Transcutaneous extracorporeal shockwave

One femorotibial joint of each animal was assigned to one of two transcutaneous ESW treatment groups. Hair was removed from the cranial aspect of the femorotibial joint and shockwave coupling gel was applied to the skin to increase contact with the trode. Femorotibial joints were held in flexion to access the weight-bearing surface of the medial femoral condyle. A total of 10,000 pulses at a frequency of 24 Hz and energy of 0.63 mJ/mm^2 were applied at a rate of 240-360 pulses/minute, using a commercially-available ESW unit (ProPulse, Pulse Veterinary Technologies, LLC, Alpharetta, GA, USA). Pulses were applied using either a 20 mm (Group E, N = 9 MFCs) or 35 mm (Group F, N = 9 MFCs) trode. All gel was removed after ESW treatment.

3.2.4 Intra-articular pin application

One femorotibial joint of each animal was assigned to one of four pin penetration treatment groups. A medial parapatellar arthrotomy was used to access the medial femoral condyle of limbs assigned to pin penetration. Femorotibial joints were held in flexion with the patella deviated laterally to access the articular, weight-bearing surface of the medial femoral

condyle. A 1.1 mm Steinmann pin was advanced to various depths, depending on the allocation of limbs to one of the four treatment groups. Drilling was accomplished using a battery-powered surgical drill. Lavage with sterile isotonic fluids was continuous during all drilling. Pin penetration of Group A (N = 4 MFCs) was to a depth of 1 mm through the articular and into the calcified cartilage layer from the articular surface; Group B (N = 4 MFCs) was to a depth of 2 mm, through the articular and calcified cartilage layers and into the subchondral bone plate from the articular surface; Group C (N = 6 MFCs) was to a depth of 8 mm, through the articular and calcified cartilage layers, subchondral bone plate and into the underlying trabecular bone from the articular surface; while Group D (N = 4 MFCs) used an abaxial approach from immediately cranial to the origin of the medial collateral ligament of the femorotibial joint and drilling the pin only through the trabecular bone and subchondral bone plate under fluoroscopic guidance. The depth of drilling for Groups A, B, and C, was justified on preliminary work and incidental observation of BMLs in other research focused on the ovine femorotibial joint. An additional two animals were included in Group C as pilot animals for this study. After drilling, joint lavage with sterile saline was performed to remove any osteochondral debris and the surgical site was closed routinely in three layers.

3.2.5 Gait evaluation

Gait was evaluated pre-operatively, daily for the first 7 days, weekly for the first month, and prior to each imaging timepoint thereafter. Animals were allowed to move freely within a 6 ft x 25 ft area that they were familiar with for gait evaluation. A semi-objective 0-4 scale was used to grade visible lameness on each hind limb. Briefly, grade 0 was defined a normal ambulation, fully weight-bearing; grade 1 indicated a slight lameness with a partial weight-

bearing gait on all steps; grade 2 indicated a moderate lameness with a combination of partial and minimally weight-bearing; grade 3 indicated a marked lameness with non-weightbearing on all steps when walking but partially weight-bearing when herded; and grade 4 indicated non-weight bearing during all ambulation.

3.2.6 Magnetic resonance imaging (MRI)

Femorotibial joints were evaluated under general anesthesia using MRI with animals placed in lateral recumbency. The animal was positioned with the foot entering the gantry first, and with the limb of interest oriented upward to achieve positioning within isocenter. Animals were rotated into the opposite recumbency for imaging of the contralateral limb. A single animal was imaged using a 1.5 T magnetic resonance scanner (GE Signa HDxt, General Electric Company, Fairfield, CT, USA) with a bore diameter of 60 cm. The remaining seventeen animals were imaged using a 3 T magnetic resonance scanner (Siemens Magnetom Skyra, Siemens Medical Solutions USA, Inc., Malvern, PA, USA) with a bore diameter of 70 cm. For both units, a knee coil was used for all imaging.

For imaging with the 1.5 T unit, sequences included proton density fat saturation (PDFS) in all planes (sagittal plane settings: TR 2967, TE 9.648, flip angle 130; dorsal plane settings: TR 2728, TE 17.104, flip angle 130; transverse plane settings: TR 3929, TE 15.552, flip angle 130); proton density (PD; sagittal plane settings: TR 2500, TE 8.48, flip angle 130; cranial plane settings: TR 2500, TE 17.104, flip angle 130); short-tau or short T1 inversion recovery (STIR; sagittal plane settings: TR 3650, TE 33.376, flip angle 90; cranial plane settings: TR 3650 TE 33.664, flip angle 90), and 3D fast spin gradient echo (3D FSPGR; sagittal plane settings: TR 11.168, TE 3.4, flip angle 20; cranial plane settings: TR 11.292, TE 3.392, flip angle 20) in the

sagittal and cranial planes; and T2 fast spin echo (T2 FSE) in the sagittal plane (TR 3086, TE 101.552, flip angle 90). All images had a 320 x 256 matrix, with voxel dimensions of 0.5 mm x 0.4 mm x 3 mm.

For imaging with the 3 T unit, sequences included PDFS in all planes (sagittal plane settings: TR 2500, TE 37, flip angle 150, 320; cranial plane settings: TR 2500, TE 48, flip angle 150, matrix 384 x 384, slice thickness 3 mm; transverse plane settings: TR 2840, TE 48, flip angle 127, matrix 384 x 384, slice thickness 3 mm); intermediate-weighted fat suppression via the Dixon method in the sagittal (TR 3500, TE 38, flip angle 123, matrix 320 x 320, slice thickness 3 mm) and cranial (TR 3500, TE 38, flip angle 122, matrix 320 x 320, slice thickness 3 mm) planes; and T1-weighted (TR 650, TE 10, flip angle 150, matrix 384 x 288, slice thickness 3 mm) and T2-weighted 3D double echo steady state in the sagittal plane (TR 11.05, TE 4.18, flip angle 25, matrix 192 x 192, slice thickness 0.6 mm). A single animal was also imaged with the STIR sequence (sagittal plane settings: TR 1900, TE 29, flip angle 121 matrix 256 x 256, slice thickness 3 mm; cranial plane settings: TR 1830, TE 27, flip angle 121, matrix 256 x 256, slice thickness 3 mm), for comparison with the 1.5 T unit. Voxel dimensions ranged from 0.3-0.6 mm x 0.3-0.6 mm x 0.6-3 mm.

3.2.7 Computed tomography (CT)

Femorotibial joints in all animals were scanned pre-operatively using conventional 64-slice helical fan-beam CT unit (Siemens Somatom Definition AS, Siemens Medical Solutions USA, Inc., Malvern, PA, USA). Post-operatively, CT evaluation of bilateral femorotibial joints was performed only if fluid signal was observed in at least one medial femoral condyle on MRI. If fluid signal was present on MRI, CT evaluation was performed immediately thereafter under

the same anesthetic episode. For CT imaging, animals were placed in lateral recumbency with both hind limbs in extension at the femorotibial joint, with the feet entering the gantry first. Both femorotibial joints were scanned simultaneously. Images were acquired in the transverse plane relative to the joint surface in 3 mm-thick section, with a 0.7 pitch, 106 mm field of view and a 512 x 512 voxel matrix.

Two sequential scans of the femorotibial joints were performed a different energy level in accordance with the manufacturer's settings for the "Dual Energy Edema" protocol for post-processing dual-energy (DE) image reconstruction. Briefly, the high-energy value for scans was 140 kVp, the low-energy value for scanning was 80 kVp. Raw CT data was reconstructed at 0.8 mm thickness x 0.8 mm increment (bone reconstruction kernel) and 2.0 mm thickness x 1.0 mm thickness (standard reconstruction kernel).

3.2.8 Image evaluation

All digital imaging obtained via MR and CT were stored within the picture archiving and communication system (PACS) at Colorado State University. Open-sourced software (Horos Project, version 3.3.6) was used for viewing and evaluating DICOM images. Additionally, images obtained using the DE protocol with CT were evaluated using the commercially-available platform available through the manufacturer (Syngo.Via, Siemens Medical Solutions, Inc., Malvern, PA, USA).

Post-operative images on MR from each animal were first evaluated for the presence of a BML. If a BML was not present on any sequence, this was recorded and no further analyses of images were performed. If a BML was present, all sequences for a given animal at a specific timepoint were graded for the following parameters: maximum condylar area, maximum BML

area, average BML signal, maximum BML signal, minimum BML signal, number of slices where a BML was present, area of the BML on each slice, adjacent muscle signal, and standard deviation of air of the background. A 10 mm^2 circular region of interest (ROI) was used to identify the signal within the BML, muscle and background air. From these parameters, the percent of the condyle occupied, signal-to-noise ratio (SNR), and contrast-to-noise ratio (CNR) of the BML were calculated.[21,22] Briefly, for the SNR the mean signal of the ROI within the BML was divided by the standard deviation of the background air in a ROI of equal size. For CNR, the signal of the ROI of the muscle was subtracted from the signal in the ROI of the BML, and then divided by the standard deviation of the background air ROI. Pre-operative images of animals with BMLs were reviewed and post-operative images were overlaid using imaging software (AnalyzeDirect, version 14.0, Overland Park, KS) in order to calculate baseline SNRs and CNRs in the same location as the post-operative BML.

Magnetic resonance images were overlaid onto CT images to view the extent of the BML. A 3 mm^2 circular ROI was used to evaluate the attenuation in Hounsfield Units (HU) within the BML in the medial femoral condyles for the CT images obtained using the bone reconstruction kernel at 140 kVp. If the BML extended beyond 3 mm^2 and the pin tract was visible, the ROI was placed adjacent to the pin tract, but excluded cortical bone. Multi-planar reconstruction was used to identify a similar location within the lateral femoral condyle of the same limb to grade the attenuation. In limbs where a BML was not visible on MR images within the limb of interest, but a BML was present in the contralateral limb, the contralateral limb was overlaid to identify a region of interest to grade the attenuation. In cases where a BML was not visible on either limb, MR images from another animal with a BML was used to identify a region of interest to grade the attenuation.

Following sequential CT scans at two energy levels, three data sets of reconstructed images were generated: an 80 kVp set, a 140 kVp set, and an average-weighted set calculated from both tube data at a ratio of 0.5:0.5 to imitate a single 120 kVp image. Blended virtual 120 kVp axial, sagittal, and cranial plane reconstructed images (D kernel) were also used for evaluation. Image sets were transferred to a specific workstation for DE image generation (SyngoVia; Siemens, Erlangen, Germany).

A three-material decomposition technique was used to create a virtual non-calcium image, as has been previously described.[23,24] A color overlay map was automatically generated for the image. Briefly, green-yellow shades corresponded to a BML, and blue-purple shades corresponded to more dense bone. Images sets for each animal at each timepoint were evaluated individually, modifying software parameters to produce the highest quality image for analysis. Briefly, resolution was set at a 2 or 3, maximum attenuation was set at 1500 HU, and threshold attenuation was set at 80-100 HU, with a higher threshold at later timepoints in the study. Three-dimensional volumetric renderings of the femorotibial joint were also generated, with normal bone in shades of blue, and BMLs in shades of green. Conventional grayscale morphologic images were utilized for immediate comparison. If a BML was visible using the color overlay on CT images, the extent of the BML was compared to MR images in all planes on fluid-sensitive sequences.

3.2.9 Macroscopic post-mortem evaluation of femorotibial joints

The femorotibial joints of all study animals were evaluated immediately after euthanasia. Joints were opened completely for evaluation of gross damage to the articular cartilage, development of osteophytes, and gross characteristics of the synovium, as previously described

for sheep and goats as per Table IIIA-C by Little et al.[25] All joints were photographed to record evidence of gross pathologic lesions. Following this, the femurs were removed *en bloc* and placed in 10% neutral-buffered formalin (NBF) at a 10:1 ratio by volume at room temperature for tissue fixation. NBF was changed to fresh solution every 48 h for 7 days. After fixation, samples were rinsed and immersed in phosphate buffered saline (PBS) solution until decalcification.

Four femurs were removed *en bloc* and not immediately fixed in NBF, but instead immediately wrapped in saline-soaked gauze and cooled for additional imaging with cone-beam CT (CBCT; see below). Samples were maintained in saline-soaked gauze and stored at 4ºC throughout imaging and then placed in 10% NBF, as described, thereafter. All imaging procedures were completed within 1 week of euthanasia.

Four additional femurs were obtained and fixed in a similar manner as described above, as control samples for comparison. Control samples were collected from three healthy, skeletally-mature ewes of similar body weight that were free of femorotibial joint disease, and euthanized for reasons unrelated to this study.

3.2.10 Cone-beam computed tomography (CBCT)

Cone-beam computed tomography imaging and analyses were performed in two phases in collaboration with the I-STAR Laboratory at Johns Hopkins University. For the first, *in vivo* phase, the femorotibial joint of a single animal with a BML on MRI was scanned using a commercially-available CBCT unit designed for equine use (Pegaso, Epica Medical Innovations, San Clemente, CA, USA). The femorotibial joint was imaged sequentially at two different

energy levels (80 kVp, 140 kVp). Raw data was reconstructed volumetrically using the FDK algorithm.[26,27]

Dual-energy decomposition data were obtained from high and low energy reconstructions to identify fractions of water or soft tissue (S), adipose or fat (F), and calcium or bone (B) using the standard image domain approach with volume conservation constraint.[28] A virtual non-calcium technique used to generate images in the ROI corresponding to the BML in the cranial plane, as has been previously described.[29–32] BMLs have previously been characterized using the following formula[23]:

$$q = \frac{F}{(S + F)}$$

This formula is the weighted sum of the attenuation of water and fat tissues to create a single soft tissue image. In the image, water will appear brighter and fat will appear darker. DE images were subjectively compared to Dixon water only images in the cranial plane.

For the second, *ex vivo* phase of work, the intact femur was taken from four animals with visible BMLs for evaluation with a custom, purpose-built benchtop CBCT system for musculoskeletal extremity imaging.[33] Femurs were scanned at two different energy levels (60 kVp, 140 kVp). At 140 kVp, a 0.255 mm Ag beam filter was also added. Images were reconstructed volumetrically on a 0.25 mm isotropic voxel grid using the FDK algorithm, as previously described.[26,27] Data from high and low energy scans were used to generate base material fraction maps of water, calcium, and adipose tissues for each voxel. Virtual monoenergetic composite images were then created using an image-based method, as described.[34] BMLs within the medial femoral condyle were defined based on the following formula:[29]

$$F * \mu_F(60\ keV) + S * \ \mu_S(60\ keV)$$

Where F is the adipose or fat fraction in the image, S is the water or soft tissue fraction, and μ is the attenuation coefficient.

Cranial plane sections through reconstructions were compared to cranial plane T2-weighted 3D double echo steady state images for subjective imaging comparison.

3.2.11 Micro-computed tomography (μCT)

Prior to μCT, the distal aspect of each femur was prepared for scanning. A single, transverse cut was made immediately proximal to the trochlear ridges, in the region of the distal metaphysis of the bone. The distal aspect of each femur—including the lateral and medial femoral condyles—was imaged with μCT (Scanco μCT 80, Scanco Medical AG, Brüttisellen, Switzerland) using an isotropic voxel resolution of 37 μm, 70 kVp tube voltage, 11 μAmp current, and 300 ms integration time. Prior to analysis, all samples were rotated so that the medial femoral condyle and any visible pin defects were oriented certically along the Z-axis. The medial femoral condyle was analyzed in each animal. A cube 3 mm^3 ROI was generated in the subchondral trabecular bone of each medial femoral condyle for analysis, positioned immediately dorsal or ventral from the visible pin defect, deep to the cortical bone. If visible, the pin tract was excluded from the ROI. For medial femoral condyles treated with ESW, the contralateral medial femoral condyle was used to identify a similar ROI for analysis. Outcome parameters for μCT included total volume (TV), bone volume (BV), bone volume fraction (BV/TV), trabecular number (Tb.N), trabecular thickness (Tb.Th), and trabecular spacing (Tb.Sp) using the direct 3D method.[35]

3.2.12 Histologic evaluation of medial femoral condyles

The medial femoral condyle from each limb was isolated through sagittal sectioning of each distal femoral sample between the lateral and medial femoral condyles. Additional sectioning of the medial femoral condyle was performed to create a 2 cm thick osteochondral section centered around the pin tract (or similar region for ESW-treated limbs). Lateral femoral condyles were stored in PBS, and medial femoral condyles were prepared routinely for histologic analyses. Medial femoral condyles were decalcified in 8% trifluoroacetic acid (TFAA, Thermo Fisher Scientific, Waltham, MA, USA), as previously described.[36] Briefly, individual medial femoral condyles were placed in a volume of TFAA sufficient for submersion at room temperature with constant agitation. Decalcification progress was checked daily via radiographic imaging, and if incomplete, the solution was replaced. Decalcification was considered complete when there were no remaining calcium deposits within the bone on radiography. When completed, samples were rinsed in running tap water for 20 minutes and stored in 70% ethanol.

Samples were then processed on an automatic tissue processor (Tissue Tek VIP E300, Sakura, Torrance, CA, USA) and embedded in paraffin. Pin-treated medial condyles were sectioned first at a 5 μm thickness on an automated rotary microtime (Leica RM2255, Leica Biosystems, Buffalo Grove IL) and placed on 50 mm x 75 mm x 1 mm large format slides. Samples were taken both adjacent and distant to the pin-treated region on the medial femoral condyles. The distance within the tissue blocks was measured for the pin-treated condyles, and slides were made from the same locations in the ESW-treated medial femoral condyle of the contralateral limb within each animal. For control samples, representative slides were taken at 500 μm distances throughout each medial femoral condyle. Sections were stained from all

samples with non-acidified Harris hematoxylin and eosin-phloxine (H&E) using a previously validated protocol.[36] Single sections adjacent from medial femoral condyles with BMLs as observed with MRI were also stained with safranin-O fast green (SOFG) and Masson's trichrome.

3.2.13 Microscopic evaluation of slide samples

Slides were evaluated macroscopically prior to microscopic evaluation. All slides from a single animal (i.e. right and left medial femoral condyles) were evaluated at the same time to account for normal variation between animals. First, slides containing sections with a visible pin tract were identified within a single animal. Following this, slides containing sections of a medial femoral condyle without a visible pin tract were physically overlaid on slides with a visible pin tract from the contralateral limb, in order to define a similar ROI within each condyle. Macroscopic evaluation of paired sections was then performed in order to generalize the extent of change within the osteochondral section. Slides with sections of medial femoral condyles taken from control animals were evaluated completely to be used for comparison.

For microscopic grading, each slide was scanning at 4X magnification to descriptively characterize changes to the articular cartilage, subchondral and trabecular bone. The ROI for microscopic grading was defined as the regions immediately adjacent (i.e. on either side) of the visible pin tract within the field of view at 4X magnification. For those samples without a visible pin tract, the previously identified region corresponding to the pin was used to define a ROI. Pathologic changes observed within the pin tract were not specifically graded unless they extended to the surrounding tissue adjacent to the pin tract.

Osteochondral sections were scored using four previously published or adapted grading scales, predominantly focused on identifying changes within the subchondral bone. The overall appearance of the subchondral bone was graded according to the scheme proposed by Aho et al (Table 3.1).[37]

In an effort to more fully characterized subchondral bone changes within the ROI, an adapted version of the murine semi-quantitative contemporary grading scale was used, as proposed by Nagira et al.[38] In lieu of evaluation of osteophytes, the tissue within the region of interest was graded, in addition to grading of the subchondral bone plate and bone volume (Table 3.2).

Both the sheep and goat[25], as well as the equine[39] Osteoarthritis Research Society International (OARSI) scoring systems were adapted and used in an effort to best describe changes within the subchondral bone. The structural changes (0-10), chondrocyte density (0-4), cell cloning (0-4), and tidemark/subchondral bone (0-3) were graded using the OARSI scoring system for sheep and goats; while the severity of the osteochondral lesion (0-4), degree of subchondral bone remodeling (0-3), and severity of osteochondral splitting (0-3) was adapted from the OARSI scoring system for horses. These OARSI scoring systems were chosen over other histological scoring systems because they have been documented to better designate early stages of osteoarthritis and have been designed for use with sheep tissue, both critical elements for this study (Tables 3.3, 3.4).

3.2.14 Histormorphometry

Sections taken from BMLs in medial femoral condyles of Group C animals stained with Masson's trichrome were assessed for histomorphometry. Histomorphometric measurements

were performed on calibrated digital slide images to quantify the percentage of new bone, background space, and fibrous tissue within the ROI using a commercially-available software (ImagePro, Media Cybernetics, Silver Spring, MD, USA). The a 1 mm^2 square ROI was created for each sample. The ROI square was center on the tissue located 3mm from the junction of the articular cartilage and subchondral bone and 1 mm away from the center of the visible pin tract (Figure 3.1).

3.2.15 Statistical analyses

Descriptive statistics (mean ± standard deviation) were reported in an effort to characterize the apperance of BMLs across timepoints on different imaging modalities and within each sequence on MRI. Categorical data were reported as median ± interquartile range (IQR), and continuous data as mean ± standard deviation. The experimental sample size (4 animals per group) was calculated using G*Power (version 3.1.1).[40] Specifically, an *a priori* power analysis was conducted using expected mean semi-quantitative scores for the apperance of BMLs in treated joints using MRI. This power analysis resulted in an effected size of 1.29, and a power of 0.95, using a 95% confidence interval and a standard deviation of 1 between groups. All data was analyzed using R software (version 4.0.3, "Bunny-Wunnies Freak Out," R Foundation for Statistical Computing 2020) in RStudio (version 1.2.1335).

Continuous data were evaluated for normality using the Shapiro-Wilk test, and visually using quantile-quantile plots. Although data was obtained from a small sample size of animals and normality was difficult to assess, quantile-quantile plots demonstrated minimal to slight departures of the data from normality. Summary statistics were implemented using the psych package for R. A linear mixed model for repeated measures was implemented in the lme4

package for R with animal and limb as random effects, and an interaction between time and treatment was evaluated. Model factors were further evaluated by Tukey-Kramer pairwise comparisons using the lsmeans package for R. In cases where data was non-normally distributed, Friedman's test (for repeated measures) or the Kruskal Wallis test (for single timepoint outcomes) were used followed by Wilcoxon pairwise comparisons with a Benjamini-Hochberg correction in the base package for R for repeated measures analyses. For single timepoint analyses, data were compared using a Wilcoxon signed rank test. A level of $P < 0.05$ was used for significance.

3.3 Results

No complications with general anesthesia, surgery, or imaging were observed, and all animals remained healthy for the duration of the study. On clinical examination, all animals were determined to be normal and free of lameness (grade 0) at baseline, prior to surgery. Results of CT and MRI examinations were considered normal for animals prior to the study. No effect of right vs. left limb were observed for any analyzed outcomes in the study.

3.3.1 Trans-cutaneous extracorporeal shockwave

No skin bruising or other complications were observed secondary to transcutaneous ESW application. Fluid signal consistent with the presence of a BML was not observed on MRI in any of the 18 medial femoral condyles treated with ESW application. No difference in the attenuation of the medial femoral condyle over time was observed on CT, and fluid signal was not observed in the medial femoral condyles treated with ESW on DE CT images. On both μCT and histologic

analyses, no differences were observed in any parameters between ESW-treated medial femoral condyles compared to control medial femoral condyles.

3.3.2 Intra-articular pin application

Two of the four animals in the pin treatment group D had a partial (< 1.1 mm diameter) breach of the articular surface where the end of the Steinmann pin was visible through within the joint. In both cases the articular cartilage in the region of the pin was damaged but still attached. The damaged articular cartilage was gently pressed back into place at the time of surgery to create a smooth articular surface on the distal medial femoral condyle. The MR examination for these two animals were reviewed, but findings were excluded from analysis. All other surgical and post-operative procedures were performed without complication.

3.3.3 Gait evaluation

All animals were determined to be sound at a walk and healthy prior to the start of the study. Two animals displayed grade 1 lameness on the limb treated with pin penetration, visible one week after surgery. The lameness in one animal resolved without further interventions by 3 weeks post-operatively, while the second animal had persistent lameness. Evaluation of the affected joint revealed moderate effusion and cytologic analysis was consistent with suppurative inflammation. This animal was managed with a single dose of intra-articular antimicrobials followed by systemic oral antimicrobial therapy based on bacterial culture and antimicrobial sensitivity evaluation, until her endpoint 4 weeks post-surgery. Images from both of these animals were included for evaluation.

3.3.4 Magnetic resonance imaging

Fluid signal within the bone on MRI was not visible in medial femoral condyles from Groups A (1 mm depth, articular and calcified cartilage layers only) or D (abaxial approach, trabecular bone and subchondral bone plate). Fluid signal within the bone, consistent with a BML, was visible for both Groups B and C. Observed BMLs were largest and persisted in medial femoral condyles from Group C throughout the 12-week study duration.

3.3.5 Magnetic resonance imaging: 1.5 T

Fluid signal within the bone was not visible until 60 days post-injury in the single animal in Group C (8 mm pin depth) imaged using the 1.5 T MR unit. On both PDFS and STIR images, the BML appeared hyperintense relative to the surrounding bone. On PDFS images, the BML encompassed 11% (cranial), 18% (sagittal), and 2% (transverse) of the medial femoral condylar area. On STIR images, the BML encompassed 7% (cranial) and 18% (sagittal) of the medial femoral condylar area. Fluid signal within the medial femoral condyle persisted until the 90-day endpoint, comprising 23% (cranial), 8% (sagittal), and 1% transverse of the medial femoral condyle area on PDFS and 4% (cranial) and 2% (sagittal) on STIR images.

3.3.6 Magnetic resonance imaging: 3 T

Detection of fluid signal was possible using Dixon, PDFS, and STIR sequences on the 3 T MR unit (Figure 3.2). Fluid signal within the bone varied slightly between sequences in the single animal imaged with all fluid-sensitive sequences using the 3T MR unit. For that animal, the percent of the medial femoral condyle with visible fluid was 100% on both cranial and sagittal plane images for all 3 sequences (i.e., Dixon water, PDFS, STIR images) at 2 weeks

post-injury. At 4 weeks post-injury, signal encompassed 100% (cranial) and 96% (sagittal) on Dixon water images; 100% (cranial), 95% (sagittal), and 60% (transverse) on PDFS images; and 100% (cranial) and 70% (sagittal) on STIR images. At 8 weeks post-injury, the percent of the condyle with visible fluid was 77% (cranial) and 47% (sagittal) on Dixon water images; 62% (cranial), 39% (sagittal), and 25% (transverse) on PDFS images; and 54% (cranial) and 37% (sagittal) on STIR images. The overall volume of the BML was largest on cranial plane images compared to sagittal plane images. The largest difference in measured BML volume between fluid-sensitive sequences was observed at 2 weeks post-injury, and over time the BML became more similar.

Fluid signal within the bone, consistent with a BML, was present in the medial femoral condyle of all animals in Groups B and C at MRI evaluation 2 weeks post-BML induction. BMLs appeared as a central region of iso- to hyperintensity surrounded by a region of hypointensity relative to the surrounding trabecular bone on Dixon out phase images. This variation in intensity is reduced on the Dixon in phase images where the BML has a more intermediate intensity that may be isointense relative to the trabecular bone. Distinctions in intensity are all but eliminated on Dixon fat only images where the BML appears as a hypointense region with minimal variation. On Dixon water phase images, the BML appears hyperintense relative to the surrounding trabecular bone. In this experimental model, the most central aspect of the BML appears as the most hyperintense region, relative to the periphery of the BML (Figures 3.3).

Similar to the Dixon water only images, BMLs appear as a hyperintense region relative to the trabecular bone on PDFS images. Experimentally-induced BMLs were also visible on sequences not specific for fluid, with an intermediate intensity on T1-weighted images. Induced

BMLs from this study were also visible on T2-weighted 3D double echo steady state images, and appeared hyperintense relative to the surrounding trabecular bone. Additionally, it was possible to see the surgically-induced defect in the articular cartilage on these images.

For Group B, BMLs were observed in the medial femoral condyle in all animals 2-8 weeks post-BML induction. BMLs were only observed in the medial femoral condyle of one of two animals at 10 and 12 weeks post-BML induction. An increase ($P < 0.001$) in the volume of fluid signal and the percent of the condyle occupied by a BML was observed in medial femoral condyles in Group B and across all MR sequences at 2 weeks post-BML induction, relative to baseline. On cranial and sagittal plane Dixon, water only images, a decrease ($P < 0.05$) in both the volume and occupied percentage of the condyle was observed at 4 weeks, post-BML induction. No change in the volume and percent of the condyle with a visible BML was observed after this time in Group B medial femoral condyles. On PDFS images in the cranial and sagittal planes, no change in the volume or percent of the condyle with a visible BML was observed after 2 weeks post-induction. In transverse PDFS images, a decrease in the volume of the BML was observed at 6 ($P = 0.05$) and 8 ($P = 0.02$) weeks, compared to 2 weeks post-induction.

An increase ($P < 0.05$) in CNR was observed on dorsal and transverse plane PDFS images at 2 and 4 weeks post-BML induction. Average and range of SNR and CNR for Group B medial femoral condyles on Dixon water only and PDFS images in the cranial and sagittal planes are shown in Tables 3.5 and 3.6.

BMLs were present in the medial femoral condyles of sheep in Group C throughout the duration of the 12-week study (Figures 3.4 and 3.5). In the medial femoral condyles for the three animals in Group C with a 12-week endpoint, the fluid signal became more defined in the region of the pin tract, extending proximally from the 8 mm drilling depth (Figure 3.5). At the 12-week

endpoint, the most central aspect of the BML remained hyperintense, and in two cases developed a circular-to-ovoid pattern, similar in appearance to a cyst-like lesion (Figure 3.4). This pattern was not observed in any Group B animals. BMLs had the largest volume and greater percentage of the medial femoral condyle affected at 2 weeks post-BML induction (Table 3.7). Compared to baseline, an increase ($P < 0.001$) in the signal in the medial femoral condyle was visible 2 weeks after BML induction on all MR sequences. On Dixon water only and PDFS images, the volume of fluid signal and the percent of the condyle occupied by the fluid signal decreased at 4 weeks post-BML induction ($P < 0.05$) compared to 2 weeks, and no difference was present when compared to baseline at all imaging timepoints for the remainder of the study (Figure 3.6). On Dixon in phase images, a decrease ($P < 0.01$) in the volume and percent condyle occupied by fluid signal was visible by 6 weeks post-BML induction, but remained increased ($P < 0.01$) relative to baseline measurements for the duration of the study.

Minimal differences were observed when comparing the volume of BML and percent condyle occupied by a BML between fluid sensitive MR sequences at each timepoint. The volume of the BML was larger ($P = 0.05$) on PDFS images compared to Dixon water only images at 6 weeks post-BML induction.

Bone marrow lesion SNRs and CNRs varied widely across the study imaging timepoints. An increase in SNR relative to baseline was observed on Dixon water only images at and 8 ($P = 0.02$) weeks post-BML induction; while an increase in SNR was observed at 2 ($P = 0.03$) and 6 ($P = 0.04$) weeks post-BML induction on PDFS images. A significant or near significant decrease in CNR was observed on Dixon in phase images at 6 and 8 weeks post-BML induction relative to both baseline ($P = 0.06$ for 6 weeks, $P = 0.04$ for 8 weeks) and 2 weeks ($P = 0.04$ for 6 weeks, $P = 0.03$ for 8 weeks) post-BML induction. A significant or near significant increase in

CNR relative to baseline was observed on PDFS images at 2 ($P < 0.01$), 4 ($P = 0.06$), 6 ($P = 0.02$), 8 ($P = 0.03$), and 12 ($P = 0.03$) weeks post-BML induction. Average and range of SNR and CNR for Group C medial femoral condyles on Dixon water only and PDFS images in the cranial and sagittal planes are shown in Tables 3.5 and 3.6.

3.3.7 Computed tomography

Measured attenuation values across medial femoral condyles were not different from one another at baseline. Attenuation values were greater ($P < 0.001$) in medial femoral condyles compared to lateral femoral condyles at baseline across all samples. A time-by-treatment interaction ($P = 0.003$) was observed in the measured attenuation values in the medial femoral condyle. Medial femoral condyles where a BML was present (i.e., Groups B and C) had greater ($P < 0.05$) attenuation values at all timepoints compared to baseline values and medial femoral condyles without a BML present (i.e., Groups A, D, E and F).

Samples from Group B trended toward a significant increase ($P = 0.06$) in the measured attenuation values at 6- and 8-weeks post-BML induction. Attenuation values from Group C samples increased over the course of the study (Figure 3.7). Samples from Group C had an increase in the measured attenuation values at 6 weeks post-BML induction compared to baseline ($P = 0.01$) and the 2-week imaging timepoint ($P = 0.03$). An increase in measured attenuation was also present at 8-weeks ($P = 0.05$) post-BML induction, and trended toward significance at 10 weeks ($P = 0.08$), when compared to the 2-week imaging timepoint.

Bone marrow lesions were successfully visualized on DE CT post-processed reconstructed images with color overlay (Figure 3.8). The region of BMLs were predominantly green, and maintained this appearance across all imaging timepoints. The fluid signal associated

with the BML had a larger area in all planes on fluid-sensitive MR sequences across all timepoints, compared to virtual non-calcium images from DE CT data sets.

3.3.8 Macroscopic examination

With one exception, all femorotibial joints were normal on gross evaluation. The one abnormal femorotibial joint was observed in the animal with the diagnosis of suppurative inflammation. Hypertrophic synovium and a grossly thickened joint capsule were visible within this joint. No evidence of gross articular damage, osteophyte development, abnormal synovium, or other evidence of osteoarthritis was present in the other 17 animals. In the medial femoral condyles of animals treated with pin penetration of the articular cartilage surface (Groups A, B and C), the pin tract was easily identified, and in all cases the articular surface was covered with fibrocartilage.

3.3.9 Cone-beam computed tomography

Dual-energy images generated from CT scan data obtained using a commercially-available veterinary system in the first, *in vivo* phase of work appeared to show the region of the BML, at least in part, when compared to fluid-sensitive MR images. The pattern of calcium-extinguished enhancement appears local to the region of the BML, without similar effects outside of this area (Figure 3.9).

For *ex vivo* DE image reconstruction, osteopenia was visible locally in the region of the BML on virtual monochromatic images acquired using a benchtop CBCT system. This region of osteopenia subjectively corresponded well to the area of the BML on MR images. Images

showed areas of enhanced water content and decreased fat content in the vicinity of the bone loss but was non-specific overall (Figures 3.10, 3.11).

3.3.10 Micro-computed tomography

No differences were observed in trabecular analysis parameters on μCT for samples from Groups A, B, D, E or F. A near-significant increase in trabecular number (mm^{-1}; $P = 0.06$) and connectivity density ($1/mm^3$; $P = 0.06$) were observed for samples from Group C medial femoral condyles compared to control samples (Figure 3.12).

3.3.11 Histological evaluation

On histologic examination of osteochondral sections from medial femoral condyles treated with ESW appeared similar to those of control samples. Osteochondral sections taken from medial femoral condyles in Groups A and D—without visible BMLs—show minimal to mild local inflammatory cell infiltrate and bone remodeling isolated to the area immediately adjacent to the pin tract.

The histologic appearance of the osteochondral sections where a BML was identified on MRI was consistent with a dynamic, active bone remodeling process. At 4 weeks post-BML induction, there was a high degree of inflammatory cell infiltrate within the pin tract and surrounding tissue. Mixed inflammatory cell infiltrate was present in multifocal clusters, subjectively greatest in the samples sacrificed at 4 weeks compared to later timepoints. When visible, the tissue within the pin tract was consistent in appearance with a necrotic sequestrum. This appearance was most clear in the 12-week samples, as sections from earlier timepoints had a central coagulum present filled with amorphous cellular debris. Dense, fibrous tissue was

visible lining the periphery of the pin tract, containing numerous osteoblasts with occasional osteoclasts locally and within the surrounding tissue, indicating processes associated with endochondral ossification (Figure 3.13).

Immediately outside of the pin tract in the surrounding bone corresponding to the region affected by the BML, mononuclear cellular infiltrate was visible, admixed with hyaline and fibrocartilage. The marrow spaces had a "frothy" appearance, indicative of fluid accumulation or edema. Dense fibrous repair tissue was visible along the boundary of the BML toward the periphery of the osteochondral section, which appeared to wall off this region from the surrounding, more normal-appearing trabecular bone. Generally speaking, the distance of this tissue from the visible pin tract correlated to the size of the BML on MRI. Within the BML at all timepoints, there was evidence of newly forming bone and endochondral ossification. In 12-week samples, the amount of dense fibrous tissue was increased relative to samples from 4 and 8 weeks, demonstrating the persistence of inflammation and remodeling within the local tissues, without a substantial histologic improvement over time.

Histological scores of osteochondral sections taken from BMLs in Groups B and C found significant differences between groups and relative to control samples. The overall appearance of the subchondral bone as described by Aho et al, approached significance for both Groups B and C ($P = 0.06$). The thickness of the subchondral bone plate in Group C sections was increased relative to both control ($P = 0.028$) and Group B ($P = 0.035$); while the thickness in Group B was increased relative to control sections ($P = 0.035$). An increase in bone volume/total volume was observed in Group C sections relative to Group B ($P = 0.04$) and control ($P = 0.012$) sections, and in Group B sections relative to control ($P = 0.04$) sections. Tissue change in the region of interest adjacent to the pin tract was different relative to control samples for sections from both

Group B ($P = 0.013$) and Group C ($P = 0.008$), with samples in Group B with increased cartilaginous matrix, and sections from Group C with increased cartilaginous matrix and some evidence of endochondral ossification.

Using the adapted OARSI scoring system, structural changes were visible in both Group B ($P = 0.04$) and Group C ($P = 0.027$) relative to control sections. Changes in chondrocyte density and cell cloning were not different in either group compared to control samples. Duplication of the tidemark as well as the presence and penetration of blood vessels in the subchondral bone plate were visible on Group C sections ($P = 0.03$) relative to control samples. Degenerative osteochondral changes, remodeling of the subchondral bone, and osteochondral splitting were all increased in Group C sections ($P = 0.02$) relative to control samples. Group B sections had increased osteochondral changes ($P = 0.026$) and subchondral bone remodeling ($P = 0.035$) relative to control samples. All observed changes were consistent across both H&E and SOFG-stained sections (Table 3.8).

3.3.12 Histomorphometry

Medial femoral condyles from the sheep in Group C euthanized at 4 weeks had 38% bone and 43% fibrosis in the ROI. The sample from the 8-week sacrifice timepoint contained 21% bone and 44% fibrosis in the ROI; while the average of the remaining four samples from the 12-week sacrifice timepoint had an average of 16.75% bone and 73% fibrosis. Histomorphometric analysis identified a decrease ($P = 0.04$) in the percentage of bone between the 4-week and 12-week timepoints.

3.4 Discussion

Experimental induction of BMLs is possible using the ovine medial femoral condyle through an acute osteochondral defect from the articular cartilage surface extending into trabecular bone. Importantly, this work suggests that the depth, not the size, of the osteochondral defect may be the most important factor to distinguish BMLs and predict the persistence of these lesions within the bone. Experimentally-induced BMLs were visible within 2 weeks of surgery using high-field MRI, and imaging characteristics are similar in appearance to what is observed in clinical cases across species. Volumetric imaging modalities of CT and MR provided similar and complimentary information about physiologic and structural changes to the subchondral and trabecular bone, supported through histological assessment of tissues. This model demonstrates that BMLs are dynamic and change over time, and their presence incites modification to the subchondral and trabecular bone without degeneration of the overlying articular cartilage. Validation of this model enables further research in this field to understand how these lesions may contribution to the degeneration of the joint.

Direct trauma to the osteochondral tissues appears to be a prerequisite for development of a BML. Although BMLs are frequently observed following an acute trauma,[41,42] they have also been observed in scenarios of chronic repetitive trauma or overload.[43,44] ESW application at 10,000 pulses was meant to replicate a scenario of chronic repetitive overload, however BMLs were not observed at any timepoint across the study. Ironically, within the past few years there have been an increased number of studies published evaluating the use of ESW to treat BMLs.[45–51] ESW is widely used with positive outcomes in the clinical treatment of numerous musculoskeletal disorders,[52] however the exact mechanism by which ESW operates is still unknown. ESW produces an acoustic wave that mechanically produces energy through the rapid

compression of a medium caused by vibration and high-speed motion.[53] ESW is believed to work mechanically, thermally, through cavitation, and biologically—including effects on bone metabolism. Biological effects include activation of cellular repair including neovascularization, vascular dilation, and tissue regeneration, expression of angiogenic growth factors, analgesia related to nerve end blockage, and inflammation and infection control.[53–61] In cases of osteonecrosis, ESW is believed to promote blood supply and bone regeneration, alleviating some of the pain response associated with this condition.[47] Unless this increase in blood flow is variable, species-specific, and transient, the findings from this study do not direct support an increase in blood supply within the bone. Furthermore, increased attenuation measurements and alterations in trabecular bone were not observed on computed tomographic modalities which contradicts reports that new bone formation is related to the energy dose during ESW application.[62] Observed differences in this study may have been due, at least in part, to the fact that the density of cortical bone is higher in sheep compared to humans,[63] and that the tissues overlying the stifle joint are thicker in the sheep than in the human, rendering ESW waves less effective in their penetration through bone. Alternatively, the ESW waveform may be ineffective in inciting subchondral and trabecular damage. A shorter pulse with a higher peak pressure, such as what is observed with shockwave lithotripsy[64] may be an alternative to investigate whether an acoustic shock wave is a viable method for induction of BMLs.

Focal, direct damage to the osteochondral tissues proved to be a consistent and reproducible method for experimental induction of BMLs in the medial femoral condyle. Damage to the cartilage layers or bone layers alone was insufficient to generate fluid signal on MRI, emphasizing the integrity of the cartilage-bone interface is critical in the pathophysiology of BML formation. The depth of injury to the subchondral bone plate is also predictive—at least

to some extent—for the persistence of BMLs. In limbs where damage did not extend beyond the subchondral bone plate (Group B), BMLs were present but regressed over time. This same pattern of regression of BMLs has been observed clinically,[65] and the ability to predict the behavior of the BML (i.e., growth versus regression) remains clinically challenging in effectively prognosticating these lesions. Results from this study would suggest that BMLs that regress may have incomplete damage to the depth of the subchondral bone plate but damage does not extend into the trabecular bone. Conversely, BMLs that persist, or even progress, may be the result of damage extending from the articular surface into the trabecular bone. If this is the case, it is likely that this damage to varying depths from the articular surface is microscopic, and the 1.1 mm Steimann pin used here is a gross exaggeration of naturally-occurring lesions. Nevertheless, the findings here would support the conclusion that variation in the depth of osteochondral damage may be related to the behavior of BMLs over time.

An *in vivo* experimental model for BMLs has been recently described in rabbits that further support the theory that extension of microdamage through all tissue layers is an inciting cause of BMLs. In the experimental model described by Matheny et al, mechanical loading following implant placement was used to create microdamage in the epiphyseal cancellous bone.[66] Fluid signal within the epiphyseal bone was diagnosed 1-2 weeks following mechanical loading and was confirmed using both STIR and T1-weighted sequences on high-field MRI. The epiphyseal location for implant placement here lacks articular cartilage, but 1.5 mm and 2 mm diameter orthopedic screws were used, extending from the bone surface into trabecular bone. The observed fluid signal within the bone was relatively small and present in both loaded and non-loaded limbs, suggesting fluid signal within bone may be part of the normal inflammatory

response.[11] Additionally, the limited time course of the study makes it challenging to assess the clinical validity of this model.

The specific pathogenesis of how a BML is formed following osteochondral trauma has not been fully clarified by this model. Current theories on BML formation focus on either an "outside-in" invasion of the marrow spaces by inflammatory cells and synovial tissue or an "inside-out" gradient of BMLs in the bone and marrow space affecting the surrounding tissues, including cartilage and synovium.[10] It is certainly also plausible that both of these theories are at work concurrently to allow for the persistence of a BML over time. In response to injury, many pro-inflammatory factors may be activated, including those found perpetually in the joint. For example, glycosaminoglycan hyaluronan (HA) polymers are rapidly metabolized following trauma to the joint, resulting in an increase in local HA production.[67–69] Extracellular hyaluronidases, reactive oxygen species, and mechanical shearing are all responsible for HA fragmentation, followed by binding to HA receptors to initiate tissue clearance.[70,71] Small HA fragments have been shown to elicit various pro-inflammatory responses, including CD44 and Toll-Like Receptor 4 activation, which in turn stimulates and perpetuates inflammation through NF-κB activation.[72,73] The pin tract used to create a focal osteochondral defect in this model provides an ideal conduit for synovial fluid access to the subchondral and trabecular bone, and which do not normally contact one another. Although the pro-inflammatory effects of HA have not been evaluated in the subchondral and trabecular bone, it is reasonable to postulate that similar pro-inflammatory effects may be expected. Degradative products of HA have been shown to perpetuate inflammation via synovial fibroblasts in rheumatoid arthritis (RA), and the high level of fibroblasts observed histologically within these experimental BMLs may suggest a similar mechanism of action for these lesions. In opposition to this theory, would be the fact that

the pin tract is rapidly covered by fibrocartilage at the articular surface, which is less stiff than bone but behaves as a viscoelastic solid under weight-bearing conditions and likely limits fluid exchange.[74] Undoubtedly, further work would be needed to substantiate such hypotheses moving forward.

A commonly discussed feature of BMLs across conditions is pain,[11,75,76] however limited reports also discuss that BMLs may be asymptomatic.[44,77,78] Pain related to BML is hypothesized to be the result of irritation secondary to increased intraosseous pressure or disruption of sensory nerves within the neurovascular bundles of the bone marrow.[79] Increased intraosseous pressure occurs because of fluid accumulation, either due to capillary leakage secondary to local modification of the capillary wall, or secondary to increased vascular pressure which may be hyperemic (i.e., due to an increased blood flow to the marrow) or congestive (i.e., from a decrease in clearance from the marrow tissue). These theories rely on evaluation of the bone as "closed" system, where there is not an opportunity for fluid egress from within the trabecular bone. The pin penetration model described here for BML induction may have created an "open" system from the trabecular bone into the joint; however, characterization of fluid flow would be required to corroborate this theory. It is unclear if this small tract is sufficiently large to provide pressure relief, but it could be possible. In some cases, core decompression techniques are used to alleviate pain, which include drilling directly into the BML.[80,81] The technique used in this study may mimic this technique, creating a BML while also alleviating pain associated with pressure change within the bone. It is also possible that the clinical assessment method used in this study was not sufficiently sensitive to detect the presence of mild pain.

It is also possible that asymptomatic cases of BMLs are a different clinical manifestation of this condition all together. In what seems contradictory, BMLs have been described as an

incidental finding and have been proposed as a non-specific response to mechanical stress incurred during activity or exercise.[43] This theory has been proposed in the case of BMLs observed in the distal limb of sport horses.[78,82,83] In these cases BMLs may be transient, representing influx of factors associated with purposeful changes in the architecture of the subchondral and trabecular bone. It would follow then that persistence of a BML may represent ongoing remodeling or inflammation, especially in cases where activity demands exceed the rate of remodeling of the subchondral bone. Further work would be needed to confirm these theories, as much of the data presented in both human and equine athletes represent imaging assessment at a single timepoint and lack histological data.

Arguably one of the most important aspects of this study was in the evaluation of how BMLs change over time. The costs and restricted access to MRI limit the ability to follow changes in BMLs over time in the clinical setting, which was a substantial advantage of this study design. BMLs are highly dynamic with changes in the appearance and volume as detected by MRI every two weeks. A 50-80% reduction in the volume of fluid signal was observed in limbs in Group C at 12 weeks, compared to measurements taken at 2 weeks. Although changes in the volume of fluid signal is conventionally represented through the validated whole-organ magnetic resonance imaging score (WORMS) system,[84] providing the raw values for the percentage of the bone affected seemed a more poignant method to demonstrate the change in volume over time.

From a clinical perspective, the variability in the appearance of the BML and relatively rapid change in volume over time solidifies the clinical challenge in interpreting and prognosticating about BMLs from a single imaging assessment.[85,86] When serial assessment is available, there is strong data to confirm that enlargement of a BML is a negative prognostic

indicator for cartilage loss and ultimate development of OA, and the severity of the BML has a positive association with the need for joint replacement in humans.[87–89] Many of these longitudinal studies have utilized STIR sequences for evaluation of fluid signal, and results from this study demonstrate the importance of sequence selection in detection of bone fluid signal. As discussed in Chapter 2, standard parameters for the STIR with a 1.5 T MR unit may under-represent the actual volume of fluid signal present within bone. The limited contrast and overall image quality inherent to STIR sequences has been recognized to limit detection of clinical BMLs.[90] Chemical-shift imaging (CSI), specifically the Dixon sequence, is a reliable method of assessment of BMLs, with numerous publications describing its value for musculoskeletal imaging.[91,92] These sequences utilize different approaches to fat suppression, STIR utilizes an inversion-based method, whereas the Dixon sequence is focused on chemical-shift based techniques. The term "chemical shift" refers to the difference in resonance frequencies, or spin rates, between protons of fat molecules and water (or non-lipid) molecules when placed in a magnetic field.[93] When scanning a region of interest, two image sets are acquired using slightly different TEs. One TE will acquire fat and water signal out-of-phase, and then the TE is adjusted (1.1 ms at 3 T[94]) and fat and water signals are acquired in phase. For in phase images, the signal received from fat and water protons in the same voxel are additive (water + fat); whereas they partially cancel each other out in out-of-phase images (water – fat). Out-of-phase images then appear darker compared to in phase images. Post-processing water only and fat only images can be created by adding (water only) or subtracting (fat only) the signal intensity from in phase and out-of-phase image sets; creating a total of 4 images for evaluation.[95] Distinct water and fat images are helpful in diagnosis and characterizing BMLs, however it is essential to be aware that changes in scanning parameters and the so-called "fat-water swapping artifact" (i.e., when field

heterogeneity results in incorrect determination of whether a voxel contains water or fat) can influence in final image produced. This study demonstrates the benefits of the Dixon sequence over the conventional STIR sequence for detection of fluid signal within bone, helping to characterize, at least in part, the changes in composition of BMLs over time.

In addition to sequence, magnet strength also impacts fluid detection.[90] Although the pin depth was the same, the detection of fluid signal as demonstrated by the percentage of the condyle with visible fluid signal, was greater with the STIR sequence on the 3 T unit compared to the 1.5 T. Higher SNRs and CNRs are well-reported with higher magnet strengths, enabling superior detection of anatomic detail.[41,96,97] Objective assessment of SNRs and CNRs were not performed between 1.5 and 3 T units in this study, but subjective evaluation is consistent with a superior image quality with a 3 T magnet strength across all sequences.

The volume of fluid signal observed in this study decreased over time on Dixon water only and PDFS image, however volume measurements remained relatively consistent on Dixon in phase images. Considering the MR and histologic data in tandem, there appears to be a change in the composition of tissues within the BML over time. In the immediate period following BML induction, hemorrhage and edematous fluid accumulate within the adipose tissue, as observed on the histological sections taken from the 4-week endpoint. This influx of fluid corresponds to the largest volume of fluid signal on both Dixon water only and PDFS MR images. Over time, the volume of fluid decreases, and in histologic sections from 8- and 12-week endpoints there is a greater proportion of fibrotic, myxomatous tissue and sclerotic bone. This corresponds to a relative decrease in the volume of the fluid signal on Dixon water only and PDFS MR images, and a larger volume on Dixon in phase images, which represent the MR signal of both fluid and fat, consistent with the composition of the observed tissues. The degree of inflammatory cell

infiltrate reduced by 12 weeks, transitioning to a high proportion of fibroblasts concentrated centrally within the BML. The formation of a necrotic sequestrum associated with the pin tract, in conjunction with peripheral sclerotic both and fibrotic tissue associated with the BML may create local tissue hypoxia precluding resolution of this lesion. These findings are characteristic in cases of chronic, non-healing wounds.[98] It is therefore then not surprising that clinical reports of clinically significant BMLs have found that <1% of patients show a decrease in BML size after 30 months.[7] These data reinforce that the absence of fluid signal on MRI does not necessarily equate with resolution of a BML, but rather may represent the transition in the characteristics of the tissue. If BMLs impair blood flow or cause an increase in intraosseous pressure, local tissue hypoxia, avascular necrosis, and fibrotic inferior repair tissue may chronically persist in these lesions over time. The use of additional sequences, such as the Dixon sequence on high-field MR can provide additional insight about the tissue composition within a BML which varies over the age of the lesion.

In addition to MRI, DE CT has the ability to provide information on the tissue characteristics of BMLs.[99] Images were acquired using tube voltages set to maximum the difference in attenuation and minimize the overlap in the spectral properties between tissues.[100] Post-processing of sequentially acquired CT data was directed at maximizing the fluid signal within the bone in the region of the BML. The images produced we able to detect fluid signal within the bone of experimentally-induced BMLs, but the volume of fluid signal was less than what was observed with MRI. These differences in volume detection between CT and MRI have been reported in previous studies.[101] There are a number of explanations for why this difference in volume may occur. First, bone sclerosis has been shown as a pitfall of the virtual non-calcium technique in the ankle.[24] Bone sclerosis can affect the CT numbers, causing both false positives

and false negatives. In this study, local sclerosis within the region of the BML was observed 6-8 weeks after surgery, however the discrepancies in BML volume were observed immediately at 2 weeks after surgical induction. A second challenge is that discrimination of water and fat tissue is inherently challenging given their proximity of attenuation values—fat ranges from -30 to -70 HU, pure water is 0 HU.[102] A higher energy separation (i.e., 60 kVp and 140 kVp) with the use of appropriate filters, settings and kernels, careful calibration of the scanner against known tissue phantoms, and the use of dual-source scanners that are highly specialized for DE imaging, are all utilized for production of the most ideal final image. In the limited number of published studies using DE CT for detection of BMLs[23,101,103–105], the emphasis has been placed on the ability of DE CT to detect the presence of a BML, more than the volume of BML detected. Across these studies, the sensitivity for BML detection with DE CT ranges from 60-100%, with increasing sensitivity in more severe cases.

Published studies have utilized conventional fan-beam CT for implementation of a DE technique, however limited results from this research suggest a DE technique may also be possible with CBCT for detection of BMLs. CBCT units are being used with an increasing frequency for musculoskeletal imaging[27,106,107], with advantages of rapid scan times, decreased radiation exposure to the patient, and the ability to produce images with high spatial resolution that increase diagnostic confidence for clinicians. Although the region of the BML was identifiable on DE images generated from data acquired using a commercial unit, the BML area was reduced and the overall image clarity was fair. In comparison, DE images generated using a purpose-built benchtop unit demonstrated improved detail, but enhancement in the region of the known BML was highly non-specific. One substantial advantage of the composite images is the generated image is sharper in appearance. By generating the three tissue fractions, and then

generating a new image with those known attenuation values for each voxel, an image is created that resembles a standard CT image, but is done so without beam hardening artifacts, improving the overall quality of the image. In this study, the lack of specificity in the region of the BML is due to non-uniformities inherent in CBCT, in particular, scatter and off-focal radiation. Further development is needed in this area combining CBCT technology with a DE technique. In principle, a DE technique with serial CBCT imaging in the human or veterinary patient affords numerous opportunities for enhanced monitoring of pathologic changes within the bone, such as BMLs, helping to better inform and prognosticate clinical management of these lesions.

In addition to generation of DE images, conventional grayscale morphologic CT data has been evaluated for diagnosis of BMLs. In comparing qualitative DE CT maps, efforts have been made to create a more qualitative method for assessment and diagnosis of BML using CT attenuation Hounsfield Units. Guggenberger et al focused on defining specific cutoff values for different bones of the ankle, while Foti et al specified a single cutoff value between bone with and without a BML.[24,108] Averaging the defined cutoff values for BMLs between these two studies, a difference between normal bone and bone with a BML is ~60 HU. Although these studies attempt to differentiate BMLs following acute (i.e., BMLs appearing in the immediate post-traumatic period) and chronic trauma (i.e., cases where symptoms were present for ≥6 months prior to BML diagnosis), the conclusions from these studies focus on an assessment of CT imaging at a single timepoint. The imaging performed in this study demonstrates how BMLs change over time, and even though a BML is present 2 weeks after surgery, a difference of 60 HU was not observed within a medial femoral condyle with a BML until 6 weeks post-surgery, as compared to baseline. Given the dynamic nature of BMLs observed through serial imaging, it is challenging to accurately define a specific difference in HU that definitively indicates the

presence of a BML, especially in the immediate period after a traumatic injury. Although there were some further changes in CT attenuation values after 6 weeks, overall, attenuation values were fairly consistent for the remaining 6 weeks of the study. Although the small number of samples and different anatomic location for this study make it inappropriate to draw broad conclusions, it does seem possible that the BMLs identified in these clinical studies were actually older than originally assumed. Additionally, it is essential to also recognize that patient- and CT scanner-related factors, including beam hardening, scatter, reconstruction artifacts and patient positioning, may have not been controlled over time,[109] influencing the observed results from this study and within the published literature.

CT evaluation of limbs with BMLs also demonstrated the presence and trajectory of structural changes within the trabecular bone. The pin tract was readily visible on multi-planar reconstruction CT images in Groups A-D. The increase in attenuation surrounding the pin was grossly visible, with decreased distinction of individual trabeculae immediately adjacent to the pin tract. BMLs have been reported to increase local bone density,[110] which likely occurs secondary to the local remodeling processes observed histologically in this study. The difference in attenuation changes between medial femoral condyles in Groups B and C emphasizes how even a minor defect extending from the articular surface through the subchondral and into the trabecular bone can have a long-term impact and promote bone remodeling. In almost all medial femoral condyles in Group C, remodeling around the pin tract created the appearance of an osseous cyst-like lesion by 12 weeks post-surgery. The relationship between BMLs and subchondral cysts in humans has previously been described, determining that the majority (up to 92% in one study[111]) of subchondral cysts form in areas where BMLs were previously observed.[13,86,111–114] Even in cases where cysts were not distinctly visible, subchondral bone

attrition, or the flattening or depression of the articular surface, has also been described with BMLs.[115] The direct relationship between subchondral cysts and OA has yet to be fully elucidated[86], however, structural changes secondary to the presence of BMLs appear to represent an irreversible progression of change to the subchondral bone, ultimately altering the normal mechanical properties of the bone and joint.

Innate differences are present in the attenuation of the medial and lateral femoral condyles of the sheep. This finding is not entirely surprising, as equal weight-bearing is not assumed across the femorotibial joint. More interesting is that changes in the attenuation secondary to BMLs are isolated to the medial femoral condyle, and attenuation remains relatively consistent in the lateral femoral condyle over the 12-week study period. These changes in attenuation in the medial femoral condyle are further defined through μCT analysis with a nearly significant increase in trabecular number and connectivity density adjacent to the pin tract over time. These are indirect indices to interpret bone stiffness, which displays increasing strength and stiffness adjacent to the pin tract over time.[116,117]

Active remodeling processes within the subchondral and trabecular bone do not equate with changes in the joint environment as whole. The pin tract on the articular surface of medial femoral condyles from Groups A, B, and C, was covered with fibrocartilaginous tissue by 4 weeks after surgery with an overall quiescent joint environment, despite the ongoing presence of BMLs within the subchondral bone. The articular cartilage surrounding the focal, full-thickness pint tract also grossly and histologically overall appeared normal, even after 12 weeks of an active BML in the subchondral and trabecular bone. Currently, BMLs and changes in articular cartilage morphology are assumed to exist in tandem, but findings from this study demand reassessment of this paradigm. As it stands, “early OA” in the knee joint is currently defined by

the following 3 criteria: (1) pain, (2), Kellgren-Lawrence grade 0-1 or II (osteophytes only), and (3) arthroscopic cartilage lesions or MRI findings demonstrating cartilage or meniscal degeneration and/or subchondral BMLs.[118–121] It stands to reason then that the criteria used to define early OA may actually represent a much later stage of disease, likely after irreversible change has occurred within the osteochondral tissues. This study would suggest that joints with clinical pain and effusion, where BMLs are visible on MRI, and cartilage morphology is abnormal have lesions that are well-over 12 weeks in age. The time course to irreversible changes in the osteochondral tissues to not well-defined at present, but undoubtedly earlier management of pathologic lesions is ideal.

At present, the histological evaluation of subchondral bone is inadequate. Subchondral bone changes are assessed in relation to changes in the articular cartilage, and fail to capture the more subtle or early changes within this tissue. This may be due, at least in part, to the fact that subchondral bone does not always follow a predictable pattern of change across all diseases and conditions. Multiple grading rubrics were modified and utilized in this study in an effort to more completely capture the degree of change within the subchondral bone secondary to BMLs. The most pronounced changes in the subchondral bone and trabecular tissues were visible immediately adjacent to the pin tract, but more subtle changes were visible distant to the pin tract, and even toward the periphery of the osteochondral sections. The combination of H&E, SOFG, and Masson's trichrome stains were used in this study for complimentary histological assessment and basic histomorphometry. It is likely that the small number of samples in this study limited the statistical detection of differences between timepoints. However, evaluation and descriptive characterization of samples identified a high proportion of changes within the subchondral bone over time. The ample proportion of monocytes, osteoblasts, and fibroblasts

provide evidence for both a marrow-derived local and systemically-mediated coordinated response to the BMLs within the distal femur. Inflammatory tissue associated with OA tends to be fibrovascular, with more scare cellular infiltration, which may be due (at least in part) to excessive biomechanical loading rather than inflammatory cell alterations.[12,14] However, similar histologic characteristics of the bone have been observed in BMLs in patients with RA, suggesting potential similarities across conditions.[122–126] In RA, BMLs are characterized by a large proportion of macrophages, plasma cells, CD8+ T cells, and B cells.[127] Immunohistochemical evaluation of both samples from patients with OA and from this model are needed to enable greater insight about the cellular similarities of BMLs across conditions.[128–130] Additional methods such as quantitative histopathology of bone[131], transcriptomics[132], and proteomics[133] have been used for evaluation of BMLs and should be considered as work in this area moves forward.

Development of an experimental model for BMLs has provided exciting insight into the complexities of this condition. Strengths of this experimental model include the fact that the ovine femorotibial joint is a well-validated preclinical model for the human knee, with similarities in bone structure and bone remodeling processes.[134] The use of skeletally-mature animals for BML induction is similar to what has been observed clinically in humans[6,11,15,16] and veterinary species,[2,3,135–137] reinforcing the applicability of these data. Although sufficient sample numbers were used based on an *a priori* power calculation, it is likely that limited numbers prevented all trends from being statistically elucidated. An *a posteriori* power calculation using trabecular analysis data from μCT determined a total of eight animals would be required to adequately discern differences secondary to BMLs. Further refinement of the described model would also be beneficial to more closely recapitulate naturally-occurring BMLs. An open

approach to the joint for pin penetration raises concerns that a mild synovitis may also be induced, which may accelerate changes within the bone. The majority of clinical reports on BMLs stemming from a traumatic etiology discuss the relationship of these lesions to OA. Although this model confirms that BMLs can exist in the absence of other degenerative changes to the articular cartilage or joint, longer-term follow-up data is needed to evaluate whether degenerative changes occur within the femorotibial joint. Imaging and histologic comparison of osteochondral samples from this model and naturally-occurring BMLs are required to ensure the validity and applicability for this model moving forward.

The clinical association between BMLs and a wide variety of inflammatory and non-inflammatory conditions of the joint emphasizes the importance for the development of an experimental model. The results of this study demonstrate that a consistent, reproductible experimental model for BMLs is possible through focal, direct trauma through the articular surface, extending into trabecular bone. Newer, non-invasive imaging techniques, such as the Dixon sequence with high-field MRI, and DE CT facilitate a more comprehensive evaluation of BMLs *in vivo*, elucidating the dynamic nature of these lesions. Changes within BMLs on MRI are paralleled by changes in the histologic appearance of the bone and local tissues. Similarities between experimentally-induced BMLs and limited data in other rheumatologic conditions suggest similarities may exist, but further work is needed to confirm these suppositions. The exact role that BMLs play in joint injury and health is still unclear, however, the importance in evaluating changes within the subchondral bone—especially those that may precede changes in the articular cartilage—is strongly affirmed through this work.

3.5 Figures

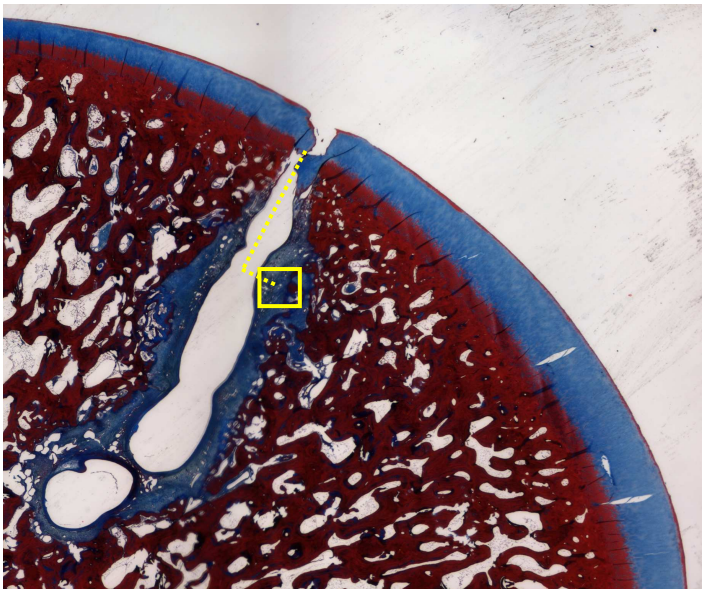

Figure 3.1 – Digital image of a representative histologic section stained with Masson's trichrome in the sagittal plane through an osteochondral region of the medial femoral condyle in surgically-induced bone marrow lesion using a 1.1 mm Steinmann pin advanced to an 8 mm depth. This sample is from the 12-week sacrifice timepoint. The region-of-interest (ROI) box (outlined in yellow) was centered 1 mm adjacent to a region 3 mm deep from the junction of the articular cartilage and subchondral bone, relative to the center of the pin tract (yellow dotted lines). Measured parameters included the amount (%) bone, fibrous tissue, and "background" within each ROI.

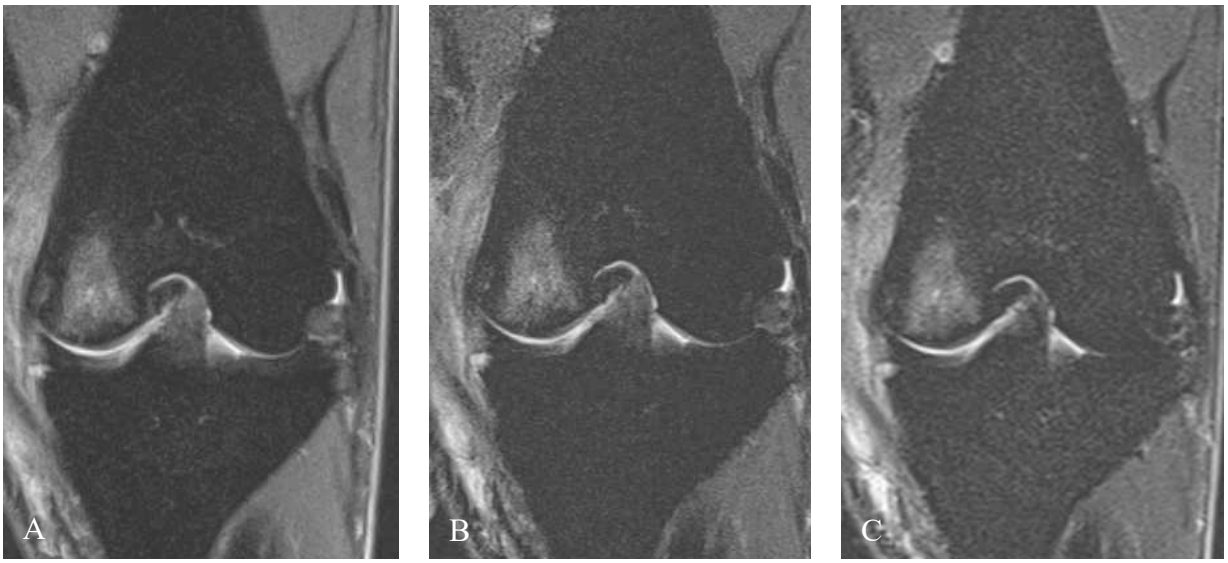

Figure 3.1 – Cranial plane images demonstrating the appearance of fluid signal across fluid-sensitive sequences on magnetic resonance imaging in a single animal at 2 weeks post-injury. Fluid-sensitive sequences include (A) Dixon, (B) proton density fat suppression (PDFS), and (c) short tau or short TI inversion recovery (STIR) sequences. The hyperintense region in the medial femoral condyle is consistent with a bone marrow lesion.

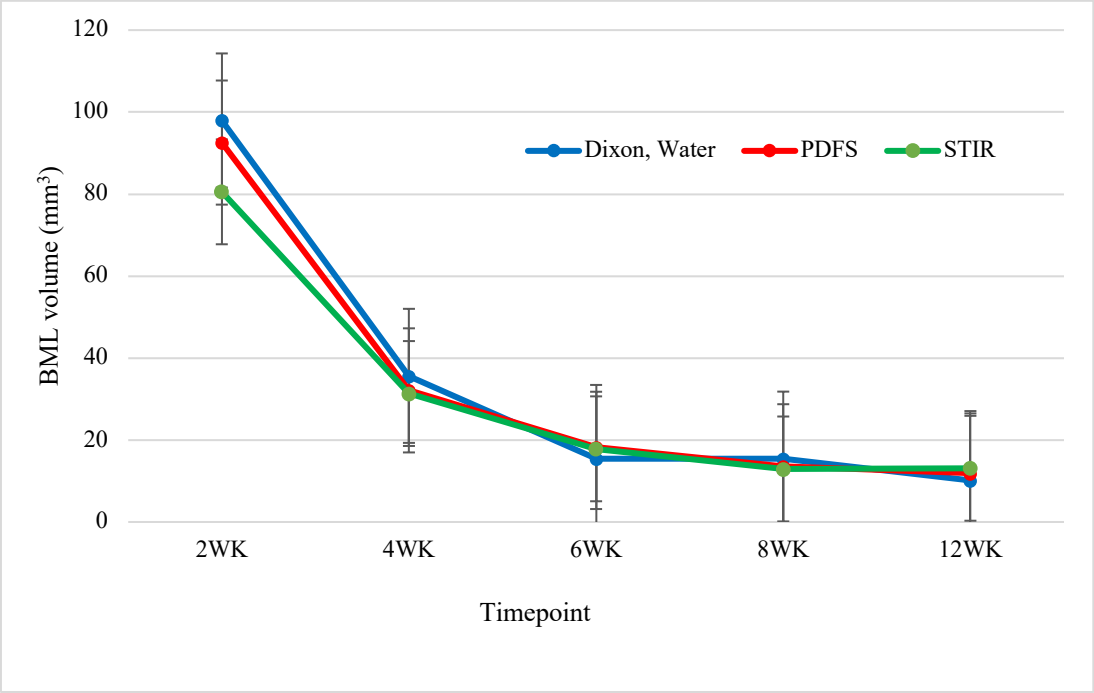

Figure 3.2 – Measured volume (mm^3) ± standard error for volume of observed bone marrow lesion in the medial femoral condyle of a single sheep between fluid-sensitive sequences using a 3 T magnetic resonance imaging system across 12 weeks. Slight differences were observed in the measured volume between fluid sensitive sequences at two weeks post-injury, but the observed differences between sequences are minimized over time. Fluid-sensitive sequences include Dixon, water only, proton density fat saturation (PDFS), and short tau or short T1 inversion recovery (STIR) sequences.

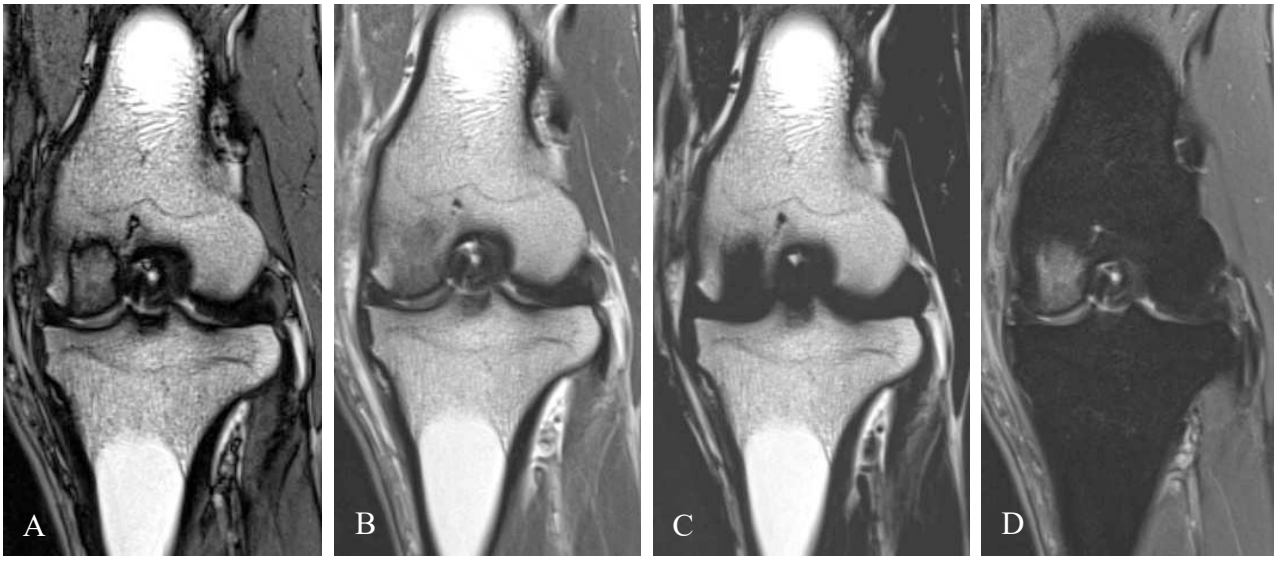

Figure 3.3 – Images obtained using magnetic resonance (MR) imaging of an experimentally-induced bone marrow lesion in the medial femoral condyle two weeks post-injury. This bone marrow lesion was induced by advancing a 1.1 mm Steinmann pin from the articular surface of the medial femoral condyle to a depth of 8 mm, through the articular and calcified cartilage, subchondral bone plate and into trabecular bone. MR images are the same slices from the four-point Dixon sequence, including (A) out of phase, (B) in phase, (C) fat only and (D) water only images.

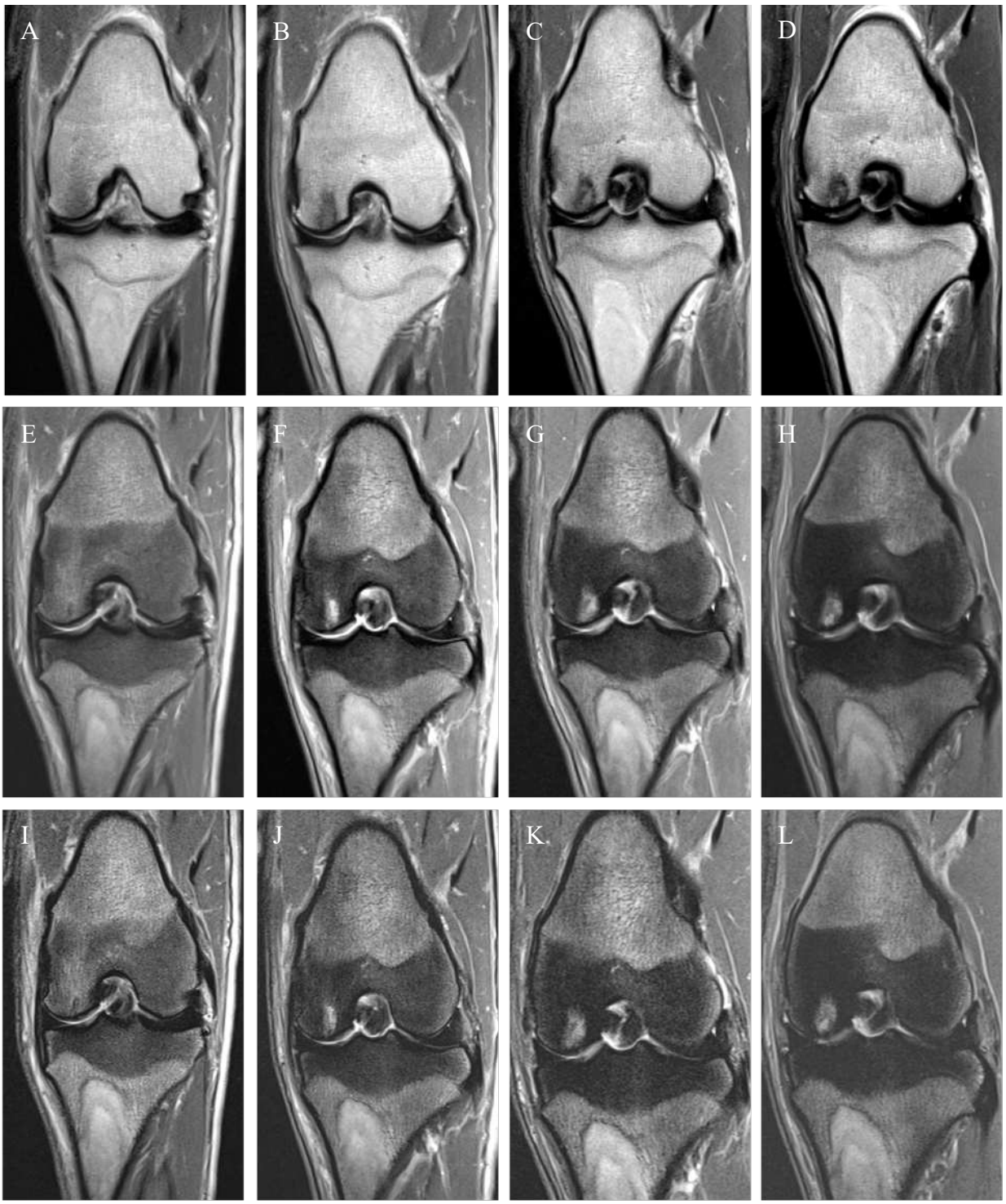

Figure 3.4 – Serial cranial plane magnetic resonance images of an experimentally-induced bone marrow lesion (BML) in the medial femoral condyle of a single animal. (A-D) Dixon in phase sequence images; (E-H) Dixon water only sequence images; (I-L) proton density fat saturation (PDFS) sequence images. Each column represents a different imaging timepoint. From the left, images in the first column are at 2 weeks post-BML induction; second column at 4 weeks; third column at 8 weeks; and fourth column at 12 weeks. A cyst-like lesion is visible in the medial femoral condyle of this limb by the end of the study.

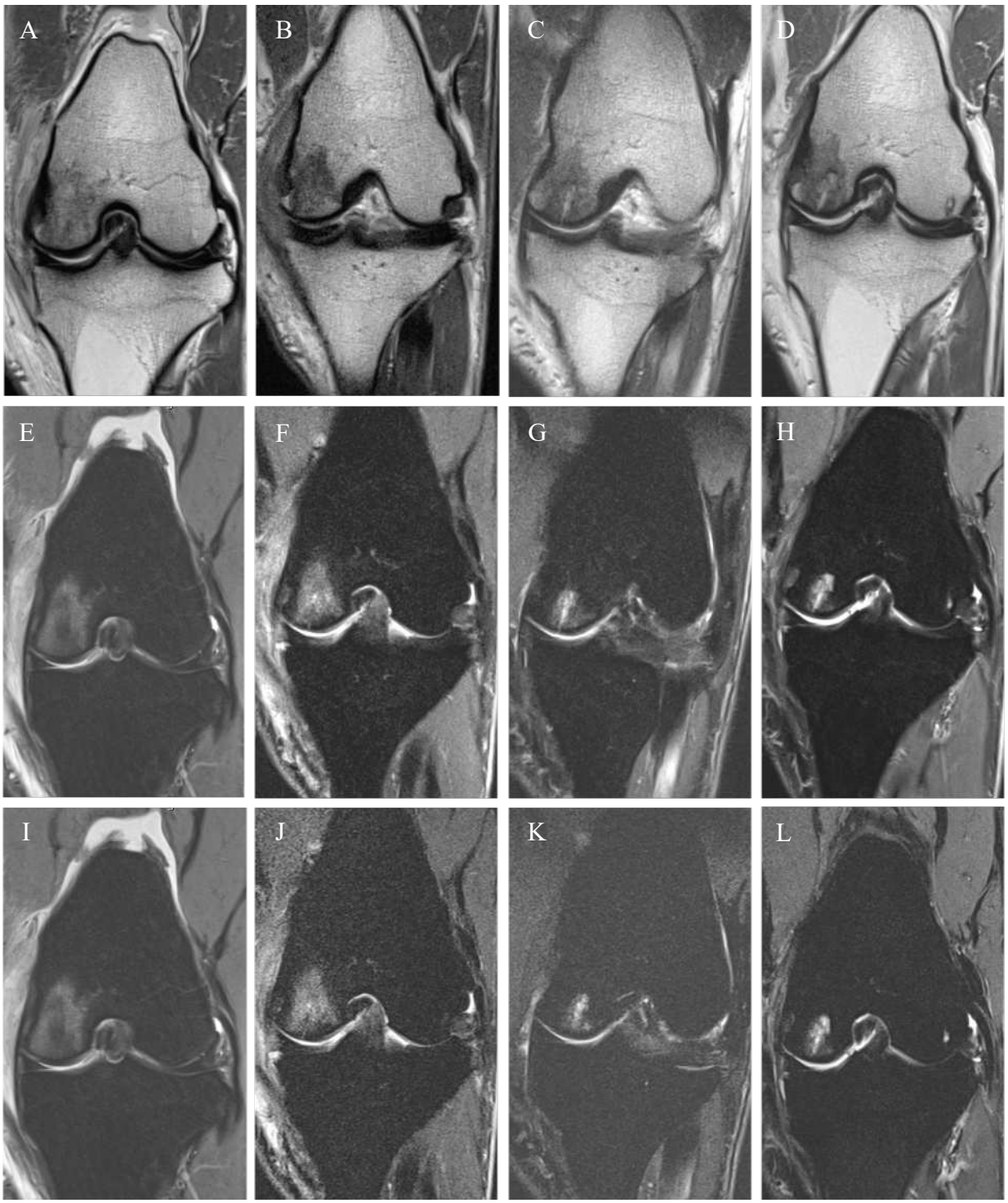

Figure 3.5 – Serial cranial plane images of an experimentally-induced bone marrow lesion (BML) in a single animal from various sequences on magnetic resonance imaging (MRI). (A-D) Dixon in phase sequence images; (E-H) Dixon water only sequence images; (I-L) proton density fat saturation (PDFS) sequence images. Each column represents a different imaging timepoint. From the left, images in the first column are at 2 weeks post-BML induction; second column at 4 weeks; third column at 8 weeks; and fourth column at 12 weeks. A linear hyperintensity persists in the original region of the pin tract, extending beyond the 8 mm drilling depth.

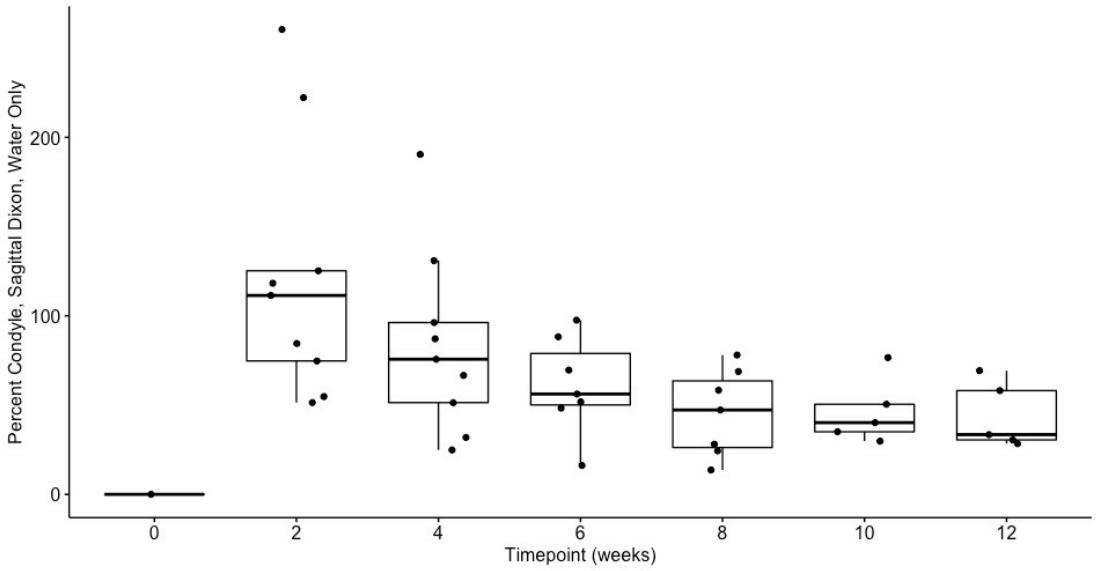

Figure 3.6 – Boxplot of mean and interquartile ranges (IQR) for the percent of the medial femoral condyle occupied by the experimentally-induced bone marrow lesion (BML) on Dixon sequence water only images in the sagittal plane. At two weeks post-injury, over 100% of the medial femoral condyle is occupied by the BML. The BML decreases in size over time for the first 6 weeks following injury and then appears to stabilize after this time for the duration of the 12-week study.

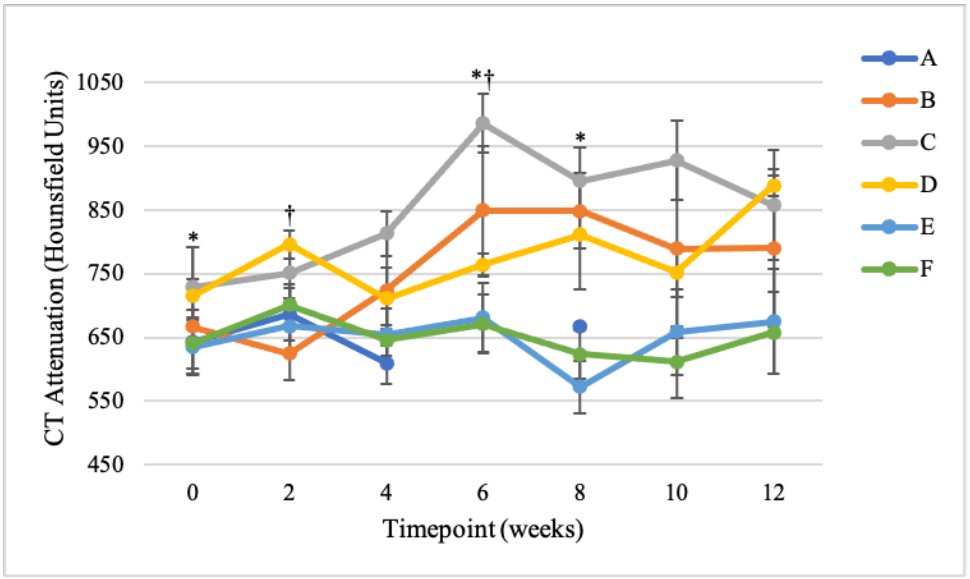

Figure 3.7 – Mean ± standard error for measured attenuation (Hounsfield Units) on computed tomography in medial femoral condyles from all treatment groups (Groups A-F). For Group C samples, an increase in attenuation was visible at 6 and 8 weeks after experimental induction of BMLs relative to baseline. Different symbols indicate significant ($P < 0.05$) comparisons between timepoints.

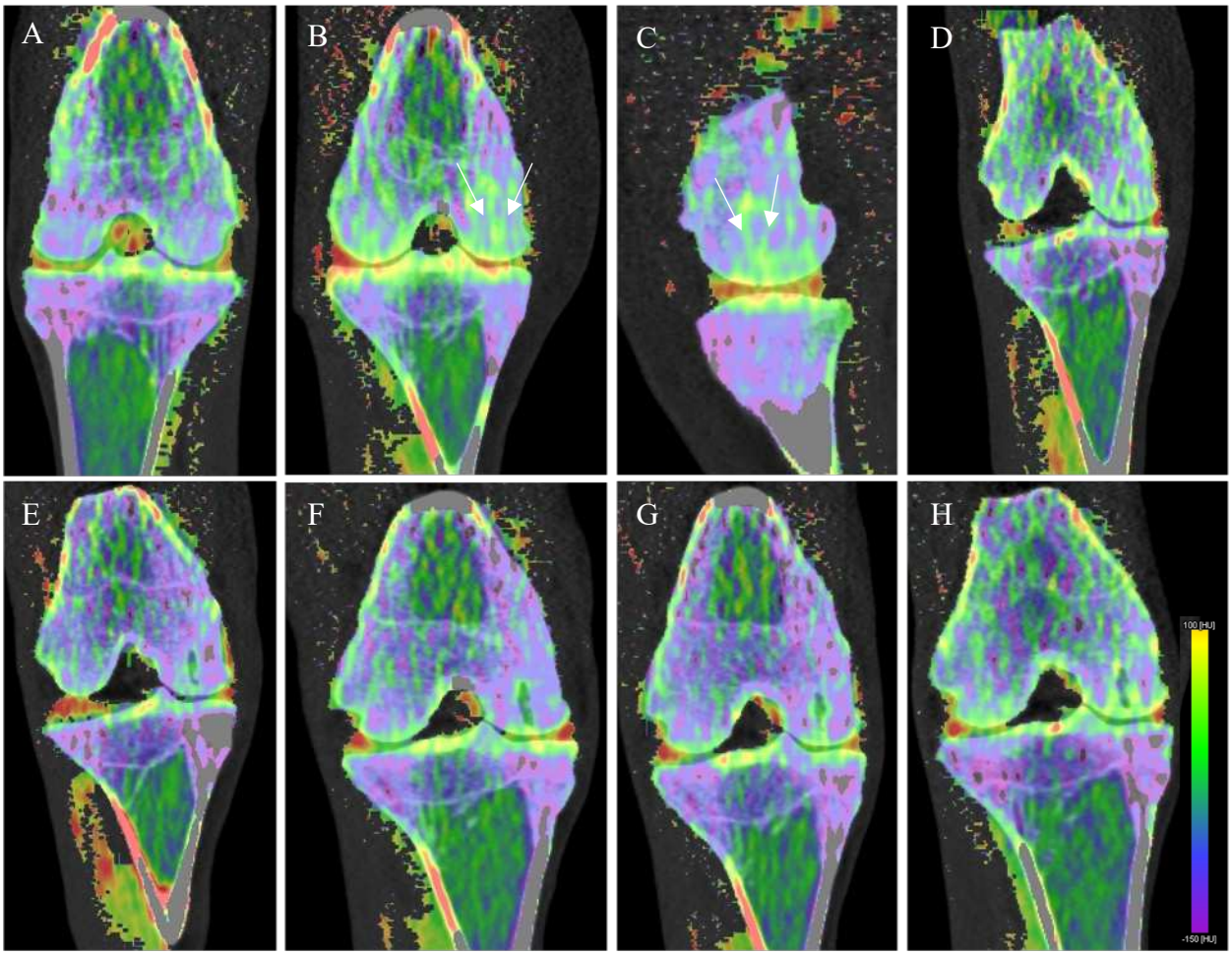

Figure 3.8 – Cranial and sagittal plane serial computed tomographic (CT) images of the femorotibial joint from a single animal with experimentally-induced bone marrow lesions in the medial femoral condyle. CT data sets of the femorotibial joint obtained with tube voltage settings of 80 and 140 kVp were post-processed using a virtual non-calcium dual-energy technique followed by color overlay using a commercially-available software. Timepoints include (A) baseline, (B, C) 2 weeks, (D) 4 weeks, (E) 6 weeks, (F) 8 weeks, (G) 10 weeks, and (H) 12 weeks post-surgery. Fluid attenuation depicted by the green/yellow color (white arrows in B and C) is visible in the medial femoral condyle beginning at 2 weeks, and persists throughout the 12-week study duration.

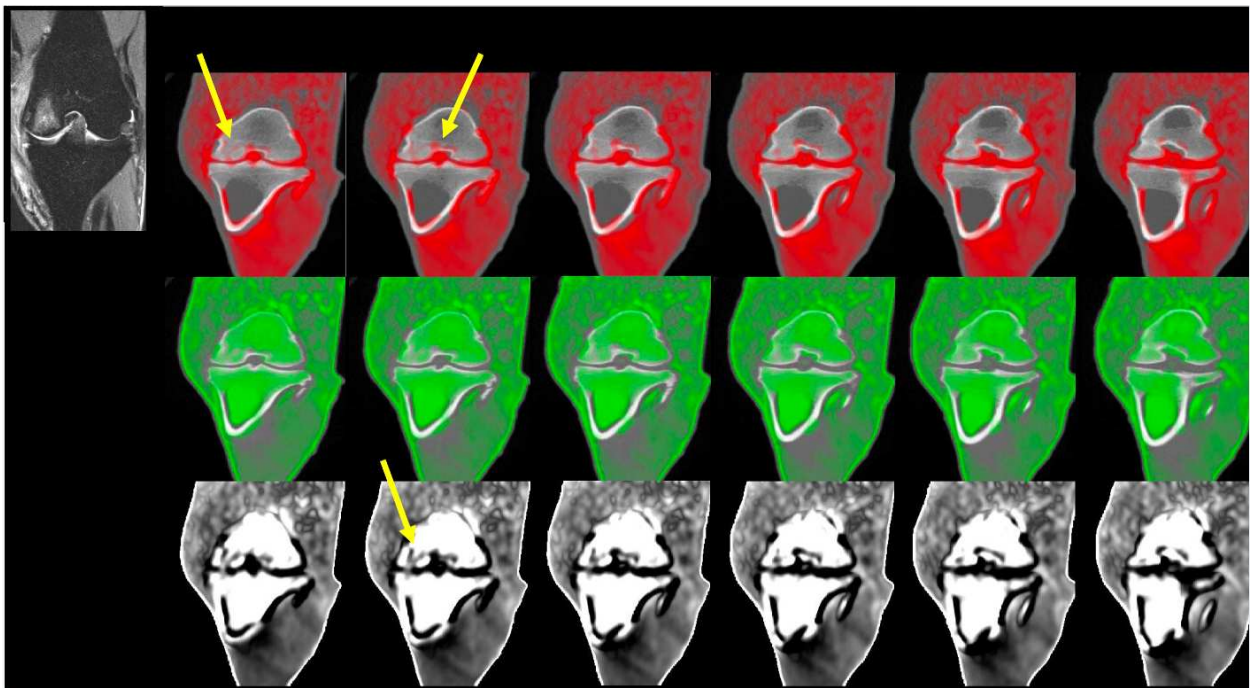

Figure 3.9 – Serial images of a medial femoral condyle with an experimentally induced bone marrow lesion in the cranial plane generated using a dual-energy calcium-extinguished decomposition technique with cone-beam computed tomography. Top row: images highlighting the soft tissue fraction; middle row: images highlighting the fat fraction; lower row: calcium-extinguished images. Upper left: a magnetic resonance image from a Dixon water only sequence is provided for comparison. Yellow arrows indicate areas with soft tissue attenuation (top row) that are visible on calcium-extinguished image (bottom row). *Images provided courtesy of Dr. Wojtek Zbijewski, Johns Hopkins University*.

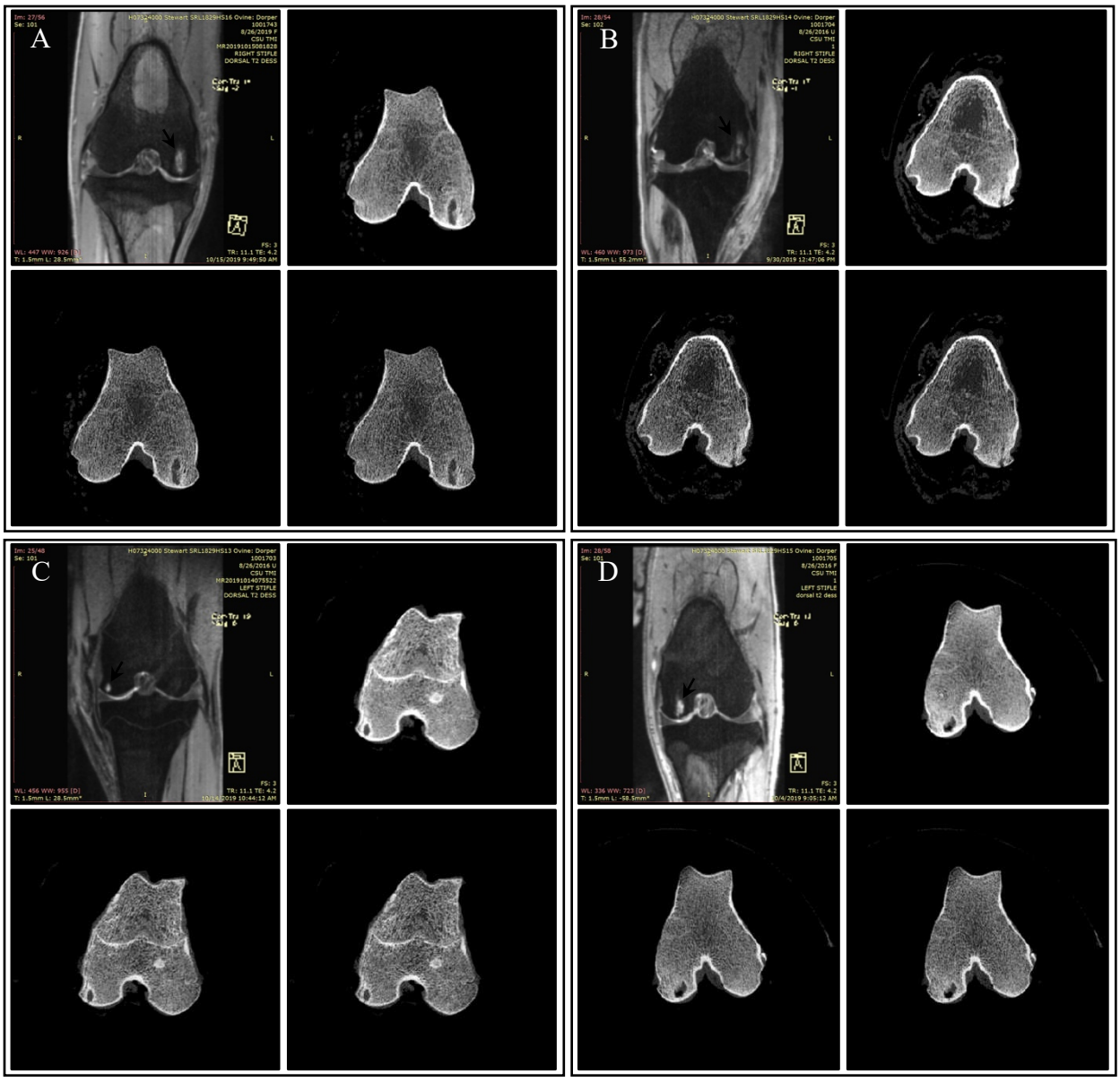

Figure 3.10 – Cranial plane images of the distal femur from 4 samples with bone marrow lesions (BMLs) obtained using magnetic resonance imaging (MRI) and cone-beam computed tomography (CBCT). Each sample is shown in a group of four images. Upper left, T2-weighted 3D double echo steady state image in the cranial plane. The BML is visible within the medial femoral condyle as a hyperintense region relative to the trabecular bone. Upper right, CBCT image of the corresponding region using 60 kVp. Lower left, CBCT image using 120 kVp. Lower right, CBCT image using 140 kVp + 0.255 mm Ag beam filtration. The bone loss associated with a BML is readily visible on the single-energy CBCT images. *Images provided courtesy of Dr. Wojtek Zbijewski, Johns Hopkins University*.

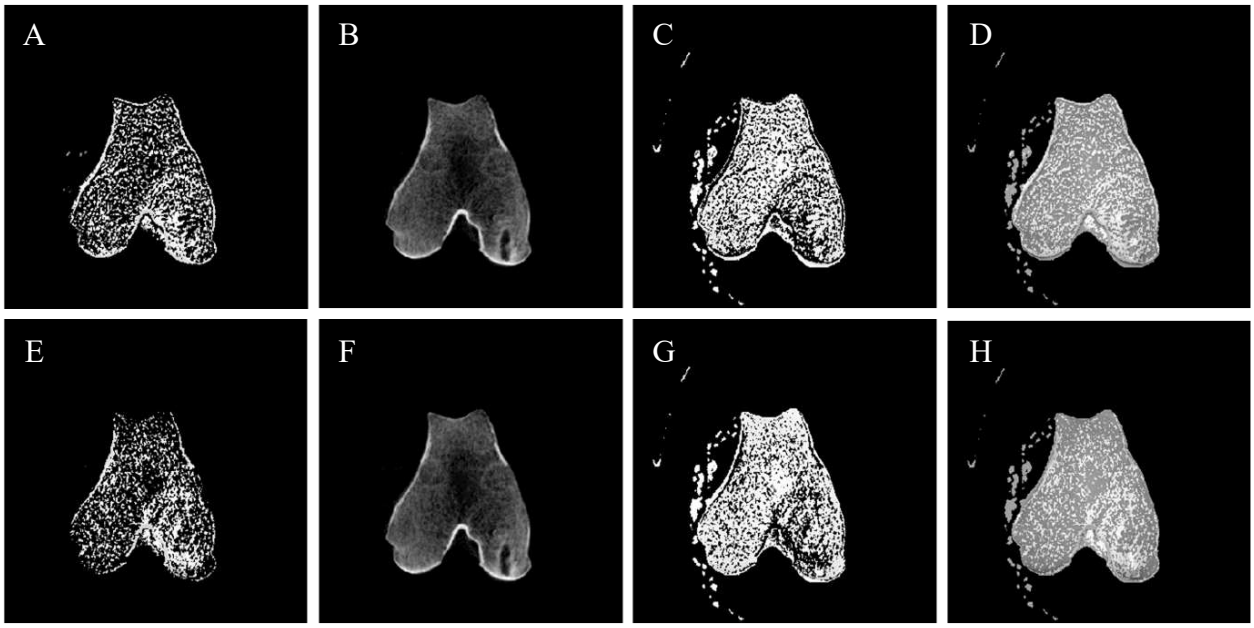

Figure 3.11 – Cranial plane images of the distal femur from a single animal with bone marrow lesions (BMLs) obtained using cone-beam computed tomography (CBCT). Data from high and low energy scans were used to generate material fraction maps of water (A, E), calcium (B, F), and adipose (C, G) tissues. Virtual monoenergetic composite images (D, H) were generated in an effort to identify BMLs within the medial femoral condyle. BMLs are somewhat visible on composite images, but conspicuity is limited by non-uniformities. Top row: high energy at 120 kVp, low energy 60 kVp; bottom row: high energy at 140 kVp + Ag, low energy 60 kVp. *Images provided courtesy of Dr. Wojtek Zbijewski, Johns Hopkins University*.

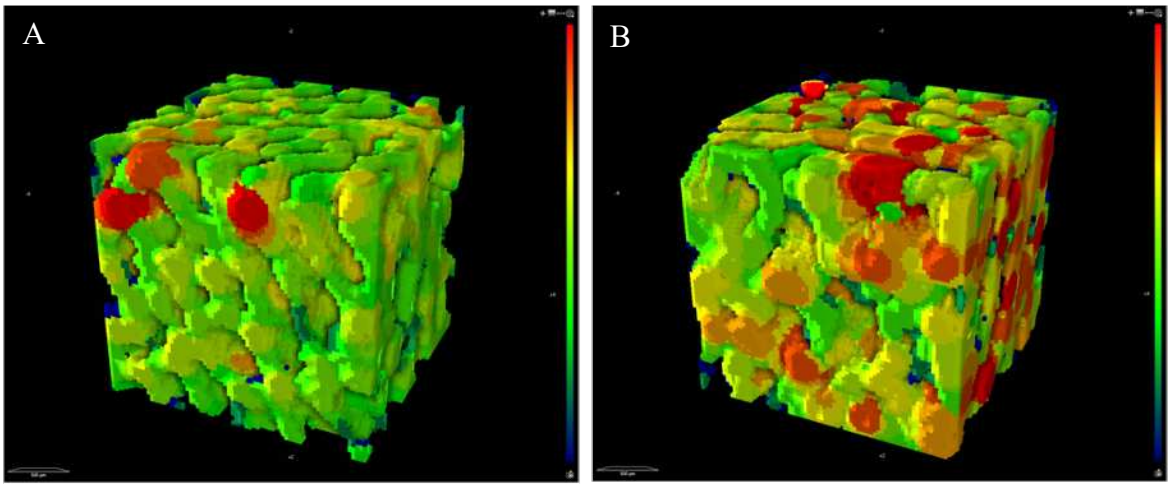

Figure 3.12 – Representative 3 mm^3 region of interest cubes used for micro-computed tomography (μCT) analysis from contralateral medial femoral condyles in the same animal at 12 weeks post-surgery for experimental induction of bone marrow lesions (BMLs). (A) Sample from medial femoral condyle treated by transcutaneous extracorporeal shockwave, (B) sample from medial femoral condyle treated by penetration of the articular surface with a 1.1 mm Steinmann pin. A BML was visible on images obtained using magnetic resonance imaging in the condyle represented by (B) but not in the contralateral limb in image (A). Attenuation values (Hounsfield Units) of bone represented by relative color scale with the red color as the greatest attenuation values, and the blue color as the lowest attenuation values.

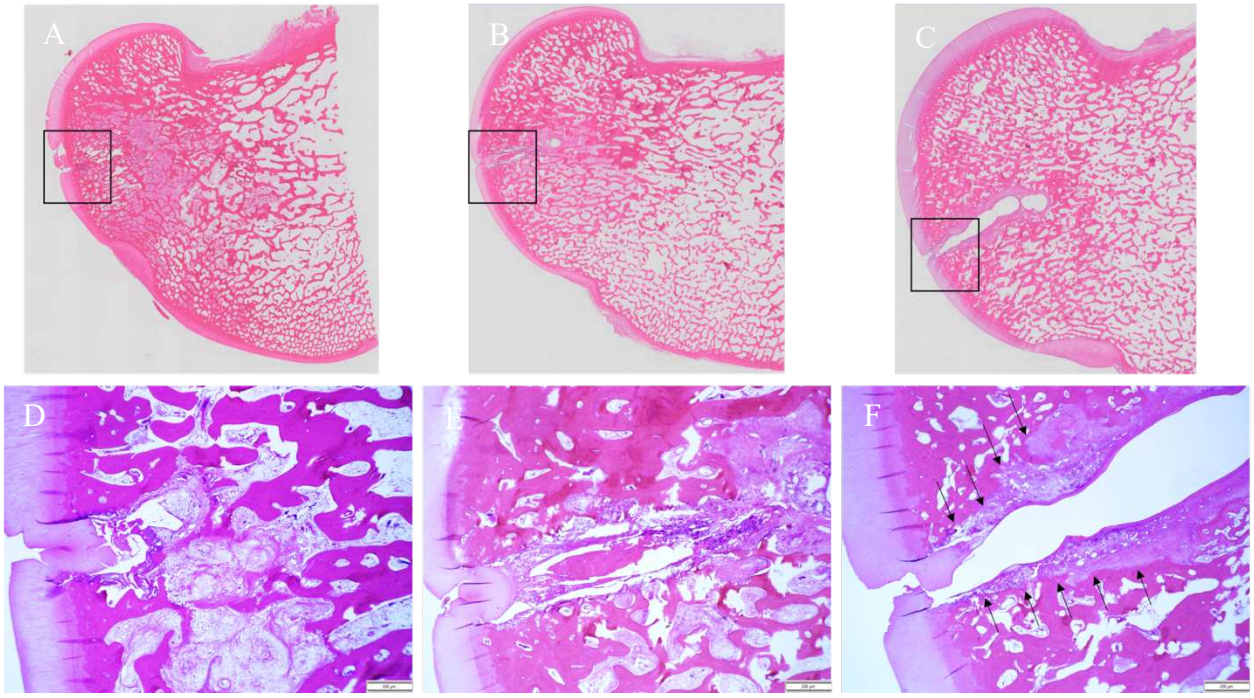

Figure 3.13 – Histologic sections with hematoxylin and eosin stain of the medial condyle of the distal femur taken from sheep at 4 weeks (A, D), 8 weeks (B, E), or 12 weeks (C, F) after experimental-induction of bone marrow lesions (BMLs). The tract of the pin used for BML induction is visible in all images. Initially, the BML is characterized by a local hemorrhage and a high level of inflammatory cellular infiltrate. By 12 weeks, dense fibrous repair tissue is present along the periphery of the pin tract, in addition to structural remodeling within the adjacent bone (black arrows). Black boxes in upper images identify regions of interest shown in lower images at higher magnification; bar (lower images) = 200 μm.

3.6 Tables

Table 3.1 – Subchondral bone grading rubric (0-3 scale) adapted from Aho et al.[37] Grade 0 corresponds to early stage osteoarthritis and extends to more advanced changes in subchondral bone in Grade 3.

Grade	Description
0	Early stage of osteoarthritis (OA). No evidence of subchondral bone sclerosis, thin subchondral bone plate and trabeculae. Articular cartilage is directly connected to bone marrow via open fenestrae in subchondral bone.
1	Grade 1. Some subchondral bone sclerosis and bone volume is increased. Thickened bone trabeculae can be seen. Cartilage contact with bone marrow still persists.
2	Grade 2. A distinct increase in subchondral sclerosis and bone volume. Fibrillation can be seen in subchondral bone plate. No contact of bone marrow to articular cartilage can be identified.
3	Grade 3. Late-stage disease. Severe subchondral sclerosis and massively increased bone volume. Bone marrow distance from cartilage increases. Subchondral bone plate flattens.

Table 3.2 – Semi-quantitative subchondral bone grading rubric, adapted from Table 2 in Nagira et al.[38] Evaluation of the subchondral bone plate, bone volume, and tissue in the region of interest were all parameters for evaluation in this study.

Parameter	Score	Description
Subchondral bone plate	0	Same as control
	1	No increase in thickness by bone-cartilage interface undulates (<110% thickness compared to control)
	2	Slight increase in thickness without angiogenesis (111-125% thickness compared to control)
	3	Slight increase in thickness with few angiogenesis (111-125%)
	4	Moderate increase in thickness with several angiogenesis (126-150%)
	5	Marked increase in thickness with several angiogenesis (151-175%)
	6	Major increase in thickness with several angiogenesis (>176%)
Bone volume (BV/TV)	0	No change
	1	Mild increase (BV/TV; 61-70%)
	2	Moderate increased (BV/TV; 71-85%)
	3	Marked increase (BV/TV; >86%)
Tissue in region of interest	0	No change
	1	Formation of cartilage-like tissue
	2	Increased cartilaginous matrix
	3	Endochondral ossification

Table 3.3 – Microscopic scoring rubric for osteochondral sections, adapted from Table IVA by Little et al.[25] For this study, parameters evaluated were relevant to the subchondral bone or entire osteochondral unit, with less specific focus on characterizing changes in the articular cartilage.

Parameter	Score	Description
Structure	0	Normal
	1	Slight surface irregularities (surface barely disturbed)
	2	Moderate surface irregularities (surface roughened)
	3	Severe surface irregularities (disruption, fissuring, fibrillation to <10% depth)
	4	Fissures to transitional zone (1/3 depth)
	5	Fissures to radial zone (2/3 depth)
	6	Fissures to calcified zone (full depth)
	7	Erosion or severe fibrillation to mid-zone (1/3 depth)
	8	Erosion of severe fibrillation to deep zone (2/3 depth)
	9	Erosion or severe fibrillation to calcified zone (full depth)
	10	Erosion or fibrillation to subchondral bone
Chondrocyte density	0	Normal
	1	Increase or slight decrease
	2	Moderate decrease
	3	Severe decrease
	4	No cells
Cell cloning	0	Normal
	1	Several doublets
	2	Many doublets
	3	Doublets and triplets
	4	Multiple cell nests or no cells in section
Tidemark/Calcified cartilage/Subchondral bone	0	Intact subchondral bone plate + single tidemark
	1	Intact subchondral bone plate + duplicated tidemark
	2	Blood vessels penetrate through subchondral bone plate to calcified cartilage
	3	Tidemark penetrated by blood vessels

Table 3.4 – Microscopic scoring rubric for osteochondral sections, adapted from Table VII by McIlwraith et al.[39] The original grading system was for osteochondral lesions as a result of spontaneous osteoarthritis in the equine metacarpophalangeal joint; which has been adapted to more broadly address osteochondral changes observed in this study associated with bone marrow lesions.

Parameter	Score	Description
Osteochondral changes	0	No visible changes in cartilage or bone
	1	Minor disruption of subchondral bone matrix; marrow spaces contain debris
	2	Moderate disruption of subchondral bone matrix; areas of matrix are fragmented and comminuted and there is a significant amount of debris within the marrow spaces. The tidemark is reduplicated and may be disrupted. The cartilage overlying the lesion is thickened with superficial erosion and fibrillation.
	3	Severe disruption of subchondral bone matrix with pale staining and abundant fibrin. The tidemark is reduplicated and often disrupted. Superficial thickening of cartilage and/or fibrocartilage present which may be completely detached from thickened deeper cartilage.
	4	Complete loss of osteochondral tissues.
Subchondral bone remodeling	0	No visible changes in cartilage or bone
	1	Advancement of the subchondral bone into the calcified cartilage layer with scalloped subchondral bone margins, but not crossing any tidemarks
	2	Subchondral bone advancement through the calcified cartilage layer, crossing one or more tidemarks but below the most superficial tidemark front
	3	Subchondral bone advancement through the calcified cartilage layer and disruption of the tidemark front
Osteochondral splitting	0	No visible changes in cartilage or bone
	1	Involve the tidemark and subchondral bone, but are simple, linear defects
	2	Have fragments and debris within the split and connections between splits
	3	Involve articular cartilage and displacement of calcified cartilage fragments into the underlying subchondral bone

Table 3.5 – Mean ± standard deviation for signal-to-noise (SNR) and contrast-to-noise (CNR) ratios from Dixon, water only images on magnetic resonance (MR) imaging of the experimentally-induced bone marrow lesions (BMLs) in the medial femoral condyles (MFCs) of sheep across the 12-week study. Baseline measurements were taken in the same location of the condyle as BMLs by overlaying MR images. Group B MFCs were treated with a 1.1 mm Steinmann pin to a 2 mm depth to the subchondral bone, and Group C MFCs had a 1.1 mm Steinmann pin to an 8 mm depth into trabecular bone. No standard deviation values are given for Group B at 10 and 12 weeks as only a single animal had BMLs visible at these timepoints. Different letters indicate a significant ($P < 0.05$) difference between measurements within a specific sequence and plane combination between timepoints.

Timepoint	Group	Plane	SNR	SNR, Maximum	SNR, Minimum	CNR
Baseline	B	Cranial	3.57 ± 0.91	--	--	-33.86 ± 12.93
		Sagittal	3.36 ± 2.46	--	--	-34.05 ± 13.21
	C	Cranial	9.44 ± 9.27	--	--	-26.89 ± 26.03[a]
		Sagittal	13.29 ± 17.37[a]	--	--	-0.76 ± 28.39
2 weeks	B	Cranial	37.49 ± 7.28	43.69 ± 7.85	7.72 ± 5.25	-5.3 ± 6.35
		Sagittal	38.55 ± 7.07	52.96 ± 9.97	12.72 ± 3.49	7.51 ± 31.1
	C	Cranial	34.41 ± 35.48	62.7 ± 25.35	8.69 ± 8.53	5.15 ± 27.5[b]
		Sagittal	24 ± 10.31	36.95 ± 11.71	9.02 ± 10.43	1.68 ± 15.59
4 weeks	B	Cranial	39.82 ± 33.07	58.43 ± 42.97	13.11 ± 5.62	-3.79 ± 0.31
		Sagittal	45.59 ± 24.66	69.49 ± 36.73	22.23 ± 11.91	-8.19 ± 20.22
	C	Cranial	37.9 ± 17.82	59.92 ± 26.19	13.74 ± 13.64	1.7 ± 13.37
		Sagittal	30.88 ± 22.34	42.22 ± 16.73	12.96 ± 12.44	0.71 ± 8.56
6 weeks	B	Cranial	16.18 ± 6.77	40.7 ± 21.34	16.29 ± 6.92	-25.85 ± 0.2
		Sagittal	41.25 ± 19.48	69.42 ± 5.83	19.99 ± 9.4	-29.73 ± 15.54
	C	Cranial	50 ± 29.76	81.91 ± 30.24	27.65 ± 14.3	-5.15 ± 21.52[b]
		Sagittal	40.56 ± 32.45	57.65 ± 33.69	18.92 ± 12.02	-0.51 ± 28.01
8 weeks	B	Cranial	22.36 ± 19.64	45.32 ± 21.99	10.84 ± 5.25	-17.95 ± 13.74
		Sagittal	26.76 ± 21.04	51.59 ± 6.67	15.25 ± 9.14	-17.56 ± 23.62
	C	Cranial	20.19 ± 21.26	50.26 ± 8.37	10.32 ± 11.04	-4.3 ± 11.29[b]
		Sagittal	61.02 ± 38.45[b]	84.72 ± 41.47	33.16 ± 34.57	-1.73 ± 16.45
10 weeks	B	Cranial	21.55	42.55	11.41	-11.94
		Sagittal	0.37	0.88	0.22	-0.34
	C	Cranial	27.11 ± 17.02	59.29 ± 22.13	13.86 ± 11.13	-3.21 ± 13
		Sagittal	44.5 ± 23.8	81.12 ± 44.87	25.42 ± 11.97	-14.01 ± 14.45
12 weeks	B	Cranial	13.05	41.72	6.13	-19.71
		Sagittal	12.99	29.02	8.05	-23.41
	C	Cranial	38.13 ± 24.58	67.64 ± 28.07	17.8 ± 9.97	-1.45 ± 23.2
		Sagittal	37.51 ± 21.77	59.61 ± 37.67	17.85 ± 9.44	-7.25 ± 12.66

Table 3.6 – Mean ± standard deviation for signal-to-noise (SNR) and contrast-to-noise (CNR) ratios from proton density fat saturation (PDFS) sequences on magnetic resonance (MR) imaging of the experimentally-induced bone marrow lesions (BMLs) in the medial femoral condyles (MFCs) of sheep across the 12-week study. Baseline measurements were taken in the same location of the condyle as BMLs by overlaying MR images. Group B MFCs were treated with a 1.1 mm Steinmann pin to a 2 mm depth to the subchondral bone, and Group C MFCs had a 1.1 mm Steinmann pin to an 8 mm depth into trabecular bone. No standard deviation values are given for Group B at 10 and 12 weeks as only a single animal had BMLs visible at these timepoints. Different letters indicate a significant ($P < 0.05$) difference between measurements within a specific sequence and plane combination between timepoints.

Timepoint	Group	Plane	SNR	SNR, Maximum	SNR, Minimum	CNR
Baseline	B	Cranial	5.21 ± 1.75	--	--	-18.35 ± 3.42[a]
		Sagittal	7.2 ± 2.07	--	--	-52.10 ± 26.37
	C	Cranial	10.76 ± 11.66[a]	--	--	-16.99 ± 8.49
		Sagittal	9.77 ± 12.05	--	--	-15.84 ± 10.27
2 weeks	B	Cranial	28.98 ± 10.39[b]	33.21 ± 3.48	14.09 ± 5.20	4.44 ± 10.72[b]
		Sagittal	34.95 ± 20.06	39.52 ± 20.37	15.67 ± 12.22	-9.78 ± 20.97
	C	Cranial	35.26 ± 23.88	42.44 ± 18.37	15.61 ± 16.55	9.29 ± 18.94
		Sagittal	39.46 ± 19.43	44.5 ± 17.64	24.24 ± 25.69	2.88 ± 14.45
4 weeks	B	Cranial	23.89 ± 12.78	31.43 ± 14.33	14.96 ± 8.27	3.14 ± 0.96
		Sagittal	44.87 ± 12.57	70.7 ± 29.29	27.38 ± 9.83	-5.28 ± 13.52
	C	Cranial	25.13 ± 7.78	38.31 ± 17.9	14.16 ± 7.64	2.57 ± 7.63
		Sagittal	38.67 ± 13.88	51.65 ± 17.84	21.44 ± 11.29	-2.74 ± 18.7
6 weeks	B	Cranial	14.78 ± 7.8[b]	23.41 ± 11.62	6.25 ± 1.31	-3.89 ± 2.71
		Sagittal	26.42 ± 3.19	58.63 ± 19.72	24.14 ± 6.4	-27.15 ± 21.61
	C	Cranial	14.78 ± 7.8	23.41 ± 11.62	6.25 ± 1.31	-3.89 ± 2.71
		Sagittal	26.42 ± 3.19	58.63 ± 19.72	24.14 ± 6.4	-27.15 ± 21.61
8 weeks	B	Cranial	12.65 ± 1.81	33.76 ± 13.3	10.28 ± 5.16	-9.48 ± 4.35
		Sagittal	26.36 ± 3.35	35.69 ± 9.25	14.35 ± 8.93	-15.04 ± 5.56
	C	Cranial	30.27 ± 22.05	44.31 ± 35.15	14.32 ± 11.2	6.34 ± 13.52
		Sagittal	432.64 ± 866.28	667.96 ± 1346.28	331.64 ± 698.01	-30.11 ± 84.85
10 weeks	B	Cranial	17.99	29.01	9.26	-0.97
		Sagittal	14.64	41.93	13.47	-14.99
	C	Cranial	30.06 ± 16.02	44.67 ± 24.05	14.13 ± 10.79	5.43 ± 14.99
		Sagittal	51.42 ± 27.19	81.22 ± 51.21	31.23 ± 16.34	-2.42 ± 12.26
12 weeks	B	Cranial	11.99	30.52	9	-7.82
		Sagittal	20.27	25.03	10.81	-25.42
	C	Cranial	33.01 ± 20.84	67.47 ± 32.81	13.74 ± 9.42	8.74 ± 13.46
		Sagittal	30.81 ± 14.36	50.13 ± 31.92	15.51 ± 4.59	-2.14 ± 5.44

Table 3.7 – Mean ± standard deviation for the percent of the medial femoral condyle with a visible bone marrow lesion (BML) and volume of BML on fluid-sensitive magnetic resonance (MR) images across time in Group C sheep. Group C treatment includes penetration of the articular and calcified cartilage, subchondral and trabecular bone layers with a 1.1 mm Steinmann pin to an 8 mm depth. PDFS: proton density fat saturation. Different letters indicate a significant ($P < 0.05$) difference between measurements within a specific sequence and plane combination at a given timepoint.

Timepoint	Plane	Sequence	Percentage of Condyle with BML	Volume of BML (mm^3)
2 weeks	Cranial	Dixon, in phase	187.53 ± 96.49	48.84 ± 27.7
		Dixon, water only	247.36 ± 135.73	70.83 ± 38.51
		PDFS	206.44 ± 82.24	65.79 ± 36.99
	Sagittal	Dixon, in phase	125.13 ± 39.15	40.27 ± 20.72
		Dixon, water only	153.68 ± 70.33	61.06 ± 35.47
		PDFS	136.98 ± 60.46	64.38 ± 42.52
4 weeks	Cranial	Dixon, in phase	134.07 ± 55.42	38.28 ± 22.68
		Dixon, water only	159.55 ± 71.71	36.3 ± 23.85
		PDFS	133.89 ± 66.61	29.88 ± 17.29
	Sagittal	Dixon, in phase	118.28 ± 67.1	31.8 ± 14.44
		Dixon, water only	107.84 ± 46.15	33.68 ± 20.82
		PDFS	115.89 ± 61.42	32.51 ± 17.11
6 weeks	Cranial	Dixon, in phase	104.29 ± 37.77	22.07 ± 16.01
		Dixon, water only	82.98 ± 32.47	16.42 ± 5.96
		PDFS	81.27 ± 24.12	16.09 ± 5.75
	Sagittal	Dixon, in phase	82.65 ± 26.6	21.79 ± 11.1
		Dixon, water only	72 ± 20.83	6.12 ± 2.32[a]
		PDFS	61.37 ± 14.1	17.66 ± 8.15[b]
8 weeks	Cranial	Dixon, in phase	99.72 ± 36.57	22.49 ± 15.46
		Dixon, water only	88.3 ± 29.94	13.14 ± 4.84
		PDFS	74.37 ± 20	12.54 ± 5.21
	Sagittal	Dixon, in phase	75.19 ± 33.17	23.1 ± 11.66
		Dixon, water only	56.11 ± 19.43	13.25 ± 5.21
		PDFS	51.43 ± 15.55	13.02 ± 3.78
10 weeks	Cranial	Dixon, in phase	80.69 ± 44.47	22.29 ± 18.04
		Dixon, water only	70.96 ± 26.25	11.64 ± 6.13
		PDFS	70.63 ± 48.73	15.73 ± 12.7
	Sagittal	Dixon, in phase	71.76 ± 36.09	17.94 ± 16.07
		Dixon, water only	50.57 ± 18.5	15.88 ± 12.52
		PDFS	45.68 ± 21.62	12.68 ± 11.16
12 weeks	Cranial	Dixon, in phase	91.91 ± 62.04	21.22 ± 20.42
		Dixon, water only	73.18 ± 37.71	11.44 ± 6.8
		PDFS	61.56 ± 24.64	10.26 ± 6.05
	Sagittal	Dixon, in phase	71.9 ± 34.41	19.04 ± 17.26
		Dixon, water only	46.58 ± 20.32	10.84 ± 7.35
		PDFS	45.06 ± 16.05	11.72 ± 8.39

Table 3.8 – Median (range) histological scores of osteochondral sections from control and pin-treated (Groups B and C) medial femoral condyles. Bone marrow lesions were visible in pin-treated animals from both Group B and Group C. Group B treatment includes penetration of the articular and calcified cartilage and subchondral bone plate. Group C treatment includes penetration of the articular and calcified cartilage, subchondral and trabecular bone. A 1.1 mm Steinmann pin was used for all pin treatments. Statistical comparisons were made using a Wilcoxon signed rank test; defined *P* values represent comparison of a specific treatment group to control samples. Parameters evaluated are defined in Tables 3.1-3.4. NC, *P* values were not calculable because of identical values between groups.

Parameter	**Control**	**Group B**	***P* Value**	**Group C**	***P* Value**
Subchondral bone overall[37]	0 (0-0)	2 (1-3)	0.06	3 (0-3)	0.06
Subchondral bone plate[38]	0 (0-0)	3 (3-5)	0.035	5.5 (5-6)	0.028
Bone volume[38]	0 (0-0)	2 (1-3)	0.04	3 (3-3)	0.012
Tissue in region of interest[38]	0 (0-0)	2 (2-2)	0.013	2 (2-2)	0.008
Structure[25]	0 (0-0)	6 (3-10)	0.04	10 (6-10)	0.027
Chondrocyte density[25]	0 (0-0)	0 (0-0)	NC	0 (0-1)	1
Cell cloning[25]	0 (0-0)	0 (0-0)	NC	0 (0-1)	1
Tidemark/calcified cartilage/subchondral bone[25]	0 (0-1)	1.5 (1-2)	0.094	2 (2-3)	0.03
Osteochondral changes[39]	0 (0-0)	2 (2-2)	0.026	3 (2-3)	0.02
Subchondral bone remodeling[39]	0 (0-0)	2 (1-2)	0.035	2 (2-3)	0.02
Osteochondral splitting[39]	0 (0-0)	0 (0-0)	NC	1.5 (1-2)	0.019

3.7 References

1. Bonadio MB, Filho AGO, Helito CP, et al. Bone Marrow Lesion: Image, Clinical Presentation, and Treatment. Magn Reson Insights 2017;10:1178623X17703382.

2. Dyson S, Murray R, Schramme M, et al. Magnetic resonance imaging of the equine foot: 15 horses. Equine Vet J 2003;35:18–26.

3. Powell SE, Ramzan PHL, Head MJ, et al. Standing magnetic resonance imaging detection of bone marrow oedema-type signal pattern associated with subcarpal pain in 8 racehorses: a prospective study. Equine Vet J 2010;42:10–17.

4. Powell SE. Low-field standing magnetic resonance imaging findings of the metacarpo/metatarsophalangeal joint of racing Thoroughbreds with lameness localised to the region: A retrospective study of 131 horses. Equine Vet J 2012;44:169–177.

5. Winegardner KR, Scrivani P V., Krotscheck U, et al. Magnetic resonance imaging of subarticular bone marrow lesions in dogs with stifle lameness. Vet Radiol Ultrasound 2007;48:312–317.

6. Felson DT, McLaughlin S, Goggins J, et al. Bone Marrow Edema and Its Relation to Progression of Knee Osteoarthritis. Ann Intern Med 2003;139:330.

7. Hunter DJ, Zhang Y, Niu J, et al. Increase in bone marrow lesions associated with cartilage loss: A longitudinal magnetic resonance imaging study of knee osteoarthritis. Arthritis Rheum 2006;54:1529–1535.

8. Haavardsholm EA, Bøyesen P, Østergaard M, et al. Magnetic resonance imaging findings in 84 patients with early rheumatoid arthritis: bone marrow oedema predicts erosive progression. Ann Rheum Dis 2008;67:794–800.

9. Felson DT, Chaisson CE, Hill CL, et al. The Association of Bone Marrow Lesions with Pain in Knee Osteoarthritis. Ann Intern Med 2001;134:541–549.

10. Eriksen EF. Treatment of bone marrow lesions (bone marrow edema). Bonekey Rep 2015;4:755.

11. Starr AM, Wessely MA, Albastaki U, et al. Bone Marrow Edema: Pathophysiology, Differential Diagnosis, and Imaging. Acta radiol 2008;49:771–786.

12. Taljanovic MS, Graham AR, Benjamin JB, et al. Bone marrow edema pattern in advanced hip osteoarthritis: Quantitative assessment with magnetic resonance imaging and correlation with clinical examination, radiographic findings, and histopathology. Skeletal Radiol 2008;37:423–431.

13. Kon E, Ronga M, Filardo G, et al. Bone marrow lesions and subchondral bone pathology of the knee. Knee Surg Sport Traumatol Arthrosc 2016;24:1797–1814.

14. Zanetti M, Bruder E, Romero J, et al. Bone marrow edema pattern in osteoarthritic knees: correlation between MR imaging and histologic findings. Radiology 2000;215:835–840.

15. Alliston T, Hernandez C, Findlay D, et al. Bone marrow lesions in osteoarthritis: What lies beneath. J Orthop Res 2018;36:1818–1825.

16. Schett G. Bone Marrow Edema. Ann N Y Acad Sci 2009;1154:35–40.

17. Fink Eriksen E, Ringe JD. Bone marrow lesions: a universal bone response to injury? Rheumatol Int 2012;32:575–584.

18. Sukul DMKSK, Johannes EJ, Pierik EGJM, et al. The Effect of High Energy Shock Waves Focused on Cortical Bone: An in Vitro Study. J Surg Res 1993;54:46–51.

19. Delius M, Draenert K, Al Diek Y, et al. Biological effects of shock waves: in vivo effect of high energy pulses on rabbit bone. Ultrasound Med Biol 1995;21:1219–1225.

20. Durst HB, Blatter RG, Orthopaedic Surgeon S Kuster CM, et al. Osteonecrosis of the Humeral Head After Extracorporeal Shock-Wave Lithotripsy. J Bone Jt Surg [Br] 2002;84-B:744–746.

21. Edelstein W, Glover G, Hardy C, et al. The intrinsic signal-to-noise ratio in NMR imaging. Magn Reson Med 1986;3:604–618.

22. Welvaert M, Rosseel Y. On the Definition of Signal-To-Noise Ratio and Contrast-To-Noise Ratio for fMRI Data. PLoS One 2013;8:e77089.

23. Pache G, Krauss B, Strohm P, et al. Dual-energy CT virtual noncalcium technique: detecting posttraumatic bone marrow lesions--feasibility study. Radiology 2010;256:617–624.

24. Foti G, Catania M, Caia S, et al. Identification of bone marrow edema of the ankle: diagnostic accuracy of dual-energy CT in comparison with MRI. La Radiol medica 2019 12410 2019;124:1028–1036.

25. Little CB, Smith MM, Cake MA, et al. The OARSI histopathology initiative – recommendations for histological assessments of osteoarthritis in sheep and goats. Osteoarthr Cartil 2010;18:S80–S92.

26. Feldkamp LA, Davis LC, Kress JW. Practical cone-beam algorithm. J Opt Soc Am A 1984;1:612–619.

27. Zbijewski W, Jean P De, Prakash P, et al. A dedicated cone-beam CT system for musculoskeletal extremities imaging: Design, optimization, and initial performance characterization. Med Phys 2011;38:4700–4713.

28. Goodsitt MM, Shenoy A, Shen J, et al. Evaluation of dual energy quantitative CT for determining the spatial distributions of red marrow and bone for dosimetry in internal emitter radiation therapy. Med Phys 2014;41:51901–51902.

29. Zbijewski W, Sisniega A, Stayman JW, et al. Dual-Energy Imaging of Bone Marrow Edema on a Dedicated Multi-Source Cone-Beam CT System for the Extremities. Hoeschen C, Kontos D, Flohr TG, eds. Proc SPIE--The Int Soc Opt Eng 2015;9412:94120V.

30. Tilley S, Zbijewski W, Siewerdsen JH, et al. A general CT reconstruction algorithm for model-based material decomposition. Proc SPIE Int Soc Opt Eng 2018;10573:356–362.

31. Tilley S, Zbijewski W, Stayman JW. Model-based material decomposition with a penalized nonlinear least-squares CT reconstruction algorithm. Phys Med Biol 2019;64:035005.

32. Lui S, Cao Q, Siewerdsen J, et al. Three-material dual energy decomposition using a constrained model-based algorithm. In: The 6th International Conference on Image Formation in X-Ray Computed Tomography.; 2020:558–561.

33. Carrino JA, Al Muhit A, Zbijewski W, et al. Dedicated Cone-Beam CT System for Extremity Imaging. Radiology 2014;270:816–824.

34. Yu L, Leng S, McCollough CH. Dual-Energy CT–Based Monochromatic Imaging. Am J Roentgenol 2012;199:S9–S15.

35. Bouxsein M, Boyd S, Christiansen B, et al. Guidelines for assessment of bone microstructure in rodents using micro-computed tomography. J bone Miner Res 2010;25:1468–1486.

36. Broomfield C, Meis N, Johnson J, et al. Optimization of ovine bone decalcification for increased cellular detail: a parametric study. J Histotechnol 2021:1–7.

37. Aho O-M, Finnilä M, Thevenot J, et al. Subchondral bone histology and grading in osteoarthritis. Malaval L, ed. PLoS One 2017;12:e0173726.

38. Nagira K, Ikuta Y, Shinohara M, et al. Histological scoring system for subchondral bone changes in murine models of joint aging and osteoarthritis. Sci Rep 2020;10:10077.

39. McIlwraith CW, Frisbie DD, Kawcak CE, et al. The OARSI histopathology initiative – recommendations for histological assessments of osteoarthritis in the horse. Osteoarthr Cartil 2010;18:S93–S105.

40. Faul F, Erdfelder E, Lang A, et al. G*Power 3: a flexible statistical power analysis program for the social, behavioral, and biomedical sciences. Behav Res Methods 2007;39:175–191.

41. Frobell RB, Le Graverand MP, Buck R, et al. The acutely ACL injured knee assessed by MRI: changes in joint fluid, bone marrow lesions, and cartilage during the first year. Osteoarthr Cartil 2009;17:161–167.

42. Filardo G, Kon E, Tentoni F, et al. Anterior cruciate ligament injury: post-traumatic bone marrow oedema correlates with long-term prognosis. Int Orthop 2016;40:183–190.

43. Kornaat P, Van de Velde S. Bone marrow edema lesions in the professional runner. Am J Sports Med 2014;42:1242–1246.

44. Zhang Y, Shu D, Yao W, et al. MRI study of changes in knee bone marrow edema-like signal in asymptomatic amateur marathon runners before and after half-marathon running. Clin Imaging 2021;80:150–157.

45. Zhang Q, Liu L, Sun W, et al. Extracorporeal shockwave therapy in osteonecrosis of femoral head a systematic review of now available clinical evidences. Med (United States) 2017;96:e5897.

46. Zhang L, Cui Y, Liang D, et al. High-energy focused extracorporeal shock wave therapy for bone marrow edema syndrome of the hip: A retrospective study. Medicine (Baltimore) 2020;99:e19747.

47. Kang S, Gao F, Han J, et al. Extracorporeal shock wave treatment can normalize painful bone marrow edema in knee osteoarthritis: A comparative historical cohort study. Medicine (Baltimore) 2018;97:e9796.

48. Gao F, Sun W, Li Z, et al. Extracorporeal shock wave therapy in the treatment of primary bone marrow edema syndrome of the knee: a prospective randomised controlled study. BMC Musculoskelet Disord 2015 161 2015;16:1–8.

49. Cao J, Zhang C, Huang H, et al. Bone Marrow Edema Syndrome of the Foot Treated with Extracorporeal Shock Wave Therapy: A Retrospective Case Series. J Foot Ankle Surg 2021;60:523–528.

50. Vitali M, Naim Rodriguez N, Pedretti A, et al. Bone Marrow Edema Syndrome of the Medial Femoral Condyle Treated With Extracorporeal Shock Wave Therapy: A Clinical and MRI Retrospective Comparative Study. Arch Phys Med Rehabil 2018;99:873–899.

51. Sansone V, Maiorano E, Pascale V, et al. Bone marrow lesions of the knee: longitudinal correlation between lesion size changes and pain before and after conservative treatment by extracorporeal shockwave therapy. Eur J Phys Rehabil Med 2019;55:225–230.

52. Liao C, Xie G, Tsauo J, et al. Efficacy of extracorporeal shock wave therapy for knee tendinopathies and other soft tissue disorders: a meta-analysis of randomized controlled trials. BMC Musculoskelet Disord 2018;19.

53. Zhao W, Gao Y, Zhang S, et al. Extracorporeal shock wave therapy for bone marrow edema syndrome in patients with osteonecrosis of the femoral head: a retrospective cohort study. J Orthop Surg Res 2021;16:21.

54. Baiano C, Romeo A, Zocco A, et al. Bone marrow edema syndrome of the hip: effectiveness of extracorporeal shock waves therapy associated with clodronate. a case report. Bone 2010;Supplement:S91–S92.

55. Wang C, Wang F, Yang K, et al. Treatment of osteonecrosis of the hip: comparison of extracorporeal shockwave with shockwave and alendronate. Arch Orthop Trauma Surg 2008;128:901–908.

56. Xu J, Chen H, Li X, et al. Optimal intensity shock wave promotes the adhesion and migration of rat osteoblasts via integrin β1-mediated expression of phosphorylated focal adhesion kinase. J Biol Chem 2012;287:26200–26212.

57. Frairia R, Berta L. Biological Effects of Extracorporeal Shock Waves on Fibroblasts. A Review. Muscles Ligaments Tendons J 2011;1:138.

58. Wang C, Huang K, Sun Y, et al. VEGF modulates angiogenesis and osteogenesis in shockwave-promoted fracture healing in rabbits. J Surg Res 2011;171:114–119.

59. Haake M, Thon A, Bette M. Unchanged c-Fos expression after extracorporeal shock wave therapy: an experimental investigation in rats. Arch Orthop Trauma Surg 2002;122:518–521.

60. Ma H, Zeng B, Li X. Upregulation of VEGF in subchondral bone of necrotic femoral heads in rabbits with use of extracorporeal shock waves. Calcif Tissue Int 2007;81:124–131.

61. Ma H, Zeng B, Li X, et al. Temporal and spatial expression of BMP-2 in sub-chondral bone of necrotic femoral heads in rabbits by use of extracorporeal shock waves. Acta Orthop 2008;79:98–105.

62. Tischer T, Milz S, Weiler C, et al. Dose-dependent new bone formation by extracorporeal shock wave application on the intact femur of rabbits. Eur Surg Res 2008;41:44–53.

63. Aerssens J, Boonen S, Lowet G, et al. Interspecies Differences in Bone Composition, Density, and Quality: Potential Implications for in Vivo Bone Research. Endocrinology 1998;139:663–670.

64. Cleveland RO, McAteer JA. Physics of Shock-Wave Lithotripsy. Smith's Textb Endourol 3rd Ed 2012;1:527–558.

65. Manara M, Varenna M. A clinical overview of bone marrow edema. Reumatismo 2014;66:184–196.

66. Matheny JB, Goff MG, Pownder SL, et al. An In Vivo Model of a Mechanically-Induced Bone Marrow Lesion. J Biomech 2017;64:258.

67. Tammi RH, Kultti A, Kosma VM, et al. Hyaluronan in human tumors: Pathobiological and prognostic messages from cell-associated and stromal hyaluronan. Semin Cancer Biol 2008;18:288–295.

68. Alaniz L, Garcia M, Rizzo M, et al. Altered Hyaluronan Biosynthesis and Cancer Progression: an Immunological Perspective. Mini-Reviews Med Chem 2010;9:1538–1546.

69. Jackson DG. Immunological functions of hyaluronan and its receptors in the lymphatics. Immunol Rev 2009;230:216–231.

70. Stern R. Hyaluronidases in cancer biology. Semin Cancer Biol 2008;18:275–280.

71. Monzon ME, Fregien N, Schmid N, et al. Reactive Oxygen Species and Hyaluronidase 2 Regulate Airway Epithelial Hyaluronan Fragmentation. J Biol Chem 2010;285:26126.

72. Loniewski KJ, Patial S, Parameswaran N. Sensitivity of TLR4- and -7-induced NFκB1 p105-TPL2-ERK pathway to TNF-receptor-associated-factor-6 revealed by RNAi in mouse macrophages. Mol Immunol 2007;44:3715–3723.

73. Hutás G, Bajnok É, Gál I, et al. CD44-specific antibody treatment and CD44 deficiency exert distinct effects on leukocyte recruitment in experimental arthritis. Blood 2008;112:4999–5006.

74. McErlain DD, Ulici V, Darling M, et al. An in vivoinvestigation of the initiation and progression of subchondral cysts in a rodent model of secondary osteoarthritis. Arthritis Res Ther 2012 141 2012;14:1–12.

75. Korompilias A V., Karantanas AH, Lykissas MG, et al. Bone marrow edema syndrome. Skeletal Radiol 2009;38:425–436.

76. Schett G, Gravallese E. Bone erosion in rheumatoid arthritis: Mechanisms, diagnosis and treatment. Nat Rev Rheumatol 2012;8:656–664.

77. Olive J, Mair TS, Charles B. Use of standing low-field magnetic resonance imaging to diagnose middle phalanx bone marrow lesions in horses. Equine Vet Educ 2009;21:116–123.

78. De Guio C, Ségard-Weisse E, Thomas-Cancian A, et al. Bone marrow lesions of the distal condyles of the third metacarpal bone are common and not always related to lameness in sports and pleasure horses. Vet Radiol Ultrasound 2019;60:167–175.

79. Eustace S, Keogh C, Blake M, et al. MR imaging of bone oedema: mechanisms and interpretation. Clin Radiol 2001;56:4–12.

80. Baumbach SF, Pfahler V, Bechtold-Dalla Pozza S, et al. Clinical Medicine How We Manage Bone Marrow Edema-An Interdisciplinary Approach. J Clin Med 2020;2020:551.

81. Calvo E, Fernandez-Yruegas D, Alvarez L. Core decompression shortens the duration of pain in bone marrow oedema syndrome. Int Orthop 2000;24:88.

82. Dyson SJ, Murray R, Schramme MC. Lameness associated with foot pain: results of magnetic resonance imaging in 199 horses (January 2001--December 2003) and response to treatment. Equine Vet J 2005;37:113–121.

83. Dyson S, Blunden T, Murray R. Comparison between magnetic resonance imaging and histological findings in the navicular bone of horses with foot pain. Equine Vet J 2012;44:692–698.

84. Peterfy CG, Guermazi A, Zaim S, et al. Whole-Organ Magnetic Resonance Imaging Score (WORMS) of the Knee in Osteoarthritis. Osteoarthr Cartil 2004;12:177–190.

85. Phan CM, Link TM, Blumenkrantz G, et al. MR imaging findings in the follow-up of patients with different stages of knee osteoarthritis and the correlation with clinical symptoms. Eur Radiol 2005 163 2005;16:608–618.

86. Kornaat PR, Kloppenburg M, Sharma R, et al. Bone marrow edema-like lesions change in volume in the majority of patients with osteoarthritis; associations with clinical features. Eur Radiol 2007;17:3073–3078.

87. Scher C, Craig J, Nelson F. Bone marrow edema in the knee in osteoarthrosis and association with total knee arthroplasty within a three-year follow-up. Skeletal Radiol 2008;37:609–617.

88. Roemer FW, Guermazi A, Javaid MK, et al. Change in MRI-detected subchondral bone marrow lesions is associated with cartilage loss: the MOST Study. A longitudinal multicentre study of knee osteoarthritis. Ann Rheum Dis 2009;68:1461–1465.

89. Tanamas S, Wluka A, Pelletier J, et al. Bone marrow lesions in people with knee osteoarthritis predict progression of disease and joint replacement: a longitudinal study. Rheumatology 2010;49:2413–2419.

90. Theysohn JM, Kraff O, Maderwald S, et al. MRI of the ankle joint in healthy non-athletes and in marathon runners: image quality issues at 7.0 T compared to 1.5 T. Skelet Radiol 2012 422 2012;42:261–267.

91. Pezeshk P, Alian A, Chhabra A. Role of chemical shift and Dixon based techniques in musculoskeletal MR imaging. Eur J Radiol 2017;94:93–100.

92. Lins CF, Salmon CEG, Nogueira-Barbosa MH. Applications of the Dixon technique in the evaluation of the musculoskeletal system. Radiol Bras 2020;54:33–42.

93. Eggers H, Börnert P. Chemical shift encoding-based water-fat separation methods. J Magn Reson Imaging 2014;40:251–268.

94. Bley TTA, Wieben O, François CCJ, et al. Fat and Water Magnetic Resonance Imaging. J Magn Reson Imaging 2010;31:4–18.

95. Van Vucht N, Santiago R, Lottmann B, et al. The Dixon technique for MRI of the bone marrow. Skeletal Radiol 2019;48:1861–1874.

96. Juras V, Welsch G, Bär P, et al. Comparison of 3 T and 7 T MRI clinical sequences for ankle imaging. Eur J Radiol 2012;81:1846–1850.

97. Crespo-Rodríguez AM, De Lucas-Villarrubia JC, Pastrana-Ledesma M, et al. The diagnostic performance of non-contrast 3-Tesla magnetic resonance imaging (3-T MRI) versus 1.5-Tesla magnetic resonance arthrography (1.5-T MRA) in femoro-acetabular impingement. Eur J Radiol 2017;88:109–116.

98. Zhao R, Liang H, Clarke E, et al. Inflammation in Chronic Wounds. Int J Mol Sci 2016;17.

99. Johnson TRC, Krauß B, Sedlmair M, et al. Material differentiation by dual energy CT: initial experience. Eur Radiol 2007;17:1510–1517.

100. Johnson TRC. Dual-Energy CT: General Principles. Am J Roentgenol 2012;199:S3–S8.

101. Björkman A-S, Koskinen SK, Lindblom M, et al. Diagnostic accuracy of dual-energy CT for detection of bone marrow lesions in the subacutely injured knee with MRI as reference method. Acta radiol 2019;61:749–759.

102. Lev MH, Gonzalez RG. CT Angiography and CT Perfusion Imaging. In: Toga AW, C MJ, eds. Brain Mapping: The Methods. Second Edi. San Diego, CA: Academic Press; 2002:427–484.

103. Cao J, Wang Y, Kong X, et al. Good interrater reliability of a new grading system in detecting traumatic bone marrow lesions in the knee by dual energy CT virtual non-calcium images. Eur J Radiol 2015;84:1109–1115.

104. Ai S, Qu M, Glazebrook KNK, et al. Use of dual-energy CT and virtual non-calcium techniques to evaluate post-traumatic bone bruises in knees in the subacute setting. Skelet Radiol 2014;43:1289–1295.

105. Seo S, Sohn Y, Lee C, et al. Dual-energy CT for detection of traumatic bone bruises in the knee joint. J Korean Soc Radiol 2013;69:487–494.

106. Stewart HL, Siewerdsen JH, Nelson BB, et al. Use of cone-beam computed tomography for advanced imaging of the equine patient. Equine Vet J 2021;53:872–885.

107. Posadzy M, Desimpel J, Vanhoenacker F. Cone beam CT of the musculoskeletal system: clinical applications. Insights Imaging 2018;9:35.

108. Guggenberger R, Gnannt R, Hodler J, et al. Diagnostic performance of dual-energy CT for the detection of traumatic bone marrow lesions in the ankle: comparison with MR imaging. Radiology 2012;264:164–173.

109. Lamba R, McGahan JP, Corwin MT, et al. CT Hounsfield Numbers of Soft Tissues on Unenhanced Abdominal CT Scans: Variability Between Two Different Manufacturers' MDCT Scanners. AJR Am J Roentgenol 2014;203:1013.

110. Lo G, Hunter D, Zhang Y, et al. Bone marrow lesions in the knee are associated with increased local bone density. Arthritis Rheum 2005;52:2814–2821.

111. Carrino JA, Blum J, Parellada JA, et al. MRI of bone marrow edema-like signal in the pathogenesis of subchondral cysts. Osteoarthr Cartil 2006;14:1081–1085.

112. Yusup A, Kaneko H, Liu L, et al. Bone marrow lesions, subchondral bone cysts and subchondral bone attrition are associated with histological synovitis in patients with end-stage knee osteoarthritis: a cross-sectional study. Osteoarthr Cartil 2015;23:1858–1864.

113. Takeuchi M, Goto T, Hamada D, et al. Bone marrow lesions and subchondral cysts develop in the same area of femoral heads on mr imaging of hip dysplasia population. Osteoarthr Cartil 2014;22:S279–S280.

114. Crema MD, Roemer FW, Zhu Y, et al. Subchondral Cystlike Lesions Develop Longitudinally in Areas of Bone Marrow Edema–like Lesions in Patients with or at Risk for Knee Osteoarthritis: Detection with MR Imaging—The MOST Study. Radiology 2010;256:855.

115. Roemer F, Neogi T, Nevitt M, et al. Subchondral bone marrow lesions are highly associated with, and predict subchondral bone attrition longitudinally: the MOST study. Osteoarthr Cartil 2010;18:47–53.

116. Odgaard A, Gundersen HJG. Quantification of connectivity in cancellous bone, with special emphasis on 3-D reconstructions. Bone 1993;14:173–182.

117. Wu Y, Adeeb S, Doschak MR. Using Micro-CT Derived Bone Microarchitecture to Analyze Bone Stiffness – A Case Study on Osteoporosis Rat Bone. Front Endocrinol (Lausanne) 2015;6.

118. Madry H, Kon E, Condello V, et al. Early osteoarthritis of the knee. Knee Surg Sport Traumatol Arthrosc 2016;24:1753–1762.

119. Luyten F, Denti M, Filardo G, et al. Definition and classification of early osteoarthritis of the knee. Knee Surg Sport Traumatol Arthrosc 2012;20:401–406.

120. Kleemann R, Krocker D, Cedraro A, et al. Altered cartilage mechanics and histology in knee osteoarthritis: relation to clinical assessment (ICRS Grade). Osteoarthr Cartil 2005;13:958–963.

121. van den Borne MPJ, Raijmakers NJH, Vanlauwe J, et al. International Cartilage Repair Society (ICRS) and Oswestry macroscopic cartilage evaluation scores validated for use in Autologous Chondrocyte Implantation (ACI) and microfracture. Osteoarthr Cartil 2007;15:1397–1402.

122. Bugatti S, Manzo A, Caporali R, et al. Inflammatory lesions in the bone marrow of rheumatoid arthritis patients: a morphological perspective. Arthritis Res Ther 2012;14:229.

123. McQueen FM, Gao A, Østergaard M, et al. High-grade MRI bone oedema is common within the surgical field in rheumatoid arthritis patients undergoing joint replacement and is associated with osteitis in subchondral bone. Ann Rheum Dis 2007;66:1581–1587.

124. Chao C-C, Chen S-J, Adamopoulos IE, et al. Structural, cellular, and molecular evaluation of bone erosion in experimental models of rheumatoid arthritis: Assessment by μCT, histology, and serum biomarkers. Autoimmunity 2010;43:642–653.

125. Anandarajah A, Thiele R, Giampoli E, et al. Patients with Rheumatoid Arthritis in Clinical Remission Manifest Persistent Joint Inflammation on Histology and Imaging Studies. J Rheumatol 2014;41:2153–2160.

126. Shimizu S, Shiozawa S, Shiozawa K, et al. Quantitative histologic studies on the pathogenesis of periarticular osteoporosis in rheumatoid arthritis. Arthritis Rheum 1985;28:25–31.

127. Dalbeth N, Smith T, Gray S, et al. Cellular characterisation of magnetic resonance imaging bone oedema in rheumatoid arthritis: implications for pathogenesis of erosive disease. Ann Rheum Dis 2009;68:279–282.

128. Campbell TM, Churchman SM, Gomez A, et al. Mesenchymal Stem Cell Alterations in Bone Marrow Lesions in Patients With Hip Osteoarthritis. Arthritis Rheumatol 2016;68:1648–1659.

129. Bugatti S, Caporali R, Manzo A, et al. Involvement of subchondral bone marrow in rheumatoid arthritis: Lymphoid neogenesis and in situ relationship to subchondral bone marrow osteoclast recruitment. Arthritis Rheum 2005;52:3448–3459.

130. Jimenez-Boj E, Nöbauer-Huhmann I, Hanslik-Schnabel B, et al. Bone erosions and bone marrow edema as defined by magnetic resonance imaging reflect true bone marrow inflammation in rheumatoid arthritis. Arthritis Rheum 2007;56:1118–1124.

131. Muratovic D, Findlay DM, Cicuttini FM, et al. Bone matrix microdamage and vascular changes characterize bone marrow lesions in the subchondral bone of knee osteoarthritis. Bone 2018;108:193–201.

132. Kuttapitiya A, Assi L, Laing K, et al. Microarray analysis of bone marrow lesions in osteoarthritis demonstrates upregulation of genes implicated in osteochondral turnover, neurogenesis and inflammation. Ann Rheum Dis 2017;76:1764–1773.

133. Zhang H, Recker R, Lee W-NP, et al. Proteomics in bone research. Expert Rev Proteomics 2014;7:103–111.

134. McCoy AM. Animal Models of Osteoarthritis: Comparisons and Key Considerations. Vet Pathol 2015;52:803–818.

135. Zani DD, De Zani D, Biggi M, et al. Use of magnetic resonance imaging in the diagnosis of bone marrow edema in the equine distal limb: Six cases. Vet Res Commun 2009;33:225–228.

136. Biggi M, Zani DD, De Zani D, et al. Magnetic resonance imaging findings of bone marrow lesions in the equine distal tarsus. Equine Vet Educ 2012;24:236–241.

137. Barrett MF, Selberg KT, Johnson SA, et al. High field magnetic resonance imaging contributes to diagnosis of equine distal tarsus and proximal metatarsus lesions: 103 horses. Vet Radiol Ultrasound 2018;59:587–596.

CHAPTER 4:

LONG-TERM ADVANCED IMAGING INVESTIGATION OF AN EXPERIMENTAL MODEL OF BONE MARROW LESIONS USING THE OVINE FEMORAL CONDYLE

4.1 Introduction

The economic and social impact of joint disease and osteoarthritis (OA) are well-described in both the human and veterinary literature.[1–4] Historically, OA has focused on changes in the articular cartilage, but more recently OA is recognized as a disease that can be affected by all the tissues of the joint, in particular the subchondral bone. Bone marrow lesions (BMLs), also referred to as "bone marrow edema," "bone bruises," or "bone contusions," appear to be early indicators of structural changes within the subchondral bone.[5–7] BMLs can only be diagnosed using magnetic resonance imaging (MRI), where fluid signal appears as high signal intensity on fluid-sensitive T2-weighted sequences, and low to intermediate signal intensity on T1-weighted images.[8] BMLs are clinically challenging as some lesions progress or accelerate degenerative processes within the joint, while other times these lesions appear to regress completely within a matter of months. BMLs are also observed across a variety of conditions and etiologies which include traumatic injuries to the bone or soft tissues of the joint, degenerative arthropathies, inflammatory, ischemic and infectious conditions within the joint, neoplastic and metabolic conditions, and are also occasionally observed incidentally.[9–12] Understanding both the biological behavior and the significance of these lesions will ultimately assist clinicians in effectively managing and prognosticating when BMLs are observed.

Despite the observed frequency and clinical relevance, there is a relative paucity of information about BMLs, with the majority of the literature focused on clinical reports and

observations. Many of these clinical reports focus on a description of BMLs at a single timepoint, recognizing the financial and logistical limitations prevent serial imaging evaluation of BMLs. Patient-specific clinical symptoms, including pain and mobility are often utilized for determination of BML progression or resolution. Since BMLs are often observed in conjunction with other co-morbidities treatment of those conditions are often the therapeutic focus.[13] Across osteoarthropathies, the presence of BMLs are often correlated with disease stage, but are typically not viewed as the inciting cause of joint degeneration.[14–17] As the role of the subchondral bone is further recognized in the etiopathogenesis of degenerative joint disease, further investigation of the impact of maladies of the subchondral bone is warranted.

Advancements in volumetric imaging techniques have greatly improved non-invasive assessment of subchondral bone *in vivo*. Chemical-shift imaging (CSI) techniques with high-field (> 1.0 Tesla) MRI have been used with increasing frequency for musculoskeletal imaging.[18,19] These techniques utilize the inherent differences in resonance frequencies, or spin rates, between protons of fat and water (or non-lipid) molecules when placed in a magnetic field.[20] Two image sets are acquired of the same region of interest using slightly different echo times (TE) settings. In conjunction with higher magnetic field strengths, a set of four images are produced with a high signal-to-noise ratio that highlights fat and water signal separately and in combination (e.g., in and out-of-phase images) providing an increased ability to characterize the tissue properties of bone and soft tissues.[21] In addition to MRI, new techniques in computed tomography (CT), such as dual-energy (DE) can also be used for evaluation of fluid within bone.[22,23] CT has typically been regarded as the superior imaging method for the assessment of bone, but often is criticized in its lack of ability to delineate soft tissue structures without the use of contrast. DE CT allows for evaluation of fluid accumulation within bone, through use of post-processing algorithms that

identify water, fat, and bone within each voxel of scan data. Both DE CT and CSI with MRI are rapid techniques that may be used for the assessment of BMLs.

The understanding of BMLs has been confined to the clinical literature, primarily because a validated experimental model for BMLs did not previously exist. A reproducible experimental model has recently been described using the medial femoral condyle of the ovine femorotibial joint. A 1.1 mm pin is directed from the joint surface to a depth of 8 mm across the articular and calcified cartilage, subchondral and trabecular bone layers. BMLs are visible in the medial femoral condyle within 14 days and are visible for at least 12 weeks. BMLs in this experimental model are highly dynamic, characterized by alterations in the appearance of the BML on MRI every 2 weeks. Histologically, BMLs are characterized by local inflammatory cell infiltrate that is gradually replaced by fibrous and fibrocartilaginous tissue, similar to what has been described in naturally-occurring BMLs.[24] The similarities between this experimental model and what has been clinically observed provides an opportunity to investigate BMLs further, in isolation of other co-morbidities within the joint. Importantly, BMLs were observed for the duration of the 12-week study without other signs of degenerative changes within the joint. The short duration of this study generated numerous questions about the relevance of these BMLs and whether they would ultimately regress or result in OA within the joint. Longer follow-up was required to further understand this experimental model and implications for BML biology and joint health.

The overarching goal of this study was to understand the long-term effects of BMLs within the ovine femorotibial joint, using the previously developed model in the medial femoral condyle. The aim of the study was to use non-invasive volumetric imaging to serially evaluate the changes in experimentally-induced BMLs over time. We hypothesized that (1)

experimentally-induced BMLs that persisted for at least 12 weeks would result in irreversible changes within the subchondral bone leading to degenerative changes in the joint; (2) experimentally-induced BMLs would follow a biological progression for degenerative changes that had previously been observed in the clinical literature; and (3) serial imaging with CT and MRI would be able to accurately depict the changes in subchondral bone. Long-term follow-up for this experimental of model of BMLs solidifies the relevance of the preclinical model and yields a greater understanding of the etiopathogenesis of BMLs and their relationship to degenerative osteoarthropathies across species.

4.2 Materials and Methods

4.2.1 Animals

Two, skeletally-mature, Dorper-cross female sheep were used for this prospective study. All animals were vaccinated, dewormed and confirmed to be healthy prior to the start of the study. Animals were housed indoors, indoors with outdoor run access, or outdoors, depending on the phase of the study, and fed a diet in accordance with the National Research Council. All procedures were approved by the Institutional Animal Care and Use Committee of Colorado State University (Kuali protocol 1181, approved 08/13/2020).

4.2.2 Experimental protocol

Physical and lameness examinations, CT and MRI examinations were performed prior to surgery. Sheep were monitored daily throughout the study for attitude, appetite, and level of comfort. On day 0, sheep were placed under general anesthesia and each medial femoral condyle was treated with penetration with a surgical pin. Sheep were monitored daily for the first week,

and then weekly for the first month, and then prior to each imaging timepoint for degree of weight-bearing in each hind limb. Serum and synovial fluid were collected prior to surgery and at each imaging timepoint. Bilateral imaging of the femorotibial joints with MRI and CT was performed 2 weeks, 3 months, 6 months, 9 months and 1 year post-operatively.

4.2.3 Intra-articular pin application

A medial parapatellar arthrotomy was used to access the medial femoral condyle of three limbs assigned to pin penetration. Femorotibial joints were held in flexion with the patella deviated laterally to access the articular, weight-bearing surface of the medial femoral condyle. A 1.1 mm Steinmann pin was advanced to a depth of 8 mm, through the articular and calcified cartilage layers, subchondral bone plate and into the underlying trabecular bone from the articular surface using a battery-operated surgical drill. After drilling, joint lavage with sterile saline was performed to remove any osteochondral debris and the surgical site was closed routinely in three layers.

For one femorotibial joint, a minimally-invasive approach was used, where a stab incision was made through the skin with the joint in flexion, and then using fluoroscopic guidance the 1.1 mm pin was advanced to an 8 mm depth into the medial femoral condyle. For this animal, joint lavage was not performed and egress of synovial fluid was not observed. Sutures were placed in the skin incision only in this animal.

4.2.4 Gait evaluation

Gait was evaluated pre-operatively, at days 1, 4, 7 and 14 post-operatively, and prior to each imaging timepoint thereafter. Animals were allowed to move freely within a 6 ft x 25 ft area

that they were familiar with for gait evaluation. A semi-objective 0-4 scale was used to grade visible lameness on each hind limb. Briefly, grade 0 was defined a normal ambulation, fully weight-bearing; grade 1 indicated a slight lameness with a partial weight-bearing gait on all steps; grade 2 indicated a moderate lameness with a combination of partial and minimally weight-bearing; grade 3 indicated a marked lameness with non-weightbearing on all steps when walking but partially weight-bearing when herded; and grade 4 indicated non-weight bearing during all ambulation.

4.2.5 Magnetic resonance imaging (MRI)

Femorotibial joints were evaluated under general anesthesia using MRI with animals placed in lateral recumbency. The animal was positioned with the foot entering the gantry first, and with the limb of interest oriented upward to achieve positioning within isocenter. Animals were rotated into the opposite recumbency for imaging of the contralateral limb. MR imaging was performed using a 3 T scanner (Siemens Magnetom Skyra, Siemens Medical Solutions USA, Inc., Malvern, PA, USA) with a bore diameter of 70 cm. A knee coil was used for imaging of all femorotibial joints.

Sequences included proton density fat saturation (PDFS) in all planes (sagittal plane settings: TR 2500, TE 37, flip angle 150, 320; cranial plane settings: TR 2500, TE 48, flip angle 150, matrix 384 x 384, slice thickness 3 mm; transverse plane settings: TR 2840, TE 48, flip angle 127, matrix 384 x 384, slice thickness 3 mm); intermediate-weighted fat suppression via the Dixon method in the sagittal (TR 3500, TE 38, flip angle 123, matrix 320 x 320, slice thickness 3 mm) and cranial (TR 3500, TE 38, flip angle 122, matrix 320 x 320, slice thickness 3 mm) planes; and T1-weighted (TR 650, TE 10, flip angle 150, matrix 384 x 288, slice thickness

3 mm) and T2-weighted 3D double echo steady state in the sagittal plane (TR 11.05, TE 4.18, flip angle 25, matrix 192 x 192, slice thickness 0.6 mm). Voxel dimensions ranged from 0.3-0.6 mm x 0.3-0.6 mm x 0.6-3 mm.

4.2.6 Computed tomography (CT)

CT evaluation of femorotibial joints was performed immediately following MRI using a 64-slice helical fan-beam computed tomography unit (Siemens Somatom Definition AS, Siemens Medical Solutions USA, Inc., Malvern, PA, USA). For CT imaging, animals were placed in lateral recumbency with both hind limbs in extension at the femorotibial joint, with the feet entering the gantry first. Both femorotibial joints were scanned simultaneously. Images were acquired in the transverse plane relative to the joint surface in 3 mm-thick section, with a 0.7 pitch, 106 mm field of view and a 512 x 512 voxel matrix.

Two sequential scans of the femorotibial joints were performed a different energy level in accordance with the manufacturer's settings for the "Dual Energy Edema" protocol for post-processing dual-energy (DE) image reconstruction. Briefly, the high-energy value for scans was 140 kVp, the low-energy value for scanning was 80 kVp. Raw CT data was reconstructed at 0.8 mm thickness x 0.8 mm increment (bone reconstruction kernel) and 2.0 mm thickness x 1.0 mm thickness (standard reconstruction kernel).

4.2.7 Image evaluation

All digital imaging obtained via MR and CT were stored within the picture archiving and communication system (PACS) at Colorado State University. Open-sourced software (Horos Project, version 3.3.6) was used for viewing and evaluating DICOM images. Additionally,

images obtained using the DE protocol with CT were evaluated using the commercially-available platform available through the manufacturer (Syngo.Via, Siemens Medical Solutions, Inc., Malvern, PA, USA).

Post-operative images on MR from each animal were first evaluated for the presence of a BML. If a BML was present, all sequences for a given animal at a specific timepoint were graded for the following parameters: maximum condylar area, maximum BML area, average BML signal, maximum BML signal, minimum BML signal, number of slices where a BML was present, area of the BML on each slice, adjacent muscle signal, and standard deviation of air of the background. A 10 mm^2 circular region of interest (ROI) was used to identify the signal within the BML, muscle and background air. From these parameters, the percent of the condyle occupied, signal-to-noise ratio (SNR), and contrast-to-noise ratio (CNR) of the BML were calculated.[25,26] Briefly, for the SNR the mean signal of the ROI within the BML was divided by the standard deviation of the background air in a ROI of equal size. For CNR, the signal of the ROI of the muscle was subtracted from the signal in the ROI of the BML, and then divided by the standard deviation of the background air ROI. Pre-operative images of animals with BMLs were reviewed and post-operative images were overlaid using imaging software (AnalyzeDirect, version 14.0, Overland Park, KS) in order to calculate baseline SNRs and CNRs in the same location as the post-operative BML.

Magnetic resonance images were overlaid onto CT images to view the extent of the BML. A 3 mm^2 circular ROI was used to evaluate the attenuation in Hounsfield Units (HU) within the BML in the medial femoral condyles for the CT images obtained using the bone reconstruction kernel at 140 kVp. If the BML extended beyond 3 mm^2 and the pin tract was visible, the ROI was placed adjacent to the pin tract, but excluded cortical bone. Multi-planar

reconstruction was used to identify a similar location within the lateral femoral condyle of the same limb to grade the attenuation.

Following sequential CT scans at two energy levels, three data sets of reconstructed images were generated: an 80 kVp set, a 140 kVp set, and an average-weighted set calculated from both tube data at a ratio of 0.5:0.5 to imitate a single 120 kVp image. Blended virtual 120 kVp axial, sagittal, and cranial plane reconstructed images (D kernel) were also used for evaluation. Image sets were transferred to a specific workstation for DE image generation (SyngoVia; Siemens, Erlangen, Germany).

A three-material decomposition technique was used to create a virtual non-calcium image, as has been previously described.[23,27] A color overlay map was automatically generated for the image. Briefly, green-yellow shades corresponded to a BML, and blue-purple shades corresponded to more dense bone. Images sets for each animal at each timepoint were evaluated individually, modifying software parameters to produce the highest quality image for analysis. Briefly, resolution was set at a 2 or 3, maximum attenuation was set at 1500 HU, and threshold attenuation was set at 80-100 HU, with a higher threshold at later timepoints in the study. Three-dimensional volumetric renderings of the femorotibial joint were also generated, with normal bone in shades of blue, and BMLs in shades of green. Conventional grayscale morphologic images were utilized for immediate comparison. If a BML was visible using the color overlay on CT images, the extent of the BML was compared to MR images in all planes on fluid-sensitive sequences.

4.2.8 Statistical analyses

Descriptive statistics were reported in an effort to characterize the apperance of BMLs across timepoints on different imaging modalities and within each sequence on MRI. Categorical data were reported as median ± interquartile range (IQR), and continuous data as mean ± standard deviation. The experimental sample size (4 samples) was calculated using G*Power (version 3.1.1).[28] Specifically, an *a priori* power analysis was conducted using expected mean semi-quantitative scores for the apperance of BMLs in treated joints using MRI obtained from the short-term ovine study using the same pin penetration model. This power analysis resulted in an effected size of 2.5, and a power of 0.95, using a 95% confidence interval and a standard deviation of 1 between groups. All data was analyzed using R software (version 4.0.3, "Bunny-Wunnies Freak Out," R Foundation for Statistical Computing 2020) in RStudio (version 1.2.1335).

Continuous data were evaluated for normality using the Shapiro-Wilk test, and visually using quantile-quantile plots. Although data was obtained from a small sample size of animals and normality was difficult to assess, quantile-quantile plots demonstrated minimal to slight departures of the data from normality. A linear mixed model for repeated measures was implemented in the lme4 package for R with animal and limb as random effects. Model factors were further evaluated by Tukey-Kramer pairwise comparisons using the lsmeans package for R. In cases where data was non-normally distributed, Friedman's test (for repeated measures) or the Kruskal Wallis test (for single timepoint outcomes) were used followed by Wilcoxon pairwise comparisons with a Benjamini-Hochberg correction in the base package for R for repeated measures analyses. For single timepoint analyses, data were compared using a Wilcoxon signed rank test. A level of $P < 0.05$ was used for significance.

4.3 Results

No complications with general anesthesia, surgery, or imaging were observed, and all animals remained healthy for the duration of the study. Results of CT and MRI examinations were considered normal for animals prior to the study. No effect of right vs. left limb were observed for any analyzed outcomes in the study.

4.3.1 Intra-articular pin application

All surgical procedures were performed without complication.

4.3.2 Gait evaluation

All animals were determined to be sound at a walk and healthy prior to the start of the study. One animal displayed grade 1 hind limb lameness in a single limb in the immediate post-operative period. The lameness resolved by the 2-week timepoint without further intervention.

4.3.3 Magnetic resonance imaging

Fluid signal within the bone, consistent with a BML, was observed in the medial femoral condyles of all joints on imaging performed 2 weeks after surgery (Figure 4.1). Fluid signal in all MFCs persisted for the duration of the 12-month study. BMLs maintained a consistent appearance across joints, and at 2 weeks appeared as a central region of iso- to hyperintensity surrounded by a region of hypointensity relative to the surrounding trabecular bone on Dixon out phase images; and reduced variation with an intermediate intensity on Dixon in phase images. On Dixon fat only images, the BML appeared as a hypointense region, and as a hyperintense

region on Dixon water only images, relative to the trabecular bone. Similar to the Dixon water only images, BMLs appear as a hyperintense region relative to the trabecular bone on PDFS images. Experimentally-induced BMLs were visible on T1-weighted images with an intermediate signal intensity, and appeared hyperintense on T2-weighted 3D double echo steady state images relative to the surrounding trabecular bone. The pin tract for BML induction was visible on most sequences and time points.

The BML appeared more organized by 3 months post-operatively, maintaining a central region of hyperintensity on Dixon in phase images, and with a decrease the size of fluid signal on Dixon water only and PDFS images (Figure 4.2). Subjectively, the BML size changed very little at the 6-month imaging time point and beyond. However, at 6 months, three of the medial femoral condyles had one or multiple coalescing circular-to-ovoid hyperintense regions visible on Dixon in phase and out phase images within the trabecular bone region, similar in appearance to a subchondral bone cyst or sequestrum (Figure 4.3). The other medial femoral condyle maintained a large circular region more distal in the medial femoral condyle within the subchondral and distal trabecular bone. In all animals, these cyst-like regions were visible at the 9- and 12-month imaging time points, with some variation in signal intensity and size (Figure 4.4).

The volume of the observed BMLs and percentage of the medial femoral condyle occupied by a BML was greatest 2 weeks after induction (Table 4.1). The volume of the BML on Dixon water only and PDFS images decreases over time, however this decrease was only statistically significant between the 2-week imaging timepoint and all later timepoints ($P < 0.001$). The trend of a decrease in BML volume was also reflected as a decrease in the percentage of the medial femoral condyle occupied by a BML. The percentage of the condyle

occupied by a BML decreased ($P < 0.001$) at the 3-, 6-, 9- and 12-month timepoints relative to the 2-week imaging timepoint. The percentage of the condyle occupied by a BML also decreased ($P = 0.05$) between the 6- and 12-month imaging timepoints. The volume of the observed BML or the percentage of the medial femoral condyle occupied by a BML remained consistent on Dixon in phase images over the course of the study.

SNRs and CNRs of the experimentally-induced BMLs varied across sequences over the study period (Table 4.2). For Dixon in phase images, SNR decreased ($P < 0.01$) at all imaging timepoints relative to baseline, and CNR decreased ($P < 0.01$) at all imaging time points relative to baseline, and decreased ($P = 0.04$) between the 2-week and 3-month imaging timepoints. In Dixon water only images, SNR was increased ($P = 0.005$) at the 2-week imaging timepoint relative to baseline, and decreased ($P \leq 0.05$) at the 6-, 9- and 12-month imaging timepoints relative to the 2-week timepoint. The CNR within the BML increased ($P < 0.05$) post-BML induction, relative to baseline values. On PDFS images, SNR increased ($P = 0.001$) at the 2-week imaging timepoint relative to baseline, and then decreased ($P \leq 0.05$) at all later imaging timepoints relative to the 2-week timepoint. CNR increased ($P < 0.05$) at the 2-week imaging timepoint relative to baseline, and remained consistent thereafter. No differences were observed between fluid-sensitive sequences (i.e., Dixon only and PDFS images) across timepoints for measurement of SNR and CNR within the BML.

4.3.4 Computed tomography

Measured attenuation values across medial femoral condyles were not different from on another at baseline. An increase ($P < 0.05$) in attenuation was observed at all imaging timepoints relative to baseline. The increase in attenuation in the region within and at the margins of the

BML persisted for the duration of the 12-month evaluation period. An increase ($P = 0.02$) in measured attenuation was also observed at the 12-month imaging timepoint compared to the 2-week timepoint. Mean CT attenuation values are shown in Figure 4.5. Subchondral and trabecular cysts were visible on CT by 6 months post-BML induction (Figure 4.6).

Bone marrow lesions were successfully visualized on DE CT post-processed reconstructed images with color overlay (Figure 4.7). The region of the BML was predominantly green, with some yellow and red, corresponding to fluid attenuation. This appearance remained consistent across all imaging timepoints. The fluid signal associated with the BML had a larger area in all planes on fluid-sensitive MR sequences across all timepoints, compared to virtual non-calcium images from DE CT data sets.

4.4 Discussion

A focal osteochondral defect extending from the articular surface into trabecular bone is sufficient to induce BMLs in the ovine medial femoral condyle that are visible on volumetric imaging for at least 12 months. Experimentally-induced BMLs were visible within 2 weeks of surgery using high-field MRI, with characteristics similar in appearance what is clinically observed across species. CT and MRI are volumetric imaging modalities that provide complimentary information about physiologic and structural changes that occur within the subchondral and trabecular bone secondary to the presence of BMLs. The duration of this study demonstrates that BMLs are dynamic and change over time, and may persist in the joint in the absence of clinical lameness. Characterization of BMLs over a 12-month period enables a greater understanding about the relationship between BMLs, clinical disease, and joint health.

The initial development for this experimental model of BMLs demonstrated that direct trauma to the osteochondral tissues is a valid method for induction of these lesions. The overarching goal of this study was to follow BMLs over time, however, a single limb in this study was treated by a minimally invasive method for pin penetration of the articular surface. One potential concern of the open approach to the femorotibial joint is that this technique may induce a local synovitis. It is possible that even low-grade synovitis may contribute to the progression of chondropathy by accelerating cartilage catabolism.[29–31] The single limb where the pin was advanced through a stab incision under fluoroscopic guidance developed a consistent BML to other limbs treated by an open approach, supporting the conclusion that changes within the joint were due to BMLs, and not the surgical approach to the joint. Modification of this model toward a minimally-invasive technique for BML induction should be considered for additional animals moving forward.

It is difficult to accurately describe the duration of BMLs based on the clinical literature. In humans with rheumatoid arthritis (RA), McQueen et al followed a single group of patients for six years.[32] BMLs were visible at each assessment point of the study, however bone erosions progressed over time. Other studies have reported that BMLs resolve in as little as 3 weeks, or may be visible for up to 2 years.[33,34] In horses with BMLs, follow-up MR study data is limited, ranging from 6-12 months after the original diagnosis.[35,36] In many cases, logistical, financial, and insurance-mediated factors limit repeat MRI studies to understand how long BMLs are present, and furthermore how they change over time. Acutely induced BMLs in this study persist for at least 12 months. The presence of these BMLs appears to have minimal influence on the health of the joint overall. Effusion within the joint was subjectively present in the immediate post-operative period but was relatively stable at the 3-month imaging timepoint and thereafter.

Sclerosis within the subchondral bone and osseous cyst lesions were visible on both MR and CT images, but degenerative changes such as osteophytes, attrition of the subchondral bone, or loss of articular cartilage in association with the osteochondral defect were not visible. A strong correlation between cartilage injury and BMLs has been described[17,37], so it is surprising that further changes within the joint were not observed at 12 months. The lack of degenerative changes may suggest that this model does not induce sufficient changes in all joint tissues or in the joint as whole to create early-stage OA, or that more substantial signs of joint disease take over 12 months to occur when a BML exists in isolation. Segal et al found that elevated articular contact stresses over 30 months result in worsening cartilage morphology and increasing BML size[38], suggesting more time may be needed to understand the effects of BMLs within the joint. It is also critical to acknowledge that BMLs are often observed and described in conjunction with other conditions within the joint, ranging from all stages of OA, RA, injuries to the anterior cruciate ligament, fractures, neoplasia, and osteoporosis.[39] This study then has the ability to describe the effects of BMLs in isolation and without other underlying or associated co-morbidities.

From a clinical perspective, it is likely that the majority of cases of BMLs are diagnosed due to pain.[8,9,40] Importantly, in this model, changes within the subchondral bone and the presence of a BML did not result in clinically-observable gait abnormalities. There are a number of reasons why this may be the case, including the fact that a bilateral hind limb model was used so changes in gait would likely be symmetrical between both hind limbs, the evolutionary consideration that sheep are prey animals and may be more adept at tolerating minor discomfort associated with osteochondral injury, or that these BMLs in this model are different from what is clinically observed and therefore have different clinical properties. Zhang et al demonstrated that

BMLs alone do appear to cause pain, as knee pain decreased with reduced BML size.[41] It is also plausible that the pain observed with BMLs reflects a later state of disease, where irreversible damage to the articular and synovial tissues has occurred, in addition to changes within the subchondral bone. BML-related pain is hypothesized to occur as a result of irritation secondary to increased intraosseous pressure or disruption of sensory nerves within the neurovascular bundles of the bone marrow.[42] Increased intraosseous pressure occurs because of fluid accumulation, either due to capillary leakage secondary to local modification of the capillary wall, or secondary to increased vascular pressure which may be hyperemic (i.e., due to an increased blood flow to the marrow) or congestive (i.e., from a decrease in clearance from the marrow tissue). Albeit small, the pin tract used to induce BMLs in this model seemingly creates an "open" system between the bone and joint. It is possible that this may be responsible for the lack of pain, as this mimics the core decompression techniques to reduce intramedullary pressure which has been reported to alleviated pain in clinical cases of BMLs.[43–47] Interestingly, some studies on core decompression report complete resolution of BMLs following treatment[43], which was not observed here.

It is important to distinguish that simply the absence of pain does not necessarily imply resolution of a BML. BMLs are often described as "self-limiting" and are managed with a period of rest from activity and treatment of the underlying condition, when applicable.[48] Arguably, this may not be the most appropriate treatment course and may perpetuate a cycle of continued remodeling within the subchondral bone, which may include the development of subchondral bone cysts. Subchondral bone cysts are commonly associated with OA in both humans and horses.[14,49–53] Subchondral bone cysts are also strongly associated with BMLs, where BMLs precede appearance of cysts.[6,7,15,24,54–57] Proposed theories for the pathogenesis of subchondral

bone cyst formation include the Bone Contusion Theory and the Synovial Breach Theory.[58] The Synovial Breach Theory describes that cysts are a result of synovial fluid entering the cavity, increasing intra-osseous pressure resulting in proliferation of myxomatous tissue within the bone marrow and cyst expansion. In contrast, the Bone Contusion Theory describes cysts as a result of microscopic contusions within the subchondral bone resulting in focal necrosis, followed by increased intra-articular pressure resulting in the extension of synovial fluid into the subchondral bone through gaps in the articular surface. Both theories may reasonably explain what was observed in this experimental model. The pin tract creates a full thickness breach of the articular cartilage, resulting in the influx of synovial fluid, as described in the Synovial Breach Theory. Additionally, the breakdown products of synovial fluid are pro-inflammatory[59,60], and this may perpetuate the local inflammation within the bone. In support of the Bone Contusion Theory is the known damage to the subchondral and trabecular bone and the histologically observed bone remodeling associated with this model.

Subchondral bone cysts within the BML may also be the result of mechanical damage to the subchondral bone followed by persistent local inflammation and remodeling, consistent with what was observed histologically in previous work with this model. Although the assertion that BMLs (and their sequela) represent damage in the subchondral bone is commonly made[61–63], there are few studies that directly analyze the effect of microdamage since the majority of the literature is in the clinical setting. It is clear however, that the type of damage—including trabecular microfracture, linear microcracks, and diffuse damage—have unique biological and mechanical effects.[64] Broadly, microdamage can result from an acute loading event or may be the result of repeated cycling a lower magnitude. Various studies have attempted to understand the relationship between the amount of microdamage incurred by the bone and the effect on the

structural tissue properties. Consistently across these studies, the conclusion is that even small amounts of microdamage (1-2% damage volume fraction) can cause a 50-60% reduction in strength with subsequent mechanical loading.[65–71] Thinning of the cartilage layer and erosions may also increase focal stress in the subchondral bone, as demonstrated through finite element analysis of the hip.[72] The biological consequences of microdamage can be monumental, and this model amplifies microdamage to a macroscopic scale. Microdamage is a well-recognized stimulus for bone resorption and remodeling, as seen here. Remodeling creates cavities within bone that may act as stress concentrators, promoting further microdamage in a cyclic fashion.[65] Cancellous bone appears to be more tolerant of this type of stress, with the ability to recover to a closer approximation of structure and function following trauma. In the context of BMLs, microdamage and subsequent remodeling secondary to the presence and persistence of BMLs may ultimately result in the formation of these subchondral cysts as a reflection of the cancellous bone mechanical properties in an attempt to stabilize after acutely induced damage. Repeated loading of the joint after damage with the pin prevents sufficient healing and fibrous tissue remains in the space. The bone adjacent to the pin tract undergoes further damage with local osteonecrosis secondary to a lack of osteocytes in the damaged area, followed by the formation of fibrotic, avascular marrow.[73–75] Multiple studies have reported incident subchondral cysts developed in regions of BMLs (up to 92%), which supports this progression of disease and the aforementioned Bone Contusion Theory.[76,77] Furthermore, 46.5% of MRI-detected subchondral cysts were present in regions without full-thickness cartilage defects, which provide clinical evidence against the Synovial Breach Theory. Certainly, not every BML observed clinically results in the formation of a subchondral cyst, but the strong association between the two conditions is worth noting.

Despite the fact that subchondral cysts are often presented as a hallmark sign of OA, and a correlation between cartilage loss and subchondral cysts has been described[14,52,78], the exact etiologic link between BMLs, subchondral cysts and OA is still under investigation. Combining information from multiple studies, a reasonably convincing etiopathogenesis can be concluded. Stemming from Ondrouch's stress-induced bone resorption theory, and intact cartilage later distributes an applied load evenly across the subchondral bone region.[49] Once cartilage thins or deteriorates in response to acute overload or chronic cycling, focal stress in this region leads to microfractures in the subchondral bone and the development of BMLs. Osteoclastic bone resorption occurs, inducing the specific formation of a cystic lesion.[79] Fibrous and fibrocartilaginous tissue within the cyst have increased expression of inflammatory cytokines, including prostaglandin E2, leading to further expansion of the cyst.[80,81] In addition to increased inflammatory cytokines, increased numbers of osteoblasts and osteoclasts are present in the region. Concurrently, MMP-1 is secreted by subchondral bone-lining cells which degrades non-mineralized type I collagen, exposing binding sites that further stimulate osteoclasts.[82–86] As OA progresses, apoptotic osteocytes continue to secrete MMP-1 advancing the cycle of inflammation and degradation.[87] Histological characterization of the induced chronic BMLs and associated subchondral cysts was not a direct outcome of this study, but further work in this area is needed to confirm this experimental model is consistent with the described etiopathogenesis. In the short-term study using this model (see Chapter 3), many cellular characteristics—including an abundance of fibrous and fibrocartilaginous tissue, increased numbers of osteoblasts and osteoclasts, and focal osteonecrosis associated with the pin tract in the region of the BML—were observed. Although additional signs of OA were not observed in the joint after 12 months, the

presence and persistence of both BMLs and subchondral cysts is strongly suggestive of early OA and mimics what has been described in the clinical literature.

In this study, subchondral cysts were visible in all limbs within the region of the BMLs by 3-6 months after surgical induction on both CT and MR images. BMLs and subchondral cysts were well-visualized across multiple MR sequences. The volume of the hyperintense fluid signal (relative to the trabecular bone) on PDFS and Dixon water only images decreased over the course of the study. The volume of the BML remained relatively consistent on Dixon in phase images, suggesting the true fluid component of the BML may decrease over time, being replaced by myxomatous tissue and sclerosis within the affected region. The presence of sclerosis within the region of the BML likely contributed in part to the discrepancy between the volume of the BML on MRI compared with DE CT.[27] Given that discrepancies in BML volume on MRI and DE CT were visible even 2 weeks after surgery prior to bone remodeling, it is likely that other factors played a role. The proximity of fat (-30 to -70 HU) vs water (0 HU) attenuation values, make it inherently challenging for correct assignment of voxels for image generation using a virtual non-calcium technique.[88] A higher energy separation (i.e., 60 kVp and 140 kVp) with the use of appropriate filters, settings and kernels, careful calibration of the scanner against known tissue phantoms, and the use of dual-source scanners that are highly specialized for DE imaging, are all utilized for production of the most ideal final image. The primary emphasis in the literature regarding DE CT for detection of BMLs is directed toward the ability of this technique to detect BMLs, rather than specifically in measuring the BML volume.[23,89–92]

Across samples, the subchondral cysts appear small to intermediate in size, and appear multi-lobulated with irregular borders. This morphology differs from other experimental work, including in the horse where experimentally-induced subchondral cysts tended to be more

spherical and larger in size.[53,93,94]Although the volume of the subchondral cysts was not specifically measured, they appear to be relatively stable over the 6-9 months, without substantial enlargement. Dramatic changes in morphological characteristics have been observed with the enlargement of clinically observed subchondral cysts in horses[81], as well as within the human literature[50,80,95–98]. CT data acquired in this study demonstrate a more distinct sclerotic rim surrounding the cyst over time with a more defined organization of surrounding bone, however, μCT analysis would be needed to confirm such observations. Based on one study, it has been argued that the drive toward a larger spherical morphology is driven by surface tension which reflects the interplay between mechanical loading, forces at the fluid-bone interface within the joint, and local remodeling within the bone.[81] Surprisingly, no correlation with cyst size and morphology and disease severity has yet been established. A more comprehensive evaluation of bone structure surrounding the cyst is warranted to fully characterize the observed changes over time.

In conclusion, these data affirm focal, acute trauma extending from the articular cartilage into the trabecular bone is sufficient to induce BMLs as detected with fluid-sensitive sequences on MRI. Serial evaluation of BMLs demonstrates persistence of the induced BML for at least 12 months and evolution of pure fluid signal toward a subchondral cyst morphology within the trabecular bone. The relationship between BMLs, subchondral cysts, and OA remains an active area of investigation, but the highly correlative relationship across clinical data defines a plausible etiology for lesion progression. Further histologic, biochemical, and mechanical investigation will yield greater insight into the long-term impact of BMLs and their relationship to joint health and function.

4.5 Figures

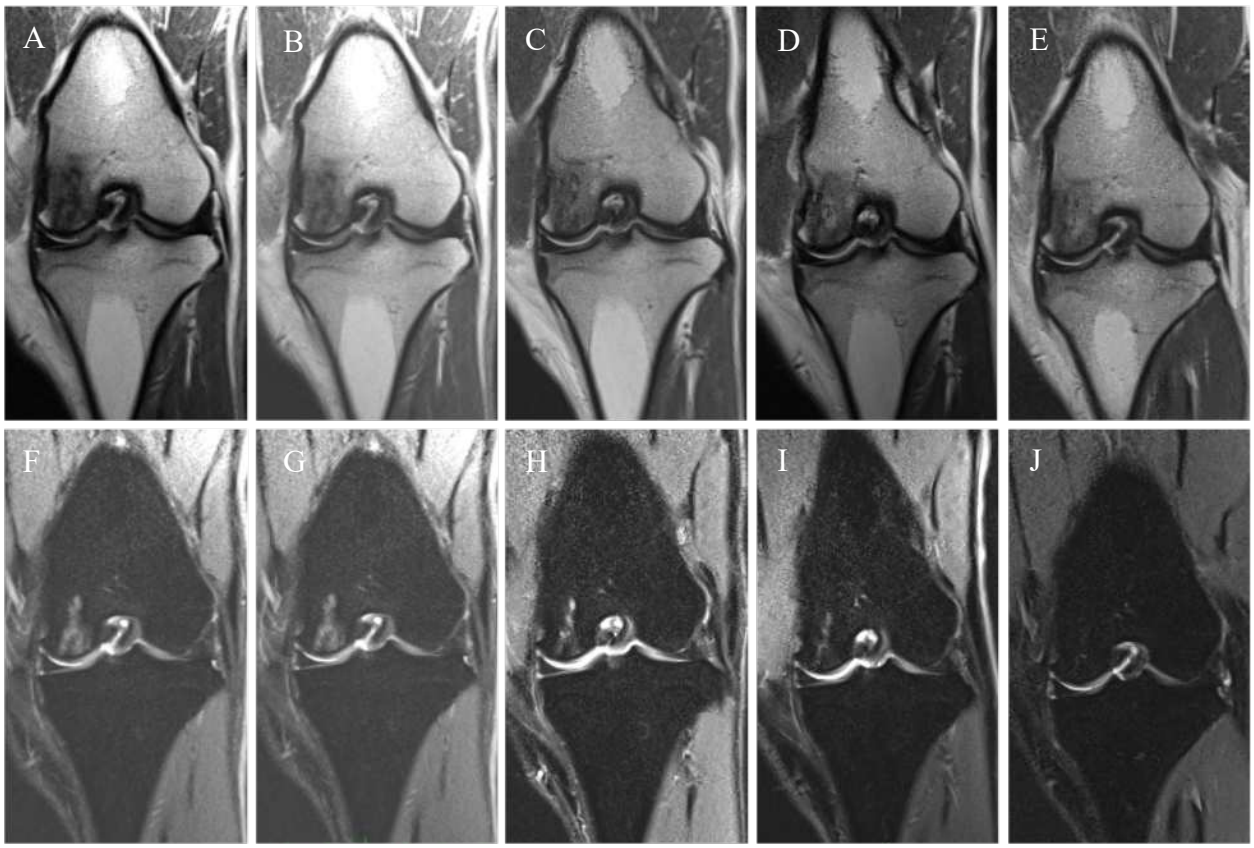

Figure 4.1 – Paired, serial cranial plane magnetic resonance images of an experimentally-induced bone marrow lesion (BML) in the medial femoral condyle of a single animal. Upper row: Dixon in phase images; lower row: Dixon water only images. Each column represents a different timepoint post-induction: (A, F) 2 weeks, (B, G) 3 months, (C, H) 6 months, (D, I) 9 months, and (E, J) 12 months. The visible fluid signal within the bone on Dixon water only images (lower row) decreased over time but remains relatively constant on Dixon in phase images (upper row).

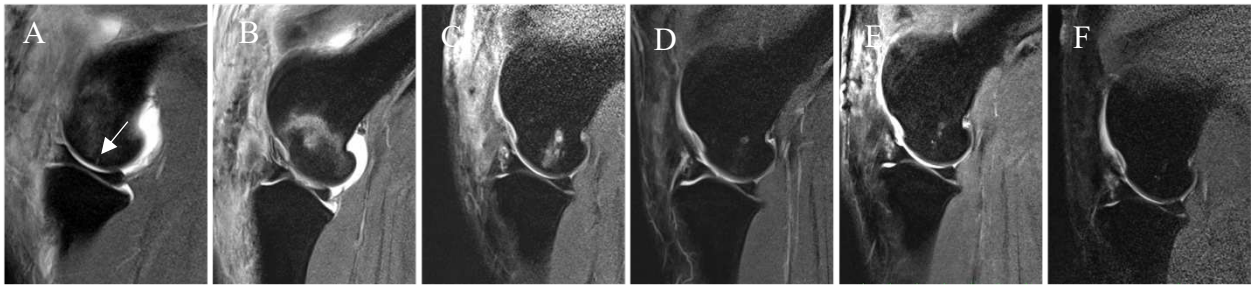

Figure 4.2 – Serial sagittal plane Dixon water only sequence magnetic resonance images of an experimentally-induced bone marrow lesion in the medial femoral condyle of a single animal. Each image represents a different timepoint, with the exception of images (A) and (B) which are sequential slices at the same timepoint, as the pin tract is visible in (A, white arrow), but the area of fluid signal is largest in (B). Imaging timepoints post-induction include: (A, B) 2 weeks, (C) 3 months, (D) 6 months, (E) 9 months, and (F) 12 months. The visible fluid signal within the bone decreases over time.

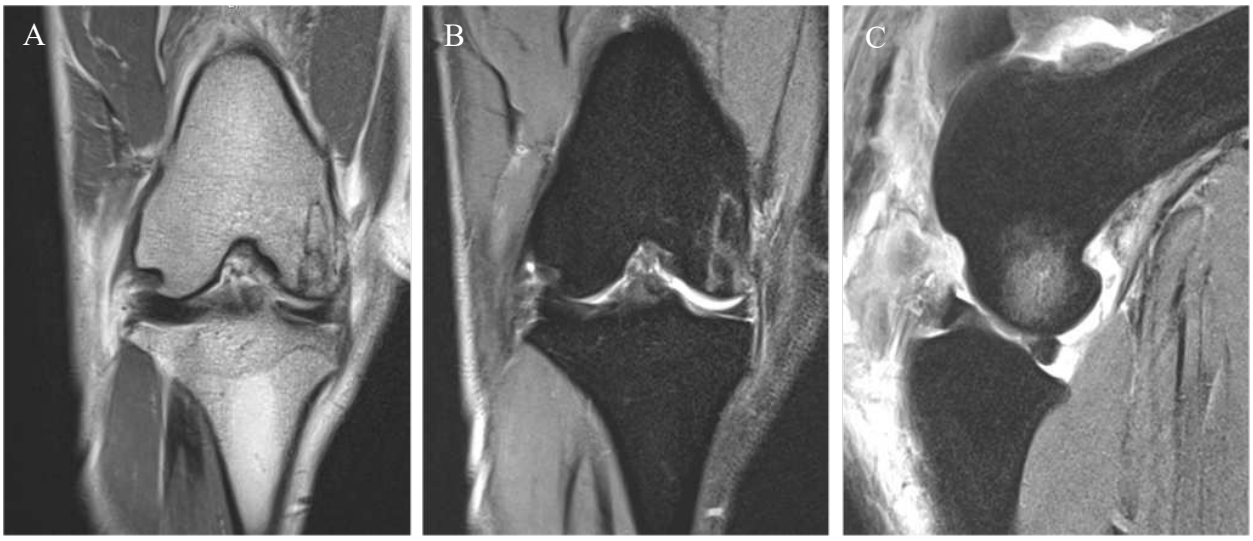

Figure 4.3 – Cranial (A, B) and sagittal (C) plane magnetic resonance images of an experimentally-induced bone marrow lesion (BML) from a single animal at 3 months post-surgery. Dixon in phase (A) and water only (B, C) images can be used to characterize the changes in fluid signal within the subchondral and trabecular bone of the medial femoral condyle. The BML has developed a multilobulated appearance, consistent with the early appearance of a subchondral cyst.

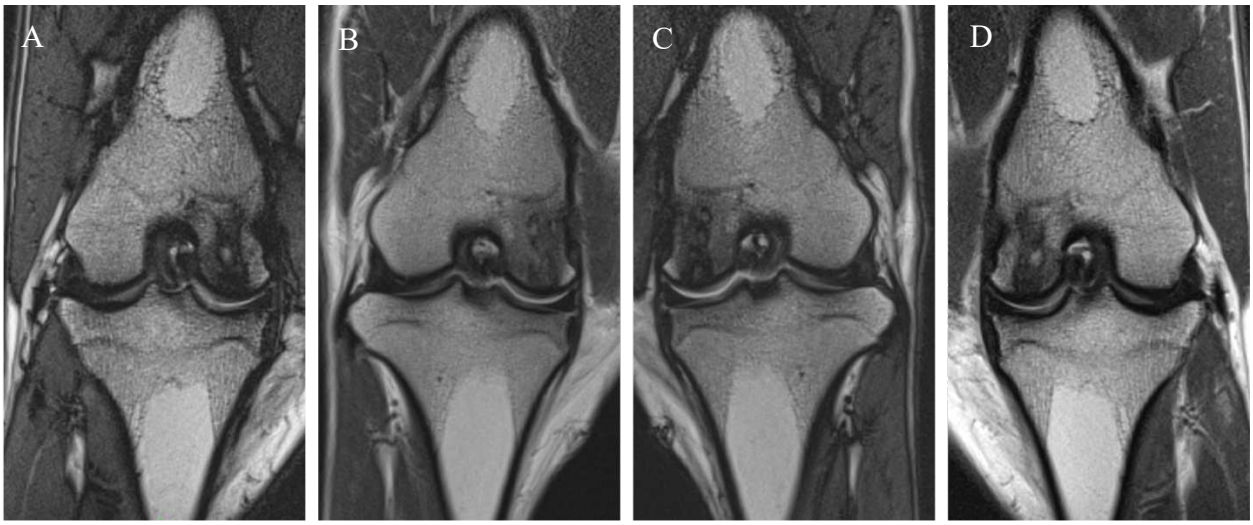

Figure 4.4 – Cranial plane Dixon in phase sequence magnetic resonance images of experimentally-induced bone marrow lesions (BMLs) in each of the four treated medial femoral condyles of two animals at 6 months post-surgery. A singular or multilobulated coalescing cystic lesion is visible in the region of the induced BML, with slight differences between limbs. Images (A) and (C) are from contralateral limbs of the same animal, images (B) and (D) are from the other study animal.

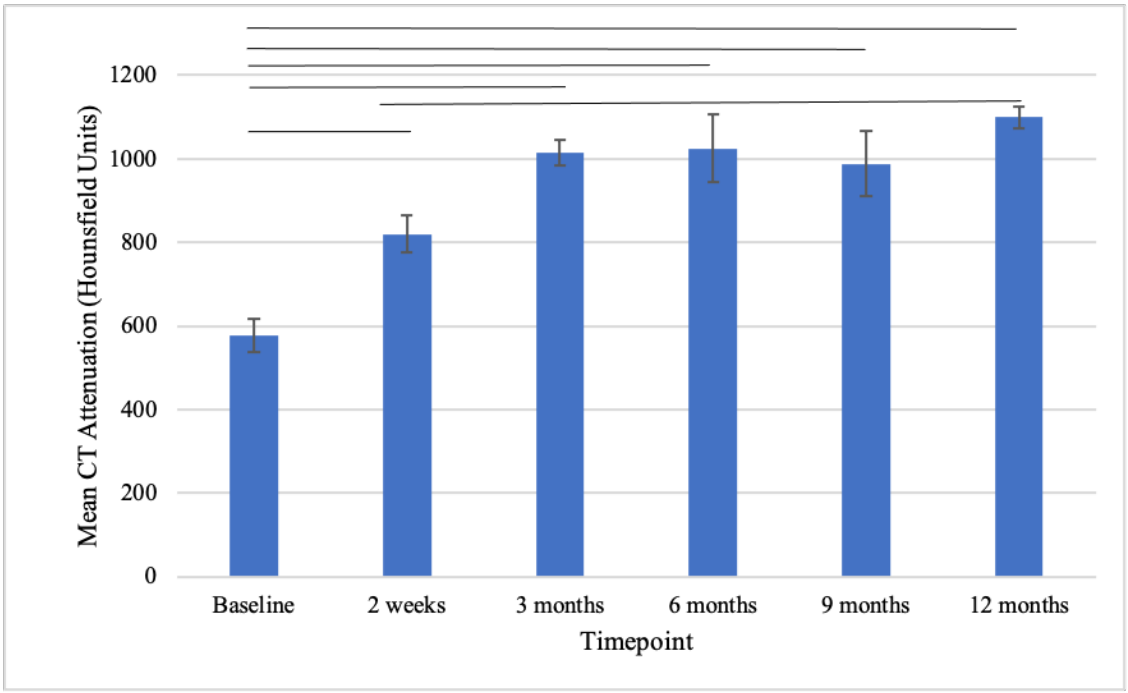

Figure 4.5 – Mean ± standard error for measured attenuation (Hounsfield Units) on computed tomography in medial femoral condyles with experimentally-induced bone marrow lesions (BMLs). An increase in attenuation was visible at all timepoints after experimental induction of BMLs, relative to baseline. Additionally, an increase in attenuation was visible at 12 months, compared to 2 weeks. Significant ($P < 0.05$) comparisons are indicated by the horizontal lines.

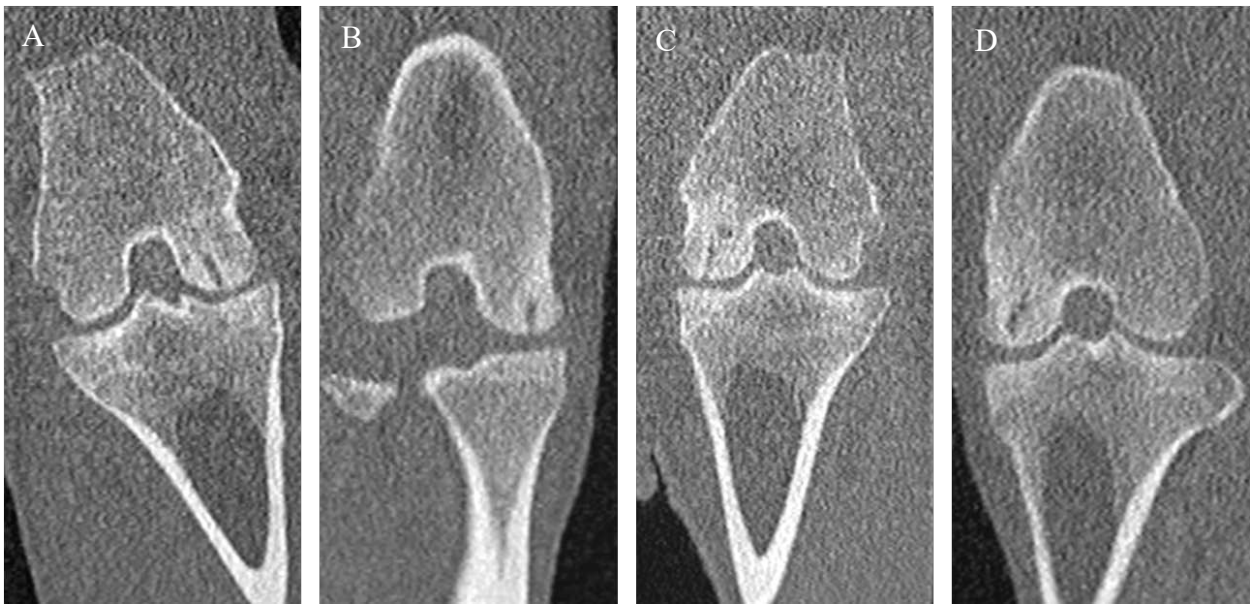

Figure 4.6 – Cranial plane computed tomographic images of experimentally-induced bone marrow lesions (BMLs) in each of the four treated medial femoral condyles of two animals at 6 months post-surgery. A singular or multilobulated coalescing cystic lesion is visible in the region of the induced BML, with slight differences between limbs. Images (A) and (C) are from contralateral limbs of the same animal, images (B) and (D) are from the other study animal.

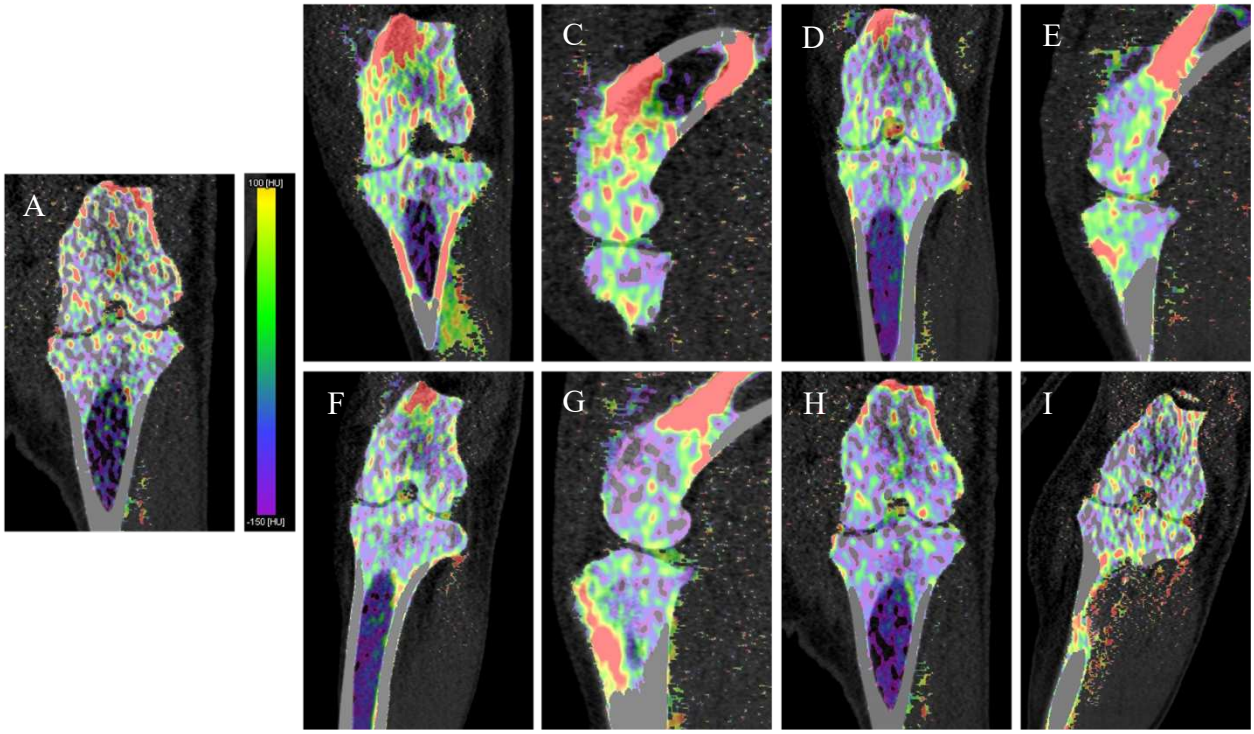

Figure 4.7 – Cranial and sagittal plane serial computed tomographic (CT) images of the femorotibial joint from a single animal with experimentally-induced bone marrow lesions in the medial femoral condyle. CT data sets of the femorotibial joint obtained with tube voltage settings of 80 and 140 kVp were post-processed using a virtual non-calcium dual-energy technique followed by color overlay using a commercially-available software. Timepoints include (A) baseline, (B, C) 2 weeks, (D, E) 3 months, (F, G) 6 months, (H) 9 months, and (I) 12 months post-surgery. Fluid attenuation depicted by the green/yellow color is visible in the medial femoral condyle beginning at 2 weeks, and persists throughout the 12-month study duration.

4.6 Tables

Table 4.1 – Mean ± standard deviation for the percent of the medial femoral condyle with a visible bone marrow lesion (BML) and volume of BML on fluid-sensitive magnetic resonance (MR) images across time. A 1.1 mm Steinmann pin was drilled to an 8 mm depth in a total of 4 medial femoral condyles through the articular and calcified cartilage, subchondral and trabecular bone layers to induce a BML. PDFS: proton density fat saturation. Difference in the number of a given symbol indicate a significant ($P < 0.05$) difference between measurements within a specific sequence and plane combination at a given timepoint.

Timepoint	Plane	Sequence	Percentage of Condyle with BML	Volume of BML (mm^3)
2 weeks	Cranial	Dixon, in phase	181.37 ± 67.17	52.34 ± 20.68
		Dixon, water only	218.45 ± 61.29*	67.59 ± 27.4*
		PDFS	167.36 ± 58.27*	58.23 ± 25.42*
	Sagittal	Dixon, in phase	147.36 ± 19.9	43.01 ± 15.82*
		Dixon, water only	162.58 ± 51.04*	64.66 ± 20.56*
		PDFS	155.9 ± 42.67*	64.07 ± 25.24*
3 months	Cranial	Dixon, in phase	192.02 ± 59.97	43.59 ± 10.17
		Dixon, water only	71.15 ± 28.52**	11.39 ± 5.07**
		PDFS	60.15 ± 31.84**	7.49 ± 3.85
	Sagittal	Dixon, in phase	124.42 ± 28.64	28.55 ± 11.4
		Dixon, water only	53.44 ± 26.24**	12.06 ± 7.11**
		PDFS	46.55 ± 16.58**†	13.23 ± 6.73*
6 months	Cranial	Dixon, in phase	141.52 ± 35.35	34.78 ± 12.37
		Dixon, water only	51.61 ± 37.38**	5.68 ± 3.08
		PDFS	33.94 ± 28.63**	9.55 ± 4.68
	Sagittal	Dixon, in phase	103.55 ± 39.47	24.43 ± 13.12**
		Dixon, water only	39.17 ± 29.85**	7.59 ± 5.71**
		PDFS	23.24 ± 12.15**	4.46 ± 2.68**
9 months	Cranial	Dixon, in phase	164.18 ± 45.16	101.33 ± 143.51
		Dixon, water only	60.44 ± 27.99**	5.3 ± 1.72**
		PDFS	36.64 ± 28.6**	2.76 ± 1.67
	Sagittal	Dixon, in phase	122.55 ± 47.13	27.7 ± 12.2
		Dixon, water only	27.99 ± 19.46**	4.56 ± 2.99**
		PDFS	21.52 ± 13.61**	4.01 ± 2.42**
12 months	Cranial	Dixon, in phase	167.35 ± 53.88	43.42 ± 16.54
		Dixon, water only	25.79 ± 22.05**	2.06 ± 1.92**
		PDFS	16.48 ± 19.92**	0.89 ± 1.04**
	Sagittal	Dixon, in phase	148.89 ± 32.87	29.3 ± 9.67
		Dixon, water only	24.25 ± 21.4**	2.48 ± 2.18**
		PDFS	8 ± 6.91**††	2.85 ± 4.4**

Table 4.2 – Mean ± standard deviation for signal-to-noise (SNR) and contrast-to-noise (CNR) ratios from Dixon in phase and water only, and proton density fat saturation (PDFS) sequences on magnetic resonance (MR) imaging of the experimentally-induced bone marrow lesions (BMLs) in the medial femoral condyles (MFCs) of sheep across the 12-month study. Different numbers of the same symbol indicate a significant ($P < 0.05$) difference between measurements within a specific sequence and plane combination between timepoints.

Timepoint	Group	Plane	SNR	SNR, Maximum	SNR, Minimum	CNR
Baseline	Dixon, in phase	Cranial	51.75 ± 10.46*	--	--	27.3 ± 9.42*
		Sagittal	48.71 ± 23.04	--	--	22.62 ± 11.38
	Dixon, water only	Cranial	37.88 ± 38.93	--	--	21.22 ± 57.29
		Sagittal	2.64 ± 1.41*	--	--	-33.63 ± 13.23*
	PDFS	Cranial	6.63 ± 2.38*	--	--	-18.26 ± 7.32*
		Sagittal	7.56 ± 6.41	--	--	-23.86 ± 13.34
2 weeks	Dixon, in phase	Cranial	33.09 ± 10.3	54.79 ± 11.91	19.29 ± 3.72	10.01 ± 8**†
		Sagittal	26.1 ± 9.76	49.58 ± 26.88	23.88 ± 9	4.85 ± 5.84
	Dixon, water only	Cranial	26.6 ± 8.34	36.79 ± 12.08	8.85 ± 5.92	159.27 ± 23.17
		Sagittal	27.72 ± 13.54**†	38.96 ± 13.78	8.64 ± 3.37	-1.61 ± 4.23**
	PDFS	Cranial	20.68 ± 9.4**†	30.46 ± 13.67	8.69 ± 3.22	-3.75 ± 10.57**
		Sagittal	17.64 ± 12.19	33.93 ± 9.42	5.81 ± 2.47	-8.65 ± 10.32
3 months	Dixon, in phase	Cranial	18.16 ± 6.96**	40.1 ± 4.32	9.01 ± 4.03	-7.59 ± 6.26**††
		Sagittal	28.36 ± 14.66	52.83 ± 27.21	15.68 ± 11.05	-0.39 ± 3.2
	Dixon, water only	Cranial	16.53 ± 2.28	27.64 ± 2.51	6.38 ± 2.15	-13.4 ± 5.31
		Sagittal	18.51 ± 11.73	33.7 ± 20.2	8.03 ± 5	-8.38 ± 4.95**
	PDFS	Cranial	12.65 ± 1.82	16.28 ± 10.49	5.6 ± 2.47	-4.52 ± 5.04**
		Sagittal	25.33 ± 14.18	49.53 ± 26.73	8.91 ± 4.34	-9.91 ± 6.46
6 months	Dixon, in phase	Cranial	20.86 ± 5.32**	37.14 ± 3.08	11.61 ± 6.3	1.91 ± 3.08**
		Sagittal	23.97 ± 13.31	43.84 ± 24.01	13.41 ± 9	5.6 ± 6.69
	Dixon, water only	Cranial	12.81 ± 3.86	24.85 ± 10.79	4.77 ± 1.14	-13.15 ± 5.09
		Sagittal	9.58 ± 2††	21.23 ± 7.91	4.37 ± 1.63	-11.889 ± 7.5**
	PDFS	Cranial	7.52 ± 1.57††	15.61 ± 5.32	7 ± 2.71	-4.54 ± 3.12**
		Sagittal	12.84 ± 6.05	33.53 ± 30.95	9.55 ± 4.68	-10.98 ± 12.22
9 months	Dixon, in phase	Cranial	31.19 ± 19.43	48.49 ± 19.09	19.48 ± 12.07	4.32 ± 10.68**
		Sagittal	29.18 ± 11.66	58.86 ± 40.98	17.8 ± 11.06	13.9 ± 19.11
	Dixon, water only	Cranial	10.66 ± 4.5	19.91 ± 7.44	5.2 ± 1.68	-22.31 ± 13.33
		Sagittal	9.51 ± 5.52††	20.35 ± 11.57	5.06 ± 4.27	-21.36 ± 12.17
	PDFS	Cranial	7.59 ± 1.45††	12.24 ± 1.81	5.85 ± 1.67	-10.24 ± 2.99
		Sagittal	11.28 ± 4.64	17.36 ± 6.57	9.22 ± 4.17	-14.99 ± 6.47
12 months	Dixon, in phase	Cranial	20.99 ± 2.69**	31.9 ± 6.25	9.24 ± 1.69	2.43 ± 7.25**
		Sagittal	22.49 ± 12.87	32.22 ± 13.31	13.69 ± 8.4	4.33 ± 2.59
	Dixon, water only	Cranial	5.37 ± 1.89	9.45 ± 3.42	4.51 ± 1.11	-17.58 ± 6.97
		Sagittal	6.33 ± 6††	9.69 ± 8.25	5.21 ± 3.61	-17.7 ± 7.19
	PDFS	Cranial	5.17 ± 1.43††	7.48 ± 2.17	5.07 ± 1.53	-9.05 ± 1.76
		Sagittal	7.89 ± 2.68	11.77 ± 5.84	6.15 ± 0.91	-17.8 ± 4.17

4.7 References

1. Cisternas MG, Murphy L, Sacks JJ, et al. Alternative Methods for Defining Osteoarthritis and the Impact on Estimating Prevalence in a US Population-Based Survey. Arthritis Care Res 2016;68:574–580.

2. Hootman JM, Helmick CG. Projections of US prevalence of arthritis and associated activity limitations. Arthritis Rheum 2006;54:226–229.

3. Hootman J, Helmick C, Barbour K, et al. Updated Projected Prevalence of Self-Reported Doctor-Diagnosed Arthritis and Arthritis-Attributable Activity Limitation Among US Adults, 2015-2040. Arthritis Rheumatol 2016;68:1582–1587.

4. McIlwraith CW, Frisbie DD, Kawcak CE. The horse as a model of naturally occurring osteoarthritis. Bone Joint Res 2012;1:297–309.

5. Haavardsholm EA, Bøyesen P, Østergaard M, et al. Magnetic resonance imaging findings in 84 patients with early rheumatoid arthritis: bone marrow oedema predicts erosive progression. Ann Rheum Dis 2008;67:794–800.

6. Felson DT, McLaughlin S, Goggins J, et al. Bone Marrow Edema and Its Relation to Progression of Knee Osteoarthritis. Ann Intern Med 2003;139:330.

7. Felson DT, Chaisson CE, Hill CL, et al. The Association of Bone Marrow Lesions with Pain in Knee Osteoarthritis. Ann Intern Med 2001;134:541–549.

8. Schett G. Bone Marrow Edema. Ann N Y Acad Sci 2009;1154:35–40.

9. Starr AM, Wessely MA, Albastaki U, et al. Bone Marrow Edema: Pathophysiology, Differential Diagnosis, and Imaging. Acta radiol 2008;49:771–786.

10. De Guio C, Ségard-Weisse E, Thomas-Cancian A, et al. Bone marrow lesions of the distal condyles of the third metacarpal bone are common and not always related to lameness in sports and pleasure horses. Vet Radiol Ultrasound 2019;60:167–175.

11. Barrett MF, Selberg KT, Johnson SA, et al. High field magnetic resonance imaging contributes to diagnosis of equine distal tarsus and proximal metatarsus lesions: 103 horses. Vet Radiol Ultrasound 2018;59:587–596.

12. Dyson S, Murray R, Schramme M, et al. Magnetic resonance imaging of the equine foot: 15 horses. Equine Vet J 2003;35:18–26.

13. Eriksen EF. Treatment of bone marrow lesions (bone marrow edema). Bonekey Rep 2015;4:755.

14. Tanamas S, Wluka A, Pelletier J, et al. Bone marrow lesions in people with knee osteoarthritis predict progression of disease and joint replacement: a longitudinal study. Rheumatology 2010;49:2413–2419.

15. Pessis E, Drapé JL, Ravaud P, et al. Assessment of progression in knee osteoarthritis: results of a 1 year study comparing arthroscopy and MRI. Osteoarthr Cartil 2003;11:361–369.

16. Roemer FW, Guermazi A, Javaid MK, et al. Change in MRI-detected subchondral bone marrow lesions is associated with cartilage loss: the MOST Study. A longitudinal multicentre study of knee osteoarthritis. Ann Rheum Dis 2009;68:1461–1465.

17. Roemer F, Neogi T, Nevitt M, et al. Subchondral bone marrow lesions are highly associated with, and predict subchondral bone attrition longitudinally: the MOST study. Osteoarthr Cartil 2010;18:47–53.

18. Pezeshk P, Alian A, Chhabra A. Role of chemical shift and Dixon based techniques in musculoskeletal MR imaging. Eur J Radiol 2017;94:93–100.

19. Lins CF, Salmon CEG, Nogueira-Barbosa MH. Applications of the Dixon technique in the evaluation of the musculoskeletal system. Radiol Bras 2020;54:33–42.

20. Eggers H, Börnert P. Chemical shift encoding-based water-fat separation methods. J Magn Reson Imaging 2014;40:251–268.

21. Van Vucht N, Santiago R, Lottmann B, et al. The Dixon technique for MRI of the bone marrow. Skeletal Radiol 2019;48:1861–1874.

22. Johnson TRC, Krauß B, Sedlmair M, et al. Material differentiation by dual energy CT: initial experience. Eur Radiol 2007;17:1510–1517.

23. Pache G, Krauss B, Strohm P, et al. Dual-energy CT virtual noncalcium technique: detecting posttraumatic bone marrow lesions--feasibility study. Radiology 2010;256:617–624.

24. Zanetti M, Bruder E, Romero J, et al. Bone marrow edema pattern in osteoarthritic knees: correlation between MR imaging and histologic findings. Radiology 2000;215:835–840.

25. Edelstein W, Glover G, Hardy C, et al. The intrinsic signal-to-noise ratio in NMR imaging. Magn Reson Med 1986;3:604–618.

26. Welvaert M, Rosseel Y. On the Definition of Signal-To-Noise Ratio and Contrast-To-Noise Ratio for fMRI Data. PLoS One 2013;8:e77089.

27. Foti G, Catania M, Caia S, et al. Identification of bone marrow edema of the ankle: diagnostic accuracy of dual-energy CT in comparison with MRI. La Radiol medica 2019 12410 2019;124:1028–1036.

28. Faul F, Erdfelder E, Lang A, et al. G*Power 3: a flexible statistical power analysis program for the social, behavioral, and biomedical sciences. Behav Res Methods 2007;39:175–191.

29. Smith M, Triantafillou S, Parker A, et al. Synovial membrane inflammation and cytokine production in patients with early osteoarthritis. J Rheumatol 1997;24:365–371.

30. Benito M, Veale D, FitzGerald O, et al. Synovial tissue inflammation in early and late osteoarthritis. Ann Rheum Dis 2005;64:1263.

31. Ayral X, Pickering EH, Woodworth TG, et al. Synovitis: a potential predictive factor of structural progression of medial tibiofemoral knee osteoarthritis – results of a 1 year longitudinal arthroscopic study in 422 patients. Osteoarthr Cartil 2005;13:361–367.

32. McQueen FM, Benton N, Perry D, et al. Bone edema scored on magnetic resonance imaging scans of the dominant carpus at presentation predicts radiographic joint damage of the hands and feet six years later in patients with rheumatoid arthritis. Arthritis Rheum 2003;48:1814–1827.

33. Mandalia V, Fogg AJB, Chari R, et al. Bone bruising of the knee. Clin Radiol 2005;60:627–636.

34. Roemer F, Bohndorf K. Long-term osseous sequelae after acute trauma of the knee joint evaluated by MRI. Skelet Radiol 2002 3111 2002;31:615–623.

35. Biggi M, Zani DD, De Zani D, et al. Magnetic resonance imaging findings of bone marrow lesions in the equine distal tarsus. Equine Vet Educ 2012;24:236–241.

36. Olive J, Mair TS, Charles B. Use of standing low-field magnetic resonance imaging to diagnose middle phalanx bone marrow lesions in horses. Equine Vet Educ 2009;21:116–123.

37. Crema MD, Nevitt MC, Guermazi A, et al. Progression of cartilage damage and meniscal pathology over 30 months is associated with an increase in radiographic tibiofemoral joint space narrowing in persons with knee OA — the MOST study. Osteoarthr Cartil 2014;22:1743–1747.

38. Segal N, Kern A, Anderson D, et al. Elevated tibiofemoral articular contact stress predicts risk for bone marrow lesions and cartilage damage at 30 months. Osteoarthr Cartil 2012;20:1120–1126.

39. Collins JA, Beutel BG, Strauss E, et al. Bone marrow edema: chronic bone marrow lesions of the knee and the association with osteoarthritis. Bull NYU Hosp Jt Dis 2016;74:24–36.

40. Korompilias A V., Karantanas AH, Lykissas MG, et al. Bone marrow edema syndrome. Skeletal Radiol 2009;38:425–436.

41. Zhang Y, Nevitt M, Niu J, et al. Fluctuation of knee pain and changes in bone marrow lesions, effusions, and synovitis on magnetic resonance imaging. Arthritis Rheum 2011;63:691–699.

42. Eustace S, Keogh C, Blake M, et al. MR imaging of bone oedema: mechanisms and interpretation. Clin Radiol 2001;56:4–12.

43. Aigner N, Meizer R, Meraner D, et al. Tapping test in patients with painful bone marrow edema of the knee. Clin J Pain 2008;24:131–134.

44. Beckmann J, Schmidt T, Schaumburger J, et al. Infusion, core decompression, or infusion following core decompression in the treatment of bone edema syndrome and early avascular osteonecrosis of the femoral head. Rheumatol Int 2013;33:1561–1565.

45. Hofmann S. The painful bone marrow edema syndrome of the hip joint. Wien Klin Wochenschr 2005;117:111–120.

46. Radke S, Rader C, Kenn W, et al. Transient marrow edema syndrome of the hip: results after core decompression. A prospective MRI-controlled study in 22 patients. Arch Orthop Trauma Surg 2003;123:223–227.

47. Calvo E, Fernandez-Yruegas D, Alvarez L. Core decompression shortens the duration of pain in bone marrow oedema syndrome. Int Orthop 2000;24:88.

48. Manara M, Varenna M. A clinical overview of bone marrow edema. Reumatismo 2014;66:184–196.

49. Ondrouch AS. Cyst formation in osteoarthritis. J Bone Jt Surg Br 1963;45:755–760.

50. Resnick D, Niwayama G, Coutts R. Subchondral cysts (geodes) in arthritic disorders: pathologic and radiographic appearance of the hip joint. AJR Am J Roentgenol 1977;128:799–806.

51. Ortved KF, Nixon AJ, Mohammed HO, et al. Treatment of subchondral cystic lesions of the medial femoral condyle of mature horses with growth factor enhanced chondrocyte grafts: A retrospective study of 49 cases. Equine Vet J 2012;44:606–613.

52. Raynauld J-P, Martel-Pelletier J, Berthiaume M-J, et al. Correlation between bone lesion changes and cartilage volume loss in patients with osteoarthritis of the knee as assessed by quantitative magnetic resonance imaging over a 24-month period. Ann Rheum Dis 2008;67:683–688.

53. Ray C, Baxter G, McIlwraith C, et al. Development of subchondral cystic lesions after articular cartilage and subchondral bone damage in young horses. Equine Vet J 1996;28:225–232.

54. Link T, Steinbach L, Ghosh S, et al. Osteoarthritis: MR imaging findings in different stages of disease and correlation with clinical findings. Radiology 2003;226:373–381.

55. Sowers M, Hayes C, Jamadar D, et al. Magnetic resonance-detected subchondral bone marrow and cartilage defect characteristics associated with pain and X-ray-defined knee osteoarthritis. Osteoarthr Cartil 2003;11:387–393.

56. Beattie K, Boulos P, Pui M, et al. Abnormalities identified in the knees of asymptomatic volunteers using peripheral magnetic resonance imaging. Osteoarthr Cartil 2005;13:181–186.

57. Hayes C, Jamadar D, Welch G, et al. Osteoarthritis of the knee: comparison of MR imaging findings with radiographic severity measurements and pain in middle-aged women. Radiology 2005;237:998–1007.

58. Milgram JW. Morphologic alterations of the subchondral bone in advanced degenerative arthritis. Clin Orthop Relat Res 1983;Mar:293–312.

59. Loniewski KJ, Patial S, Parameswaran N. Sensitivity of TLR4- and -7-induced NFκB1 p105-TPL2-ERK pathway to TNF-receptor-associated-factor-6 revealed by RNAi in mouse macrophages. Mol Immunol 2007;44:3715–3723.

60. Hutás G, Bajnok É, Gál I, et al. CD44-specific antibody treatment and CD44 deficiency exert distinct effects on leukocyte recruitment in experimental arthritis. Blood 2008;112:4999–5006.

61. Rangger C, Kathrein A, Freund M, et al. Bone bruise of the knee: histology and cryosections in 5 cases. Acta Orthop Scand 1998;69:291–294.

62. Lynch T, Crues J, Morgan F, et al. Bone abnormalities of the knee: prevalence and significance at MR imaging. Radiology 1989;171:761–766.

63. DeAngelis JP, Spindler KP. Traumatic Bone Bruises in the Athlete's Knee. Sports Health 2010;2:398.

64. Burr DB, Martin RB, Schaffler MB, et al. Bone remodeling in response to in vivo fatigue microdamage. J Biomech 1985;18:189–200.

65. Alliston T, Hernandez C, Findlay D, et al. Bone marrow lesions in osteoarthritis: What lies beneath. J Orthop Res 2018;36:1818–1825.

66. Lambers FM, Bouman AR, Rimnac CM, et al. Microdamage Caused by Fatigue Loading in Human Cancellous Bone: Relationship to Reductions in Bone Biomechanical Performance. PLoS One 2013;8:e83662.

67. Hernandez CJ, Lambers FM, Widjaja J, et al. Quantitative Relationships Between Microdamage and Cancellous Bone Strength and Stiffness. Bone 2014;66:205.

68. Follet H, Viguet-Carrin S, Burt-Pichat B, et al. Effects of preexisting microdamage, collagen cross-links, degree of mineralization, age, and architecture on compressive mechanical properties of elderly human vertebral trabecular bone. J Orthop Res 2011;29:481–488.

69. Vashishth D, Koontz J, Qiu S, et al. In vivo diffuse damage in human vertebral trabecular bone. Bone 2000;26:147–152.

70. Burr D, Forwood M, Fyhrie D, et al. Bone microdamage and skeletal fragility in osteoporotic and stress fractures. J Bone Miner Res 1997;12:6–15.

71. Fazzalari N, Forwood M, Manthey B, et al. Three-dimensional confocal images of microdamage in cancellous bone. Bone 1998;23:373–378.

72. Dürr H, Martin H, Pellengahr C, et al. The cause of subchondral bone cysts in osteoarthrosis: a finite element analysis. Acta Orthop Scand 2004;75:554–558.

73. McErlain DD, Ulici V, Darling M, et al. An in vivoinvestigation of the initiation and progression of subchondral cysts in a rodent model of secondary osteoarthritis. Arthritis Res Ther 2012 141 2012;14:1–12.

74. Theodorou S, Theodorou D, Agnantis N, et al. Osteonecrosis of the tibial plateau: magnetic resonance imaging appearances with quantitation of lesion size and evidence of a pathogenesis of meniscal injury. J Comput Assist Tomogr 2010;34:149–155.

75. Saini A, Saifuddin A. MRI of osteonecrosis. Clin Radiol 2004;59:1079–1093.

76. Carrino JA, Blum J, Parellada JA, et al. MRI of bone marrow edema-like signal in the pathogenesis of subchondral cysts. Osteoarthr Cartil 2006;14:1081–1085.

77. Crema MD, Roemer FW, Zhu Y, et al. Subchondral Cystlike Lesions Develop Longitudinally in Areas of Bone Marrow Edema–like Lesions in Patients with or at Risk for Knee Osteoarthritis: Detection with MR Imaging—The MOST Study. Radiology 2010;256:855.

78. Marra M, Crema M, Chung M, et al. MRI features of cystic lesions around the knee. Knee 2008;15:423–438.

79. Sabokbar A, Crawford R, Murray D, et al. Macrophage-osteoclast differentiation and bone resorption in osteoarthrotic subchondral acetabular cysts. Acta Orthop Scand 2000;71:255–261.

80. von Rechenberg B, Leutenegger C, Zlinsky K, et al. Upregulation of mRNA of interleukin-1 and-6 in subchondral cystic lesions of four horses. Equine Vet J 2001;33:143–149.

81. Walker WT, Silverberg JL, Kawcak CE, et al. Morphological characteristics of subchondral bone cysts in medial femoral condyles of adult horses as determined by computed tomography. Am J Vet Res 2016;77:265–274.

82. Kaspiris A, Khaldi L, Grivas TB, et al. Subchondral cyst development and MMP-1 expression during progression of osteoarthritis: An immunohistochemical study. Orthop Traumatol Surg Res 2013;99:523–529.

83. Chambers TJ, Fuller K. Bone cells predispose bone surfaces to resorption by exposure of mineral to osteoclastic contact. J Cell Sci 1985;76:155–165.

84. Breckon JJW, Papaioannou S, Kon LWM, et al. Stromelysin (MMP-3) Synthesis Is Up-Regulated in Estrogen-Deficient Mouse Osteoblasts In Vivo and In Vitro. J Bone Miner Res 1999;14:1880–1890.

85. Li J, Liao E-Y, Dai R-C, et al. Effects of 17b-estradiol on the expression of interstitial collagenases-8 and-13 (MMP-8 and MMP-13) and tissue inhibitor of metalloproteinase-1 (TIMP-1) in ovariectomized rat osteoblastic cells.

86. Holliday LS, Welgus HG, Fliszar CJ, et al. Initiation of Osteoclast Bone Resorption by Interstitial Collagenase. J Biol Chem 1997;272:22053–22058.

87. Sasaki K, Takagi M, Konttinen YT, et al. Upregulation of matrix metalloproteinase (MMP)-1 and its activator MMP-3 of human osteoblast by uniaxial cyclic stimulation. J Biomed Mater Res Part B Appl Biomater 2007;80B:491–498.

88. Lev MH, Gonzalez RG. CT Angiography and CT Perfusion Imaging. In: Toga AW, C MJ, eds. Brain Mapping: The Methods. Second Edi. San Diego, CA: Academic Press; 2002:427–484.

89. Björkman A-S, Koskinen SK, Lindblom M, et al. Diagnostic accuracy of dual-energy CT for detection of bone marrow lesions in the subacutely injured knee with MRI as reference method. Acta radiol 2019;61:749–759.

90. Cao J, Wang Y, Kong X, et al. Good interrater reliability of a new grading system in detecting traumatic bone marrow lesions in the knee by dual energy CT virtual non-calcium images. Eur J Radiol 2015;84:1109–1115.

91. Ai S, Qu M, Glazebrook KNK, et al. Use of dual-energy CT and virtual non-calcium techniques to evaluate post-traumatic bone bruises in knees in the subacute setting. Skelet Radiol 2014;43:1289–1295.

92. Seo S, Sohn Y, Lee C, et al. Dual-energy CT for detection of traumatic bone bruises in the knee joint. J Korean Soc Radiol 2013;69:487–494.

93. Kold S, Hickman J, Melsen F. An experimental study of the healing process of equine chondral and osteochondral defects. Equine Vet J 1986;18:18–24.

94. Frisbie D, Kisiday J, Kawcak C, et al. Evaluation of adipose-derived stromal vascular fraction or bone marrow-derived mesenchymal stem cells for treatment of osteoarthritis. J Orthop Res 2009;27:1675–1680.

95. Jeffcott L, Kold SE. Radiographic examination of the equine stifle. Equine Vet J 1982;14:25–30.

96. Reilingh ML, Bergen CJA van, Blankevoort L, et al. Computed tomography analysis of osteochondral defects of the talus after arthroscopic debridement and microfracture. Knee Surgery, Sport Traumatol Arthrosc 2016;24:1286.

97. Robinson D, Winson I, Harries W, et al. Arthroscopic treatment of osteochondral lesions of the talus. J Bone Joint Surg Br 2003;85:989–993.

98. Kolker D, Murray M, Wilson M. Osteochondral defects of the talus treated with autologous bone grafting. J Bone Jt Surg - Ser B 2004;86:521–526.

CHAPTER 5:

DEVELOPMENT OF AN EXPERIMENTAL MODEL OF BONE MARROW LESIONS USING THE RODENT FEMORAL CONDYLE

5.1 Introduction

Considerable strides have been made toward understanding the pathophysiology of osteoarthritis (OA) through the use of preclinical animal models, with *in vivo* models recreating the complex interactions between tissues and combinations of biological stimuli.[1] OA is now understood as both a disease of the articular cartilage and underlying subchondral bone. Bone marrow lesions (BMLs) are frequently observed within the subchondral bone and appear to play an important role in the pathogenesis of OA.[2] BMLs are characterized as decreased signal intensity on T1-weighted images, and intermediate to high signal intensity on T2-weighted images. The presence and severity of BMLs are well-correlated to progression of osteoarthropathy, emphasizing the importance in focused understanding of this condition.[2]

Preclinical models of OA can be divided into primary and secondary etiologies,[3] including spontaneous and genetically modified naturally-occurring models,[4,5] in addition to surgical or chemically induced models.[6–10] Regardless of etiology, BMLs appear to both incite and result from biomechanical alterations in the joint, resulting in pain and disability.[11–13] While these models are all valuable for understanding OA, they discuss BMLs only in the context of other pathologic lesions making it challenging to discern the specific contribution to clinical and structural changes within the joint. Therefore, the development of an animal model of BMLs with a focus on joint mobility is needed to better characterize the biological behavior of BMLs and investigate the primary effects of BMLs on joint mobility.

Previous work in the ovine femorotibial joint has demonstrated that focal damage to the osteochondral unit through direct penetration of the articular and calcified cartilage, subchondral and trabecular bone layers is sufficient to create a BML with a similar appearance to what is clinically observed. The main advantages of this model include the visibility of BMLs on high-field MRI and the similarities in size and shape to what has been reported in the human knee joint. Disadvantages of this model are primarily due to the fact that there are a limited number of validated biological assessment assays for sheep, so cellular, molecular, and immunologic data from this model is limited at the current time. Clinical assessment of the ovine gait abnormalities is primarily qualitative, limiting the conclusions that can be made. Importantly, extrapolation of this experimental model into another species validates the previous conclusions made about the relationship between osteochondral damage and BMLs, and facilitates an opportunity to more comprehensively and objectively assess the clinical, cellular, and biological mechanisms underlying BMLs.

The femorotibial joint of the rat is well-validated as preclinical animal model for OA.[14] Rats are relatively easy to walk over force plates, enabling assessment of a number of variables related to gait-patterns and weight-bearing in models related to OA.[15,16] Quantitative gait-related data is difficult to obtain in other preclinical animal species, making the rat an ideal animal model to gain further insight about the clinical effects of these lesions. The objective of this study was (1) to validate an experimental model for BMLs using the rat medial femoral condyle, adapting the previously described methods from the sheep; (2) to optimize assessment of experimentally-induced BMLs using high-field MRI; (3) to document the clinical manifestations of induced BMLs using longitudinal tacking of individual animals via voluntary mobility analysis; and (4) to describe the similarities and differences in the histological appearance of

BMLs. The validation of this model in a small animal species would facilitate additional opportunities to explore methods for cellular, molecular, and genetic characterization of the etiopathogenesis of BMLs.

5.2 Materials and Methods

5.2.1 Animals

Eight, skeletally-mature Sprague Dawley rats (N = 4 males, N = 4 females) were used for this prospective study. Animals were purchased from a commercial vendor (Charles River Laboratory, Wilmington, MA, USA) at 14 weeks of age and allowed to acclimate to the vivarium for 14 days. Rats were housed individually in solid-bottom cages were corncob bedding, maintained at 22-24°C on a 12-hour light/dark cycle, and monitored daily by a veterinarian. Commercially-available irradiated water and food were available *ad libitum* for the duration of the study. All procedures were approved by the Institutional Animal Care and Use Committee of Colorado State University (Kuali protocol 1155, approved 07/27/2020) and University of Colorado Anschutz Medical Campus.

5.2.2 Experimental protocol

Bone marrow lesions were surgically induced in the medial femoral condyle of each hind limb using a modification of the previously described surgical pin penetration procedure. MR imaging of the femorotibial joints was performed pre-operatively, and at 3, 14, 45 and 90 days post-operatively. Quantitative gait analysis was performed pre-operatively and on average, once per week during the post-operative period. Serum was collected at each imaging timepoint. Rats were euthanized at either 14, 45, or 90 days post-injury via CO_2 inhalation with confirmatory

cervical dislocation. Joints were grossly evaluated and synovial fluid was collected following euthanasia. Medial femoral condyles were designated for histological assessment or RNA extraction.

5.2.3 Bone marrow lesion induction

Rats were anesthetized using a mixture of isoflurane (2-4%) and oxygen. Limbs were clipped and aseptically prepared for surgery. A medial parapatellar arthrotomy was used to access the medial femoral condyle of limbs assigned to pin penetration. Femorotibial joints were held in flexion with the patella deviated laterally to access the articular, weight-bearing surface of the medial femoral condyle. A 22-gauge needle was advanced to a depth of 2 mm using a mallet, through the articular and calcified cartilage layers, subchondral bone plate and into the underlying trabecular bone from the articular surface. After removal of the needle, lavage of the joint was performed with sterile saline to remove any osteochondral debris and the surgical site was closed routinely.

5.2.4 Gait evaluation

Quantitative gait evaluation included voluntary weight bearing using the Tekscan Rodent Walkway System (Tekscan, Inc., South Boston, MA, USA) pre-operatively, day 4 and once per week post-injury until each animal's endpoint. Prior to the start of the study, rats were acclimated to the system over 3 days. For each gait analysis timepoint, rats were allowed to walk naturally across sensors over the Tekscan Walkway for three trials per day, and sensor videos were analyzed for 12 weight bearing and gait parameters including maximum force, force-time impulse, and maximum force symmetry values (front/hind, left/right, left front/right front, left

hind/right hind). The three runs taken at each gait analysis timepoint were averaged and utilized for statistical comparisons. Specific information on methods to calculate each mobility parameter were available through the manufacturer-specific manuals.

5.2.5 Magnetic resonance imaging

Rats were placed under general anesthesia for bilateral MRI of the femorotibial joints with animals placed in lateral recumbency. The animal was positioned with the foot entering the gantry first, and with the limb of interest oriented upward to achieve positioning within isocenter. Animals were rotated into the opposite recumbency for imaging of the contralateral limb. MR imaging was performed using a 9.4 T scanner (Bruker BioSpec, Bruker Scientific Instruments, Billerica, MA, USA) with a bore diameter of 30 cm, using a rat body coil. Rats were imaged at baseline (N = 4), and 3 (N = 4), 14 (N = 6), 45 (N = 4) and 90 (N = 4) days post-injury.

Sequences included proton density fat saturation (PDFS; cranial plane settings: TR 2600, TE 32, flip angle 180; sagittal plane settings: TR 2600, TE 32, flip angle 180) and intermediate-weighted fat suppressed (IWFS; cranial plane settings: TR 1234.08, TE 24, flip angle 180; sagittal plane settings: TR 2283, TE 24, flip angle 180) sequences in the sagittal and cranial planes; T2-weighted (TR 10, TE 2.855, flip angle 30) and T1 rapid imaging with refocused echo (RARE; TR 843, TE 7.5, flip angle 180) sequences in the sagittal plane. All images had a 320 x 320 matrix with voxel dimensions of 0.3 mm x 0.3 mm x 1.2 mm.

5.2.6 Image evaluation

Open-sourced software (Horos Project, version 3.3.6) was used for viewing and evaluating DICOM images obtained via MR. Post-operative images on MR from each animal

were first evaluated for the presence of a BML. If a BML was present, all sequences for a given animal at a specific timepoint were graded for the following parameters: maximum condylar area, maximum BML area, average BML signal, maximum BML signal, minimum BML signal, number of slices where a BML was present, area of the BML on each slice, adjacent muscle signal, and standard deviation of air of the background. A 0.55 mm^2 circular region of interest (ROI) was used to identify the signal within the BML, muscle, and background air. From these parameters, the percent of the condyle occupied, signal-to-noise (SNR), and contrast-to-noise ratio (CNR) of the BML were calculated. Briefly, for the SNR the mean signal of the ROI within the BML was divided by the standard deviation of the background air in a ROI of equal size. For CNR, the signal of the ROI of the muscle was subtracted from the signal in the ROI of the BML, and then divided by the standard deviation of the background air ROI. Pre-operative images of animals with BMLs were reviewed and post-operative images were overlaid using imaging software (AnalyzeDirect, version 14.0, Overland Park, KS) in order to calculate baseline SNR and CNR in the same location as the post-operative BML.

5.2.7 Macroscopic post-mortem evaluation of femorotibial joints

Rats were euthanized at 14 (N = 2), 45 (N = 2) or 90 (N = 4) days post-injury. Hind limbs were removed at the coxofemoral joint for immediate evaluation of the femorotibial joints. Joints were opened completely for subjective evaluation of gross damage, macroscopic changes to the synovium, bone or soft tissues. Following gross evaluation, the right hind limb was placed in 10% neutral-buffered formalin at a 10:1 ratio by volume at room temperature for tissue fixation for 7 days. After fixation, samples were rinsed and immersed in PBS solution until decalcification. The left hind medial femoral condyle was isolated and free from all attached soft

tissues and removed *en bloc*. The left medial femoral condyle was immediately submerged in RNAlater (ThermoFisher, Life Technologies, Carlsbad, CA, USA) and stored overnight at 4°C. The supernatant was removed and samples were then stored at -80°C, per the manufacturer's instructions.

Four femurs were collected from two additional animals and fixed in a similar manner as described above, as control samples for comparison. Control samples were collected from two healthy, skeletally-mature rats of similar body weight that were free of femorotibial joint disease, and euthanized for reasons unrelated to this study.

5.2.8 Serum and synovial fluid collection

Synovial fluid was aseptically collected from both femorotibial joints using joint lavage immediately following euthanasia on all animals. With the joint open, 500 µl of phosphate buffered saline (PBS) was injected and aspirated from the femorotibial joint a total of three times using a 30-gauge U-100 syringe. Synovial fluid was stored at -80°C. Blood was collected on study days 0 (N = 8), 3 (N = 4), 14 (N = 6), 45 (N = 2), and 90 (N = 4) for serum. Blood samples were collected from the tail vein antemortem, and from the cardiac ventricles immediately post-euthanasia. All serum samples were stored at -80°C.

5.2.9 Histologic evaluation of femorotibial joints

Medial femoral condyles designated for histologic evaluation were prepared routinely for analyses. Right hind limbs were decalcified in a 10% solution of ethylenediaminetetraacetic acide (EDTA) at a pH 7 at room temperature. EDTA was replaced twice weekly for 8-10 weeks. All soft tissues were removed and the femorotibial joint was removed *in situ* via a transverse cut

through the distal metaphysis of the femur and a transverse cut at the junction of the proximal and middle thirds of the tibia. A sagittal cut was made between the lateral and medial femoral condyles prior to processing. Samples were then processed on an automatic tissue processor (Tissue Tek VIP E300, Sakura, Torrance, CA, USA) and embedded in paraffin. Femorotibial joints were sectioned at 5 μm thickness on an automated rotary microtime (Leica RM2255, Leica Biosystems, Buffalo Grove IL) and stained with hematoxylin and eosin (H&E) for histolopathologic evaluation using a previously validated protocol.[17]

5.2.10 Statistical analyses

Descriptive statistics were reported in an effort to characterize the apperance of bone marrow lesions across timepoints within each sequence on MRI and histologically on H&E sections. Continuous data were reported as mean ± standard error. The experimental sample size (8 total animals) was calculated using G*Power (version 3.1.1).[18] Specifically, an *a priori* power analysis was conducted using expected mean semi-quantitative scores for the apperance of bone marrow lesions in treated joints using MRI obtained from a similar experimental model in sheep. This power analysis resulted in an effected size of 3.0, and a power of 0.95, using a 95% confidence interval and a standard deviation of 1 between groups. All data was analyzed using R software (version 4.0.3, "Bunny-Wunnies Freak Out," R Foundation for Statistical Computing 2020) in RStudio (version 1.2.1335).

Continuous data were evaluated for normality using the Shapiro-Wilk test, and visually using quantile-quantile plots. Although data was obtained from a small sample size of animals and normality was difficult to assess, quantile-quantile plots demonstrated minimal to slight departures of the data from normality. A mixed model for repeated measures was implemented

in the lme4 package for R. For parameters that quantified individual limb changes (e.g. stride length, percent swing stride, etc.), groups were compared using a mixed model for repeated measures, implemented in the lme4 package for R. Limb, timepoint, animal sex, and the interactions of these variables were also evaluated. Significant model factors were further evaluated by Tukey-Kramer pairwise comparison post-hoc tests using the lsmeans or the emmeans packages for R. In cases where data was non-normally distributed, Friedman's test was used followed by Wilcoxon pairwise comparisons with a Benjamini-Hochberg correction in the base package for R for repeated measures analyses. For weight bearing paramters that demonstrate the relationship between limbs (e.g. weight bearing symmetry parameters), a repeated measures one-way ANOVA with Tukey-Kramer pairwaise post-hoc comparisons was utilized. For correlation between parameters, a Pearson Correlation Analysis was conducted. A level of $P < 0.05$ was used for significance.

5.3 Results

No complications with general anesthesia or surgery were observed during the study. Two animals (one male, one female) became acutely non-weightbearing in the right hind limb within one week following surgery. Lameness was reduced with administration of non-steroidal anti-inflammatory medications. Both animals were euthanized at 14 days after surgery. MRI of the right hind limb was consistent with edema within the extra-articular soft tissues. On gross evaluation of the affected limbs, both animals had a similar inflammatory response within the extra-articular muscles and fascia, consistent with an inflammatory reaction to the suture. All data and samples were collected on these animals, but quantitative gait data was excluded from analysis.

5.3.1 Gait evaluation

All gait assessments were performed with three trials per animal per timepoint. There was no effect of sex on any gait parameters, unless otherwise noted.

For voluntary weight bearing parameters, a time-by-sex interaction was observed for animal body weight ($P < 0.01$) over the course of the study. Body weight decreased in all animals in the immediate post-operative period, and then increased beginning approximately 2-3 weeks after surgery for the remainder of the study.

No differences we observed between right and left forelimb and hindlimb pairs, demonstrating a symmetrical gait following BML induction. An increase ($P < 0.01$ left, $P < 0.05$ right) in maximum force (kg) was observed in the forelimbs between days 40-81, but remained constant in the hind limbs (Figure 5.1A). A moderate association ($R^2 = 0.63$) was found between maximum force and stride velocity in the forelimbs, while a weak association ($R^2 = 0.32$) was found in the hind limbs, demonstrating animal speed did not solely dictate force measurements. Force time impulse (percent body weight*seconds) was greater ($P < 0.001$) in the hind limbs than the forelimbs at baseline, and trended toward an overall decrease ($P = 0.06$) in the hind limbs during the study, most notably at day 40 (Figure 5.1B). An increase ($P < 0.01$) was observed between the fore/hind limb maximum force at day 40, suggesting decreased hind limb loading was associated with increased forelimb loading.

Voluntary walking demonstrated an increase ($P < 0.05$) in both forelimb gait velocity (cm/sec) and gait cycles per minute from baseline until day 81, after which time both parameters decreased to near baseline values (Figure 5.2A, B). A decrease ($P < 0.05$) in the number of stances taken along the length of the Tekscan walkway was identified from days 26-74. An

increase ($P < 0.05$) in stride length (cm) and stride velocity (cm/sec) in both forelimbs from days 26-74 was identified, normalizing at the end of the study period (Figure 5.1C, D). With the exception of stride length at days 26 ($P = 0.02$) and 74 ($P = 0.03$) for the right hind limb, stride length and stride velocity remained constant in the hind limbs throughout the study period. Maximum force (kg) in the forelimbs increased ($P < 0.05$) between days 40-81, compared to baseline or day 4 post-injury; whereas, maximum force remained constant in the hind limbs for the duration of the study. Maximum peak pressure (MPa) was increased ($P < 0.01$) in the left forelimb at day 74 relative to baseline and day 19, and approached significant ($P = 0.07$) in the right forelimb, as well. Swing time (sec) decreased ($P < 0.05$) in the right hind limb at study day 26 and later, compared to day 12. No differences were identified for stance time (sec), swing time (sec), stride time (sec), or stride acceleration (cm^2/sec).

5.3.2 Magnetic resonance imaging

Fluid signal within the bone, consistent with a BML, was visible within the medial femoral condyle of all animals imaged between 3 and 14 days after surgery (Figure 5.3). BMLs were well-observed on PDFS sequences, and appeared hyperintense relative to the trabecular bone. BMLs were also visible on T1 RARE images in the sagittal plane with an intermediate signal intensity. BMLs were variably visible on paired IWFS images, with intermediate to decreased signal intensity relative to the trabecular bone. The articular cartilage defect associated with the area of needle impact through the articular surface was inconsistently visible across sequences and timepoints (Figure 5.4).

On PDFS images, the experimentally-induced BMLs encompassed 60% (cranial) and 25% (sagittal) of the medial femoral condylar area at 2 weeks post-surgery. Fluid signal was

visible on at least two sequences on every limb at the 90-day endpoint, and encompassed approximately 25-50% of the medial femoral condylar area, depending on the plane and fluid-sensitive sequence. No change in the total volume of the BML or the percent of the medial femoral condyle occupied by fluid signal was visible on sagittal or dorsal plane PDFS images over the course of the study. For PDFS images in the dorsal plane, there was a near-significant trend for a decrease ($P = 0.06$) in SNR and increase ($P = 0.07$) in CNR between days 14 and 90, and 0 and 90, respectively.

These same trends were not observed for fat only and water only IWFS images. For fat only images, the total volume of fluid signal increased between days 3 and 45 ($P < 0.01$) and 14 and 45 ($P = 0.01$) on dorsal plane images, and was consistent thereafter. Sagittal plane in phase images approached significance for an increase ($P = 0.08$) between days 3 and 45. The percent of the medial femoral condyle occupied by a fluid signal increased ($P < 0.05$) between days 3 and 14 compared to days 45 and 90 on both sagittal and dorsal plane images. No change in SNR or CNR was observed for fat only images across all timepoints.

For water only images, an increase ($P < 0.05$) in total volume and percentage of the medial femoral condyle occupied by a fluid signal was observed at days 45 and 90, compared to days 3 and 14 on both sagittal and dorsal plane images. No differences were observed in SNRs in either plane, and the CNR in the sagittal plane showed a non-significant trend toward an increase ($P = 0.09$) over time. For water only images, the maximum size and highest conspicuity of the BML was identified at 45 days post-injury.

Fluid signal within the bone was also visible on sagittal plane RARE sequences with a high level of anatomic detail. The total volume of the increased ($P < 0.001$) at days 14, 45 and 90, compared to day 3, and the percent of the condyle occupied nearly followed this trend ($P =$

0.08). A near-significant decrease ($P = 0.06$) in SNR was observed between 0 and 45 days, while no change in CNR was observed (Table 5.1).

5.3.3 Histological evaluation of femorotibial joints

All femorotibial joints were normal on gross evaluation. Increase fluid accumulation was visible within the subcutaneous and deep muscle layers in the two animals previously described. The needle puncture site on the medial femoral condyle was identified in each limb. No macroscopic evidence of synovitis, osteophytosis, or other degenerative processes were visible in any limb.

Histological changes within the bone corresponded to the region of increased signal on MRI. At 14 days, the BML was composed of dense tissue with cellular and acellular characteristics. Inflammatory and fibroblastic cellular infiltrate were visible within the BML, as well as bony, cartilaginous, and amorphous cellular debris. Large, multinucleated cells were intermixed within the region of the BML. Cellular infiltrate surrounded and extended beyond the immediate regions adjacent to the defect, however normal osteochondral tissues were visible distant to the BML region. Marrow spaces within the trabecular bone were difficult to discern with the high level of infiltrate.

The osteochondral defect remains visible at 45 and 90 days after surgery. Over time, inflammatory cell infiltrate was replaced by an increase in cartilaginous matrix and endochondral tissues. The repair tissue observed within the defect had a higher cellularity than that of the native articular cartilage. Blood vessels were intermixed within the repair tissue. Osteoblasts and occasional osteoclasts were identified at all timepoints at the edges of the defect and locally within the surrounding tissue. Thickening of the subchondral bone was present at 45 days, but

was more apparent at 90 days post-operatively. The extent of changes associated with the BML became more localized, with the surrounding, normal-appearing trabecular bone more readily visible. At 90 days, active remodeling was visible within the osteochondral tissues in all samples (Figure 5.5).

5.4 Discussion

A reproducible experimental model for BMLs is possible using the medial femoral condyle in the rat. Quantitative gait data demonstrated that the presence of BMLs in the femorotibial joint results in measurable differences in mobility parameters assessed via voluntary movement. The appearance of experimentally-induce BMLs was consistent in using this novel animal model, with hyperintensity within the medial femoral condyle on fluid-sensitive sequences, relative to the intensity within the trabecular bone. This fluid signal persists within the bone for at least 90 days, and was not associated with gross degenerative changes within the joint. Histologically, evidence of local inflammation and fibroplasia was visible within the osteochondral tissues. These findings present an additional preclinical animal model for evaluation of the effects of BMLs within the joint.

The experimental model for BMLs described here was an extrapolation from the previously validated pin penetration model using a 1.1 mm Steinmann pin to an 8 mm depth through the articular cartilage into trabecular bone of the medial femoral condyle, as described in sheep. Impacting a 22g needle to a 2 mm depth in this study was a modification of the previous technique scaled for the relative size of the rat medial femoral condyle. A disadvantage of using the needle however, was the fact that it is nearly impossible to impact a blunt-tipped, hollow-core standard needle (based on preliminary work), so the sharp point at the end of each needle

was preserved. It is possible that this may have affected the appearance of the experimentally-induced BMLs here to some degree, since a cartilage "ring" was affected here, as opposed to a cartilage "plug", as described for the sheep. More ideally, a solid-core 22g, blunt-tipped needle would be ideal to better mimic the ovine model. Additionally, the subchondral and trabecular bone in the rodent femoral condyle was surprisingly hard, and the differences in bone structure (discussed further below) may warrant further consideration for optimization of this experimental model moving forward. Similar to the pin penetration model, this needle model mimicked a traumatically-induced etiology for BML development.

The major symptom in humans with BMLs is pain, regardless of the underlying etiology. Pain is also recognized with BMLs in animals with various manifestations of lameness reported in dogs[19] and horses[20,21]. Many studies discussing BMLs also report co-morbidities, such as injury to the anterior cruciate ligament[22,23] or osteoarthritis[24,25] in the affected joint. These co-morbidities make it challenging to study functional alterations in gait and weight-bearing secondary to BMLs, and discern what aspects of pain or gait alterations are solely attributable to BMLs. Numerous studies have reported how acute biomechanical alterations may cause BMLs, how a direct association to gait alterations has not been established.[11,26,27] Previous studies have shown that reestablishing the normal joint biomechanics may mitigate BMLs, or even cause them to complete resolve, suggesting that functional mobility may play a critical role the behavior of BMLs. BMLs have been shown in more chronic scenarios of osseous stress, and may present without clinical symptoms or other pathologic lesions.[28] There is a growing body of evidence that these asymptomatic cases may actually be a precursor to or a subclinical stress fracture.[28–31] Therefore, mobility modifications may be a more accurate method to identify subclinical abnormalities with acute BMLs. Mobility in pre-clinical models can be evaluated

using spatial (position-based), temporal (time-based), or kinetic (force-based) methods. The data obtained through voluntary movement encompasses all forms of functional mobility alterations, and longitudinal tracking of individual animals over the experimental study provided a comprehensive understanding of the clinical manifestations of BMLs in the medial femoral condyle.

Temporal parameters reflected the fact that rats placed less weight on their hind limbs over time (increase stride length, increase stride velocity, decrease force time impulse in hind limbs), and shifted weight to their forelimbs (increased maximum force for fore/hind limb symmetry). Outside of gait evaluation—which was performed on the same day at the same time of day each week—rats were maintained in standard individual cages with limited space for prolonged activity. Rats also moved faster across the force plates during the study (increased gait velocity, increase gait cycles per minute), suggesting extended periods of voluntary activity may have create some discomfort. These data would suggest that rats were demonstrating compensatory behavior with their forelimbs and a result of induced BMLs affecting their hind limbs. Non-invasive kinetic methods to evaluate weight-bearing distribution in rats have been validated as a sensitive measure to predict limb dysfunction post-injury.[32] Interestingly, no significant changes were detected in the stance phase or swing phase of the stride. This may have been due to the fact that the experimental model utilized both hindlimbs, so a distinct change which might be seen in these parameters if only one limb were affected would not have been observed.

Fluid signal observed within the medial femoral condyle on MRI was consistent with a BML. The fluid signal appeared hyperintense on PDFS and IWFS images, and intermediate on T1-weighted images. BMLs were most consistently visible on PDFS images, and did not appear

to change in total volume over the course of the study. On water only images using an IWFS sequence, the BML was more visible over time, with an increase in observed volume at days 45 and 90. These differences between sequences suggests the BML is dynamic and may change in composition over time. Normal bone marrow is a fat-rich tissue, particularly in the distal aspect of the femur which is not a prominent hematopoietic site.[33] At 14 days, the increased signal intensity in PDFS images likely represents a combination of fluid and fat, and is likely visible due to partial fat saturation failure and field inhomogeneities. The water only IWFS sequence is not optimized to image fat, and detection of this combination of tissues results in a smaller volume of the BML at early timepoints. As the BML ages, it contains a larger amount of fluid, which presents as a more even appearance in the volume of signal intensity between the PDFS and IWFS sequences. For this model, the first 45 days after BML induction appear to be critical for changes in BML volume and tissue characteristics. Intracortical remodeling of bone in adult rats is reported to occurring quickly with microdamage—reducing by almost 40% in 10 days.[34] However, the focal defect associated with the needle tract here is more substantial than microdamage secondary to bone fatigue as reported in the Bentolila et al study, so it is reasonable that bony remodeling is actively occurring over the 6 weeks following BML induction, changing the appearance of this lesion on MRI. The maintenance of BML volume and percentage of the medial femoral condyle affected by the BML for fat only IWFS image, suggests sclerosis and remodeling within the bone, especially at the later timepoints. Sclerosis and haversian remodeling within the subchondral and trabecular bone is consistent with what was observed in later timepoints in the experimentally-induced BMLs in the ovine femorotibial joint.

BMLs were still visible after 90 days in the medial femoral condyle of rats. Histologic evaluation of BMLs in the rat femur followed a similar progression to what was observed in the ovine femur. Histologic evaluation timepoints were slightly different in this study compared to timepoints in the sheep study. At 14 days, the proportion of inflammatory cell infiltrate was pronounced in the rat model, demonstrating the intensity of the physiologic response to trauma to the bone. Although dense repair tissue predominates at 90 days in both the rat and the sheep, the characteristics of the tissue differ. The increase in endochondral tissue observed in the rat likely is related to the ability of these animals to spontaneously heal articular cartilage defects[14], and the young age of these animals. Further follow-up would be worthwhile to understand how the BML may demonstrate healing or resolution over a longer period. It would also be worthwhile to examine whether these characteristics are different in more aged animals, which arguably may be more relevant to what is observed in older humans.

Rats were chosen due to their large size (relative to mice) for surgery and imaging, inherent exercise ability for mobility outcomes, and the fact they are a validated preclinical animal model for investigation of OA.[35] Skeletally maturity in rats is reached by 16 weeks of age, however weight and skeletal measurements taken over the study demonstrate that rats were still growing. Therefore, the results presented here may be particularly relevant for adolescents and young adults (i.e., 13-25 years of age) who develop BMLs secondary to acute traumatic injuries.

Caveats and limitations of this study include that a bilateral hind limb model was used for BMLs. While a bilateral design was selected in order to gather the strongest data for validation of this experimental model, it does not typically represent the clinical scenario, where BMLs tend to affect one limb. Further studies are warranted to fully characterize the compensatory

effects on unaffected limbs. Baseline measurements in animals were used as a reference standard for serial mobility evaluation, however changes in some parameters, such as stance time, stride time, and swing time, may have been under-represented. Days 74-88 also demonstrated notable differences in mobility parameters from earlier timepoints, and a longer study duration would be needed to understand if these changes represent normalization of mobility parameters or correlate with more chronic changes within the bone and joint. Confirmation of BMLs in all limbs was possible at all timepoints, however, conspicuity of lesions was not always possible across all sequences. BMLs were frequently only observed on one or two 1.2 mm slices using the aforementioned MR system, making ideal positioning of the animal critical for comprehensive evaluation. Judicious interpretation of MR images is also critical, as normal microstructures in the rat knee may be misinterpreted for arthritic changes.[36] A 22-gauge needle provided a consistent appearance of the BML, however a larger gauge or solid-core needle may create a larger BML which would be more easily identified. As with any preclinical animal model, there are aspects of rodent bone which do not fully recapitulate sheep, horse, or human bone. Structurally, cortical bone contributes to a much greater proportion in bone mass in the rodent femur compared to humans.[37] Young (<8 months old) rats lack Haversian systems, however continuous intracortical bone remodeling does occur, but appears to be a more age-related phenomenon and is greater in older rats.[38,39] The biomechanics of the rat stifle joint are also different from humans, resulting in different patterns of cartilage loading.[14,40] Despite these differences, the relative size of the rat and availability of high-resolution imaging options for assessment of joint structures *in situ* make this an appropriate preclinical model. Although this study was sufficiently powered for experimental model validation, increasing the number of

animals in the study may further elucidate the significance of some of the observed trends across mobility and imaging parameters.

The results from this study demonstrate a consistent and reproducible experimental model for BMLs using the femorotibial joint of the rat, altered mobility within affected limbs, and histological evidence of persistent inflammation within the BML. The imaging and histologic findings are similar to what has been reported clinically in dogs, horses and humans; and was similar to the experimental model described in sheep.[19–21,41–45] The subclinical gait-modifying effects of BMLs in the absence of other lesions advances demonstrates that alterations in the subchondral bone can affect the functionality of the joint as a whole. Collectively, this work provides an additional preclinical animal model for evaluation of BMLs, enabling a greater understanding of the biological effects of this condition. Future work focused on the cellular characteristics and gene expression of BMLs will yield a greater understanding of this condition in the pathophysiology of joint health and disease across species.

5.5 Figures

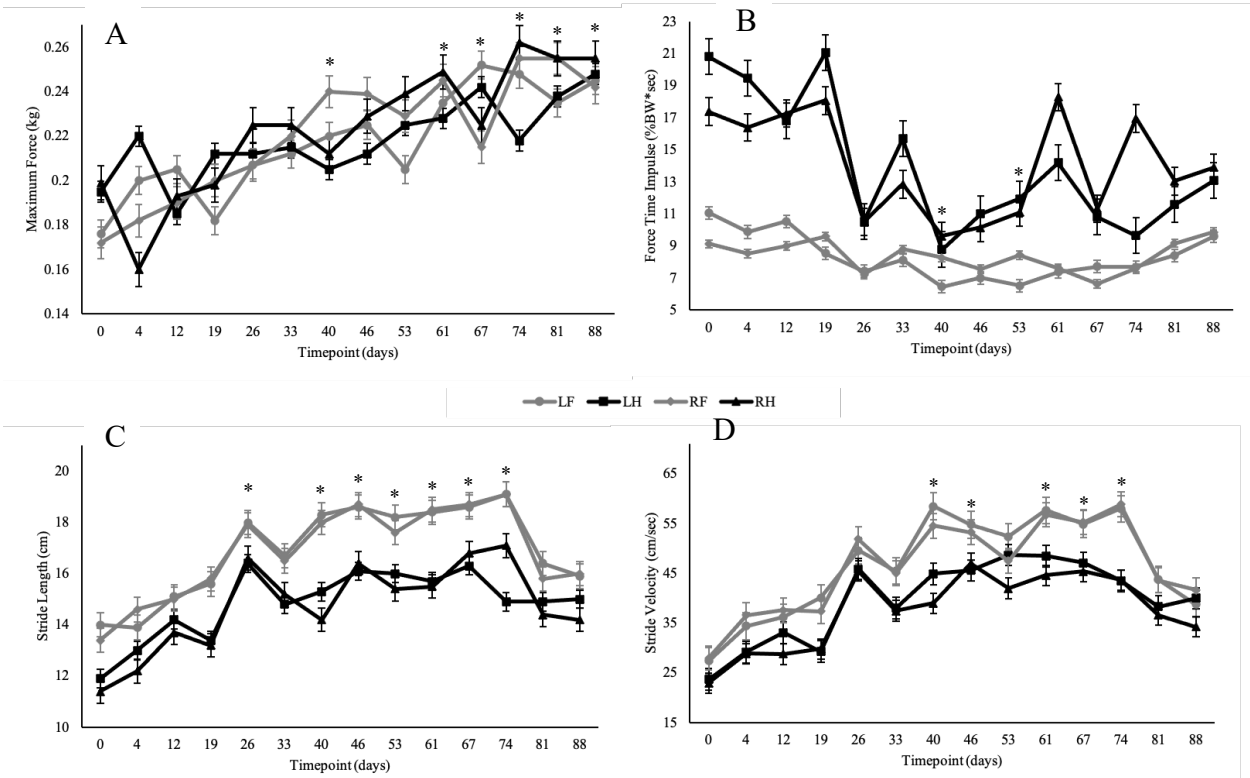

Figure 5.1 – Voluntary weight bearing gait parameters from analysis using the Tekscan Rodent Walkway System before (Timepoint 0) and after (Timepoints 4-88) experimental induction of bone marrow lesions in the right and left hind limbs of male and female rats. Mean ± standard error values for (A) stride length (cm), (B) stride velocity (cm/sec), (C) maximum force (kg), and (D) force time impulse (percent body weight*seconds). Asterisk indicates a significant ($P <$ 0.05) difference between a given timepoint and baseline (day 0) in the forelimbs.

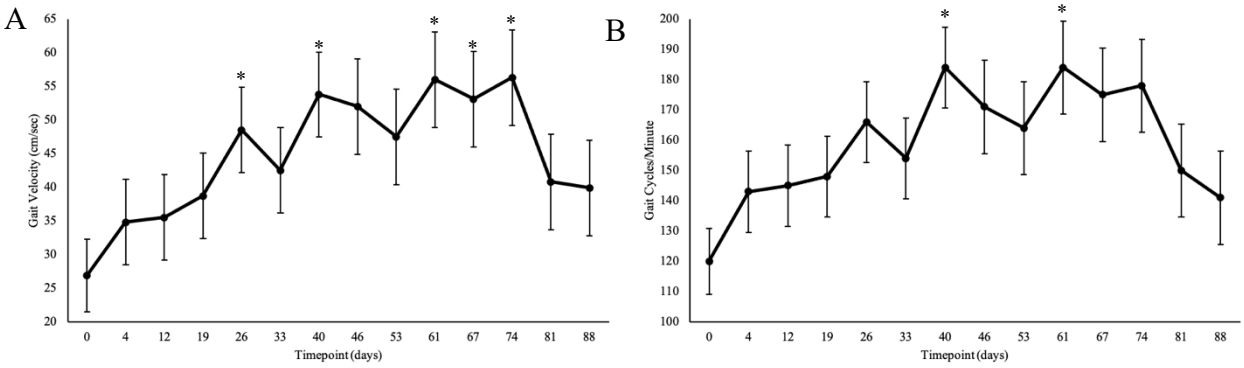

Figure 5.2 – Voluntary weight bearing gait parameters from analysis using the Tekscan Rodent Walkway System before (Timepoint 0) and after (Timepoints 4-88) experimental induction of bone marrow lesions in the right and left hind limbs of male and female rats. Mean ± standard error values for forelimb (A) gait velocity and (B) gait cycles per minute. Asterisk denotes a significant difference ($P < 0.05$) between timepoint and baseline values.

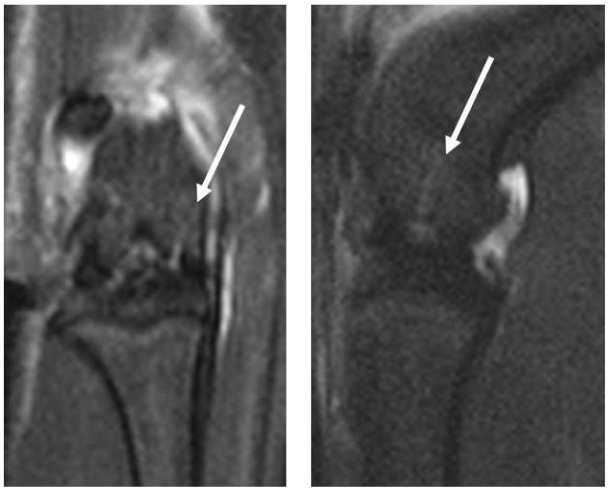

Figure 5.3 – Cranial (left) and sagittal (right) plane proton density fat suppressed images of the femorotibial joint treated with direct penetration of the articular surface of the medial femoral condyle with a 22-gauge needle to a depth of 2 mm. A bone marrow lesion is visible as increased signal intensity within the subchondral and trabecular bone of the medial femoral condyle (white arrow).

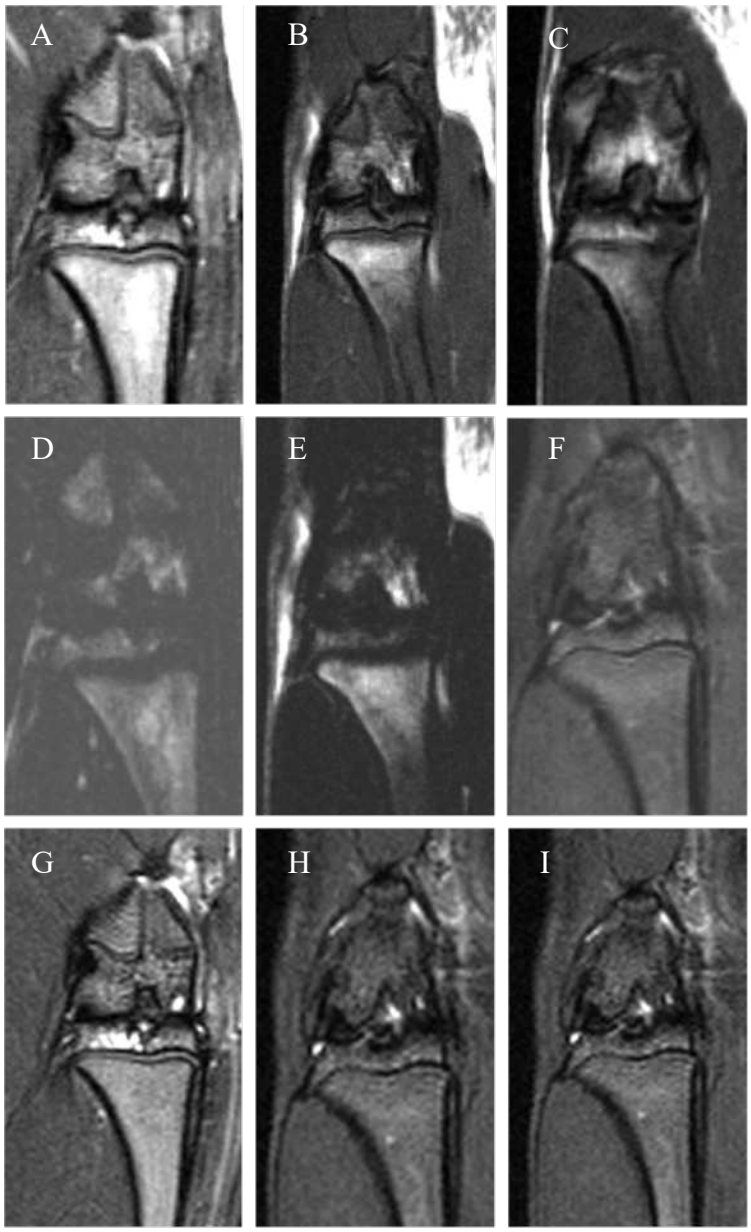

Figure 5.4 – Serial cranial plane images of experimentally-induced bone marrow lesions (BMLs) from various fluid-sensitive sequences on magnetic resonance imaging (MRI). (A-C) Intermediate-weighted fat suppression fat only sequence images; (D-F) intermediate-weighted fat suppression water only sequence images; (G-I) proton density fat saturation (PDFS) sequence images. Each column represents a different imaging timepoint. Left column, 14 days post-BML induction; middle column, 45 days post-BML induction; 90 days post-BML induction. A linear hyperintensity is visible in the medial femoral condyle and persists throughout the 90-day study, extending beyond the 2 mm impact depth.

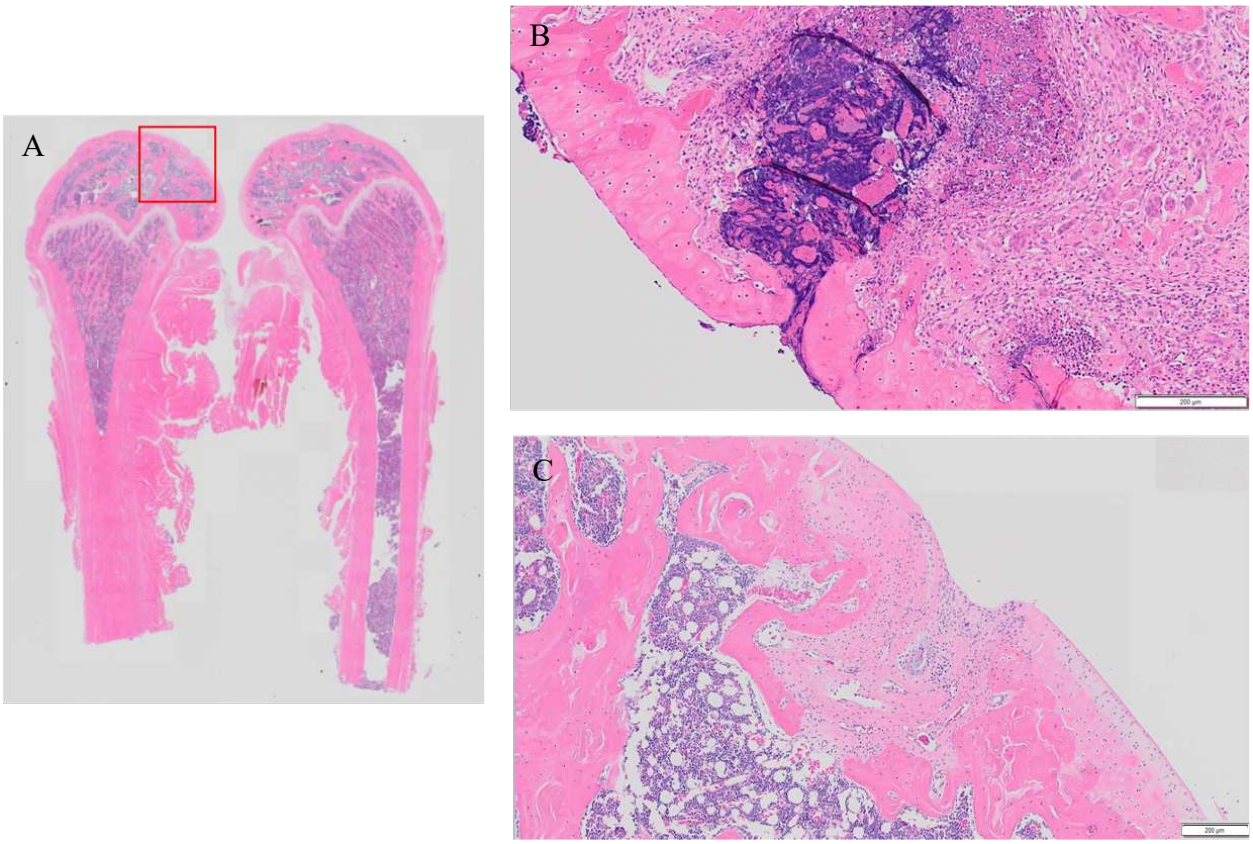

Figure 5.5 – Histologic sections with hematoxylin and eosin stain from the distal femur of a rat with experimentally-induced bone marrow lesions (BMLs). Low magnification (A) of both medial (left) and lateral (right) femoral condyles demonstrates localization of the BML. BMLs are dynamic, characterized by predominantly inflammatory cell infiltrate at 14 days after experimental induction (B), which is gradually replaced by fibrous repair tissue, an increase in cartilaginous matrix, and a thickening of the subchondral bone plate by 90 days (C).

5.6 Tables

Table 5.1 – Mean ± standard error for the percent of the medial femoral condyle with a visible bone marrow lesion (BML), volume of BML, signal-to-noise (SNR) and contrast-to-noise (CNR) ratios of BMLs from intermediate-weight fat suppressed (IWFS) and proton density fat saturation (PDFS) fluid-sensitive magnetic resonance (MR) images across the 90-day study. Baseline measurements were taken in the same location of the condyle as BMLs by overlaying MR images. Different letters indicate a significant ($P < 0.05$) difference between timepoints for a specific sequence and plane combination.

Timepoint	Plane	Sequence	Perc. Condyle BML	Vol. of BML (mm^3)	SNR	CNR
Baseline	Cranial	IWFS, fat only	--	--	21.1 ± 3.43	5.142 ± 3.74
		IWFS, water only	--	--	8.6 ± 5.13	5.23 ± 4.67
		PDFS	--	--	16.3 ± 1.88	-2.45 ± 3.46
	Sagittal	IWFS, fat only	--	--	10.21 ± 2.17	-3.47 ± 2.47
		IWFS, water only	--	--	4.27 ± 1.14	2.624 ± 1.018
		PDFS	--	--	7.52 ± 1.15	-3.52 ± 1.79
3 days	Cranial	IWFS, fat only	9.06 ± 30.5[a]	0.545 ± 1.92[a]	18.6 ± 4.48	-1.166 ± 3.74
		IWFS, water only	16.5 ± 9.95[a]	0.674 ± 1.4[a]	4.59 ± 6.27	1.63 ± 4.67
		PDFS	76.7 ± 22.6	5.6 ± 1.598	16.8 ± 2.47	-7.06 ± 3.46
	Sagittal	IWFS, fat only	18 ± 9.78[a]	2.03 ± 0.972	8.66 ± 2.39	-6.38 ± 2.47
		IWFS, water only	9.02 ± 9.08[a]	1.44 ± 1.06[a]	4.57 ± 1.45	0.076 ± 1.018
		PDFS	28.2 ± 9.89	3.92 ± 1.31	10.83 ± 1.38	-3.72 ± 1.79
14 days	Cranial	IWFS, fat only	41.9 ± 16.5[a]	2.534 ± 1.04[a]	20.6 ± 2.9	-0.935 ± 2.79
		IWFS, water only	40.2 ± 7.33[a]	1.88 ± 1.1[a]	14.72 ± 5	6.98 ± 3.51
		PDFS	58.2 ± 14.1	3.33 ± 0.993	19.8 ± 1.58	-5.5 ± 2.68
	Sagittal	IWFS, fat only	29 ± 8.71	4.28 ± 0.684	11.42 ± 1.85	-3.49 ± 2.03
		IWFS, water only	24.6 ± 10.98	3.43 ± 1.34[a]	4.01 ± 1.72	-0.701 ± 0.751
		PDFS	28.3 ± 7.57	3.79 ± 1.01	8.41 ± 1.08	-4.32 ± 1.41
45 days	Cranial	IWFS, fat only	136.24 ± 23.7[b]	8.808 ± 1.49[b]	18.5 ± 3.85	8.435 ± 4.3
		IWFS, water only	88.5 ± 8.86[b]	6.938 ± 1.31[b]	14.44 ± 5.88	12.51 ± 5.34
		PDFS	58.4 ± 20.2	5.01 ± 1.428	13.6 ± 2.22	-8.26 ± 3.89
	Sagittal	IWFS, fat only	42.1 ± 10.65[b]	5.79 ± 1.222	11.25 ± 2.81	-4.59 ± 2.7
		IWFS, water only	66.33 ± 10.94[b]	9.68 ± 1.33[b]	7 ± 1.72	1.326 ± 1.206
		PDFS	41 ± 10.65	4.82 ± 1.41	8.55 ± 1.53	-2.32 ± 2
90 days	Cranial	IWFS, fat only	52.03 ± 20.1[a]	4.482 ± 1.26	13.6 ± 3.4	-0.639 ± 3.71
		IWFS, water only	62.2 ± 7.42[b]	5.185 ± 1.13[b]	13.13 ± 5.11	10.54 ± 4.63
		PDFS	49.5 ± 20.2	2.46 ± 1.428	12.5 ± 2.23	-14.39 ± 3.42
	Sagittal	IWFS, fat only	45.8 ± 9.65[b]	4.31 ± 0.894	10.42 ± 2.26	-5.19 ± 2.44
		IWFS, water only	25.86 ± 9.16	3.98 ± 1.09[a]	5.56 ± 1.43	1.555 ± 1.033
		PDFS	52 ± 12.05	7.52 ± 1.6	6.84 ± 1.74	-8.13 ± 1.77

5.7 References

1. Little C, Hunter D. Post-traumatic osteoarthritis: from mouse models to clinical trials. Nat Rev Rheumatol 2013;9:485–497.

2. Tanamas S, Wluka A, Pelletier J, et al. Bone marrow lesions in people with knee osteoarthritis predict progression of disease and joint replacement: a longitudinal study. Rheumatology 2010;49:2413–2419.

3. Kuyinu E, Narayanan G, Nair L, et al. Animal models of osteoarthritis: classification, update, and measurement of outcomes. J Orthop Surg Res 2016;11:19.

4. Bendele A. Animal models of osteoarthritis. J Musculoskelet Neuronal Interact 2001;1:363–376.

5. Lampropoulou-Adamidou K, Lelovas P, Karadimas E, et al. Useful animal models for the research of osteoarthritis. Eur J Orthop Surg Traumatol 2014;24:263–271.

6. Bouchgua M, Alexander K, André d'Anjou M, et al. Use of routine clinical multimodality imaging in a rabbit model of osteoarthritis - part I. Osteoarthr Cartil 2009;17:188–196.

7. Maynard R, Villani D, Schroeder W, et al. Surgical Induction of Posttraumatic Osteoarthritis in the Mouse. Methods Mol Biol 2021;2230:91–103.

8. Lorenz J, Grässel S. Experimental osteoarthritis models in mice. Methods Mol Biol 2014;1194:401–419.

9. Consden R, Doble A, Glynn LE, et al. Production of a chronic arthritis with ovalbumin. Its retention in the rabbit knee joint. Ann Rheum Dis 1971;30:307–315.

10. Ross T, Kisiday J, Hess T, et al. Evaluation of the inflammatory response in experimentally induced synovitis in the horse: a comparison of recombinant equine interleukin 1 beta and lipopolysaccharide. Osteoarthr Cartil 2012;20:1583–1590.

11. Schweitzer M, White L. Does altered biomechanics cause marrow edema? Radiology 1996;198:851–853.

12. Sadatsuki R, Ishijima M, Kaneko H, et al. Bone marrow lesion is associated with disability for activities of daily living in patients with early stage knee osteoarthritis. J Bone Min Metab 2018;37:529–536.

13. Kayode O, Day G, Mengoni M, et al. Mechanical consequences of bone marrow lesions in the tibiofemoral joint: a finite element study. In: Orthopaedic Proceedings.; 2020:103-B:SUPP 2, 61.

14. McCoy AM. Animal Models of Osteoarthritis: Comparisons and Key Considerations. Vet Pathol 2015;52:803–818.

15. Clarke K, Heitmeyer S, Smith A, et al. Gait analysis in a rat model of osteoarthrosis. Physiol Behav 1997;62:951–954.

16. Hoffmann M, Hopf R, Niederreiter B, et al. Gait changes precede overt arthritis and strongly correlate with symptoms and histopathological events in pristane-induced arthritis. Arthritis Res Ther 2010;12:R41.

17. Broomfield C, Meis N, Johnson J, et al. Optimization of ovine bone decalcification for increased cellular detail: a parametric study. J Histotechnol 2021:1–7.

18. Faul F, Erdfelder E, Lang A, et al. G*Power 3: a flexible statistical power analysis program for the social, behavioral, and biomedical sciences. Behav Res Methods 2007;39:175–191.

19. Winegardner KR, Scrivani P V., Krotscheck U, et al. Magnetic resonance imaging of subarticular bone marrow lesions in dogs with stifle lameness. Vet Radiol Ultrasound 2007;48:312–317.

20. Olive J, Mair TS, Charles B. Use of standing low-field magnetic resonance imaging to diagnose middle phalanx bone marrow lesions in horses. Equine Vet Educ 2009;21:116–123.

21. Barrett MF, Selberg KT, Johnson SA, et al. High field magnetic resonance imaging contributes to diagnosis of equine distal tarsus and proximal metatarsus lesions: 103 horses. Vet Radiol Ultrasound 2018;59:587–596.

22. Filardo G, Kon E, Tentoni F, et al. Anterior cruciate ligament injury: post-traumatic bone marrow oedema correlates with long-term prognosis. Int Orthop 2016;40:183–190.

23. Gong J, Pedoia V, Facchetti L, et al. Bone marrow edema-like lesions (BMELs) are associated with higher T1ρ and T2 values of cartilage in anterior cruciate ligament (ACL)-reconstructed knees: a longitudinal study. Quant Imaging Med Surg 2016;6:661.

24. Felson DT, McLaughlin S, Goggins J, et al. Bone Marrow Edema and Its Relation to Progression of Knee Osteoarthritis. Ann Intern Med 2003;139:330.

25. Kornaat PR, Kloppenburg M, Sharma R, et al. Bone marrow edema-like lesions change in volume in the majority of patients with osteoarthritis; associations with clinical features. Eur Radiol 2007;17:3073–3078.

26. Yochum T, Barry M. Bone marrow edema caused by altered pedal biomechanics. J Manip Physiol Ther 1997;20:56–59.

27. Grampp S, Henk C, Mostbeck G. Overuse edema in the bone marrow of the hand: demonstration with MRI. J Comput Assist Tomogr 1998;22:25–27.

28. Lazzarini K, Troiano R, Smith R. Can running cause the appearance of marrow edema on MR images of the foot and ankle? Radiology 1997;202:540–542.

29. Major N. Role of MRI in prevention of metatarsal stress fractures in collegiate basketball players. Am J Roentgenol 2006;186:255–258.

30. Gil H, Levine S, Zoga A. MRI findings in the subchondral bone marrow: a discussion of conditions including transient osteoporosis, transient bone marrow edema syndrome, SONK, and shifting bone marrow edema of the knee. Semin Musculoskelet Radiol 2006;10:177–186.

31. Chantelau E, Richter A, Ghassem-Zadeh N, et al. “Silent” bone stress injuries in the feet of diabetic patients with polyneuropathy: a report on 12 cases. Arch Orthop Trauma Surg 2007;127:171–177.

32. Pardes A, Freedman B, Soslowsky L. Ground reaction forces are more sensitive gait measures than temporal parameters in rodents following rotator cuff injury. J Biomech 2016;49:376.

33. Schett G. Bone Marrow Edema. Ann N Y Acad Sci 2009;1154:35–40.

34. Bentolila V, Boyce TM, Fyhrie DP, et al. Intracortical remodeling in adult rat long bones after fatigue loading. Bone 1998;23:275–281.

35. Gerwin N, Bendele AM, Glasson S, et al. The OARSI histopathology initiative – recommendations for histological assessments of osteoarthritis in the rat. Osteoarthr Cartil 2010;18:S24–S34.

36. Wang H, Wang Y-XJ, Griffith J, et al. Pitfalls in interpreting rat knee joint magnetic resonance images and their histological correlation. Acta radiol 2009;50:1042–1048.

37. Bagi C, Wilkie D, Georgelos K, et al. Morphological and structural characteristics of the proximal femur in human and rat. Bone 1997;21:261–267.

38. Kalu DN. The ovariectomized rat model of postmenopausal bone loss. Bone Miner 1991;15:175–191.

39. Baron R, Tross R, Vignery A. Evidence of sequential remodeling in rat trabecular bone: Morphology, dynamic histomorphometry, and changes during skeletal maturation. Anat Rec 1984;208:137–145.

40. Cook JL, Hung CT, Kuroki K, et al. Animal models of cartilage repair. Bone Joint Res 2014;3:89.

41. Martig S, Boisclair J, Konar M, et al. MRI characteristics and histology of bone marrow lesions in dogs with experimentally induced osteoarthritis. Vet Radiol Ultrasound 2007;48:105–112.

42. Zani DD, De Zani D, Biggi M, et al. Use of magnetic resonance imaging in the diagnosis of bone marrow edema in the equine distal limb: Six cases. Vet Res Commun 2009;33:225–228.

43. Biggi M, Zani DD, De Zani D, et al. Magnetic resonance imaging findings of bone marrow lesions in the equine distal tarsus. Equine Vet Educ 2012;24:236–241.

44. O'Hare A, Shortt C, Napier N, et al. Bone marrow edema: patterns and clinical implications. Semin Musculoskelet Radiol 2006;10:249–257.

45. Akhavan S, Martinkovich S, Kasik C, et al. Bone Marrow Edema, Clinical Significance, and Treatment Options: A Review. J Am Acad Orthop Surg 2020;28:e888–e899.

CHAPTER 6:

SUMMARY, CONCLUSIONS, AND FUTURE DIRECTIONS

6.1 Significance of Work

The goal of the research presented in this dissertation was to critically explore bone marrow lesions (BMLs) as an indicator of subchondral bone disease, and the use of volumetric imaging modalities for the detection of fluid within bone. Compelling reports have been published citing BMLs as early indicators of structural deterioration of the subchondral bone, suggesting the presence of these lesions may serve as a marker for maladaptive change within the subchondral bone and articular cartilage. At present, there is a relative paucity of information about the biological behavior of BMLs, as in some cases BMLs appear to accelerate degenerative change within the joint, while in other cases they resolve completely. The long-term implications of BMLs on joint health remains under investigation. BMLs are typically diagnosed using magnetic resonance imaging (MRI), but advancements in volumetric imaging in both MRI and computed tomography (CT) provide additional opportunities for more comprehensive characterization and monitoring of these lesions over time. Development of an experimental model and optimization of advanced imaging techniques are paramount for understanding the complex biological processes that may influence joint homeostasis secondary to BMLs. The body of work included in this dissertation begins with preliminary studies investigating volumetric imaging capabilities for detection of fluid signal within bone and assessment of the subchondral bone, and progresses to the use of preclinical animal models for the development of an experimental model of BMLs.

An overview of subchondral bone injury and disease, as well as an overview of CT and cone-beam CT (CBCT) technology is described in Chapter 1. Preliminary equine cadaveric work with CT and CBCT suggests the CBCT is quickly developing as a rapid and economical musculoskeletal imaging technique that can provide a high level of spatial detail. Clinical use of CBCT in human medicine and dentistry has yielded additional avenues for investigation of this technology in the veterinary sector. With further optimization, CBCT may be a viable alternative volumetric imaging technique to conventional MRI for assessment of fluid within bone.

In an effort to understand the current capabilities and limitations for imaging fluid within bone using MRI, an *ex vivo* experimental model was developed as described in one of the three preliminary studies presented in Chapter 2. The first preliminary study focused on the development of an *ex vivo* bone fluid model served two purposes: first to explore the capabilities of conventional fluid-sensitive sequences using high-field (1.5 T and 3 T) MR units, and to assess whether MR was a sufficiently sensitive technique to distinguish between biological fluid types based on signal intensity. An experimental model for bone fluid was able to be created through injection of fluid through a cannulated screw into cadaveric equine bone, however different biological fluids were not able to be distinguished, likely given the inherent similarities between fluids due to their overall high water content. Interestingly, the short tau or short T1 inversion recovery (STIR) sequence, which is conventionally used for fluid detection within bone, substantially under-represented the distribution and visible signal for fluid within bone. Modification of the inversion time (TI) facilitated a greater amount of fluid detection using this sequence. A greater magnet strength and use of chemical-shift imaging (e.g., Dixon sequence) enabled a greater detection of known fluid signal within bone.

The second preliminary study in Chapter 2 was focused on an exploration of a limited-view technique for CT. Using a biological phantom and μCT, pixel sparsity regularization proved to be the most ideal technique for visualization of subchondral bone and trabecular detail. Diagnostic quality images could be generated from only 60 projections, compared to a standard 360 projections after the application of a novel algorithm (L1A). Application of sparse-view image reconstruction techniques to data acquired using a CBCT unit resulted in improved image quality with a reduction in artifacts.

The final preliminary study in Chapter 2 assessed the use of tomosynthesis for evaluation of the equine metacarpophalangeal joint, in comparison to radiography, CT and MRI. Tomosynthesis was comparable to radiography for evaluation of subchondral bone, and in one case was more accurate for diagnosis of a pathologic lesion, likely due to the ability of this modality to reduce superimposition of structures. Tomosynthesis remained inferior to CT and MRI, but findings from this study suggest it may be an economical option for musculoskeletal imaging in the horse to provide complimentary information and further detail in cases where a lesion is suspected on radiography.

These small-scale imaging studies discussed in Chapter 2 supported further investigation of BMLs and optimization of volumetric imaging modalities for diagnosis. Chapter 3 focuses on the development of an *in vivo* experimental model for BMLs using the medial femoral condyle of the ovine femorotibial joint. Using this preclinical model for the human knee, direct, focal trauma to all layers of the osteochondral unit, including the articular and calcified cartilage, subchondral and trabecular bone, was sufficient to induce a BML within 14 days of surgery. Transcutaneous application of extracorporeal shockwave was unsuccessful to induce BMLs within the subchondral bone. The induced BML was visible for the duration of the 90-day study.

Findings from this study support the conclusion that BMLs are dynamic, and rapidly change over time. These changes can be characterized, at least to some degree, using the volumetric imaging modalities of CT and MRI. Serial imaging using chemical-shift imaging sequences on MRI facilitated an understanding of how BMLs begin as an influx of fluid and transition to a greater proportion of bone sclerosis due to remodeling within the subchondral and trabecular bone. These findings were also supported through evaluation of BMLs using ante-mortem CT and post-mortem μCT. BMLs can be identified using more contemporary methods with CT, including a dual-energy technique. Macroscopic evidence of osteoarthropathy within the femorotibial joint was not present within 90 days, and the focal pin tract was covered by fibrocartilage within 4 weeks of surgery. Changes observed *in vivo* were further supported through histological assessment of the tissues within the BML, which begin as primarily an inflammatory cellular infiltrate and progress to more dense fibrous tissue over time. Findings from this study demonstrate that the presence of a BML within the subchondral and trabecular bone promotes substantial bone remodeling prior to observable changes within the articular cartilage.

A limitation of this study is the fact that macroscopic evidence of degenerative changes within the joint were not observed after 90 days. The previously developed experimental model in the ovine medial femoral condyle was used again in Chapter 4 for long-term evaluation of BMLs within the femorotibial joint. Experimentally-induced BMLs persist in the medial femoral condyle for at least 12 months, with subchondral cysts visible in the region of the BML by 6 months. These subchondral cysts are visible on both CT and MRI, and correspond to structural changes in the surrounding bone. This work demonstrates how damage to the subchondral bone

can cause irreversible damage and accelerate degeneration of the joint. Further work focused on characterization of the histologic changes in the joint will also be beneficial for this research.

Chapter 5 adapts the aforementioned experimental model for BMLs in the sheep to the rat medial femoral condyle. Consistent with observations from the ovine model, acute, focal trauma to the osteochondral unit is sufficient to create a BML that persists for at least 90 days. The ability to perform quantitative gait assessment is a strong benefit of this model. Gait analysis demonstrated a decrease in hind limb loading and a compensatory increase in forelimb loading after BML induction. It would seem that BMLs may induce subtle changes in gait that can be detected through quantitative methods, and may impact not only the affected joints, but secondarily the supporting joints. Induced BMLs in the rat femorotibial joint have consistent characteristics to those BMLs observed in the sheep, including being observed within 14 days using fluid-sensitive sequences on MR. Histologically, these lesions are also similar and demonstrate an initial influx of inflammatory cellular infiltrate followed by fibrous and fibrocartilaginous repair tissue.

These studies reinforce that a consistent, reproducible experimental model for BMLs is possible, and reflects naturally-occurring, clinical disease states. BMLs appear to be a conserved response to osteochondral damage across species, and preclinical small and large animal models show a consistent response, providing numerous opportunities for translational application of these data. The objectives of these studies included the development of a reproducible experimental model of BMLs that mimic clinical disease, the optimization of volumetric imaging for fluid detection within bone, the characterization of the histologic attributes of BMLs in the absence of other pathologic lesions within the joint, and the validation of novel translational

research models to better understand the role and importance of BMLs across conditions, species, and clinical scenarios.

6.2 Future Directions

There are numerous possibilities for directions for further expansion of these research foci. There is a paucity of information about the underlying cellular, molecular, and immunologic mechanisms of BMLs, all of which warrant further investigation. Amalgamation of information on BMLs across species and conditions—including osteoarthritis, traumatic ligamentous soft tissue injury, rheumatoid arthritis, osteoporosis—is critical to more fully synthesize what is known about this conserved response. Additionally, a greater exploration about the potential role of synovial fluid is needed to understand if this transudate or its breakdown products play a role in inducing or perpetuating BMLs. Samples acquired in these studies could be used for to identify expression of specific cell markers using immunohistochemistry; and complementary techniques of RNA sequencing and proteomics (or metabolomics) likely also hold a role for identifying and quantifying key RNA transcripts and proteins (or metabolic pathways) at play. Use of the sheep and rat preclinical animal models has demonstrated value, and it also may be worthwhile to extrapolate this experimental model into other animals to take advantage of assays and techniques validated in other mammalian species.

Arguably, histologic comparison of this experimental model to naturally-occurring BMLs is needed. Osteochondral samples obtained from clinical cases with naturally-occurring BMLs is possible through coordinate collaboration with others in the veterinary and human medical fields. The techniques used in these studies can be replicated for analysis of clinical osteochondral samples, characterizing similarities and differences. Ultimately once validated, this model may

be used to focus on preserving the health of the subchondral bone and for the development of targeted interventional therapies, as necessary, to mitigate the negative progression of BMLs across species and conditions. The results of this dissertation affirm the importance of the subchondral bone in maintaining the health and function of the articular cartilage and joint as a whole.